Diamond and silicon carbide surface modification for hostile environment applications

by James Beattie

Thesis for the degree of Doctor of Philosophy in the

Faculty of Science, Agriculture and Engineering

July 2020

Acknowledgements

I would like to take this opportunity to thank my supervisor Jon Goss for his expertise, measure and his continual availability for small questions and catch-up chats. Your guidance throughout has been invaluable.

I want to thank all my friends and colleagues who have made my four years in Newcastle a joyous time both inside and outside the office. I'm grateful to have known and made good friends with such wonderful people whom I adore and look forward to seeing for many years to come.

To my family for their support and encouragement, I love you all very much.

Lastly, I would like to share some words of wisdom that best encapsulate my time during my PhD.

> I fear not the man who has modelled ten thousand atoms once, but the man who has modelled one atom ten thousand times.
>
> — Bruce Lee

> I'm just a normal, functioning member of the human race, and there's no way anyone can prove otherwise.
>
> — Mark Corrigan

> I'm too drunk to taste this chicken.
>
> — Colonel Sanders

Abstract

Wide bandgap semiconductors represent exciting new areas of research where they hold considerable advantages over traditional semiconductors, in particular the area of power electronics. Specifically, silicon carbide (SiC) and diamond have received much attention over the years for their high breakdown field, thermal conductivity and resistance to radiation. Materials that can maintain operation with considerable device longevity in extreme environments that enhance efficiency and performance of a given system are highly sought after and attract considerable levels of research. Additionally, demands for more performance out of each device requires a competitive price point, utilising scalable fabrication methods resulting in transistors of smaller dimensions at each generation. The scaling down of these electronics has necessitated atomic level control over thin films of high uniformity and quality. Atomic layer deposition makes possible the formation of monolayer and even sub-monolayer surface coverages. If realised, the potential to radically modify a surface through a thin layer of this type is substantial. Experimentally, creating these layers and subsequently measuring and visualising their electronic properties and structure remains challenging. Constructing theoretical models of such surfaces provides atomic level insight, acting as a validatory platform for experimentally observed surface characteristics and an introductory viability test for new ideas. Density functional theory supplies the means to accurately represent the structure and energy of a given system, where theory and experiment are shown to be in excellent agreement in a number of key areas. In this thesis, it is shown that both SiC and diamond can be modified by chemical termination. Key data include the electronic properties and binding energies. It has been found that SiC modification through the addition of basic elements like hydrogen, chlorine and fluorine leads to positive EAs. Intriguingly lithium termination leads to an EA of almost zero. Lithium termination is unexpectedly non-metallic, revealed only through analysis of the electronic band structure. Additionally, it is necessary to obtain information on the energetic favourability of the position of single atoms to single monolayers atop the surface. Crystallogens (Si and Ge) on diamond are studied as a function of fractional monolayer coverage. Indeed, periodicity and geometry play a crucial role in uncovering the lowest energy structure. A 67% coverage is shown to represent the equilibrium coverage of the diamond surface terminated by Si and Ge, creating negative EA surfaces of -1 eV. Links can be drawn between experimentally observed resonant states of the same coverage with band structure data, supporting our conclusions. Electron affinity forms a key feature of the project, where its value factors in numerous surface focused applications. In the area of emission, a low or negative electron affinity puts the vacuum level just above

or even below the conduction band. Tailoring surfaces to emit more efficiently reduces power consumption and increases electron beam current density, where >1 A/cm^2 applications are at the cutting edge of research areas including particle physics and energy harvesting. This project explores different surfaces of diamond and silicon carbide under a range of novel terminations, focusing mainly on structural, thermodynamic and electronic properties.

Publications

• Beattie, J. M. A., et al. "Electron-affinity and surface-stability of aluminium-oxide terminated diamond surfaces." Diamond and Related Materials 94 (2019): 137-145.

• Beattie, J. M. A., et al. "Structure and electron affinity of silicon and germanium terminated (001)-(2 × 1) diamond surface" Journal of Physics: Condensed Matter 31.39 (2019): 395001.

• Beattie, J. M. A., et al. "Structure and electron affinity of $(11\bar{2}0)$–X 4H–SiC surface." Applied Surface Science (2020): 145986.

• Beattie, J. M. A., et al. "Structure and electron affinity of the (0001) surfaces: A methodological approach for polar systems" Journal of Physics: Condensed Matter (2020) – Under review.

Contents

Acronyms

AIMPRO	Ab Initio Modelling Program.
ALD	Atomic Layer Deposition.
ARPES	Angle Resolved Photoelectron Spectroscopy.
b2b	Back to Back.
BCC	Body Centred Cubic.
CBM	Conduction Band Minimum.
CD	Charge Density.
CVD	Chemical Vapour Deposition.
DAP	Diamond Amplified Photocathode.
DFT	Density Functional Theory.
DoS	Density of States.
EA	Electron Affinity.
FCC	Face Centred Cubic.
FET	Field Effect Transistor.
GGA	Generalised Gradient Approximation.
HCP	Hexagonal Close Packing.
HGH	Hartwigsen-Goedecker-Hutter.
ISFET	Ion-sensitive FET.
KS	Kohn-Sham.
LDA	Local Density Approximation.
LEED	Low-energy Electron Diffraction.
MOSFET	Metal-oxide-semiconductor FET.
MP	Monkhorst-Pack.
NEA	Negative Electron Affinity.
NV	Nitrogen Vacancy.
PBC	Periodic Boundary Condition.
pDoS	Projected Density of States.
PEA	Positive Electron Affinity.
SEE	Secondary Electron Emission.
SiC	Silicon Carbide.
SOI	Silicon on Insulator.
TEC	Thermionic Energy Converter.

VBM	Valence Band Maximum.
WF	Work Function.
XPS	X-ray Photoelectron Spectroscopy.

Mathematical Notation

A_{R}	Richardson constant.
E	Electric field.
E_0	Incident electron beam energy.
E_{H}	Hartree energy.
E_{ads}	Surface formation energy per surface site.
E_{cbm}	Conduction band minimum.
E_{crit}	Critical electric field.
E_{c}	Conduction band.
$E_{\mathrm{e-i}}$	Electron-ion energy.
E_{f}	Fermi energy.
E_{g}	Band gap.
E_{ii}	Ion-ion energy.
E_{i}	Total system energy.
E_{k}	Kinetic energy.
E_{slab}	Electric field across the slab.
E_{step}	Surface potential step.
E_{surf}	Surface energy.
E_{tot}	Total slab energy.
E_{vac}	Electric field across the vacuum.
E_{vbm}	Valence band maximum.
E_{v}	Valence band.
E_{xc}	Exchange-correlation energy.
J	Current density.
N_{d}	Doping density.
Q	Total charge.
T	Temperature.
V_{b}	Breakdown voltage.
V_{i}	Potential energy.
Z_{disp}	Surface normal displacement.

Z_{i}	Ion of mass Z.
$\Delta\ E_{\mathrm{bulk}}$	Bulk and slab energy alignment shift.
$\Delta\ V_{\mathrm{slab}}$	Potential difference across the slab.
Γ	Brillouin-zone centre.
β	Field enhancement factor.
χ	Electron affinity.
$\hat{H}$	Hamiltonian.
$\hbar$	Planck's constant.
μ_{x}	Chemical potential of a given bulk species.
ϕ	Work function.
ψ	Wave function.
ψ_{KS}	Kohn-Sham Wavefunction.
ψ_{pseudo}	Pseudopotential wavefunction.
ψ_{true}	True wavefunction.
$\vec{\mathbf{r}}$	Position vector.
$\vec{d}$	Internuclear displacement vector.
$\vec{k}$	k-space.
$\vec{p}$	Dipole moment.
$a.u.$	Atomic units.
$a0$	Lattice constant.
d	Distance.
eV	Electron volt.
k_{B}	Boltzmann constant.
m	Electron mass.
n	Charge density.
$n \times m$	Surface area.
q	Charge of an electron.
Å	Angstrom.

1. Rationale

1.1 Introduction

When designing a device, one of the first and most important steps is to consider the choice of material. It is upon this which all future processing decisions rely. With a myriad of semiconductor materials, device types and structures, the material must deliver adequate performance to both physically and electronically meet the desired specifications. High-power devices in particular must withstand extreme temperatures, hostile environments, large switching voltages and high electric fields.

At room temperature, silicon is still king – although the current default material for sub 100 °C electronics, it is not well suited for extreme environments [1, 2, 3]. With a room temperature bandgap of only 1.1 eV, the instrinsic carrier concentration increases to a significant fraction of the total carrier concentration at temperatures above 100 °C. Silicons intrinsic carrier concentration at room temperature is of the order of 10^{10} cm^{-3}. For temperatures above this, carriers have enough energy to jump from the valence band to the conduction band purely from thermal activation, creating an ambient current even under reverse bias [4, 5]. To counteract this, some high temperature integrated circuits utilise high doping concentrations, but this creates larger electric fields which can lead to breakdown, parasitic capacitance increases and may interfere with scaling limits [6]. For sensing applications, an increase in thermal carriers would increase dark current [7], reducing the signal to noise ratio and rendering the device unable to differentiate between a real signal and thermal noise. Semiconductors with large bandgaps (>2.5 eV) have intrinsic carrier concentrations many orders of magnitude lower than silicon at room temperature [8], allowing them to perform at temperatures several times greater than silicon and still resist thermal activation of carriers at high doping/intrinsic carrier ratios.

At temperatures around 300 °C the doping carrier concentration of Si is effectively eliminated [9], reverting a p-n diode or transistor to just a resistor. Silicon-on-insulator (SOI) technology provides a path to extend the temperature range of silicon to $200 - 300$ °C for low power output applications. At high powers, self-heating at internal junctions and high electrothermal stress means silicon devices can not perform in this range [10]. Another drawback is the increased fabrication costs, where it may become more feasible for single use wide bandgap circuits to be employed if costs are comparable.

In the $300-600$ °C temperature range silicon undergoes plastic deformation [11], and atoms begin to diffuse creating defects. At temperatures where silicon is unusable, devices fabricated from

wide bandgap semiconductors should be able to operate comfortably with minimal performance losses.

High power devices require low on-state resistance, high thermal conductivity, high operating frequency and low switching losses [12, 13]. The breakdown voltage is an important reference for high power devices as it is the maximum reverse bias a diode can withstand before conducting in the opposite direction. Breakdown voltage is proportional to:

$$V_{\mathrm{b}} \sim \frac{\varepsilon E_{\mathrm{crit}}^2}{2qN_{\mathrm{d}}} \tag{1}$$

where E_{crit} is the critical electric field, ε is the permittivity, q is the charge of an electron and N_{d} is the doping density. Normalised for doping density and drift region width, wide bandgap semiconductors can withstand orders of magnitude higher blocking voltages [14]. Drift regions for any given breakdown voltage are thinner for wide bandgap semiconductor materials [15] compared to smaller bandgaps. This lowers on-state resistance, decreases device response time and increases device efficiency.

When exposed to high energy radiation, silicon suffers due to the relatively low carrier removal rate energy [16]. Irradiating semiconductors leads to the formation of deep centres [17]. If in an n-type region for example, these centres could become acceptors, transferring charge from the conduction band. This would reduce the mobility of the device, affecting conductivity and increasing bulk resistivity [18]. A relationship between carrier removal rate and lattice constant was made [19] where smaller lattice constants, and in general a wider bandgap, have a higher resistance to the removal of carriers.

For such devices operating in harsh conditions, technological advances can be found through the use of alternative semiconductors.

1.2 Diamond

Diamond is a solid allotrope of elemental carbon, renowned mainly for its hardness and visual clarity. Diamond co-ordinates tetrahedrally to 4 nearest neighbours with a bondlength of 1.54 Å at an angle of 109.5° (Figure 1). The covalent bonding arrangement sp^3, although chemically similar to another carbon allotrope graphite (sp^2), is what provides the foundation for diamonds superlative mechanical and optical properties [20, 21]. A lesser known use for diamond is in the world of electronics.

Whilst technically an electrical insulator, intrinsic bulk diamond posesses remarkable qualities in areas that other semiconductors can not live up to (Table 1). Carrier mobility influences the

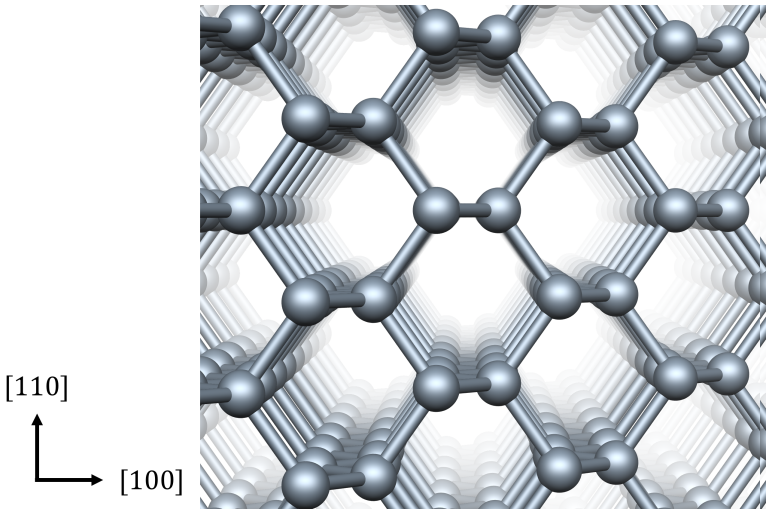

Figure 1: A repeated bulk diamond cell with crystallographic directions included.

Table 1: Fundamental properties of a select number of semiconductors [22, 23]. Where anisotropy factors in the properties are reported at their most favourable values.

Property	Diamond	4H–SiC	GaN	Si
Bandgap (eV)	5.45	3.23	3.45	1.12
Breakdown field ($kVcm^{-1}$)	10000	3000	5000	300
Hardness (Mohs)	10	9	6	6
Electron mobility ($cm^2V^{-1}s^{-1}$)	2200	1000	1250	600
Hole mobility ($cm^2V^{-1}s^{-1}$)	1600	115	850	600
Thermal conductivity ($Wcm^{-1}K^{-1}$)	20	5	1.3	1.5

response time of a device thus any high performance device must seek to maximise the mobility. Thermal conductivity allows diamond devices to handle high power and high temperatures more easily, dissipating heat itself where other devices may have to adapt specific heat management systems [24]. A wide bandgap more easily resists thermal activation of carriers in to the conduction band and contributes to a large breakdown field, further bolstering its use in power electronics [25]. Couple this with extreme radiation hardness [16] and relative chemical and biological inertness, it becomes an obvious choice for extreme environment electronics.

On paper, one might think this would warrant the widespread use of such a material in every day devices. Diamond's "Achilles' heel" lies in the lack of a sufficiently shallow n-type dopant. This limits the materials use in low-temperature CMOS technology and other NMOS applications. Table 2 shows that somewhat shallow p-type doping is possible with boron, where considerable amounts of energy have gone into finding suitable doping species for diamond [27, 28, 29, 30,

Table 2: Most common diamond dopants [26] and their position above the valence band (p-type) and below the conduction band (n-type).

	Element	Activation Energy (eV)
n-type	Nitrogen	1.70
	Phosphorus	0.60
p-type	Boron	0.37

31, 32].

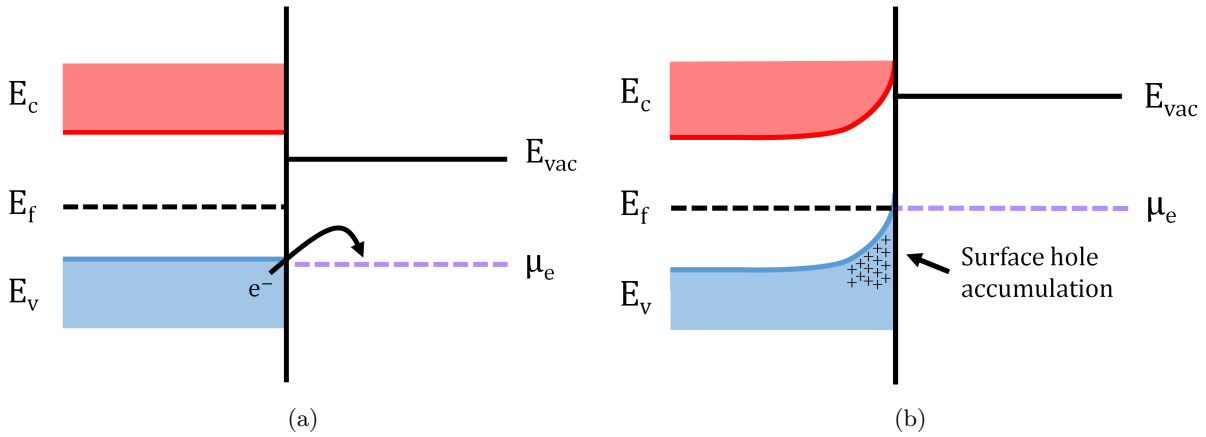

Figure 2: Hydrogen terminated diamond prior to (a) and after (b) electron charge transfer from the valence band maximum to acceptor states in the surface aqueous layer (μ_e) and the hole accumulation that results from chemical equilibrium.

Although boron is considered a shallow dopant with respect to other diamond impurities, the activation energy required is still high enough to give a low ionization fraction at room temperature [33]. An unusual type of doping is possible with diamond, facilitated by the ability to form a negative electron affinity (NEA), introduced in Section 3.7 [34, 35, 36, 37]. The mechanism is best explained by the energy levels shown in Figure 2. An electron accepting reservoir in the form of an aqueous layer is physisorbed atop the hydrogenated surface. Acceptor states in the aqueous layer must have a Fermi level or electrochemical potential (μ_e) lower than the valence band top of diamond. Electron transfer from the valence band to the adsorbate acceptor is energetically favourable. One proposed mechanism for charge transfer is the redox reaction of hydronium atoms into hydrogen and water [38]. Holes accumulate at the diamond surface until the Fermi levels align and reach equilibrium. The result is an areal hole density typically between 10^{13}–10^{14} cm^{-2} with p-type conductivity and mobility in the region of 10–100 cm^{2}V^{-1}s^{-1} [39].

This makes possible the realisation of unique diamond FETs [40, 41, 42].

Prior to this, tribological studies dominated the research into diamond surfaces where the material was generally considered to be electrically inactive for most applications. This discovery helped spark a host of diamond surface centred work [43, 44, 45, 46, 47], establishing the material as an exciting prospect for a range of potential power applications [48, 49, 50].

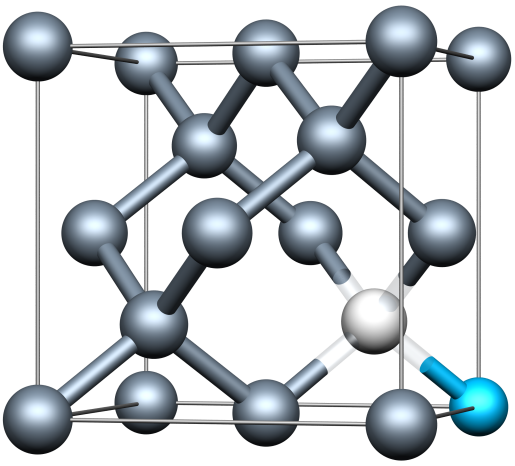

Figure 3: Diamond fcc lattice with a substitutional nitrogen (blue) and a carbon vacancy (white).

Nitrogen-vacancy (NV) centres in diamond (Figure 3) have garnered considerable interest in areas such as quantum computation [51] and magnetometry [52]. The spin-state of the NV centre can be controlled by light sources and magnetic and electric fields, consequently being read out optically using photoluminescence techniques [53]. The NV^- charge state exhibits the best spin and optical properties where the centre is preferrentially close to the surface for increased sensitivity of high-resolution magneteometry; these attractive features are not observed for NV^0. Unfortunately, near-surface NV^- centres are unstable close to the surface of pure crystalline diamond [54] as well as nanodiamonds [55], while ion-implanted NV centers prefer the neutral charge state [56] at the surface. Reverting the state back to minus is critical, with chemical termination providing a measurable and consistent method for surface charge control. DFT and experimental techniques reveal that the aqueous hole layer created via H termination sucks charge from the negative charge state [57] making it neutral, where as oxygen, hydroxyl and fluorine terminations preserve the negative state [58, 54]. This allows the gating of the surface with, for example, a metal or chemical solution [59, 60], shifting the surface chemical potential via field-induced band bending. Shifting between states can be achieved by an alternating voltage applied at the surface.

In a similar vein, nanodiamonds [61] have emerged as a promising candidate for bio-labelling and imaging of chemical reactions at the molecular level [62]. NV^- centres implanted in nanodiamonds have superior physical properties with high biocompatibility and low toxicity [63], which

can easily be decorated with a wide range of functional groups for therapeutic compound delivery systems [64]. Further advances are expected with research into a wider range of potential biomolecules with focus on the reproducability of consistent surface and defect properties [65] and the aim to increase spin-coherence times [66].

1.3 Silicon Carbide

For much the same reason as to why diamond makes an excellent prospective power device (Section 1.2), silicon carbide (SiC) also excels. SiC like other binary tetrahedral materials exists in many different polytypes. The stacking sequence of each bilayer and the degree of rotation with respect to the next bilayer determines the overall structure and polytype of the material.

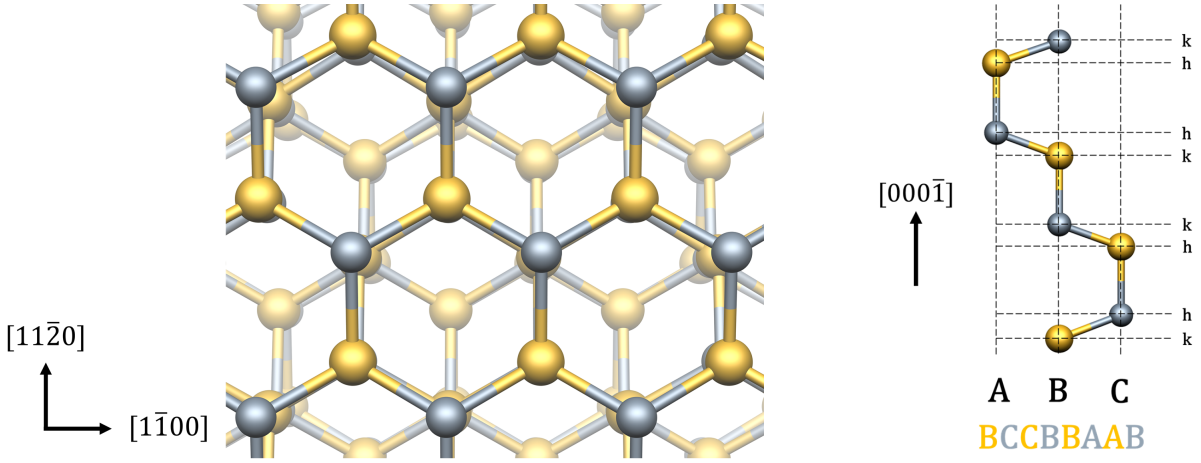

(a) (b)

Figure 4: Bulk 4HSiC cell repeated as viewed down the [0001] direction (a). The stacking sequence (b) specific to the 4H polytype in the [000$\bar{1}$] direction with the positions of Si and C in the hexagonal (h) and cubic (k) inequivalent sites. Yellow and dark-gray spheres represent silicon and carbon atoms respectively.

In all, there exists over 200 different polytypes [67] where the electronically significant ones are 3C, 4H and 6H. As Table 3 suggests, bulk 4H outperforms the other polytypes at transport properties, breakdown field and impurity levels. With 4H wafer diameters overtaking 6H at lower micropipe densities (< 5 cm^{-3}) [68] it has become the polytype of choice for research and device manufacturing.

The main advantage SiC has over diamond are the shallower n– and p–type dopants available (Table 3), however when compared with Si it has inferior mobility and deeper p–type donors.

Table 3: Comparison of the three main silicon carbide polytypes [69, 70, 71]. Where anisotropy factors in the properties are reported at their most favourable values.

	4H	6H	3C	Si
Bandgap (eV)	3.23	3.10	2.40	1.21
Breakdown field ($kVcm^{-1}$)	3200	3000	1800	300
Intrinsic carrier concentration (cm^{-3})	10^{-7}	10^{-5}	10^{-1}	10^{10}
Electron mobility ($cm^2V^{-1}s^{-1}$)	800	400	750	1250
Thermal conductivity ($Wcm^{-1}K^{-1}$)	3.0–3.8	3.0–3.8	3.0–4.0	1.5
Donor energies at h,k sites (meV)	N: 42, 84 P: 53, 93	N: 85, 140 P: 80, 110	N: 50	P: 45 As: 54
Acceptor energies at h,k sites (meV)	Al: 200, 200 B: 300, 300	Al: 240, 240 B: 300, 300	Al: 270	Al: 67 B: 45

Like silicon, SiC is "blessed" with the ability to also grow SiO_2 as a native oxide, encouraging its use in FET applications with a built in dielectric. Yet the thermally grown oxide produces an interface riddled with interface states that keep the mobility orders of magnitude below bulk SiC [72]. Resolving the issue of the interface would revolutionise SiCs use in industry and has therefore lead to decades of research into the passivation and identification of the electrically active defects [73, 74, 75]. With the desire to move to higher κ oxides for MOSFET applications [76], the deposition of a metal oxide will create a SiO_2 sublayer [77] as oxygen reacts with surface silicon on as-grown samples, even at low annealing temperatures [78].

Controlling the thickness of the oxide has shown to be an important factor in recent work where reported mobilities are in the region of 70–100 $cm^2V^{-1}s^{-1}$ [79, 80].

SiC enjoys frequent use in many key areas of electronics including sensing [81], uninterruptable power supplies [82], high power short circuit detectors [83] and high power density control units in hybrid vehicles [84] amongst many others.

1.4 Why Surfaces?

Semiconductor surfaces are of great importance in industry. The reaction of surfaces exposed to gases and radiation under a variety of pressures and temperatures is vital for the assertion of viability and longevity for any device. Stabilising a surface via a barrier layer encapsulates the material, maintaining its initial features as a temporary measure in a device manufacturing step

or preventing outside forces interrupting or hindering operation. Beyond protection, enhancement of a device through surface modification too is desirable. For example the efficiency with which an instrument operates dictates the level of power consumption. More efficient devices waste less power thus reducing overheads. The potential to reveal a wide range of capabilities and new science not possible without a terminating species compels considerable research in the area.

One area of application in which surfaces are a dominant factor is electron emission. The ejection of electrons over or through a surface potential barrier, common to all semiconductors and metals, into vacuum is governed by the four main emission phenomena [85]. The source of the energy and method through which the barrier is overcome dictates the emission type. The applications of emission are detailed with particular emphasis on barrier reduction through surface treatments.

1.5 Thermal Emission

Reducing heat waste and increasing the efficiency of power generation is a constant pressure facing a more populous world. Energy harvesting devices that can convert heat directly to electricity offer a practical way of increasing energy efficiency. Thermionic Energy Converters (TEC) [86, 87] are heat engine devices with a theoretical maximum efficiency derived from Carnot's law [88, 89]. The heat source could be waste heat produced as a byproduct of a separate heat engine (energy scavenging) or by the direct supply of thermal energy including laser [90] and solar [91] heating. The temperature difference between a hot emitter and cold collector forms the basis for the work done by electrons that traverse the evacuated interelectrode gap.

Figure 5 shows a typical semiconductor thermionic emitter diagram. The emitter work function Ψ_e should be low to maximise emission current densities. However the collector work function Ψ_c should be lower than the emitter where absorbed collector electrons induce the potential difference V_0. As the collector would emit electrons more easily if both electrodes were at the same temperature, it is therefore essential to maintain the temperature differential to ensure the dominant flow of electrons from emitter to collector and prevent back emission. These electrons do work in an electrical load connected to the device before returning to the emitter side to complete the circuit.

The Richardson-Dushman equation states the relationship for thermionic emission current density:

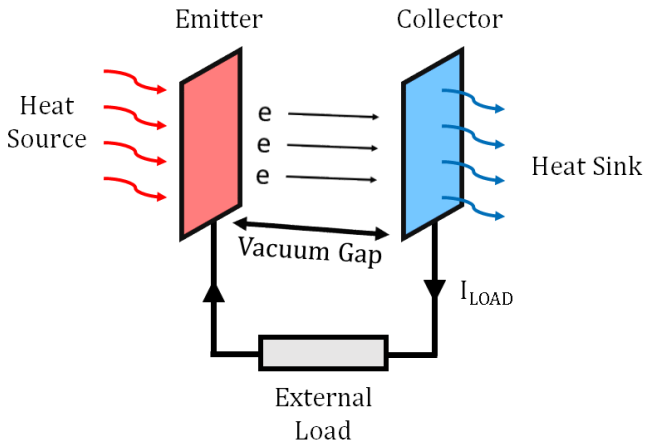

(a)

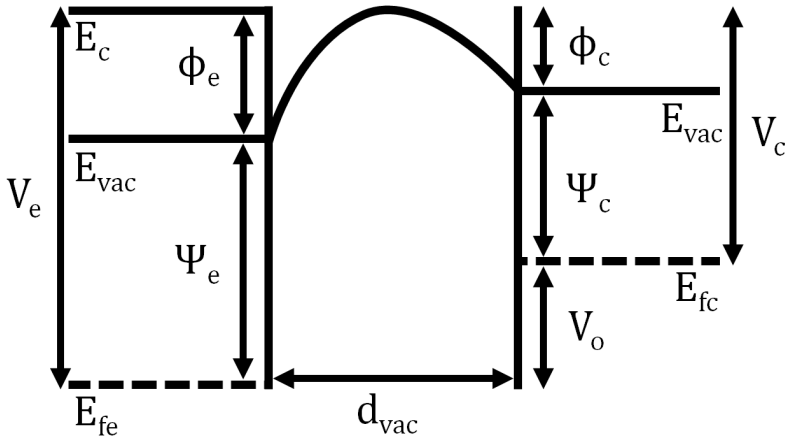

(b)

Figure 5: Schematic showing typical TEC (a) and the energy band diagram associated for an NEA emitter and collector (b). The output voltage V_0 is the difference between V_e and V_c of the emitter and collector respectively. V_e and V_c are composed of the sums of the electrode work function and space charge barrier $\Psi_e + \phi_e$ and $\Psi_c + \phi_c$ respectively. The emitter has an NEA where vacuum potential E_{vac} is below the conduction band minimum E_c.

$$J(T) = A_R T^2 \exp\left[\frac{-\psi}{k_B T}\right] \tag{2}$$

where J is the current density, A_R is the Richardson constant, ψ is the work function, k_B is the Boltzmann constant and T is temperature.

Lower Work Functions (WF) increase the current density and lower the operating temperature. The Richardson constant A_R is material dependent and thus strongly influenced by crystallinity, doping type, doping concentration and choice of substrate [92]. The theoretical maximum of A_R for metals is 120 $\mathrm{Acm^{-2}K^{-2}}$ and should ideally be as large as possible. Ultra low work functions of 0.67 eV have been reported [92] with phosphorus doped diamond but with a fitted A_R on the

order of 10^{-7} $Acm^{-2}K^{-2}$ the output current density remains low in the region of ~ 0.1 $mAcm^{-2}$. Therefore it is crucial to exert fine control over processing parameters for consistent emission properties.

Typically, metals are employed for TECs. A wide range of refractory metals coated with single element monolayers and oxides are available with Cs coated W being the most common, providing a low work function of 1.3 eV with operating temperatures above 700 °C [93]. These metals would often be paired with other refractory materials for thermal management, limiting device lifetime [94].

Diamond/SiC are excellent candidates for TECs due to:

- **Work Function** Through a wide variety of terminations, in conjunction with n-type doped diamond films, diamond TECs can exhibit work functions lower than the conventional metals (<1.3 eV), with values of 0.9 eV reported for phosphorous doped hydrogen terminated diamond films at sub 500 °C temperatures [95]. However, desorption of hydrogen begins at temperatures above 700 °C, limiting the range over which these devices can operate. SiC too, although not currently proven to exhibit an NEA, can be used to create TECs for solar electricity generation and enjoys order of magnitude increase in thermionic current through cesium coatings [96, 97].

- **Thermal Conductivity** Two of the highest thermal conductivities amongst most metals and semiconductors (Table 1).

- **Radiation Resiliance** Bombardment from high radiation exposing environments is possible, with nuclear and high temperature power generation proving hostile environments but key targets for energy harvesting.

- **Controlled growth** Precise control over growth and surface structures can permit enhanced performance through grooved/stepped electrodes [98, 94].

- **Substrate Interface** Diamond and SiC readily form interfaces with many elements making the identification of a suitable substrate more manageable. A rhenium layer on diamond is reported to enhance thermionic current with a large Richardsons constant [99], and rhenium contacts on 6H–SiC are ohmic and stable up to 1000 °C with suggested applicability to a SiC TEC [100].

Unsurprisingly, lowering the barrier to emission isn't the only target for the realisation of high efficiency TECs.

The space charge effect represents a significant barrier to high output current densities by creating an additional electrostatic barrier to emission. Electrons which are emitted create a

buildup of negative charge in the inter-electrode region. Low energy electrons which otherwise would emit from the surface are screened and limit their contribution to output current.

One way of limiting this is by reducing the inter-electrode area to the μm range [101]. There are obvious technological hurdles to manufacturing this in addition to the requirement of sufficient temperature differences between the hot emitter and cool collector, yet also advantages in the Schottky enhancement effect, lowering the barrier to emission through strong electric fields [96].

Another mitigation technique is to fill the inter-electrode region with a space charge neutralising gas, of which there are many instances including cesium [94]. Reports of methane gas facilitating charge transfer from the emitter surface *and* mitigation of the space charge effect with a work function (WF) of 1.18 eV have been made [102]. Theoretical results indicate that an NEA emitter surface can significantly reduce space charge build-up, out-performing TECs without an NEA with a greater inter-electrode distance [103, 104].

Employing surface treated, wide-bandgap semiconductors such as diamond or SiC to lower the operating temperature compared to conventional metals and increase the efficiency and lifetime of such a device in a radiative environment, is a step forward in the realisation of thermoelectric energy scavenging devices, with much work still to be done in the area of surface treatments and energy sources [91, 105].

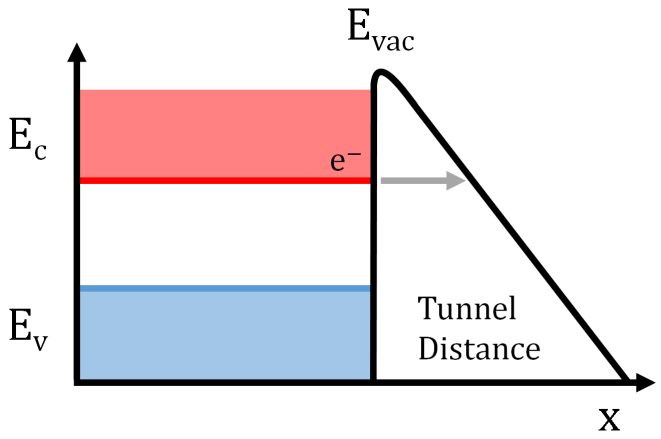

Figure 6: Band energy diagram of a field emission device where x is position.

1.6 Field Emission

Field emission is the ejection of electrons from a surface into vacuum by the application of an electric field as displayed by Figure 6. The electric field narrows the vacuum potential with a sufficiently high field permitting tunnelling of electrons from the surface of the semiconductor to the vacuum. Emission current density is governed by Fowler-Nordheim general equation:

$$J = \frac{(A\beta^2 E^2)}{\psi} \exp\left[\frac{-(B\psi^{3/2})}{\beta E}\right] \tag{3}$$

where A and B are constants, E is the electric field arisen from the applied potential V at a distance d between cathode and anode, β is the field-enhancement factor and ψ is the work function [106].

The more negative the EA, the lower the work function and hence an increasingly large current density. To take advantage of the NEA surface properties, electrons must be in the conduction band. Figure 7 illustrates how a metal back-contact can act as an efficient source of electrons, injecting into the conduction band of the semiconductor and accelerating to the surface through an electric field to be emitted into the vacuum through no additional barrier [107, 108].

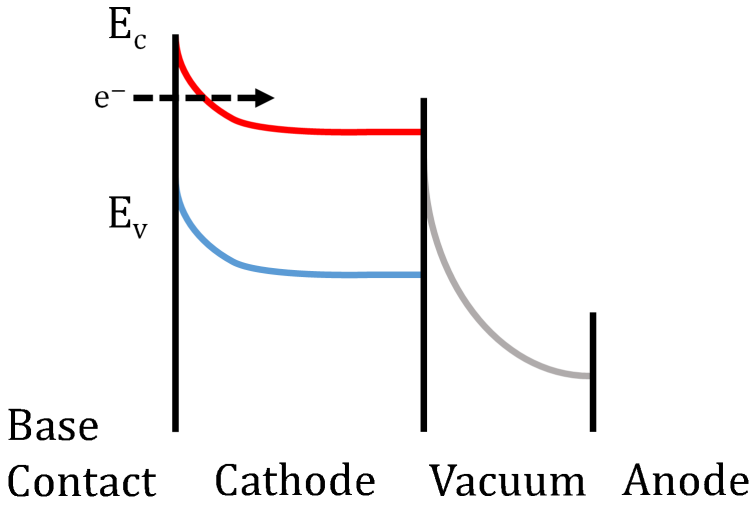

Figure 7: Band structure of a back contacted semiconductor emitter under bias.

Field enhancement factor, β, has strong tip geometry influence, where a reduction in tip radius to the order of several nanometres is responsible for marked increase in emission current density [109].

Consequently, dense pyramidal arrays of sharp emitters are one avenue for geometry optimisation where highly developed experimental techniques permit high quality CVD diamond field emitter arrays (FEA) [110, 111].

Diamond FEAs in particular have advantages over existing metal based cold cathodes, in that they are capable of withstanding high temperatures from Joule heating at high per–tip current densities. Certain catastrophic failure modes such as explosive evaporation are possible with metals and other semiconductors [112, 113] that are much less common with diamond due to its tendency for gradual self limiting evaporation [110]. Figure 8 shows the layout of a gated field emitter tip.

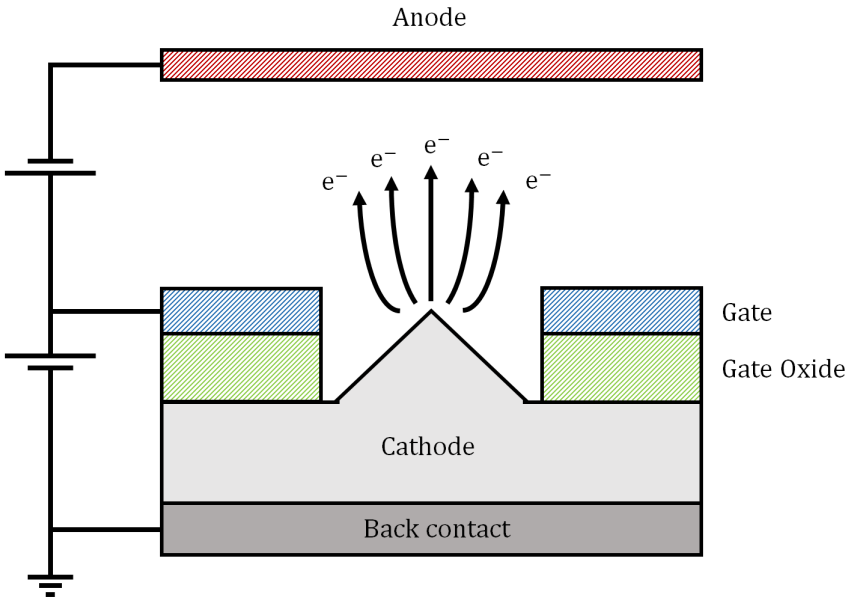

Figure 8: A simplistic gated diamond emitter setup.

Non-uniformity of array tips is another failure mechanism. Tips that are too sharp can cause arcing to the anode from high emission current damaging the tip and tips that are too wide won't turn on [110]. Emission instability from contaminants and micro-protrusions on the tip can also force tips to turn off reducing their work rate [110, 114].

Ultra-thin coating materials can produce this NEA and also preserve the local-field enhancement factor, β, that arises from atomically sharp emitters. Furthermore, strongly exothermic reactions with the semiconductor surface also increase the temperature range over which an emitter can perform (through Joule heating or extreme environments) before experiencing desorption and NEA reversal.

Efficient emission of electron beams has a multitude of other uses including the generation of electromagnetic radiation from microwave through to x-ray, where free-electron lasers offer a unique insight into atomic level structural changes in chemical reactions [115, 116]. Other experimental measuring techniques like e-beam lithography rely on cathode rays for operation [117, 118]. Cathode rays also find uses in pollution abatement, where harmful gases produced by industrial sources can be destroyed and recycled into usable products such as ammonia [119, 120].

1.7 Secondary Electron Emission

Primary electron sources amplified by an intermediate layer can be used to produce secondary emission beams with currents many times greater than the incident beam [121]. A simplified diagram of the process is provided in Figure 9.

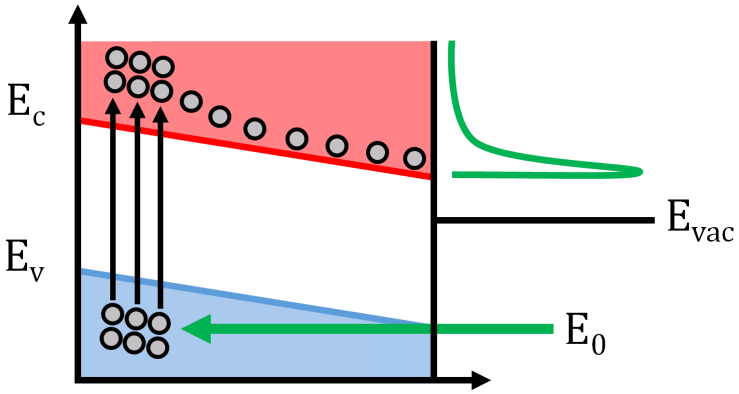

Figure 9: Band diagram representation of the secondary electron emission process. Incident beam E_0 promotes electrons from the valence band E_v to the conduction band E_c. These secondary electrons diffuse to the NEA surface via the application of an electric field and emit in to the vacuum. A typical energy distribution curve is displayed in green.

High current densities (>10 A/cm^2), ultra-low emittance, long lifetimes and radiation resistant materials are the list of qualities necessary for devices that make use of Secondary Electron Emission (SEE) such as linear electron accelerators, free electron lasers and electron amplifiers [122, 123, 124].

Photocathodes such as Cs:GaAs or KCs_2Sb enjoy high quantum efficiencies of 1–10% but have short lifetimes, unreliable fabrication methods and achieving >100 mA currents presents a major technical challenge [123].

A Diamond Amplified Photocathode [125] (DAP) builds on the efficiencies of a classical photocathode whilst providing unparalleled benefits through diamonds material properties:

- **Gain** Amplifier gain, calculated as the ratio of emitted to incident electrons, has been reported as high as 178 [126], an order of magnitude greater than conventional SEE materials [127, 128] and current densities two orders of magnitude greater than the photocathode alone [129]. A high gain means fewer dynode stages are necessary to achieve a detectable current, therefore the whole device is smaller and easier to manufacture. Less dynode stages in turn reduces the time from the initial photocathode emission to detection thus resulting in better time resolution and signal discrimination in electron counting mode [130].

- **NEA** If EA is positive, Figure 9 shows that the vacuum level lying above the main electron-distribution peak will block most electrons from emission. As the EA is made lower and negative, a greater proportion of the electrons which populate the bottom of the conduction band can be emitted in to the vacuum. A more negative EA increases the emitter gain. However, as more electrons are emitted at a greater energy range, the energy distribution

of emission increases hence a larger emittance [131]. Research into suitable terminations to induce air-stable emission with a larger NEA are on-going.

- **Carrier mobility** Diamond has one of the highest saturated carrier drift velocities at 2×10^7 cm.s^{-1} at electric fields in the MVcm^{-1} range [132]. Internal electric fields of a similar order are required at the device level to reduce recombination losses of slow drifting secondary electrons and minimise the emission delay, where picosecond response times are required for certain applications [133, 134]. Carrier mobility is directly related to crystalline quality and defects, therefore a high quality single-crystal CVD diamond sample is preferential [135] for the rapid thermalisation of electrons to the CBM [136]. Thermalised electrons have a high mean free path which increases their escape depth thus a higher fraction of generated secondaries can be emitted [137].

- **Mechanical Properties** The thermal conductivity of diamond is roughly 20 Wcm^{-1}K^{-1} (Table 1) allowing efficient thermal management of high energy incident beams (>5 keV) where other materials would suffer from thermal degradation. The diamond layer also acts as a barrier between the photocathode and the target, shielding the more radiation susceptible photocathode from high energy particles in an accelerator environment and ion back-bombardment (Table 4).

The quantum efficiency and current density demands of a wide variety of emitters can be realised, not necessarily by the optimisation of just one device, but a combination of two or more that work in tandem to deliver device specification at increasingly higher device lifetimes. Diamond amplifiers provide all the mechanical and electrical properties of the bulk material whilst also providing a two order of magnitude increase in current density with ultra-low emittance.

Electron emission governs a vast field of research delving into areas such as material choices, emission mechanisms, surface and geometry optimisation and efficiency maximisation. Science continues to push the boundaries of whats possible, necessitating the advancement of materials and devices to supply the next generation of research where the surfaces of wide bandgap semiconductors features as a major contributor.

1.8 Electrochemistry

The efficiency of electrochemical reactions are dominated by material choice and the ability to provide a wide range of voltages to induce the desired reaction [138]. Electrochemical windows, hardness, surface control and current densities are all important factors where wide-bandgap semiconductors like diamond are expected to excel. Simple terminations of thin films can tune

the wettability [139] of surfaces changing from hydrophobic to hydrophilic, finding a multitude of uses in electrocatalysis and electrosynthesis. Electrodes may also be placed in harsh environments containing acidic and alkaline solutions on opposite ends of the pH scale [140]. Surface functionalisation of wide-bandgap semiconductors can offer more control over the process, either by making a surface more chemically inert to prevent electrode fouling or more sensitive to increase the rate of reaction.

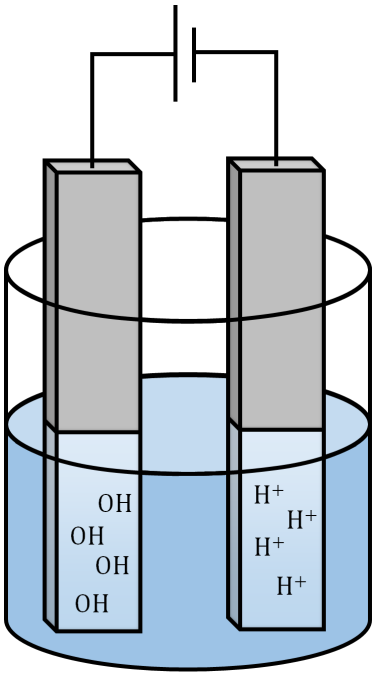

Figure 10: Electrolysis of water into hydroxyl radicals and hydrogen gas by diamond electrodes.

Materials such as diamond [141] perform excellently in electrochemical processes. In water, gaseous hydrogen creation begins at -1.25 V and oxygen at 2.3 V for single-crystal diamond [142] (Figure 10). This large chemical-potential window permits a larger range of reactants that disassociate in to ions and cations to be investigated without the interference from water splitting that would otherwise not be possible for other electrodes.

Measuring the potential response of a reactant using voltammetry is also heavily surface termination dependent. Hydrogen terminated diamond showed a fast electron transfer whilst oxygen termination had a slower rate of transfer and a lower steady state current attributed to electrostatic dipole layer and site blocking [143].

Photo-illuminated diamond can be used as an efficient source of electrons to induce the reduction of N_2 to NH_3 [144]. The high energy position of the conduction band in conjunction with a NEA surface creates the conditions for the reduction of a wide variety of compounds inaccessible to most other semiconductors. Other harmful and difficult to reduce compounds like CO_2 [145] and indeed even the synthesis of new compounds is possible with functionalised diamond [146].

The induced p-type surface conductive layer from hydrogen termination (Section 1.2) has garnered a multitude of uses including sensing systems in liquid electrolytes. Hydrogen terminated surfaces are sensitive to Cl and Br ions [41] and can be shown to exhibit pH sensitivity using ion-sensitive FETs (ISFETs) [42].

Chemically modified diamond surfaces also act as a vehicle for the attachment of organic molecules. Diamond shows high selectivity and stability in a range of solutions [147] and is more robust compared to alternative substrate materials [148, 149].

1.9 Sensors

The sensing and detecting of volatile gases and high–energy radiation in extreme environments demands a material capable of maintaining operation in these high–pressure high–temperature scenarios. Silicon still enjoys widespread use in sensor technologies, but suffers from catastrophic radiation damage from silicon atom displacement that degrades the performance of the device, drastically reducing sensor lifetime [2] and increasing leakage current and bulk resistivity.

Table 4: Threshold energy of defect formation for different semiconductors [150].

	GaAs	Si	Ge	Diamond	4H–SiC
Threshold Energy (eV)	8–20	13–20	16–20	40–50	22-35

Other semiconductors, including SiC, are very capable of performing in these environments [151, 16]. The amount of energy required to displace an atom within the crystal lattice for a radiation detector should be as high as possible, so as to avoid the creating of performance limiting defects such as charge traps. Table 4 is one indicator shows that wide–bandgap semiconductors would excel under the bombardment of high energy particles, and in general extreme environments, with 4H–SiC at the forefront [152, 153].

In regards to sensing, the modification of silicon carbide surfaces changes the selectability of a surface to a specific gas. This is important as other competing gases present in the atmosphere could trigger a false positive response. As an example of gas–selectivity, palladium functionalisation is highly selective to the absorption of hydrogen (Figure 11), a reversible process suitable for use at high temperatures [154, 155]. Tuning a surface to be selective of a wide range of gases with a fast response time under a range of temperatures is of great importance to improving gas sensors [156]. Indeed, SiC is employed to sense a wide variety of environmental variables including temperature and strain [157].

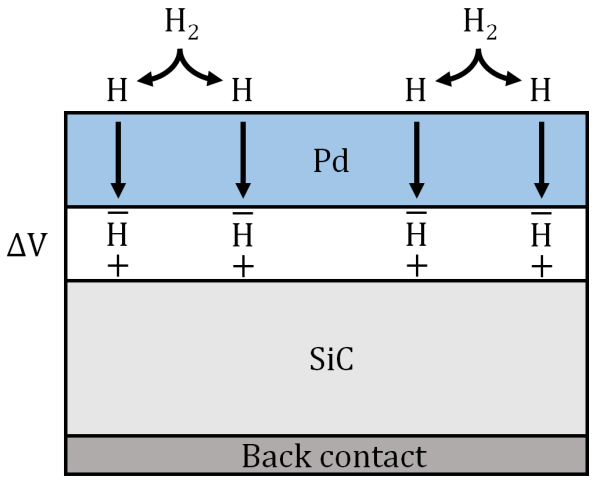

Figure 11: Palladium permeable to hydrogen sits atop 4H–SiC. An interfacial dipole region shifts a CV trace by δV, indicating hydrogen has been sensed.

Biosensing is an emerging application for SiC, where surfaces decorated with biomolecules and other organic groups are biocompatible [158, 159] gaining interest in the medical field. The ability to model the interactions simple compounds have on SiC surfaces such as water [160] is still very computationally demanding with the Si- and C-faces of SiC exhibiting different properties when exposed to stimuli, an interesting factor to consider for SiC material growth. Tuning a surface to be selective of a wide range of molecules is of great importance to improving the use of SiC over silicon as a sensor *in vivo* and in harsher environments.

Diamond's biosensing capability is also outstanding, acting as an excellent substrate upon which the adsorption of a range of molecules can be electrochemically detected and strongly bound, whilst retaining full functionality of the molecule itself [161].

Both diamond and SiC and their functionalisation of monolayer adatoms and chemical groups make their use as sensors in both air and water an exciting prospect for further research and application.

1.10 Summary

As detailed above surfaces exist as crucial device aspects whether they directly or indirectly feature in the overall operation and performance of a device. How terminating species influence the electronic and structural properties of a material have profound consequences for a multitude of applications both beneficial and detrimental to operation. Much research is yet to be done in this area for all wide bandgap semiconductors but in particular with SiC and diamond, whose properties form the basis of significant current and future interest for devices now and in the decades to come.

2. Background Theory

2.1 Why Model?

Section 1 detailed the superlative properties wide bandgap semiconductors have over smaller bandgap semiconductors with particular emphasis on their use in hostile environments, but one of the major issues that surrounded these materials was the commercial adoptability and consistent high-quality growth [162, 163, 164, 165]. The material growth and device creation recipes for silicon have been modified, improved and perfected over 60 years of concentrated global development and the widespread proliferation of electronics through consumerism. SiC and diamond are relatively new materials and given their more niche areas of suitability are not yet at the same advanced stage of processing. Vast amounts of effort in the past two decades have been poured into materials research including but not limited to defects [166, 167] and doping [168, 169, 170]. The commercial processes required to grow and modify the intrinsic structure for devices are becoming more well known, thus devices are more frequently being realised and implemented where their superior properties can flourish [171, 26, 172].

Modelling can often provide the means to test an initial hypothesis or indeed deconstruct and detail unexplained phenomena that current experimental techniques can not resolve. It permits the detailed and controlled study of material characteristics as a function of only a few chosen variables. Experimentally, the independent evaluation of those effects alone may not be possible without having to consider a whole host of other potentially dominant processes. Furthermore, cost is often an issue when one looks to either conduct growth in-house or purchase the material pre-made from a third party.

Modelling frequently sets forth the first step in a long chain of research that emanates from the preliminary data. Generally speaking the ability to build crystal surfaces and evaluate them under a variety of terminations, faces and species types can be quicker and more cost effective than if you were to attempt the equivalent experimentally. When working in tandem with experiment, being able to produce a consistent picture with both experimental and theoretical data pointing towards the same conclusion is invaluable when compared to either sets of data standing alone.

2.2 The Schrödinger Equation

In order to generate realistic models of materials, universal equations which apply to single and many-atom systems must be solvable in both a realistic time frame and to a sufficiently high degree of accuracy. Schrödinger's equation provides us with the means to calculate the wave function of a system of particles.

$$\hat{H}\Psi_i = E_i\Psi_i \tag{4}$$

where Ψ_i is the particle wave function, E_i is the total system energy, and $\hat{H}$ is the Hamiltonian. Expanding a simple Hamiltonian into its constituent parts we arrive at:

$$\left[\frac{-\hbar^2}{2m}\nabla^2 + V_i(\mathbf{r})\right]\Psi_i(\mathbf{r}) = E_i\Psi_i(\mathbf{r}) \tag{5}$$

where $\frac{-\hbar^2}{2m}\nabla^2$ and $V_\mathrm{i}(\mathbf{r})$ are the kinetic and potential energy operators respectively, and $\mathbf{r}$ is the position vector. $V(\mathbf{r})$, E, and Ψ are generally unknown for a typical system. The problem is that the wave function is related to the probability density of finding a particle in a given position and so dictates the potential, but the potential simultaneously depends on where the electrons are situated, described by the wave function. The Schrödinger equation can be expressed as a eigenvalue (energy of the system) and eigenvector (wave function of system) problem. Solving the Schrödinger equation for a trivial system such as a single hydrogen atom is mathematically and computationally simple, as there is only one electron and one electron-nucleus interaction to account for.

The problem becomes exponentially more difficult when an increasing amount of electrons are added to the system. At atomic distances, the equations describing the motion of electrons in a system are coupled, and thus must be solved simultaneously. If a system of electrons can be imagined, the physical properties of one electron is determined by the combination of the interaction of all other electrons. Perturbation of a single electron has a knock-on effect on every electron which each, in turn, produce knock-on effects repeated *ad infinitum*. For any sizeable system, this becomes a task impossible to solve for modern day computing and may remain as such for the foreseeable future.

2.3 The Born-Oppenheimer Approximation

The problem in its current form is not sustainable for systems beyond the trivial and must be simplified. One immediate gain can be made in relation to the interaction between the nucleus and electrons of an atom.

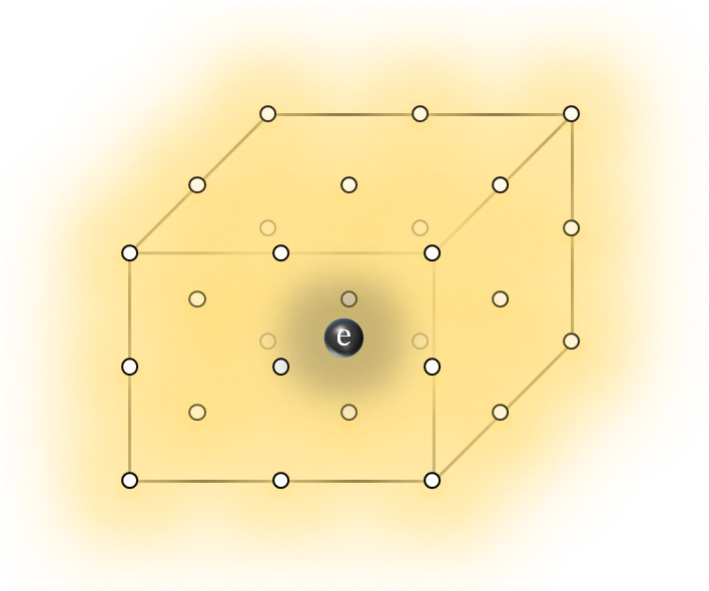

Figure 12: An electron (e) moving in a periodic potential of fixed nuclear sites (white dots).

An approximation of the kinetic energy $E_{\mathrm{k}}[n]$ can be made with the desire to separate the motion of an atom's nucleus and its respective electrons [173]. Nuclei are so massive in comparison, their relative motion is very small allowing us to assume that they simply modulate the wavefunction of passing electrons.

$$\Psi_{tot}(r, R) = \chi(R)\Psi(r, R) \tag{6}$$

The complete wavefunction Ψ_{tot} is a product of χ, the arising potential of the fixed nuclear site at co-ordinates R and $\Psi(\mathrm{r}, \mathrm{R})$, the electronic wavefunction (Figure 12). This is a powerful initial simplification which produces a set of more manageable Schrödinger equations. However, they still can not yet be solved for exactly as $\Psi(\mathrm{r}, \mathrm{R})$ includes the many-body electron interaction terms as mentioned in Section 2.2.

2.4 Hartree Method

Early attempts at tackling this issue were formulated by Hartree [174], who made the assumption that many-electron wave functions could be expressed simply as a set of many single-electron wave functions. This provided N equations for an N-electron system, where the motion of a single electron is decoupled from all other electrons and is able to be treated as a single particle. The main failure of this approach is its incompatibility with the Pauli exclusion principle, which states that the wave function of two identical electrons must be anti-symmetric under exchange:

$$\Psi(\mathbf{x_1}, \mathbf{x_2}) = -\Psi(\mathbf{x_2}, \mathbf{x_1}) \tag{7}$$

The many-electron wave function set in Hartree's equation is symmetric, which effectively ignores the exchange potential acting on electrons in a system. Neglecting the electron-electron interaction, the independent electron approximation is used in the nearly-free electron model where Bloch's theorem [175] is employed to describe the electronic band structure of crystals and the origin of the band gap.

2.5 Hartree-Fock Method

Hartree-Fock [176] improved upon this by describing the wave function of a many-electron system in a Slater determinant that satisfied the anti-symmetric properties of fermion exchange, where any two identical fermions with the same spin orbitals have a wave function of zero. This simple 2-wave function system can be expressed as a linear combination of separate anti-symmetric wave functions:

$$\Psi(\mathbf{x_1}, \mathbf{x_2}) = \frac{1}{\sqrt{2}} \left\{ \chi_1(\mathbf{x_1})\chi_2(\mathbf{x_2}) - \chi_1(\mathbf{x_2})\chi_2(\mathbf{x_1}) \right\} \tag{8}$$

which can be generalised to an N particle system:

$$\Psi(\mathbf{x_1}, \mathbf{x_2}, ..., \mathbf{x_N}) = \frac{1}{\sqrt{N!}} \begin{vmatrix} \chi_1(\mathbf{x_1}) & \chi_2(\mathbf{x_1}) & \cdots & \chi_N(\mathbf{x_1}) \\ \chi_1(\mathbf{x_2}) & \chi_2(\mathbf{x_2}) & \cdots & \chi_N(\mathbf{x_2}) \\ \vdots & \vdots & \ddots & \vdots \\ \chi_1(\mathbf{x_N}) & \chi_2(\mathbf{x_N}) & \cdots & \chi_N(\mathbf{x_N}) \end{vmatrix} \tag{9}$$

The Hamiltonian of this system again results in many-electron wave functions described as a set of single-electron wave functions, but with an added term from the inclusion of Pauli's exclusion principle: the exchange potential. In a surprising turn of events, despite having adapted to be more universally applicable with obeying Pauli's exclusion principle, the initial Hartree-Fock approach gives poorer results than its predecessor. There is in fact another energy term still being ignored called the correlation potential. Even though the Hartree-Fock method is better from a formal point of view, it is less accurate than the simple Hartree method because of the errors effectively cancelling each-other out.

The Pauli exclusion principle states that no two identical electrons can occupy the same quantum state simultaneously. This means that any electron with a certain spin will repel and be repulsed by other electrons with a similar spin. Therefore, there is a region surrounding this electron which is spatially depleted of same-spin negative charge, a relative positively charged region of space called an exchange hole. Ignoring spin, another hole exists in the regions surrounding electrons as a result of electrostatic repulsion called a correlation hole. There are two energy terms associated with these exchange and correlation holes: one is a simple electrostatic attraction between the oppositely charged particles, the other is a interaction effect from other correlated electrons as they act on the total electron and hole pair.

Both these theories failed to completely solve the entire wave function picture for many-electron systems. This is in part due to not obeying already existing theories to do with quantum particles, but also from a poor initial assumption that a many-electron wave function could be separable in to a set of single-electron wave functions. Post Hartree-Fock methods such as Coupled Cluster and Configuration Interaction do include the correlation term but the computational effort of solving a set of Schrödinger equations still remains a significant deterrent to its use.

2.6 Density Functional Theory

An alternative method to Hartree-Fock theory was necessary to efficiently include the correlation energy and find a less computationally expensive way to evaluate the spatially dependent energy terms. Density functional theory (DFT) gained traction after the work of Hohenberg-Kohn [177] and Kohn-Sham [178]. Hohenberg and Kohn were able to prove that there is a 1:1 relationship between the charge density and the ground state wavefunction, where the ground state of a system is defined to be the electron density which minimises the total energy functional of that system. A brief insight into the proof developed by Hohenberg and Kohn shows this to be true.

If we first assume that the opposite is true, in that the external potential can not uniquely be defined by the charge density, there should be two potentials V_1 and V_2 that have the same charge density n. Then through applying the variational principle, where Ψ_1 and Ψ_2 are two example normalised wave functions and H_i is a Hamiltonian with potential V_i and energy E_i, then:

$$\begin{aligned} E_1 = \langle \Psi_1 | H_1 | \Psi_1 \rangle &< \langle \Psi_2 | H_1 | \Psi_2 \rangle \\ &= E_2 + \langle \Psi_2 | V_1 - V_2 | \Psi_2 \rangle \\ &= E_2 + \int (V_1 - V_2) n(\mathbf{r}) d\mathbf{r} \end{aligned} \tag{10}$$

But we can also show:

$$E_2 < E_1 + \int (V_2 - V_1) n(\mathbf{r}) d\mathbf{r} \tag{11}$$

Adding this equation leads us to the strange expression:

$$E_2 + E_1 < E_1 + E_2 \tag{12}$$

which simply does not make sense. This implies that there is no solution of V_1 and V_2 with the same charge density n, so the potential has to be a unique functional of n. This also demonstrates that we can find how the energy depends on the charge density $n(\mathbf{r})$ as a function of only 3 variables. In Hartree-Fock theory, for only a single atom of helium it is necessary to approximate the wave function as a function of 8 variables, or $4N$ variables (x, y and z spatial components and spin) where N is the number of electrons in a system. Reducing the number of independent variables shows how DFT can find the minimum energy of a system much faster than in Hartree-Fock.

Hohenberg and Kohn have shown that a unique functional of the ground state charge density exists and that the variational principle can be applied to minimise the total energy, however the problem of forming the set of equations still remains. Kohn and Sham proposed that a system of interacting particles be replaced by a system of non-interacting particles that move through an effective potential whose charge density sums to the same charge density as the true system.

Each energy term of the Hamiltonian can be expressed as functionals of charge density n:

$$E[n] = E_{\mathrm{k}}[n] + E_{\mathrm{e-i}}[n] + E_{\mathrm{H}}[n] + E_{\mathrm{xc}}[n] + E_{\mathrm{i-i}} \tag{13}$$

The electron-ion, ion-ion, and Hartree (electron-electron) energy expressions are intrinsically related to the charge density and easily expressed as functionals:

$$E_{\mathrm{e-i}}[n] = -\int n(\boldsymbol{r}) \sum_{a} \frac{Z_a}{|\mathbf{r} - \mathbf{R_a}|} d\mathbf{r} \tag{14}$$

$$E_{\mathrm{i-i}}[n] = \frac{1}{2} \int \sum_{a \neq b} \frac{Z_a Z_b}{|\boldsymbol{R_a} - \boldsymbol{R_b}|} \tag{15}$$

$$E_H[n] = \frac{1}{2} \int \frac{n(\mathbf{r_1}) n(\mathbf{r_2})}{|\mathbf{r_1} - \mathbf{r_2}|} d\mathbf{r_1} d\mathbf{r_2} \tag{16}$$

where Z_{i} refers to ions at sites $\mathbf{R_i}$ and $n(\mathbf{r_i})$ is the charge density at position r_{i}.

These charge densities can be solved to give a set of one-electron Kohn-Sham equations. The square of the Kohn-Sham wavefunctions summed over N occupied states gives the charge density:

$$n(\mathbf{r}) = \sum_{\mathrm{KS}=1}^{N} |\Psi_{\mathrm{KS}}(\mathbf{r})|^2 \tag{17}$$

where $\Psi_{\mathrm{KS}}(\mathbf{r})$ is the one electron wavefunction. This calculated charge density will be compared to the initial charge density used to build the Hamiltonian. An iterative procedure described in Section 3.2 details the energy minimisation procedure necessary to find the ground state charge density. This effective potential is of course fictional where we can only attempt to replicate the true physical system. One glaring issue is that as it stands the Hamiltonian is incomplete. There is no known form of the full exchange correlation term.

2.7 Exchange-Correlation Functional

A significant portion of the error in the energy term comes from the expression for the exchange-correlation potential. The simplest known way to express the term as a function of the charge density is:

$$E_{xc}[n] = \int n(\mathbf{r})\epsilon_{xc}(n)d\mathbf{r} \tag{18}$$

where $\epsilon_{\mathrm{xc}}(n)$ is the exchange-correlation energy density. The exchange-correlation potential is a many-body problem so needs to be approached under a number of assumptions. $\epsilon_{\mathrm{xc}}(n)$ is known exactly for a fictitious array of equally distributed, interacting atoms with a uniform charge density called a local homogeneous electron gas. The energy term for this system depends purely on the local electron interaction and can be described using only the charge density.

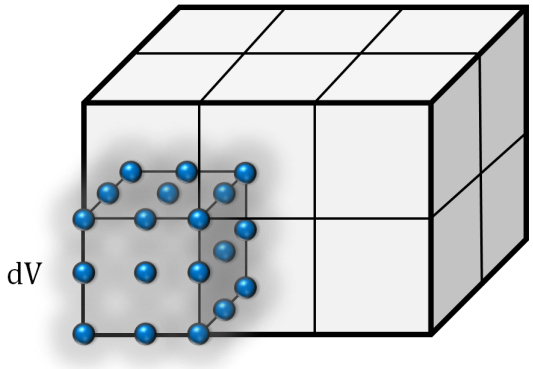

Figure 13: Small volume dV filled with local homogeneous electron gas as part of a larger total cell volume.

If a system being modelled is divided up into small regions dV as illustrated in Figure 13, and the charge density at any arbitrary point in the volume is known, the exchange-correlation term is known exactly if that charge density were to exist as a uniform homogeneous electron gas everywhere in space. The individual terms can be added up over the entire system volume and an approximation for the energy term is formed called the local density approximation (LDA) [179]. Other approximations exist including the generalised gradient approximation (GGA) [180] which more effectively describes a rapidly varying charge density by taking the slope of the charge density into account.

The approximation's limitations come from the assumption that the charge density in any small volume is uniform which is not true in general, and definitely not true for a system of atoms. The underestimation of the band gap [181] is a common observable flaw in the approximation, where for diamond it can be more than 1 eV less than experimentally measured values.

One important observable difference between the two functionals is in the lattice constant, where LDA and GGA are known to underestimate and overestimate respectively. Taking a two atom bulk diamond cell, minimising the energy through isotropic variations in the volume of the cell will reveal the equilibrium lattice constant. Changing only the functional of a system reveals fundamental dependencies.

Table 5: Comparison of calculated bulk modulus and lattice constant of 2 atom bulk diamond as a function of functional with experimental values [182, 183].

	LDA	GGA	Experiment
Lattice Constant (Å)	3.532	3.573	3.567
Bulk Modulus (GPa)	463	430	442

Table 5 shows that LDA underestimated the lattice constant and overestimates the bulk modulus and *vice versa* for GGA. Comparative calculations for important observables such as surface formation energy and electron affinity show a small enough variation within the total running error of the calculation so as to be within the total running error of a given calculation. For the purposes of the thesis, the choice of functional is not paramount when the physical need for one does not outweigh the other.

2.8 Summary

With the relationship between the charge density and each energy term established, the foundation is set for the possibility to create, model and analyse the properties of infinitely many structures including surfaces, defects and nano-particles across a range of scientific fields. The methods and procedures by which each energy term is formulated represents the main differences between variations of DFT and the software packages that support them. Each has their respective advantages and disadvantages, the main being a classic compromise between speed and accuracy. The following chapter lays out how AIMPRO performs the fundamentals. Furthermore, some of the decisions a user is faced with are explored, including analysis methods crucial to upcoming results.

3. AIMPRO Methodology

All calculations are performed using the in-house DFT modelling software package AIMPRO (Ab Initio Modelling PROgram). AIMPRO prides itself on the speed and accuracy with which it achieves self-consistent solutions and the ability to model large systems composed of 1000 atoms [184] or more with only modest memory requirements [185, 186]. With respect to the forthcoming surfaces calculations, this allows the user to perform many hundreds and even thousands of different optimisations and rank order the resulting structures by energy to provide more confidence that the lowest energy model is indeed the most likely to occur in nature. The following sections detail how certain core functions and analyses are implemented and rationalised including their effects on computational parameters including time to completion and accuracy.

3.1 Pseudopotential

The electronic states of an atom can be categorised as two different types – core states, which do not significantly participate in bonding and are highly localised and valence states, which are involved in bonding with neighbouring atoms. Binding energies between core electrons and the nucleus are usually very large compared to the binding energy of valence electrons, so core states numerically dominate the total energy of a system [187]. Valence binding energies can be orders of magnitude smaller than core binding energies. Large errors in core state representation would therefore drown out small differences in the valence states. Valence electrons are required to be simultaneously orthogonal to all other core electrons in the same atom, so their wave functions exhibit an oscillatory behaviour to satisfy the orthogonality condition, often with steep peaks. It becomes very difficult to model sharp peaks with plane wave and Gaussian basis sets as they require a vast quantity of functions to achieve convergence, translating to a large computational cost. The vast majority of this complexity can be negated by the use of pseudopotentials to represent the core electrons. This approach is adopted in most codes including AIMPRO. Some software packages, classed as all electron models [188, 189], opt to include core electrons in their calculations. This can be advantageous when performing analyses specific to the core states such as hyperfine calculations [190].

In order for the resulting energies and forces to be valid, pseudopotentials must have the following properties. The pseudo-wave functions and the wave functions with the full coulomb potential are identical outside a certain cut-off radius which can be thought of as a quality factor as

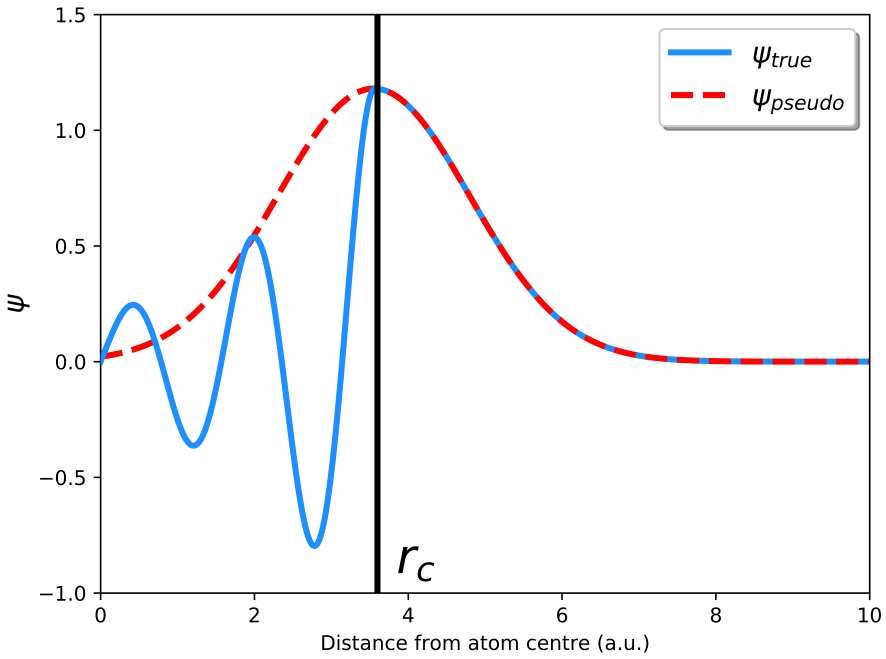

Figure 14: True oscillatory nature of wavefunction (blue) and pseudopotential wavefunction representations (red) of core electrons.

depicted in Figure 14. The choice of cut-off radius r_c should be large enough to exclude any rapidly varying parts of the true pseudopotential, whilst still satisfying the condition $\Psi_{\text{pseudo}} = \Psi_{\text{true}}$ outside the core. One way is to pick a point half-way between the last node and the maximum wave function amplitude [191]. The pseudo-wave functions are nodeless or have nodes with relatively less-sharp peaks, and so can be described with a fewer number of plane waves or Gaussians. The motion of the electrons can now be separated from that of the core, where the electron wavefunction is modulated by the fixed potential as in Figure 14. AIMPROs standard is to use Hartwigsen-Goedeker-Hutter (HGH) pseudopotentials [192].

3.2 Self Consistency

Self consistency within DFT means that the charge density from the Kohn-Sham potential is the same charge density used to generate the potential. The potential of the system is calculated with an initial input charge density n_{i_0} taken from the neutral atoms of the structure. The potential experienced by each particle in a system of non-interacting particles can be determined exclusively from the charge density. This potential is used to solve the Kohn-Sham equations from which the sum of the squares of the wavefunctions hence output charge density n_{o_0} is formed. The condition for self-consistency is that the input and output charge densities are equivalent to within some tolerance (Figure 15).

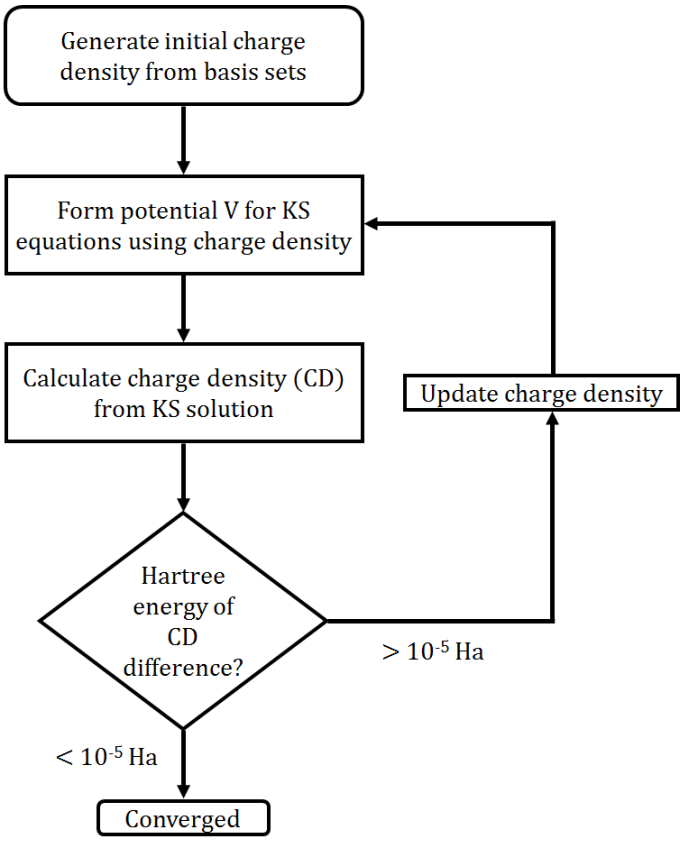

Figure 15: Steps to achieve self consistency.

The coefficients of the output charge density are optimised by a weighted average and re-fed through the self consistency process once more, arriving at a more accurate description of the system. A default tolerance of 10^{-5} Ha Hartree energy of the difference of the input and output charge density is where they are deemed converged.

3.3 Forces

AIMPRO utilises a conjugent gradients scheme [193] to find the energy minimum. A conjugate gradients method is preferred over a steepest descents method as the previous search directions are retained and new search directions are conjugate to the former. Without the information of previous directions the algorithm may pursue a less efficient route.

During an optimisation run, once the self-consistent energy has been calculated the next step is to evaluate the forces. Each atom is displaced in the direction of the forces to minimise its energy and another self-consistency cycle will begin. The forces on each atom are reduced iteratively until the point where the largest force on any one atom is below the default optimisation threshold of 10^{-3} a.u. The size of the forces are found utilising Hellmann-Feymann theorem [194].

Once the forces on each atom are known, a conjugent gradient scheme is employed to find the path to achieve the equilibrium structure. The new atom position $\mathrm{R}^{'}_{\mathrm{lx}}$ is found by:

$$R^{'}_{lx} = R_{lx} + wd^{'}_{lx} \tag{19}$$

with R_{lx} being the old position, w coefficient is that which minimises the free energy of the system and $d^{'}{}_{\mathrm{lx}}$ is the direction of movement determined by a combination of the forces on the atom and the previous search direction.

A problem with this procedure is that on the global energy and position scale the algorithm can often not identify a local minimum.. In the case of the cleaved (001)-(1×1) surface covered in Section 4.1.2, the surface atoms sit in a local minima and require a small perturbation through an energy barrier to satisfy surface dangling bonds and reconstruct to the (2×1) arrangement.

The number of iterations and overall time required for optimisation strongly depends on the complexity and disorder of the initial structure with respect to the final atom positions. This combined with the need for potentially thousands of calculations requires a pragmatic approach to obtaining a desired solution in the most efficient manner possible.

3.4 Basis Sets

Because we can not solve the wave function of a many electron system analytically, it can be expanded as a set of basis functions that usually take one of two forms: plane waves and Cartesian Gaussian orbitals. AIMPRO uses a combination of both for the wave function and charge density bases. The basis set is initialised in Gaussian form, Fourier transformed in to plane wave form and the charge density basis is a set of plane waves where Bloch's theorem can be used to describe the periodicity of the crystal structure.

Bloch waves are a useful way of describing wave functions as plane waves in a periodic crystal potential,

$$\psi(\boldsymbol{r}) = \mathbf{e}^{i\mathbf{k}\cdot\mathbf{r}} u(\mathbf{r}) \tag{20}$$

where $\psi(r)$ is the Bloch wave, $\mathbf{e}^{i\mathbf{k}\cdot\mathbf{r}}$ is a plane wave with wave vector $\mathbf{k}$ and position $\mathbf{r}$, and $u(\mathbf{r})$ is the periodic potential. A wavefunction can only be a Bloch wave if $u(\mathbf{r})$ is a periodic potential with the same periodicity as the crystal lattice where $u(\mathbf{r}+\mathbf{T}) = u(\mathbf{r})$, and you multiply that by a plane wave. The potential can now also be expanded and expressed as a plane wave charge density basis function, allowing the wave function to be described completely as a sum of these plane waves. This particular basis form allows for very efficient fast Fourier transform [195] when

calculating the kinetic and potential contributions when the Hamiltonian is diagonal. Also, no assumptions are taken as to the true wave function with plane waves, but this requires 2 orders of magnitude more functions per atom compared Gaussian orbital representation.

In AIMPRO, Gaussian basis functions are used to expand the Kohn-Sham electron orbitals. They have the advantage of having analytical integrals which can be evaluated rapidly compared to other basis types. Additionally, they are much more localised and decay from the orbital site faster than plane waves.

The localised Gaussian orbitals have the form [191]:

$$\phi_i(r - \mathrm{R}_i) = (x - R_{ix})^{n_1}(y - R_{iy})^{n_2}(z - R_{iz})^{n_3} e^{-\alpha_i (r - R_i)^2} \tag{21}$$

where the exponential term $e^{-\alpha_i (r-R_i)^2}$ is the Gaussian function for the orbital i at a distance r from the atomic centre R_i, whose width is augmented by the exponent α_i. The polynomial describes the projection of the orbital in the dimensions x, y, and z from the centre atom.

Through combinations of the n term you can create the different types of orbitals (s,p,d etc.), where an s orbital would have values $n_{\mathrm{i}} = 0$ and i = 1,2,3. From here the wavefunctions hence charge density can be expanded to construct a charge density matrix.

The majority of a slab will be composed of the material on which any termination sits, and so will represent the majority of computational effort. Table 6 illustrates how the choice of basis affects key observables.

Table 6: How choice of wavefunction basis affects certain measurables of a 2 atom diamond bulk cell.

Parameter	dddd	ddpp	pppp
Functions per atom	40	28	16
Total energy (Ha)	-11.426	-11.425	-11.407
Lattice constant (a.u.)	6.676	6.674	6.700
Run time (s)	25	15	10

The parameter nomenclature is understood as so: each letter represents a value of the Gaussian exponent fitted to minimise the energy of the material it was used to build. The exponents are then varied to minimise the energy for the current system. Each letter represents an exponent with orbitals up to and including that type. The letter 'p' then represents orbitals up to and including p-type with 4 functions for each (p_x,p_y,p_z and s), and the letter 'd' represents up to and including d-type orbitals where there are 10 functions for each. Generally speaking, more

functions up to and including a higher orbital angular momentum will result in a more accurate description of the atomic orbitals and charge density. The downside is the increase in computational effort, where the time to completion scales cubically with the number of functions.

The effects of a few basis functions are listed in Table 6 for bulk diamond. Here it can be seen that the more functions there are the lower the total system energy, hence a more well converged set of parameters [196, 197], the trade-off being an increase in the time to completion. A mix of orbital angular momenta in the form of 'ddpp' provides both the polarisation functions [198] in 'd' and the smaller 'p' functions reduce the run time whilst reproducing parameters close to that of 'dddd' (Table 6). This may be a more prudent choice of basis when time and memory are limiting factors.

Mixing plane wave and Gaussian basis sets like this combines the advantages [199] of both basis types. Great computational efficiencies can be had by using the Gaussian orbitals to capture most of the properties of the orbitals using only a small amount of atom-centred basis functions. The cut-off energy for plane waves need not be a large number to converge the energy of the system to a great degree of accuracy.

3.5 Brillouin Zone Sampling

Calculating properties such as the charge density and bandstructure of a solid requires a charge density integration over the Brillouin zone. Exploiting a property of Blochs theorem, it is sufficient to know only the solution of the wave function for the first Brillouin zone, as the periodic potential is the same in all neighbouring zones except for the plane wave phase factor $\mathbf{e}^{i\mathbf{k}\cdot\mathbf{r}}$.

The advantages of the supercell approach utilising periodic boundary conditions (Section 3.6) are reflected in the sampling, where the potential arising from the charge density in all Brillouin zones is identical. Therefore the sampling need only be sufficient to describe the unit cell.

As calculating the charge density is such a fundamental part of DFT, a large amount of computational effort is dedicated towards finding its solution. It is then of great importance that the method used is as efficient as possible at evaluating the integrals over the Brillouin zone. The method used by AIMPRO was devised by Monkhorst and Pack [200] in 1976, who said only special sets of k-points in the Brillouin zone are necessary to provide an efficient method to evaluate the integrals. The equation describes the sequence of numbers u that includes the number of k-points chosen X for the reciprocal lattice vector in the same direction $\vec{b}_1$

$$u_x = \frac{2x - X - 1}{2X} \qquad (x = 1, 2, 3..., X) \tag{22}$$

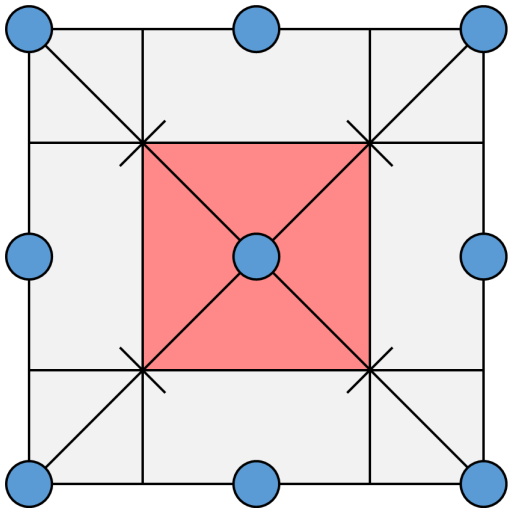

Figure 16: Reciprocal lattice points in blue and the corresponding Brillouin Zone for a square lattice in red.

which is then expanded as a linear combination of the k points and reciprocal lattice vectors in their respective directions.

$$\vec{k}(x,y,z) = u_x\vec{b}_1 + u_y\vec{b}_2 + u_z\vec{b}_3 \tag{23}$$

These set of points allow for the integration of a function f that is totally symmetric and periodic in $\vec{k}$ space: [200]

$$f(\vec{k}) = \sum_{m=1}^{\infty} f_m A_m(\vec{k}) \tag{24}$$

where the periodicity can be described in terms of the plane wave expansion of the charge density to achieve a final solution.

Sampling is analogous to the trapezium rule method for evaluating the area under a curve. The area is split up in to a number of strips an equal distance apart. With an increase in the number of strips, the answer converges towards the exact analytical solution. For 3D materials, it is necessary to specify how many k points are required in each direction in proportion to the reciprocal lattice vectors that defines the mesh that the Brillouin zone is split up into. If for example the lattice type is simple cubic, the cell size is equal in all three directions in space, so an $N \times N \times N$ mesh would give a uniform density. If the lattice was orthorhombic, and the second lattice vector was twice as long as the first (half as long in reciprocal space), one

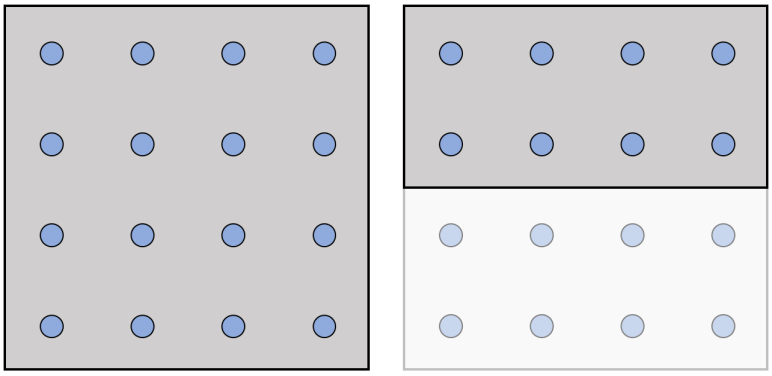

Figure 17: 4×4 2D Array of k-points in reciprocal reduced to 2×4 by doubling the size of the real space cell in one direction whilst maintaining density.

would only need half the number of k-points describing it in that direction to remain uniform (Figure 17).

The choice of sampling should then form an integral part of any calculation. To find the required parameters for convergence, a sample calculation should be performed with varying sampling densities.

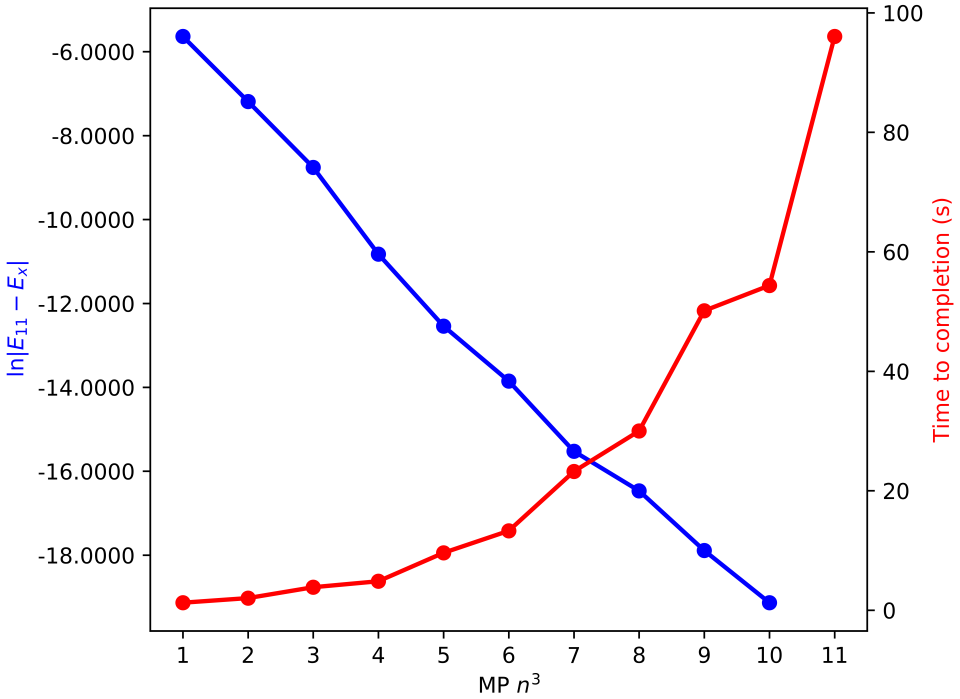

Figure 18: The dependence of total energy and time to completion on sampling density for bulk GaN. The energy (blue) is represented as the logarithm of the difference of the final energy (MP 11^3) and the given energy for that sampling.

Figure 18 shows that the energy continues to converge as a function of sampling albeit with an increasingly tiny step change, where the Hartree energy difference between 6^3 and 7^3 is below 1×10^{-7} Ha. The time to completion however increases exponentially, showing that an

arbitrarily high sampling is not beneficial for large volumes of calculations as the total time to completion could increase by orders of magnitude.

Fewer k-points are needed for surface structures under periodic boundary conditions due to symmetry operations. When the distance between surface and periodic image is sufficiently large (as in a surface calculation), there is no interaction between electrons in the surface normal direction. Consequently there is no electronic dispersion in this direction and requires only 1 k-point for the sampling, rendering the Brillouin zone effectively 2D.

3.6 Periodic Boundary Conditions

Periodic boundary conditions (PBCs) are applied to simulate an infinitely expansive crystal system from an original unit cell. Bulk materials have identical structural repeats in all directions called supercells.

Supercells can be described in terms of a Bravais lattice, where infinite crystal arrays in three dimensions can be described by integer translations of the basis vectors:

$$\mathbf{R} = n_1\mathbf{a}_1 + n_2\mathbf{a}_2 + n_3\mathbf{a}_3 \tag{25}$$

where $\mathbf{a}_\mathrm{x}$ are the primitive lattice vectors and n_x are the vector scaling factors. With a choice of any integer n the point $\mathbf{R}$ will be in an equivalent position but for a different cell.

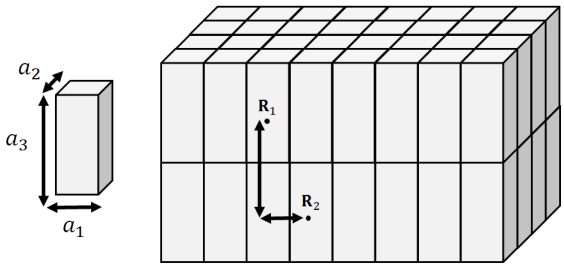

Figure 19: A unit cell (left) described by 3 lattice vectors and a supercell equivalent (right) with adjacent images.

Figure 19 shows a unit structure and its repeated equivalent with an integer vector displacement in two directions from $\mathbf{R}_1$ to $\mathbf{R}_2$.

Isolating a surface requires infinitely repeating and conjoining images (repeats) in all directions but the surface normal, where a sufficiently large vacuum space is introduced between one repeat and the other. This is necessary as without it one can imagine a structure with vacuum on all sides. This would introduce surface effects and reconstructions on all sides of the material which

would prevent specific surface isolation and investigation. These structures are referred to as slabs because they look like large slabs of material stacked on top of each other.

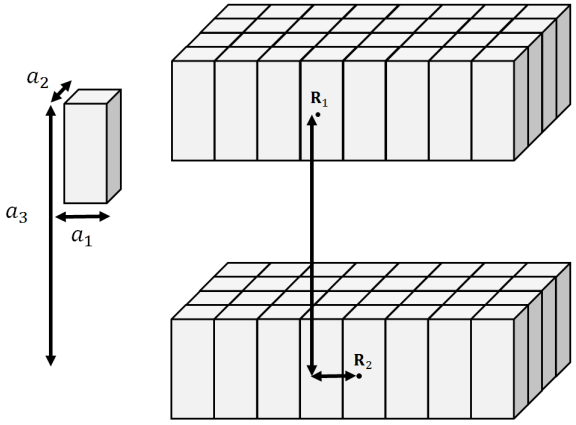

Figure 20: A unit cell (left) described by 3 lattice vectors and a supercell equivalent (right) with adjacent images and a vacuum in the a_3 direction.

Figure 20 is identical to that of Figure 19 except with the introduction of vacuum and surfaces in one direction, again arriving in an identical image with an $\mathbf{a}_3 + \mathbf{a}_1$ displacement.

The lattice parameter in the surface normal direction must be large enough to introduce sufficient vacuum to prevent image-image interaction and allow for the charge density to comfortably extend to zero. If the vacuum is insufficient the proximity of the surfaces will induce artificial forces and the surface energy will not be fully converged.

3.7 Surface Physics and Electron Affinity

Homonuclear diatomic molecules have symmetrical interatomic charge density and the same effective nuclear charge. Pure diamond is tetrahedrally co-ordinated and can be viewed as 4 pairs of identical C-C molecules. At the surface however, cleavage of C–C bonds and chemisorption of foreign species from external sources will create heteropolar bonds. Different effective nuclear charges will create asymmetrical charge densities between the two atoms for the formation of polar bonds and electric dipoles.

The degree to which an atom will attract charge is referred to as electronegativity. Pauling electronegativity is dimensionless and the general trend is that electronegativity increases with increasing period number and increasing group number; francium has a value of 0.7 and fluorine a value of 3.98 [201].

Point charge surface dipole moments are vectors quantities and their magnitude is described by:

$$\vec{p} = Q\vec{d} \tag{26}$$

where Q is the total charge of the system and $\vec{d}$ is the internuclear displacement vector. The result can be imagined as if electrons have been partially transferred from one atom to the other.

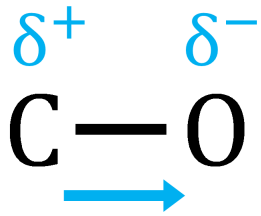

Figure 21: A carbon monoxide molecule with partial charges and resulting electric dipole moment

If we take the example of carbon monoxide (Figure 21) there is a redistribution of electron charge from the carbon to oxygen. Oxygen is a much more electronegative atom than carbon with a value of 3.44 to carbon's 2.55, consistent with the charge displacement and electric dipole pointing towards the oxygen atom.

The direction and magnitude of a surface dipole is therefore strongly dictated by the electronegativity difference of the semiconductor material and the terminating species. Diamond (carbon) has a relatively large electronegativity value of 2.55 compared to other conventional semiconductors like silicon (1.90) and germanium (2.01).

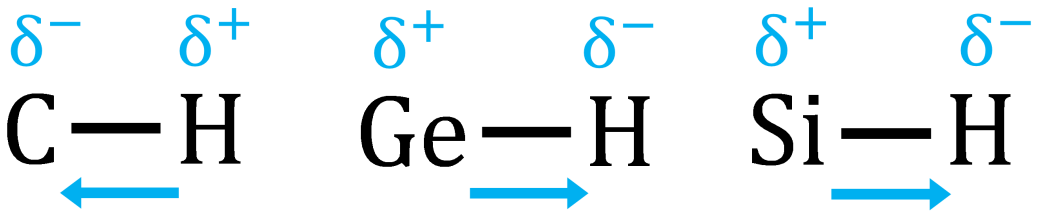

(a) (b) (c)

Figure 22: Varying semiconductor and hydrogen polar molecules with respective electric dipole moment

Figure 22 is a simplistic description of some dipoles and their respective direction when bonded to hydrogen. When terminating a surface with hydrogen, the direction of the dipole for silicon and germanium represents a potential increase and a potential drop for diamond. The potential step in the surface normal direction is directly proportional to the change in electron affinity of the surface.

The general electron affinity equation of an unterminated surface is:

$$\chi = E_{\text{vac}} - E_{\text{c}} \tag{27}$$

Where E_{vac} is the potential of the vacuum and E_{c} is the conduction band minimum. When an adsorbing species is added to the surface, the electron affinity will change as a result of the electrostatic dipole arising from the nature of the interation with the surface:

$$\chi = E_{\text{vac}} - E_{\text{c}} + E_{\text{step}} \tag{28}$$

Where E_{step} is the potential drop at the surface as a result of the adsorbing species. Depending on whether the potential step is positive or negative the electron affinity will increase or decrease respectively. This makes diamond (and various other materials) an interesting prospect because depending on the terminating species the potential drop could be significant; to the point where the electron affinity is even negative.

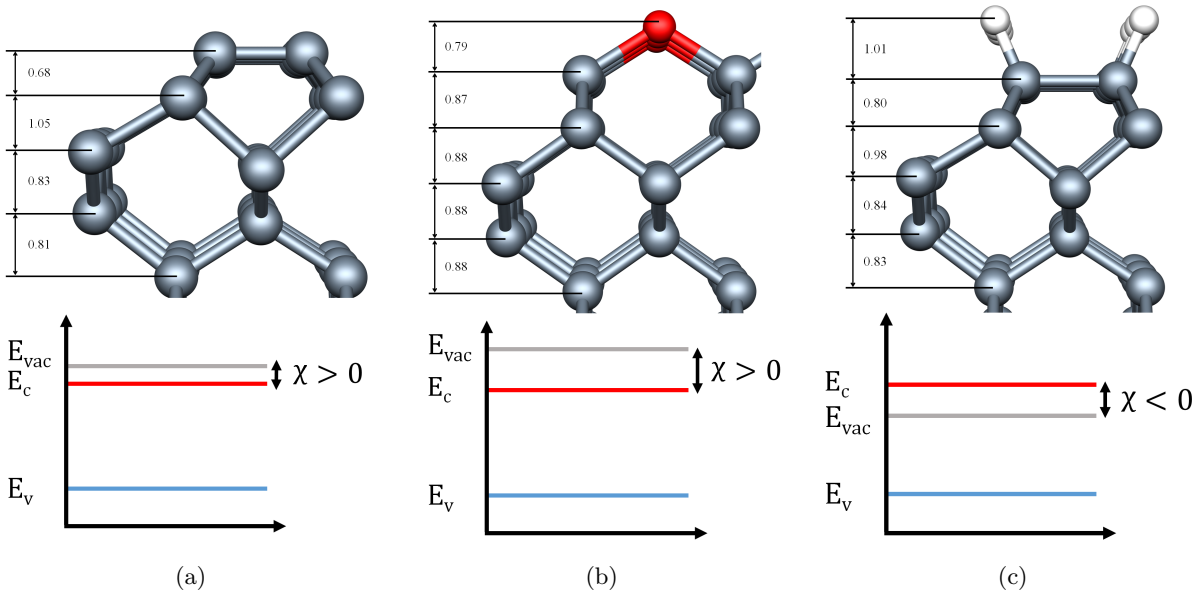

Figure 23: Varying diamond (001)-(2×1) surface adsorbate with simplistic description of the vacuum potential E_{vac} with respect to the conduction band E_{c} and valence band E_{v}. Dark-grey, red and white spheres represent carbon, oxygen and hydrogen respectively.

Figure 23 shows how different terminations can create a range of surface effects including a considerable magnitude and polarity change in the electron affinity.

Calculating the electron affinity within a DFT context is not as straight-forward as the classical band diagram might suggest. The accurate description of excited states is a known limitation of DFT [181], where only the ground state wave function is known. Methodological adjustments are necessary [202] to arrive at EA values that agree with experiment to an acceptable degree of accuracy.

The general form of Equation 28, where E_{step} is zero, requires three standard terms: E_{vac} the

vacuum potential, $E_{\mathrm{v_{vbm}}}$ the highest occupied band and the band gap E_{g}:

- E_{vac} In order to establish the vacuum potential, bulk diamond must be cleaved in a way to expose the surface in question to vacuum. Standard procedure is to employ the slab method using periodic boundary conditions, where the material is repeated infinitely to simulate the bulk material for the in-plane directions and the surface in the surface normal direction described in Section 3.6. The electrostatics of the system referenced to the vacuum are then calculated to reveal the model specific E_{vac} depicted in Figure 24.

- $E_{\mathrm{v_{vbm}}}$ The valence band maximum is derived from a calculation of the bandstructure from the bulk material. It is not appropriate to use the $E_{\mathrm{v_{vbm}}}$ from the slab model as the surface structure and any termination will influence its value.

- E_{g} As discussed above, to avoid problems associated with the value of the band gap the experimental band gap value from literature can be used as a constant to add to arrive at the conduction band minimum.

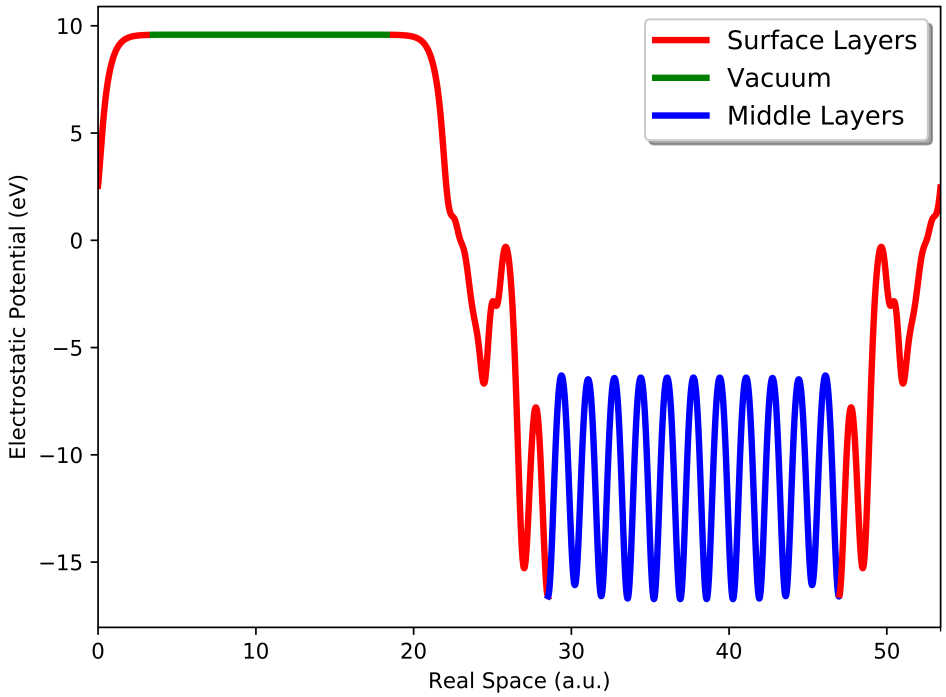

Figure 24: Electrostatic potential analysis of a silicon dioxide terminated diamond slab structure.

The last piece of the puzzle is to address the issue between the two reference potentials of the bulk and slab models. As the vacuum potential is system dependent, a variety of factors can influence its value with reference to the total energy scale. It is necessary to align the potentials of the bulk and slab in order to establish an equal reference upon which the EA can be found.

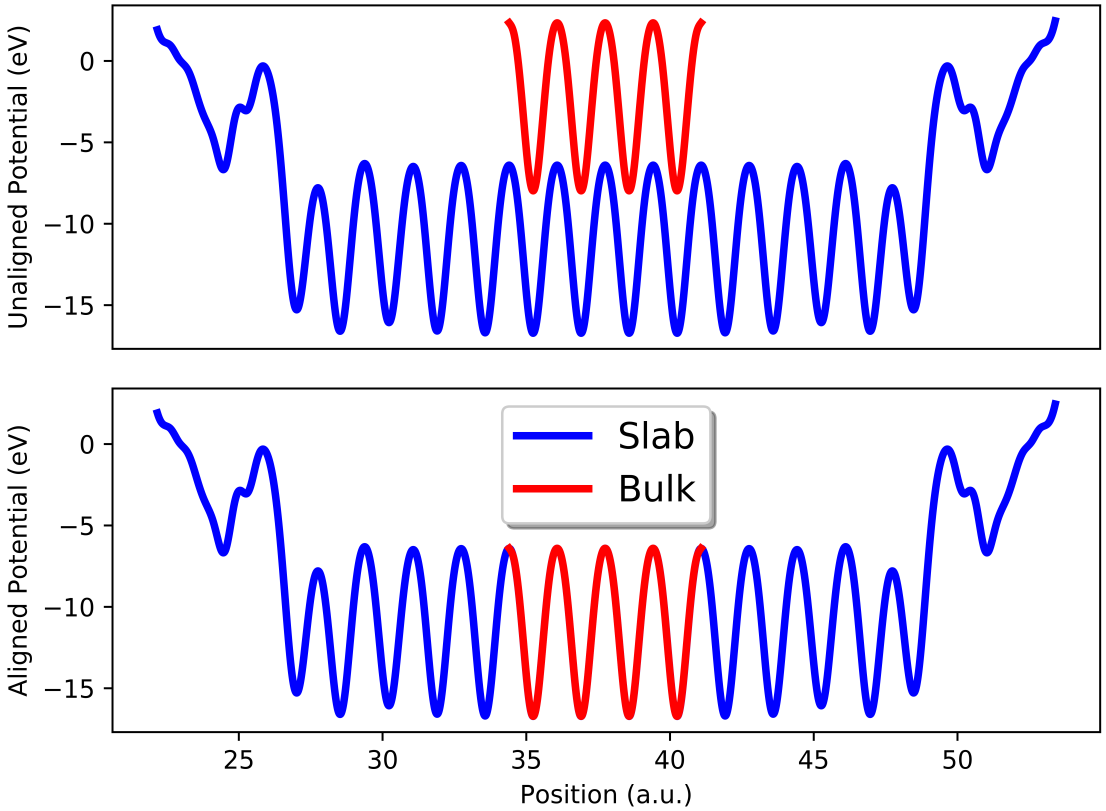

Figure 25: Bulk potential peaks aligned with the middle of the slab potential peaks.

Figure 25 shows the correction necessary to bring both models to the same reference potential. Matching slab peak with bulk peak requires an added value ΔE_{bulk}. The alignment must be over the central slab peaks where the structure most resembles the bulk material, away from the surfaces. All slab models must be sufficiently thick to prevent long range surface dipole penetration through most of the structure. Typical slab thicknesses and the convergence of surface energies are discussed widely in literature [203, 204].

Finally, we arrive at the general expression for any given surface:

$$\chi = (E_{\text{vac}}) - (E_{\text{vbm}} + E_{\text{g}} - \Delta E_{\text{bulk}}) \tag{29}$$

The vacuum size of Figure 24 needs to be sufficiently large to avoid any spurious interactions with adjacent slabs that could influence the forces on the surface atoms and ultimately their final geometry. The vacuum officially begins when the charge density of the system trails to zero and the potential is flat, shown by the green region on Figure 24. The treatment of vacuum is touched upon in more depth in Section 3.8. A large vacuum of > 30 a.u. can accommodate unexpected changes in the surface such as desorption, considerable dipole surface normal displacements and slowly trailing charge densities. Increasing the vacuum thickness has only a small impact on time to completion, so it is best advised to err on the side of a larger vacuum.

3.8 Ghost Atoms

The evanescent decay of wavefunctions into the vacuum must be described by localised Gaussian orbitals used to build all Kohn-Sham states. True wavefunctions decay exponentially as $e^{-\alpha_i(r-R_i)}$ where as Gaussian orbitals decay more rapidly as $e^{-\alpha_i(r-R_i)^2}$, shown in Figure 26. This implies that trailing charge densities that extend significantly into the vacuum and their electronic states are not being adequately represented at the surface creating a shift in the vacuum potential. As the aims are largely centred upon the effect chemical termination of semiconductor surfaces has on electron affinity, the correct treatment of the surface and near-surface regions is of great importance. Additional Gaussian functions can be added to the vacuum

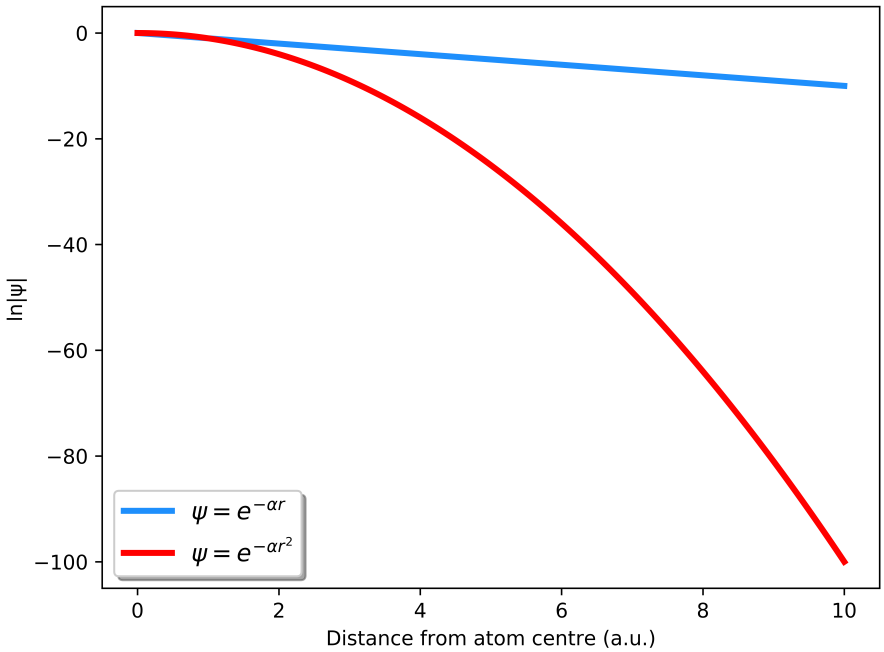

Figure 26: How the true (blue) and basis set representation (red) of the wavefunction decay with distance from a point charge.

which take the form of pink spherical structures arranged in a cuboidal array above and below each slab surface which may be referred to as ghost atoms, visible in Figure 27. These ghost atoms have 16 functions each up to and including p with four exponents whose co-ordinates are centred on the atoms. Wavefunctions in the vacuum now decay more slowly and more accurately represent the surface electronic states [205]

The impact that ghost atoms have on accuracy and time to completion have been investigated and compared to other known sources of error including the functional.

Table 7 shows that adding a single layer of ghost atoms in this case has a significant impact on electron affinity whilst also only increasing self consistent field time by the order of several percent. The ghost atom model represents an increase of up to 0.6 eV in electron affinity where

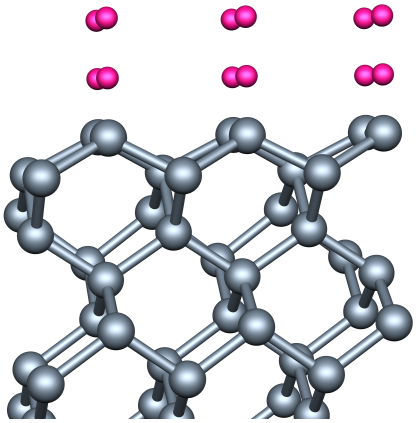

Figure 27: Two layer cuboidal array of pink ghost atoms above the (001)-(2×1) unterminated diamond surface

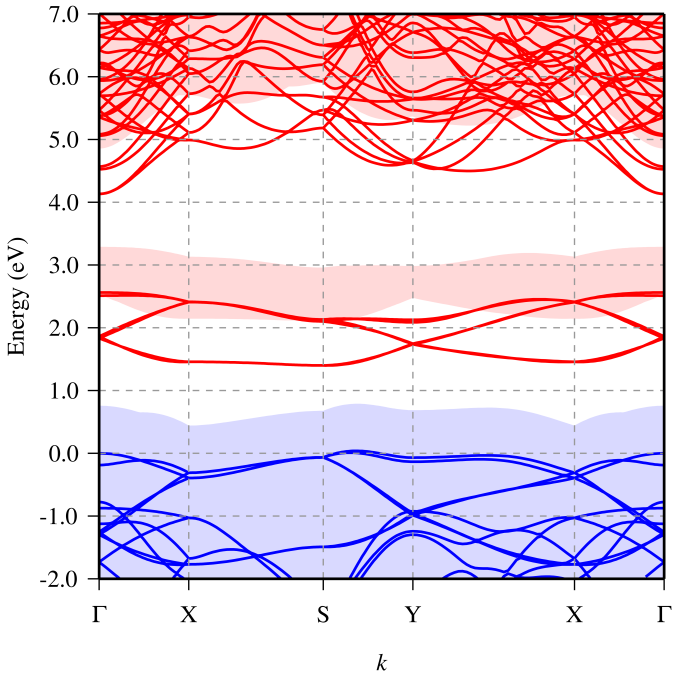

Figure 28: Calculated electronic states of the unterminated (001)-(2×1) diamond surface with 1 layer of ghost atoms is overlaid on the same structure without ghost atoms (shaded region). 0 eV on the energy scale represents the VBM of the ghost atom surface

the vacuum potential was underestimated, suggesting there was inaccuracy of the representation of the evanescence of the charge density in to the vacuum. Beyond a single layer however there are diminishing returns on the accuracy of the vacuum potential as the charge density in the vacuum approaches zero. The difference in time for self consistency however is notable, where 3 layers of ghost atoms for each surface represents an increase by a factor of 2.5 over just a single layer in this case (84 atom slab).

Further illustration can be taken from the band structure of Figure 28, where a noticeable downward electrostatic shift in the electronic states for the ghost atom system of 0.77 eV is seen

Table 7: Effects of varying layers of ghost atoms compared to an identical (001)-(2 × 1) unterminated system with no ghost atoms. Time to completion represents the time to establish self consistent field normalised to a no ghost atom run and Relative Energy is the energy difference between the lowest energy structure (given by 3 layers of ghost atoms) and the other quoted structures.

	No ghost	1 layer	2 layers	3 layers
Relative Energy (eV)	0.88	0.11	0.03	0.00
Time to completion	1.0	1.05	1.50	2.71
EA (eV)	0.08	0.64	0.73	0.74
Average C–C (Å)	1.52	1.52	1.52	1.52

for 1 layer of ghost atoms compared to none. The electron affinity increases to 0.74 eV with 3 layers which agrees well with previous work [202]. The needs and role of ghost atoms can

Table 8: Effects of varying layers of ghost atoms compared to an identical (001)-(2 × 1) hydrogen terminated system with no ghost atoms. Time to completion represents the time to establish self consistent field normalised to a no ghost atom run and Relative Energy is the energy difference between the lowest energy structure (given by 3 layers of ghost atoms) and the other quoted structures.

	No ghost	1 layer	2 layers	3 layers
Relative Energy (eV)	0.04	0.02	0.01	0.00
Time to completion	1.0	1.32	1.54	1.64
EA (eV)	-1.82	-1.82	-1.81	-1.81
Average C–C (Å)	1.52	1.52	1.52	1.52

then be better understood by examination of a hydrogen terminated (001)-(2×1) surface where the change in electron affinity of 10 meV (Table 8) is negligible and the time to self consistency increases by almost a factor of two. The delocalised surface states of the unterminated diamond surface need additional Gaussian functions to be fully described while the hydrogen effectively localises excess charge to the surface with little or no charge trailing in to the vacuum. Further evidence for this is the overlap illustrated in Figure 29.

The need for ghost atoms should be evaluated on a case by case basis and shouldn't necessary be included in all structures by default.

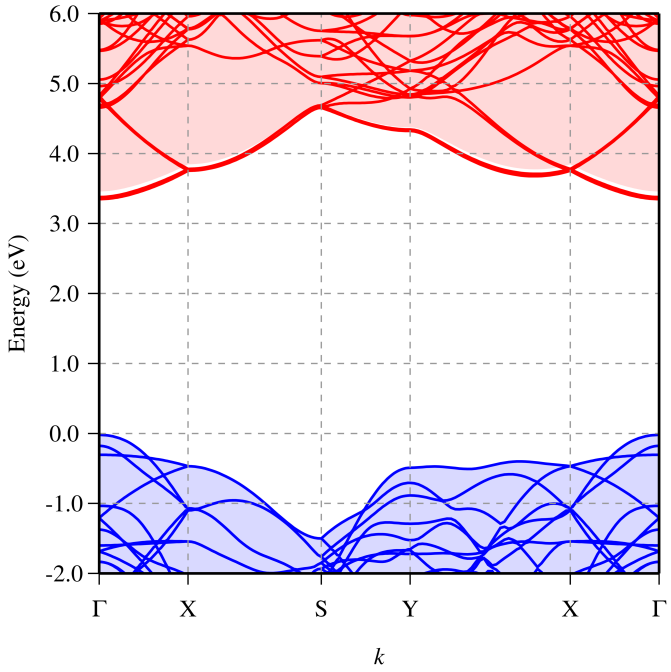

Figure 29: Calculated electronic states of the hydrogen terminated (001)-(2×1) diamond surface with 1 layer of ghost atoms is overlaid on the same structure without ghost atoms (shaded region). 0 eV on the energy scale represents the VBM of the ghost atom surface

3.9 Surface Energy

How suitable a species is to terminate a surface rests on how energetically favourable the final structure is compared so some known bulk energy values. There are many ways to classify these energies but one established method for surfaces is the surface adsorption energy or absolute surface energy [206, 207, 208].

The nature of the periodic boundary conditions enforced in surface calculations necessitate two surfaces, one at each end of the slab. Inversional symmetry around the centre of the structure ensures centrosymmetric calculations where the geometry and electronic structure are identical at each surface. Therefore the energy of the surface can be directly inferred from the total energy of the slab, the number of atoms, and the bulk reference energy per atom. The surface energy per surface site of the unterminated surface is given by

$$E_{\mathrm{surf}}^{\mathrm{n\times m}} = \frac{1}{2nm}\left\{E_{\mathrm{tot}} - N\mu_{\mathrm{C}}\right\} \tag{30}$$

where $n \times m$ is the number of surface sites per surface, E_{tot} is the total energy of the calculation, N is the number of bulk atoms and μ is the chemical potential of the bulk reference. The chemical potential is the total energy per atom of the bulk material being modelled.

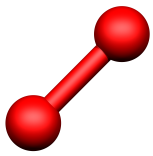

(a) O_2

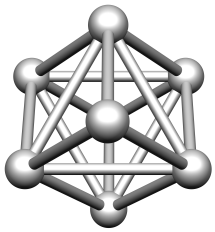

(b) Aluminium

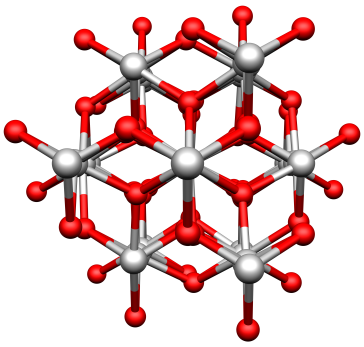

(c) Al_2O_3

Figure 30: (a) O_2 (b) Aluminium (c) Al_2O_3 bulk references.

For a single element material like silicon, diamond or germanium this is easily found. Added complexity comes from compound materials, where bulk references for the constituent elements must also be found and the ratios taken in to account. Taking Al_2O_3 as an example, the chemical potentials for aluminium and oxygen must come from their own bulk references. If the aluminium and oxygen are in equilibrium with bulk aluminium oxide, we get the equation:

$$E^T(Al_2O_3) - 2\mu_{Al} - 3\mu_O = 0 \tag{31}$$

The chemical potential for each element will vary on the reservoir chosen, shown in Figure 30. If for example the chemical potential for oxygen μ_O is taken from O_2, the aluminium chemical potential μ_{Al} is dependent on that. If the reservoir is switched and the initial chemical potential is from aluminium, there will be a chemical potential range for both elements where typically the most favourable limits are taken. The total number (N_x) of adsorbates and their chemical potentials (μ_x) and the unterminated surface (E_{unterm}) are then taken away from the total terminated slab energy to give the equation:

$$E_{surf}^{n\times m} = \frac{1}{2nm}\{E_{tot} - E_{unterm} - N_{Al}\mu_{Al} - N_O\mu_O\} \tag{32}$$

where $2nm$ is the total number of surface sites. The final value of the surface adsorption energy tells you the energy gain or loss to create the particular surface arrangement from the

bulk materials per surface site. A large negative value suggests that that particular geometry is energetically favourable therefore more likely to occur in nature, where a positive value quantifies the additional energy input required for formation.

3.10 Summary

This chapter represents the methods by which DFT is implemented in AIMPRO. How each part of the Schrödinger equation is solved as a function of the charge density through a set of algorithms and approximations is laid out and scrutinised for their validity. Where appropriate, the choices behind each parameter set and the effects therein aims to provide some confidence for the reader that they have been understood, are well reasoned and represent a realistic system to a high degree of accuracy. The analysis methods are well established, providing consistently reproducible measurables that agree well with experimental results. In the next chapter, more specific examples in the form of simple surfaces and terminations are given, with the aim of providing further confidence in the conclusions presented in the results sections.

4. Diamond Surfaces

The foundation of any surface, defect or interface for slab and cluster models is rooted in the definition of the primitive bulk cell. It is with this that all other structures are created and analysed for their properties. Therefore one can only ascribe confidence in the latter after proving confidence in the former.

All crystal structures are defined by a combination of their basis and lattice. A basis is the smallest possible configuration of atoms that when placed at each point within the lattice and repeated in all three spatial directions possesses the full symmetry of the material.

4.1 Fundamental Aspects

4.1.1 Defining the cell

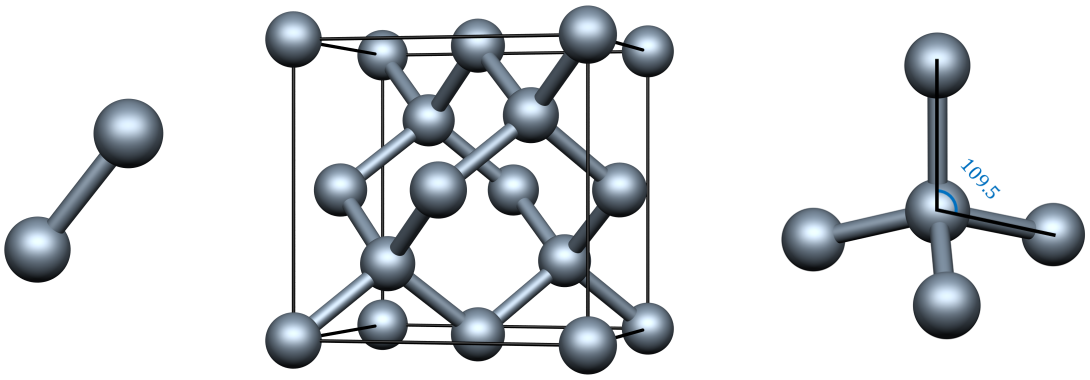

(a) (b) (c)

Figure 31: 2 atom diamond basis (a), a single FCC lattice of diamond (b) and a tetrahedron of carbon (c).

Bulk diamond is constructed from a 2 atom basis (Figure 31(a)) at positions (0,0,0) and $\frac{a_0}{4}(1+1+1)$ (where a0 is the lattice constant) in a face-centred cubic (FCC) lattice as in Figure 31(b).

Figure 31(c) shows a tetrahedrally co-ordinated four atom group of carbon atoms through an angle of 109.5°. The optimised lattice constant of diamond is 3.53 Å and the interatomic distance is calculated at 1.53 Å; within 1% of both theory and experiment [196, 209, 182]

Diamond has an indirect band gap of 5.45 eV and a calculated band gap of 4.2 eV (Figure 32) [210, 211], a value consistent with the underestimation of the band gap within DFT [181].

All surfaces with a set of chosen lattice vectors can be constructed from a linear combination of

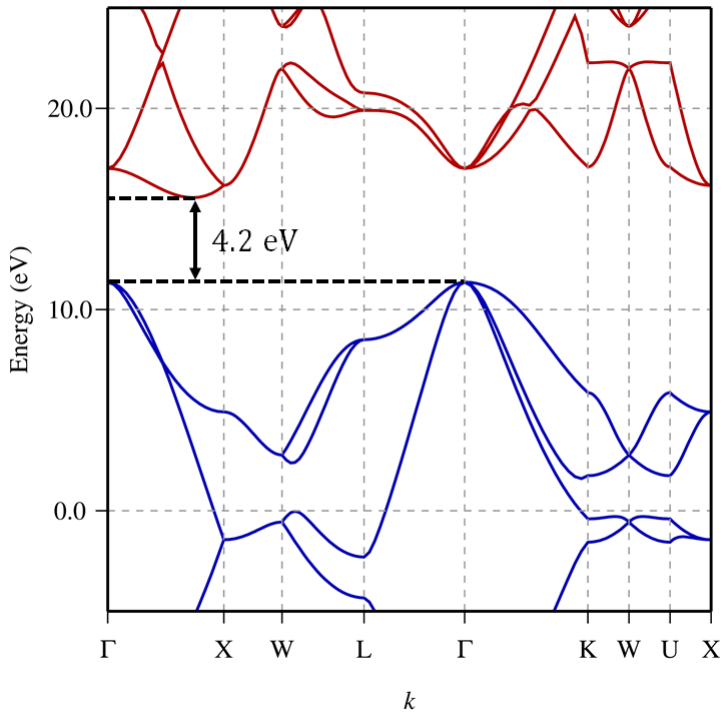

Figure 32: Bandstructure of 2 atom bulk diamond with calculated indirect bandgap of 4.2 eV.

the primitive lattice vectors and the 2 atom diamond basis. Section 7.1 details the procedure to determining the geometry and volume of such a structure.

The two most important diamond surfaces are the (001) and (111) as high quality thin films are more easily achieved with a lower defect density compared to higher-index surfaces. Higher index surfaces typically grow faster than low-index surfaces leading to unstable CVD growth, with very rough surfaces prone to high residual stress and cracking [212, 213, 214].

4.1.2 (001) Surfaces

(001) faceted surfaces have several advantages over their (111) counterpart including higher mobility, lower cost and the ease with which the surface is polished [215]. Additionally, (111) faces can be very defective with high rates of twin formation and stacking faults causing structural degredation and surface instability [216, 217].

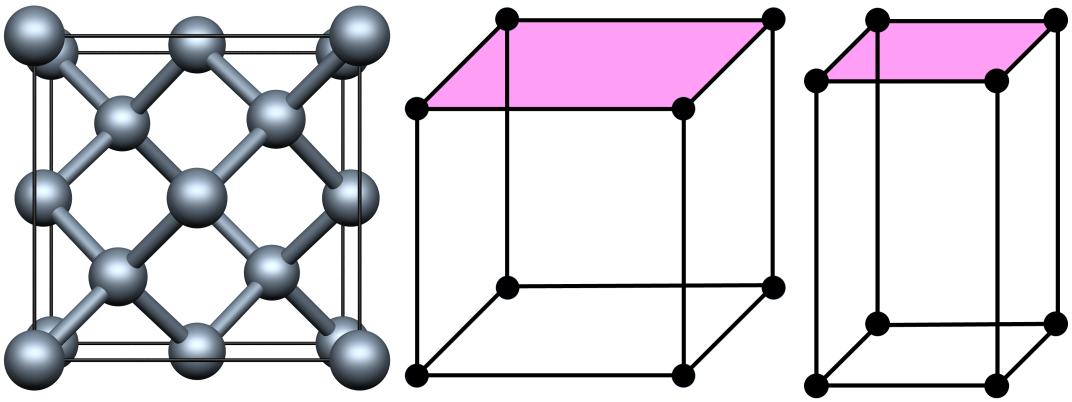

(a) (b) (c)

Figure 33: Bulk FCC diamond as viewed down the (001) direction (a). The (001) plane projection is shown in pink for a cubic (b) and orthorhombic (c) lattice type common to the (001) surfaces.

The (001) surface is the cubic face of diamond (Figure 33) and thus is best represented by a cuboidal lattice like tetragonal or orthorhombic. These structures require the in-plane lattice vectors to be at right angles to the chosen (001) surface and also orthogonal to themselves. The choice of in-plane lattice vectors in this example are (110) and ($\bar{1}$10).

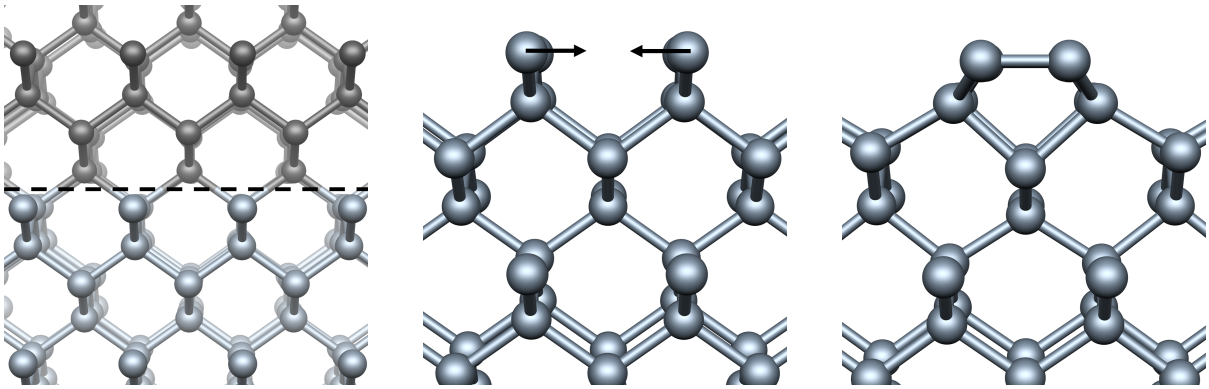

(a) (b) (c)

Figure 34: Describing the process of cleaving bulk diamond (a) with (001) lattice vectors and perturbing the cleaved surface (b) to achieve the (2×1) reconstruction (c) as viewed down the ($\bar{1}$10) direction.

Cleaving the (001) diamond cubic surface (as in Figure 34) removes two adjacent atoms in the tetrahedral network leaving two dangling surface bonds. This so-called (1×1) surface is unstable, and can lower its energy (1.5 eV per surface site) by reconstructing with adjacent cleaved surface atoms to form the (2×1) π-bonded dimer, characteristic of the surface. Typical dimer bond lengths are 1.37 Å (Figure 35), agreeing with both calculated and experimental results [218, 219].

The surface has a PEA of 0.74 eV, again conforming to that of similar work [220].

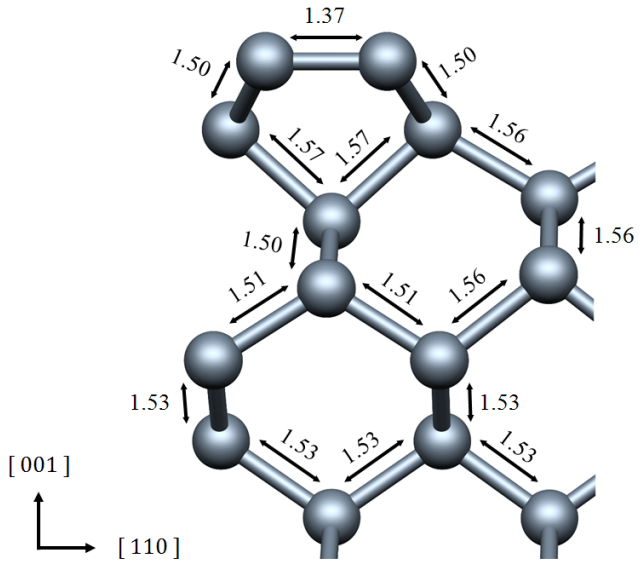

Figure 35: (001)-(2 × 1) surface structure as viewed down the ($\bar{1}$10) direction with bond lengths in Å.

Figure 36 shows the π and $\pi*$ surface states of the unterminated (001)-(2×1) surface, labelled in the bandstructure of Figure 36(c).

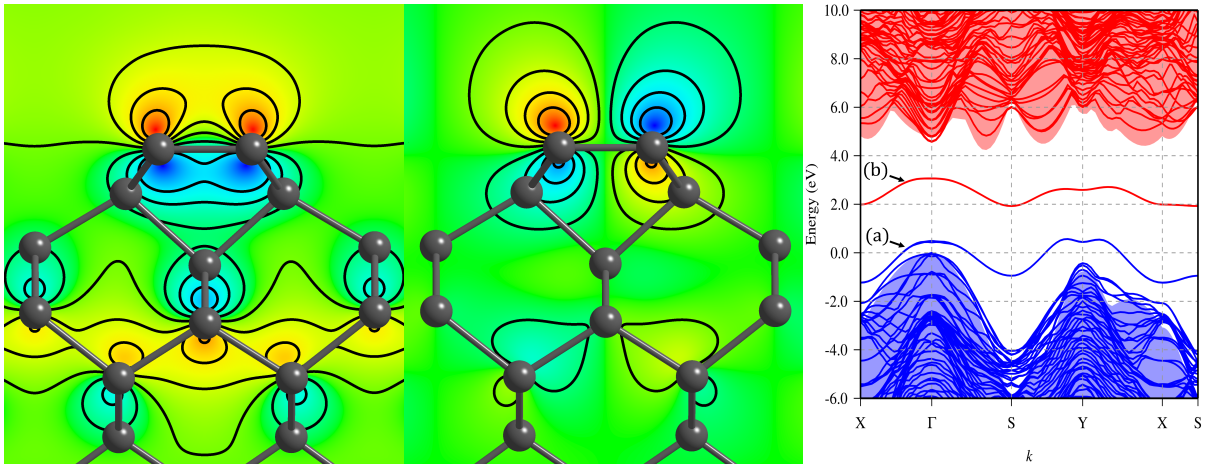

(a) (b) (c)

Figure 36: Wave function visualisation for the (001)-(2×1) unterminated surface as viewed down the ($\bar{1}$10) direction. Plots of the wavefunction at Γ for the π (a) and $\pi*$ (b) states labelled in the band structure (c) which depicts electronic structure of the unterminated diamond surface superimposed on top of shaded bulk diamond region. VBM of bulk diamond set to 0 eV.

Two of the most common terminations a diamond surface may exhibit are hydrogen and oxygen. Polishing and planarizing techniques [221] often take place in ambient gases that include oxygen and hydrogen containing groups. Exposure to atmospheric conditions would also introduce a

Table 9: Caclulated EA (eV) and surface formation energy (eV per surface site) as defined in Sections 3.7 and 3.9 respectively, for the most stable oxygen and hydrogen terminated (001) and (111) surfaces.

	EA	E_{surf}
(001)-(2×1)-H	−1.81	−2.15
(111)-(1×1)-H	−1.64	−2.53
(001)-(1×1)-O	2.71	−3.26
(111)-(1×1)-O	3.06	−1.34

wide range of groups including H_2O, hydroxyl (OH) and ozone (O_3). Additionally hydrogen and oxides are regularly exploited in device applications listed in Section 1.2, and as such deserve discussion.

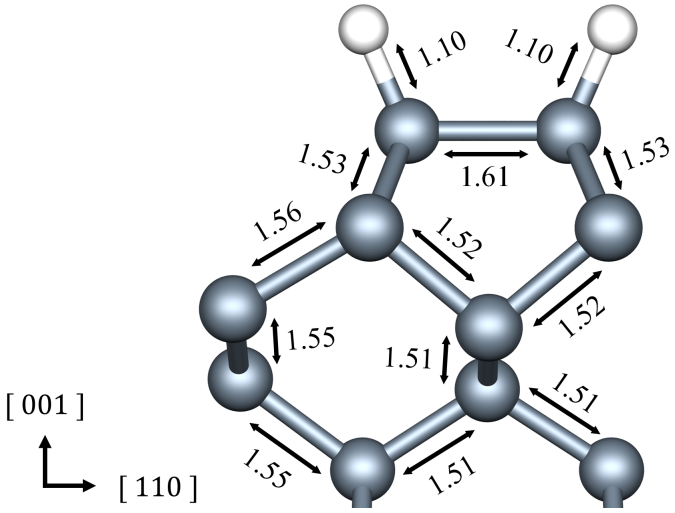

Figure 37: Hydrogenated (001)-(2 × 1) surface structure as viewed down the ($\bar{1}$10) direction with bond lengths in Å.

Figure 37 illustrates the surface structure of hydrogen terminated diamond. The C–C dimer bond length has increased from 1.37 Å to 1.61 Å, in good agreement with other calculated work [222, 223] and LEED experiment [224]. A C–H bond length of 1.10 Å is consistent with reported C–H radical bond lengths [205, 223]. Table 9 indicates that the energy gain per surface site for the hydrogen terminated surface when compared to the unterminated surface is 2.15 eV, which is in agreement with previous studies [205, 223]. Hydrogen, having a more positive electronegativity than carbon by 0.35, will be expected to induce an NEA (Chapter 3.7) and indeed, Table 9 shows a value of −1.81 eV, comparable with both experimental [225] and calculated values [202].

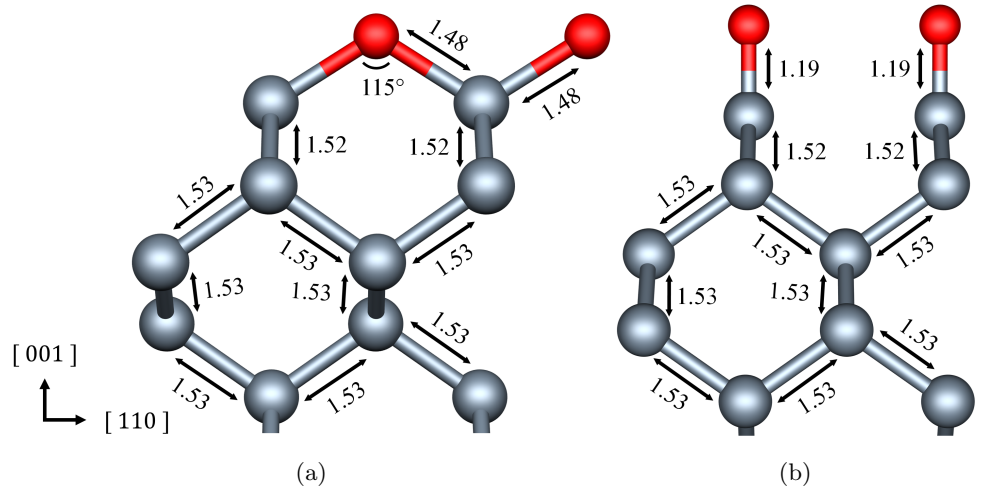

(a) (b)

Figure 38: Ether (a) and ketone (b) arrangements of the oxygen terminated (001)-(1×1) diamond surface as viewed down the $(\bar{1}10)$ direction. Bond lengths in Å.

One may envisage two types of bonding for the (001)-surface: C-O-C bridge (ether) and C=O double bond (ketone). Figure 38(b) is a metastable arrangement and exists in a local energy minima. Perturbing the surface and optimising the structure prefers a C-O-C arrangement, such as in Figure 38(a), where each oxygen is co-ordinated with two surface carbons. The ether bridge configuration represents a gain in energy of 0.61 eV per surface site and indeed is the prevailing structure observed in experiment [224]. Carbon–oxygen bond lengths of 1.19 Å and 1.48 Å for the ketone and ether surfaces respectively are to within 1% of previous calculations [205]. As oxygen is very electronegative, with a Pauling value of 3.44, large PEAs of 2.71 eV displayed in Table 9 are typical, agreeing well with other work [202].

4.1.3 (111) Surfaces

The (001) surface however is not without its frailties compared to (111). Phosphorous doped n-type (001) typically exhibits reduced activity of donors responsible for high resistivity, whereas (111) oriented diamond is close to 100% in terms of active and available phosphorous atoms [214, 215, 30]. NV centres are aligned along the <111> directions, hence using (111)-oriented diamond would be beneficial for quantum information and metrology applications [226].

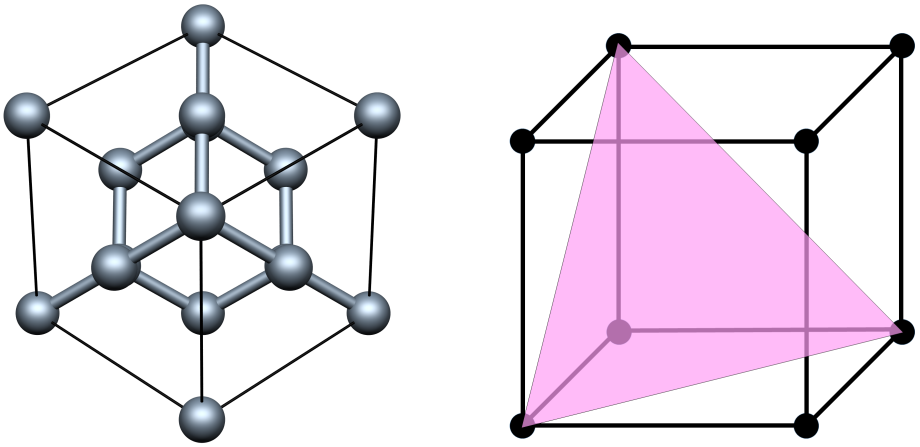

(a) (b)

Figure 39: Bulk FCC diamond as viewed down the (111) direction (a) accompanied by a (111) plane projection in an FCC system (b) highlighted in pink.

The (111) surface can be represented as a hexagonal surface and as such is best described by a hexagonal lattice (Figure 39). The surface normal direction (111) must be at right angles to both the in-plane lattice vectors, which in turn must be at 60° or 120° to themselves. The choice of in-plane vectors here are $(\bar{1}\bar{1}0)$ and (010).

Cleaving the (111) surface along the dotted line (Figure 40(a)) reveals carbon surface atoms that are bonded to 3 carbon atoms with 1 dangling bond. However (111) has two cleavage planes, so why do we choose to cleave the plane along the dotted line? If the surface was cleaved the next layer down where the layers are closer together, this would break 3 bonds per surface atom, taking roughly three times the energy to cut compared to the plane chosen in Figure 40. The most preferred cleavage plane would generally be one that requires the least energy [227, 228] and thus explains our structure. The arrangement of Figure 40(b) is metastable, where there is an insignificant barrier to reconstruction with only small in-plane displacements required to force reconstruction to the (2×1) Pandey chain resulting in a 0.80 eV per surface site energy gain, in excellent agreement with literature [205]. In experiment to force reconstruction requires annealing at a high temperature, typically up to 900 °C [229]. Furthermore the reconstruction

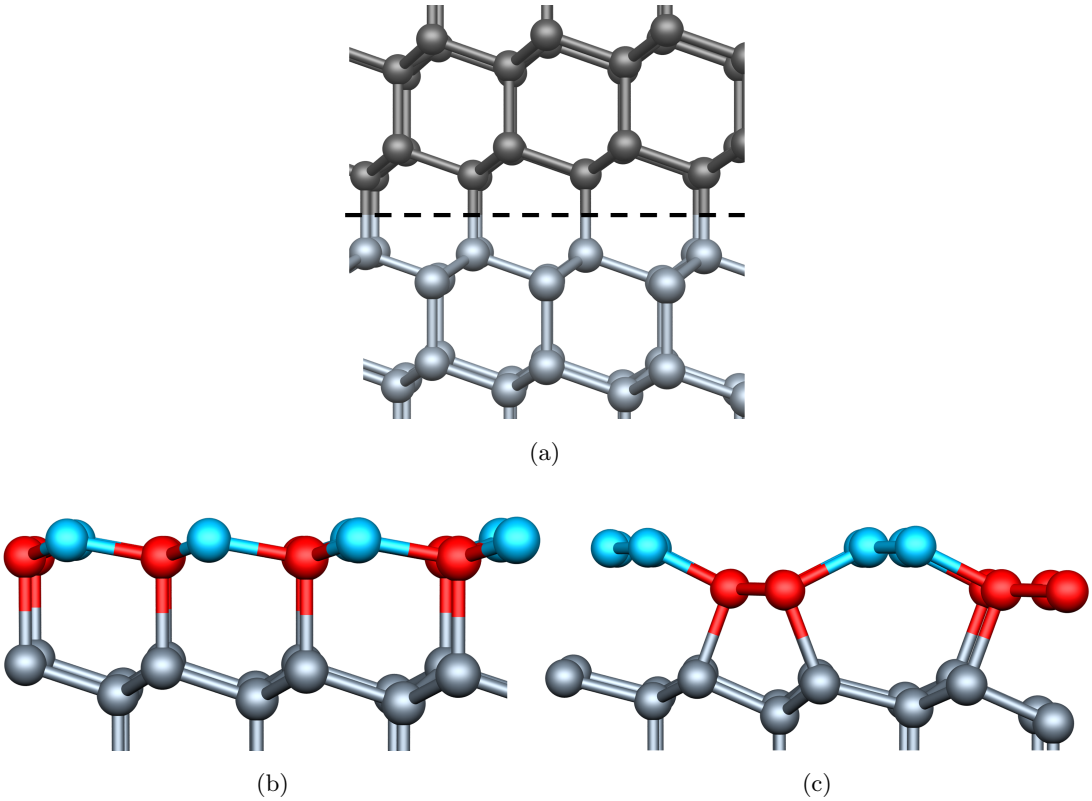

Figure 40: The process by which (111) oriented bulk diamond is cleaved (a) to reveal the (1×1) surface (b) and perturbing the cleaved surface to achieve the (2×1) reconstruction (c) as viewed down the $(\bar{1}\bar{1}0)$ direction. First and second layers are in bright blue and red respectively, to show how they rearrange.

continues to persist at temperatures well beyond 900 °C [230, 231]. Figures 40(b) and (c) shows how the first two layers re-arrange themselves post-reconstruction. The first layer is part of a 6 member ring and forms a 3-fold co-ordinated zig-zag chain along the surface and the second layer sits lower in the surface normal direction and forms a fully co-ordinated 5 member ring.

The zig-zag chain bond lengths of Figure 41(a) are significantly shorter than the bulk diamond bond length of 1.53Å by 0.10Å [232]. The disruption to the surface is reflected in the widely varying bond lengths for the first 6 surface layers, which only begin to reach bulk interatomic distances beyond around the 7th and 8th layer. The unreconstructed surface of Figure 41(b) however is much less fractious to the succeeding layers, presenting as bulk-like at only the 5th layer and beyond.

Pandey chain reconstruction has a slight PEA of 0.29 eV, within 0.06 eV of reported values [205].

Figure 42 reflects the structures creating the properties of Table 9. Hydrogen termination again exhibits a NEA, smaller than that of the (001)-(2×1) surface by 0.17 eV. The (1×1)-surface is lower in energy by 0.37 eV per surface site than the (2×1) reconstruction. Oxygen termination again favours the (1×1) unreconstructed surface, with a large PEA of 3.06 eV and an exothermic

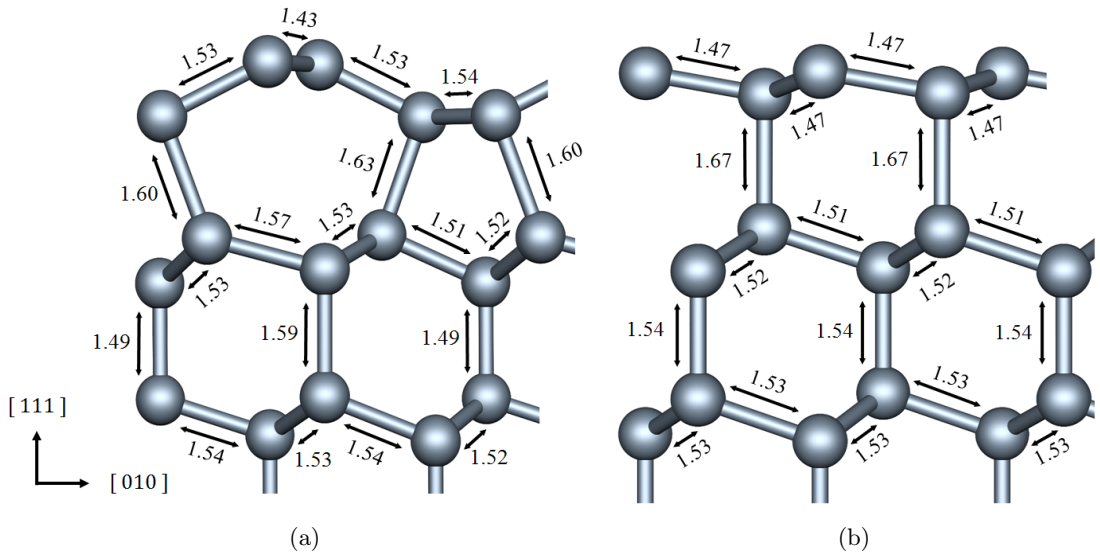

(a) (b)

Figure 41: (2×1) (a) and (1×1) (b) structures of the unterminated (111) diamond surface as viewed down the $(\bar{1}\bar{1}0)$ direction. Bond lengths in Å.

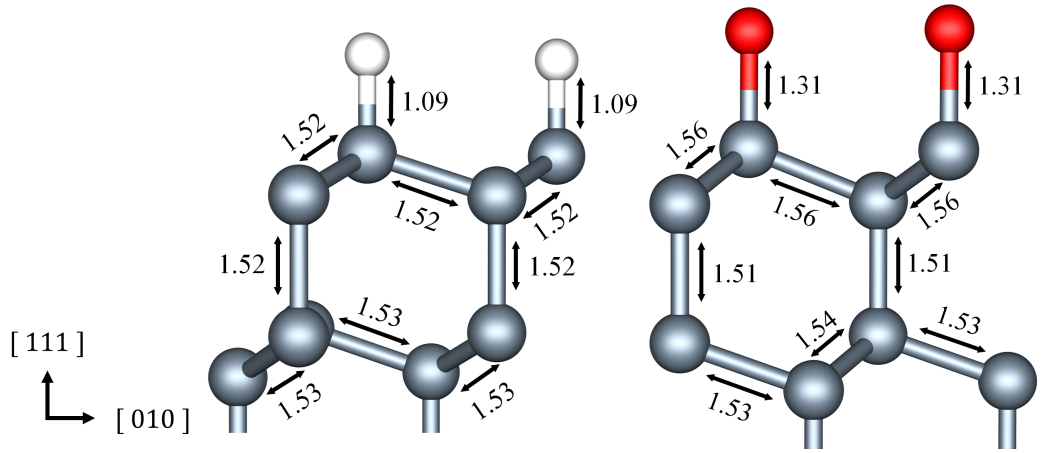

(a) (b)

Figure 42: (1×1) (111) surfaces terminated with (a) hydrogen and (b) oxygen viewed down the $(\bar{1}\bar{1}0)$ direction. Bond lengths in Å.

reaction with the surface of magnitude 1.34 eV per surface site.

The extensive detailing of bulk diamond and the two surfaces of note, (100) and (111), have shown that we can accurately reproduce the geometry, structure, electron affinity and surface energy observed in both theory and experimental data. It is upon these foundations that the novel surface terminations in the next sections depend.

4.2 Aluminium Oxide

For emission purposes, in the pursuit of a large and thermally stable NEA many terminations have been considered including metals and metal-oxides [46, 233, 234, 235]. Amongst the metal oxides, copper oxide produces a small NEA of −1.2 eV and low thermal stability, whereas titanium oxide has a sizeable adsorption energy of −7.6 eV per Ti atom and a large NEA of −3.1 eV [236]. Cesium oxide [237] coated surfaces produce an NEA of −1.3 eV, and X-ray photoelectron spectroscopy reveals this condition is thermally stable up to 500°C. Theoretically, lithium oxide terminated diamond has a binding energy of 4.7 eV/Li atom, and NEAs as large as −3.9 eV [238] and magnesium oxide adsorption has NEAs up to −2 eV [239].

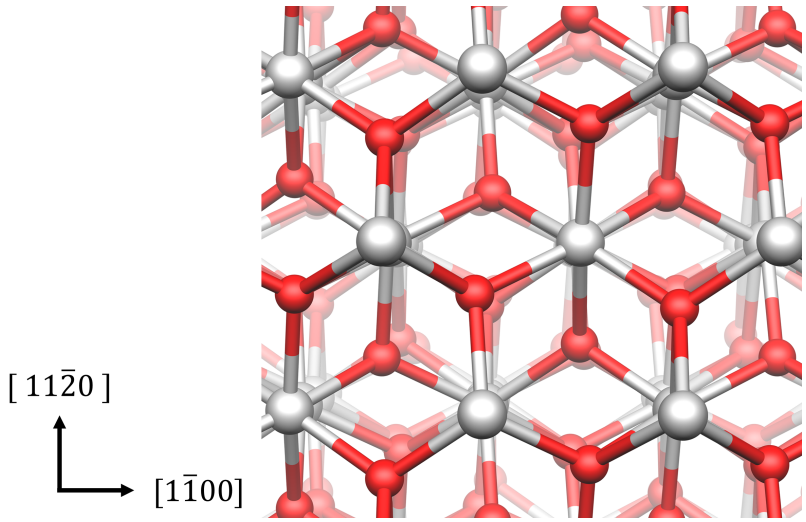

(a)

Figure 43: Bulk α– Al_2O_3 as viewed down the [0001] direction. White and red spheres represent aluminum and oxygen respectively.

The range of stabilities and NEAs for different treatments should be considered alongside viability of an industrial process for production of the coating if the properties are to be exploited in applications such as field emission. Aluminium oxide, an inexpensive and ALD compatible [240] material that is already integrated in technology, might be expected to produce the conditions needed for an NEA. However, to engineer a favorable surface for emission it is necessary to understand how the electron affinity changes as a function of stoichiometry and surface arrangement. The size of the surface electric dipole in-part reflects the difference in the electronegativities of the constituent atoms, which are 2.55, 3.44 and 1.61 for C, O and Al respectively on the Pauling scale [241]. This means that electrons tend to be displaced from Al and C towards O, so that for a diamond–O-Al structure, two sets of opposing dipoles are created. Where the Al–O dipoles dominate, a NEA is expected to arise, but this condition requires both the appropriate stoichiometry to produce favorable oxidation states, and favorable geometry with sufficient Al–O

displacement normal to the surface. Since it is known that oxygen-terminated surfaces have a large PEA [242, 243], if insufficient Al-coverage is achieved an NEA is unlikely to be formed, and if there is excessive aluminium, Al–Al interactions may reduce the Al–O dipoles and also negatively impact the EA. Understanding these mechanisms is crucial for consistent NEAs in device fabrication.

This section presents the results of density functional theory based simulations of Al_xO_y layers on (001)- and (111)-oriented diamond surfaces.

Bulk, stoichiometric, alpha phase aluminium oxide (Figure 43) is modeled as the reference structure for energetics, where structural markers such as a Al–O bond length of 1.84Å is within 1% of both previous theory and experimental work [244, 245] and a theoretical bandgap of 6.45 eV is also in good agreement.

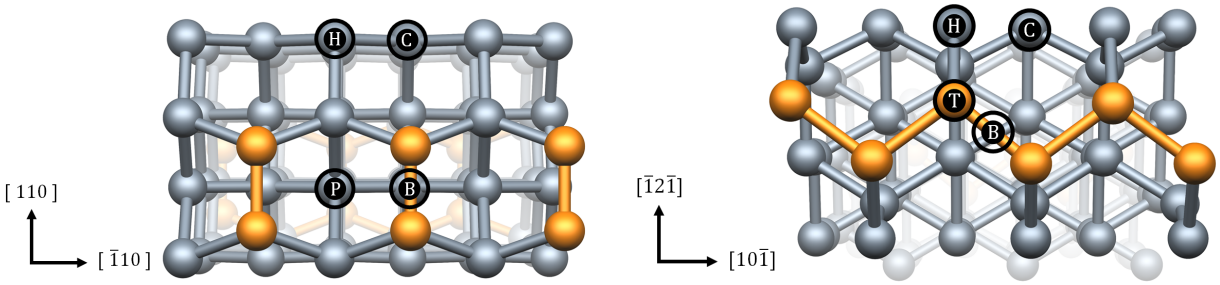

Figure 44: Plan-views of unterminated diamond surfaces illustrating the periodicity and high-symmetry adsorbate sites [246, 46]. (a) (001)-(2×1) and (b) (111)-(2×1). Surface sites are highlighted in yellow.

Considered are a wide range of structures, varying with either Al or O in contact with diamond. Diamond–Al–O or mixed C–Al and C–O interfacial bonds are significantly less energetically favorable than diamond–O–Al arrangements, and it is concluded that in equilibrium C–O bonds form the interface between diamond and the metal. It was previously shown that the interface between diamond and metal-oxides involves oxygen singly bonded to the diamond [236], and can be thought of as diamond–O^- for determination of stoichiometry. Then, although corundum is $Al_2^{+3}O_3^{-2}$, the interfacial layer is expected to be $Al_1^{+3}O_3^{-1}$. In order to assess the relative stability of this stoichiometry, AlO_2 and Al_2O_3 arrangements have been examined. In the following are data relating to structure, energy and EA for (001) and (111) diamond surfaces. The underlying surface geometry and periodicity plays a significant role in the arrangement of Al on an O-terminated surface in terms of obtaining the desired stoichiometry. To begin are arrangements with an O:Al ratio of 3.

4.2.1 AlO_3

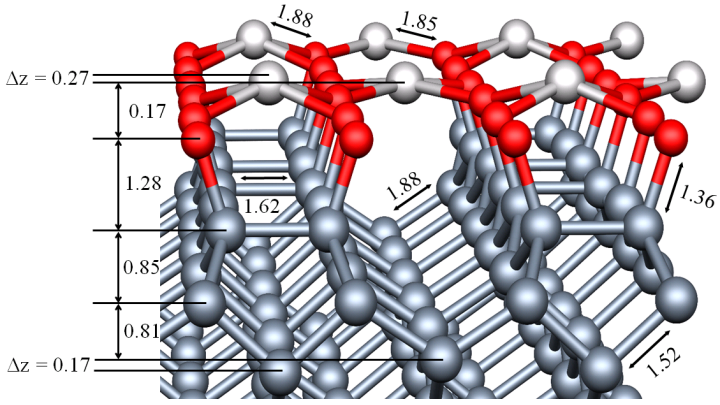

(a)

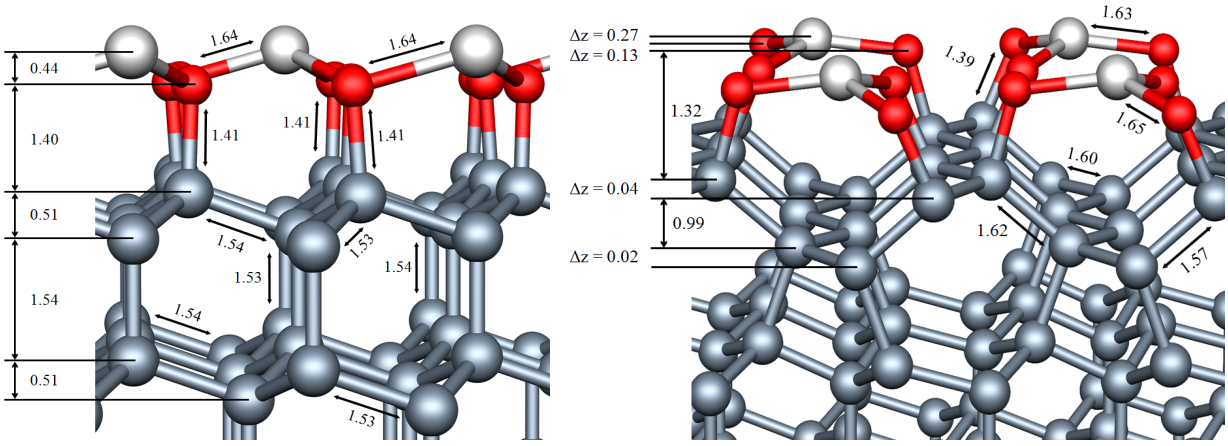

(b) (c)

Figure 45: AlO_3 terminated diamond surfaces. (a) (001)-(2×1), (b) (111)-(1×1), and (c) (111)-(2×1). Lengths in Å. Red, light-gray, and dark-gray spheres represent O, Al, and C, respectively. Schematics are viewed approximately along the $[1\bar{1}0]$ direction.

The (001)-surface (Figure 44(a)), with their respective high-symmetry site labels, has one oxygen atom per surface site. Figures 45(a) and 46(a) shows the lowest energy structure obtained, with half the Al atoms at P, and half at H, which results in co-ordination of the Al-ions with four O-ions, but no Al-Al bonds. Angles have been included in Figure 46(a) to highlight the effects of Al–O and C–O dipole sizes in the surface normal direction. All C–O angles are given with respect to the (001) plane in the [110] direction. C–O angles in the four corners surrounding the P site are 106.9°. As for the 4 C–O surrounding the H site Al, those which form the Al–O–Al zigzag network are 106.7° and the remaining outside two C–Os are 108.5°. A similar structure with Al over reconstructions (P and B-sites) is less energetically favorable by 0.3 eV per surface C-atom. Addition of all Al at P-sites means they each co-ordinate with four oxygen atoms, but also form Al-Al bonds.

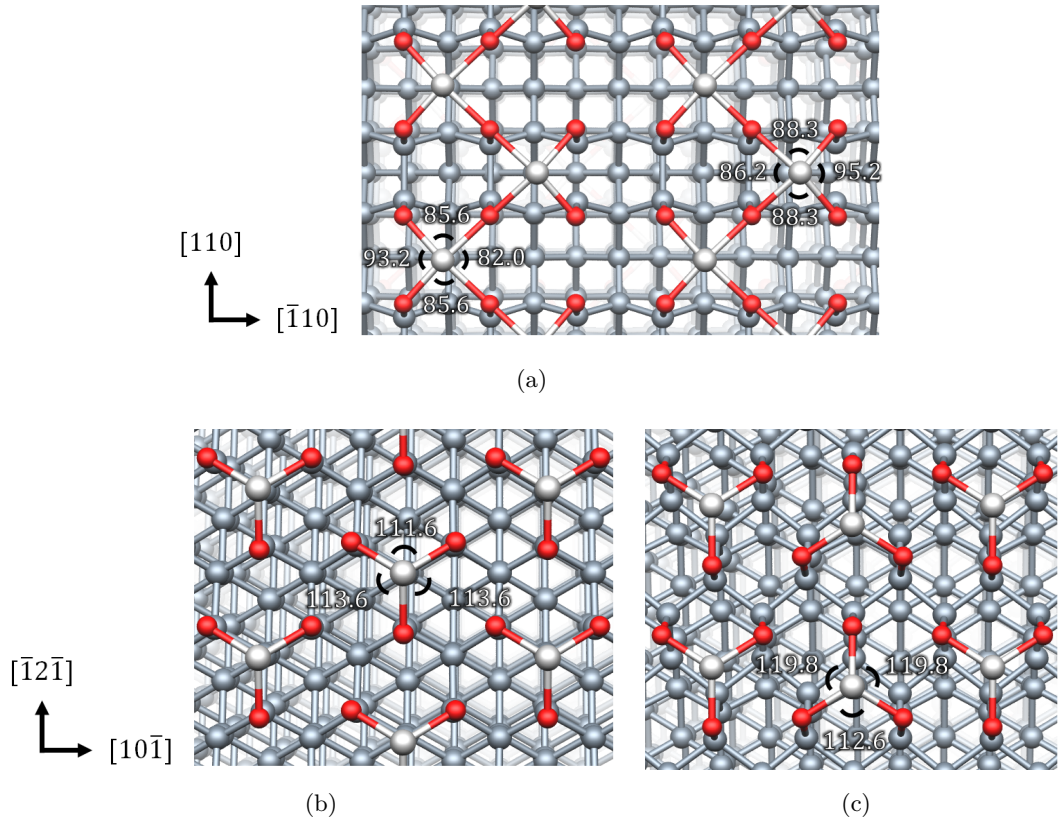

Figure 46: Plan view of structures shown in Figure 45. AlO_3 (a) (001)-(2×1), (b) (111)-(1×1), and (c) (111)-(2×1) terminated diamond surfaces with Al-O bond angles as viewed from above. Lengths in Å. Colours are as in Figure 45.

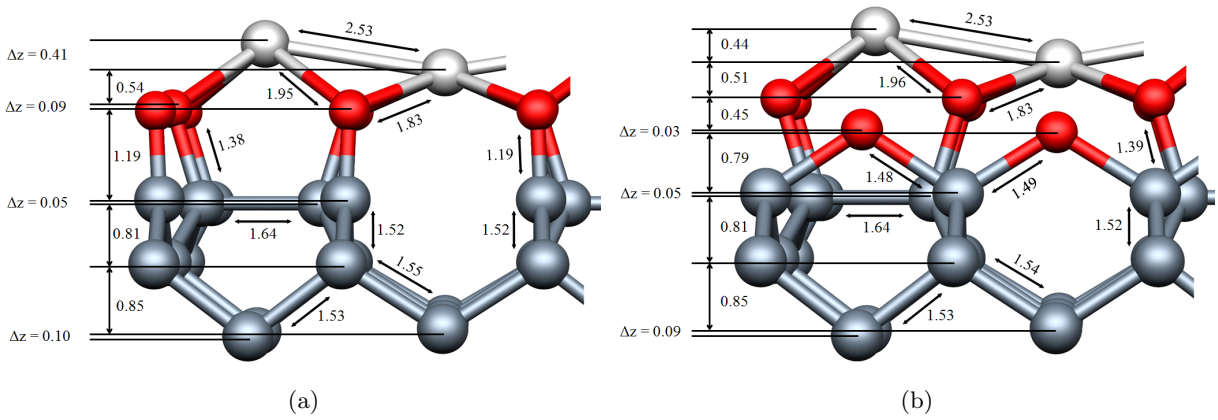

Figure 47: Example AlO_3 terminated (001)-(2×1) surfaces exhibiting (a) ketone and (b) ether configurations. Colours and directions are as in Figure 45.

Additionally (001) surfaces are examined with structures where surface oxygen are not all coordinated with Al, whilst retaining the same Al:O ratio. Two structures illustrated in Figure 47 represent ether and ketone bonding, the ketone structuring being only barely metastable, rearranging into the ether form following a small displacement of the ketone O-atom. The unterminated single and double C–O bond lengths are 1.48 Å and 1.19 Å, respectively, in good agreement

with previous theory for O-terminated diamond [205]. The electronic structure is represented in Figure 48, highlighting the intriguing dispersion of surface states within the bandgap.

The highest occupied surface states are a doubly degenerate pair, spanning 0.3–1.3 eV above the VBM. There is little to no dispersion of these states in the $S-Y$ and $\Gamma-X$ ([110]) branches yet $\Gamma-Y$ and $\Gamma-S$ ([1$\bar{1}$0]) are approximately 1.0 eV apart. The nature of these states are conveyed through AIMVIEW illustrations of the orbital angular momentum (Figures 49 and 50).

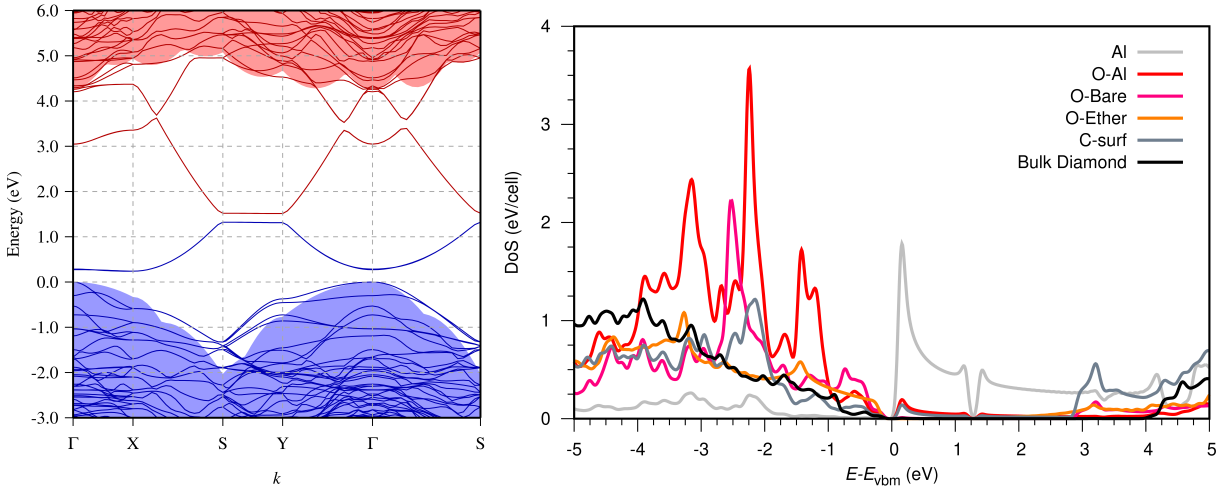

(a) (b)

Figure 48: Electronic band structure of AlO_3 terminated (001)-(2×1) surfaces ether configuration (a) (Figure 47(b)) and the pDoS spectra for the Al, O co-ordianted with Al (O–Al), bare O with no Al (O–Bare), diamond (001)–(1×1) ether (O–Ether), carbon surface atoms and carbon bulk layer atoms (b).

The highest occupied state of Figure 48(a) is very close to the VBM at Γ, and both Figures 48(b) and 49(a) show that this state is dominated by a continuous aluminium state along the chain of bonded Al-Al atoms with some minor contributions from the adjacent O atoms in the surface normal direction. At S, the orbitals centred on the Al atoms are much more confined, situated on those with a larger O–Al Z_{disp}.

Additionally, the surface is not metallic. The highest occupied and lowest unoccupied surface states at their smallest are only 0.1 eV apart (Figure 48(a)). This too can be seen in the pDoS of Figure 48(b) with a sudden drop to 0 eV/cell at 1.3 eV. A set of unoccupied surface states straddle the Fermi energy S, extending deep in to the bandgap. The highest occupied and lowest unoccupied are unsurprisingly similar, however Figure 50(b) orbitals are centred on the Al atoms closest to the surface again with minor contributions from co-ordinated O. Despite this, the state at Γ is entirely associated with the C–O–C bridge.. The dispersion of this state is similar to those previously observed for a fully ether terminated diamond surface [205].

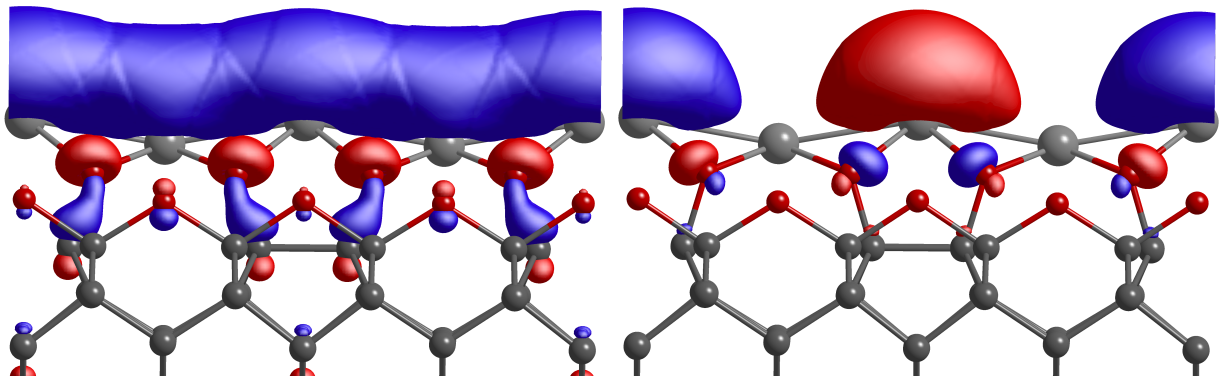

(a) (b)

Figure 49: Isosurface plots showing the highest energy occupied surface state of Figure 48(a) at Γ (a) and S (b). Silver, red and dark-grey spheres represent aluminium, oxygen and carbon atoms respectively.

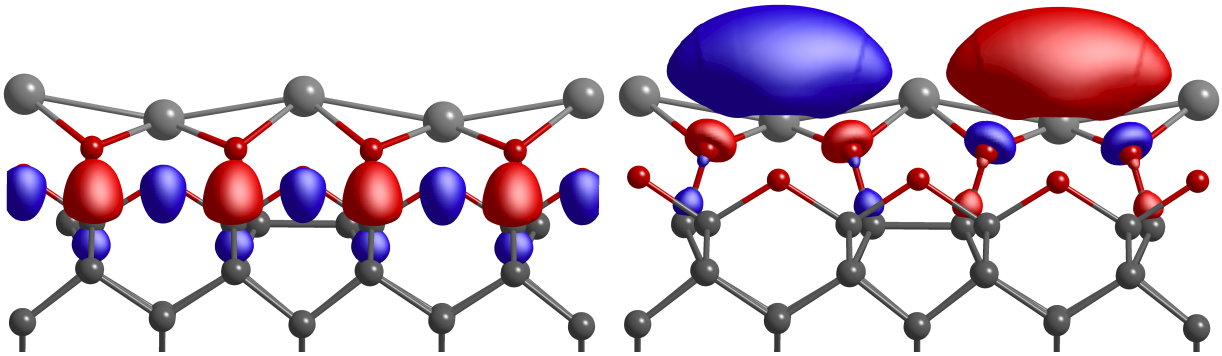

(a) (b)

Figure 50: Isosurface plots showing the lowest energy unoccupied surface state of Figure 48(a) at Γ (a) and S (b). Silver, red and dark-grey spheres represent aluminium, oxygen and carbon atoms respectively.

The structures in Figure 47 have PEAs of 1.0 eV and 1.20 eV for the ether and ketone surfaces respectively. The PEAs in these cases may reflect the dominance of the PEA of O-terminated diamond [205] and the reduction of the ionicity of the Al-O groups arising from direct Al–Al interactions: Figure 45 illustrates Al–Al inter-nuclear distances of 2.53 Å, 12% shorter than those in Al metal (2.86 Å [247]). It is important to note that no examples of AlO_3 termination where oxygen is not co-ordinated with Al are found, and it is a uniform ionic arrangement that would be predicted to form in nature. In the case of the two structures in Figure 47, ether is more energetically favorable than ketone-containing AlO_3 surfaces by 29 meV per surface site, but less favorable than the structure in Figure 45(a) by 80 meV per surface site.

Next, the (111)-(1×1) surface. In the absence of reconstruction, the termination of the surface sites by oxygen yields C–O bonds pointing directly away from the surface. Examined are a

mixture of arrangements of Al on this surface, with the lowest energy found being illustrated in Figures 45(b) and 46(b). The Al atoms exist at alternating sites, equidistant from three O-sites, forming AlO_3 islands covering the surface, with the Al ions lying 0.44Å further from the diamond than the layer of O-ions. Figure 46(b) shows how the Al atoms are co-ordinated with O from above and the angles associated. The smaller 111.6° is a consequence of the bottom O atom displacement being solely in the $[1\bar{2}1]$ whereas the two other O atoms of the triangle are displaced in a combination of the $[\bar{1}2\bar{1}]$ and $[\bar{1}01]$ directions. All C–O bonds point 3.9° off the surface normal away from the Al atom along the bond direction. Turning to the (111)-(2×1) reconstructed surface, Figure 44(b), high-symmetry surface sites are labelled analogously to the (001)-surface, with the addition of the top (T) site lying directly over a surface site. The lowest energy structure is illustrated in Figures 45(c) and 46(c), which locates the Al atoms at C-sites, forming islands similar to the (111)-(1×1) surface, but with the surface normal displacement of Al ions with respect to some oxygens much smaller at just 0.27 Å. Figure 46(c) shows the Al–O angles. Al–O bondlengths in the $[\bar{1}2\bar{1}]$ direction are 0.02Å smaller than the other two pairs of Al–O. The C–O associated with this Al–O pair is solely in the $[\bar{1}2\bar{1}]$ direction, pointing 15.5° degrees towards the Al atom along the bond direction with respect to the [111] surface normal. The other two Al–O pairs point in the $[\bar{1}\bar{1}2]$ and $[2\bar{1}\bar{1}]$ directions. The C–O bonds associated with these pairs point predominantly in the $[\bar{1}2\bar{1}]$ direction with a larger 24.9° bend away from the surface normal as can be seen in Figure 45(c), and a small 3.4° angle away from the Al in the $[10\bar{1}]$ direction. Although the reconstruction yields a lower energy in the case of the unterminated diamond, the AlO_3 termination, although metastable, is significantly less energetically favourable than the (1×1) case.

Table 10: Calculated EAs (eV), formation energies (eV per diamond surface site), and O–Al displacement in the surface-normal direction (Å) for AlO_3 termination.

	(001)-(2×1)	(111)-(1×1)	(111)-(2×1)
EA	−2.1	−3.4	−2.3
E_{ads}	−0.90	−0.97	−0.17
O–Al Z_{disp}	0.2–0.3	0.4	0.1–0.3

Table 10 lists the calculated adsorption energies and EAs for the three types of surface terminated with AlO_3. There is a relatively large NEA of 2.1 eV and adsorption energy of 0.90 eV per surface site for the (001)-(2×1) surface.

The NEAs of the lowest energy structures for the (111)-(1×1) and (111)-(2×1) are more negative than the (001)-(2×1) surface, and in particular that of the (1×1) surface is ∼66% larger than

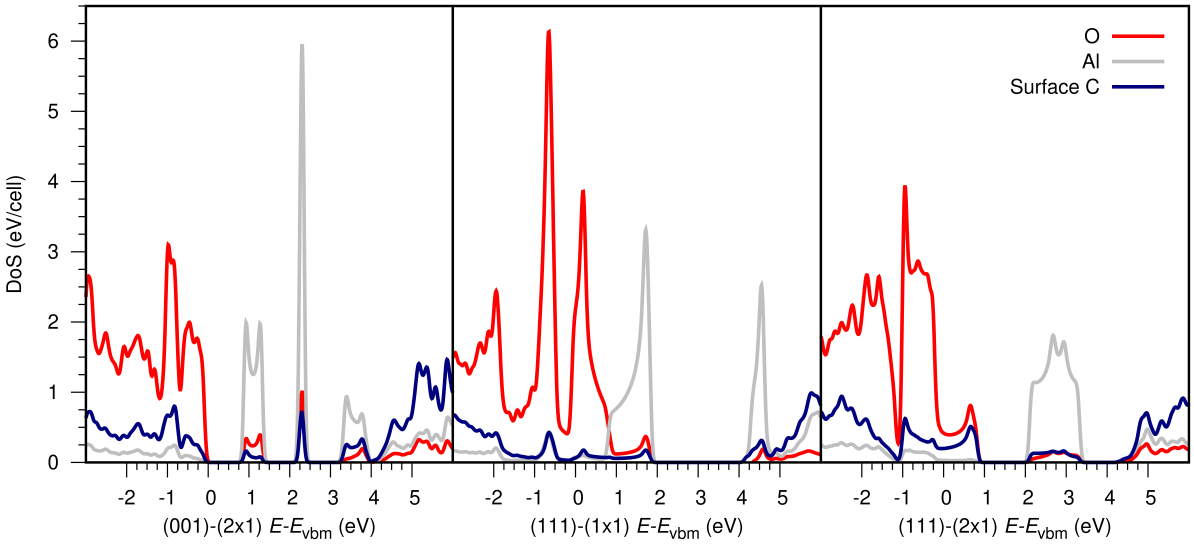

Figure 51: pDoS spectra for Al, O and surface C layers on the (001)-(2×1) (a), (111)-(1×1) (b) and (111)-(2×1) (c) surfaces with AlO_3 stoichiometry.

the (001) surface. The larger NEA for the (111) surface is consistent with both the larger normal displacement of the Al ions from the O ions and with the lower co-ordination. The hexagonality of the (111) surfaces naturally lends itself to a 3-fold co-ordination of the Al with O as can be seen in Figures 46(b) and (c). Figure 51 helps further explain the origin of such large NEAs. Taking the (111)-(1×1) surface as an example, distinct and strong peaks between oxygen and aluminium are seen at −0.75 and 1.75 eV, and 0.25 and 1.75 eV respectively. Visualisation of these states and their locality can be seen in Figure 52. Large inward pointing Al–O dipoles originating from charge localisation and high DoS peaks are clearly observed.

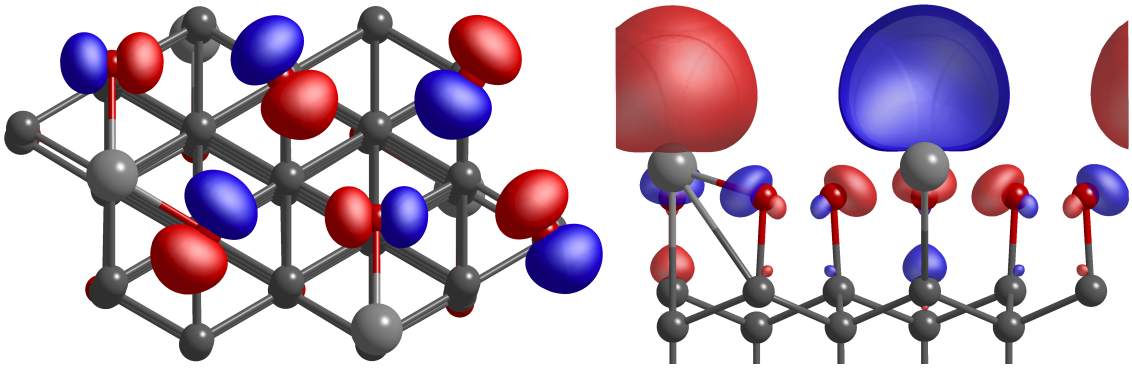

(a) (b)

Figure 52: Isosurface plots showing the oxygen peak (a) at −0.75 eV and the aluminium peak (b) at 1.75 eV for the AlO_3 stoichiometry on (111)-(1×1) of Figure 51 at Γ. Silver, red and dark-grey spheres represent aluminium, oxygen and carbon atoms respectively.

For the most energetically favorable AlO_3 terminated surface, the band structure is presented in Figure 53(a). The underlying diamond valance and conduction bands are highlighted, iden-

tifying degenerate, unoccupied surface states around 0.8–1.5 eV above the valence band. The overlapping is indicative of the surface being metallic. This too is seen in Figure 51(b) at 0.8 eV. These have been examined for their localisation and are clearly vacuum states, resembling those presented previously [205] for H-terminated diamond, and is a consequence of the large, negative electron affinity. This state is indicative of incompletely ionized Al. The relatively simple band structure reflects the overall fully bonded nature of the AlO_3 termination, and helps explain the relative stability of this termination.

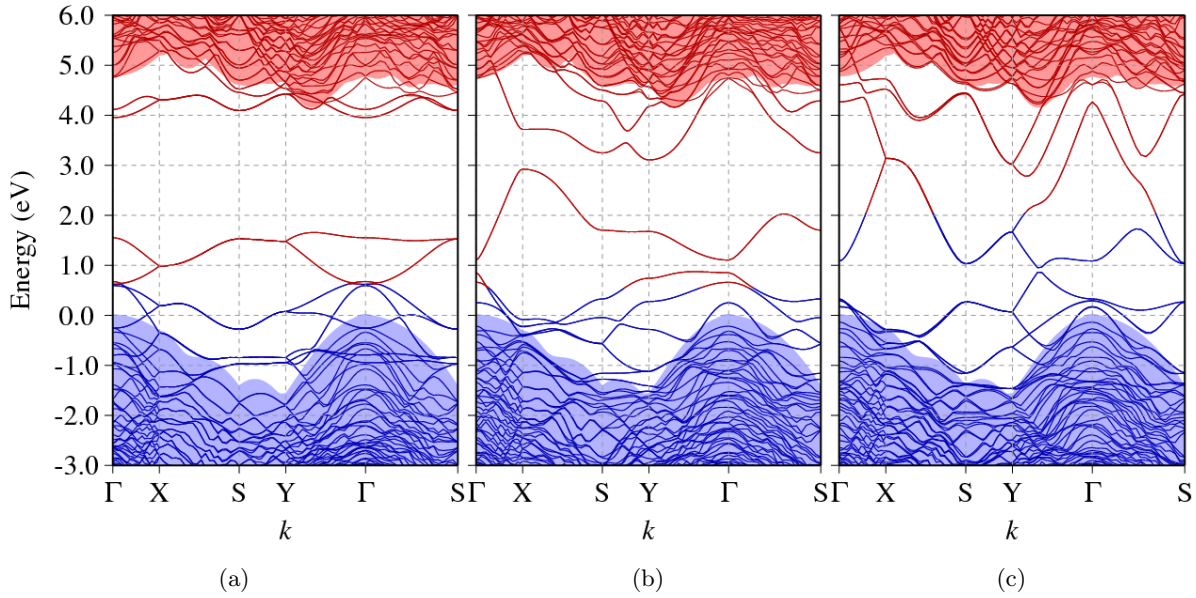

Figure 53: Electronic band structures of the (111)-(1×1) surface for (a) AlO_3, (b) AlO_2, and (c) Al_2O_3 stoichiometries, along high symmetry branches of the two dimensional, orthorhombic surface Brillouin zone. The labels for the k-axis follows the conventional definitions [248]. The energy scale is defined so that zero is the valence band maximum of bulk diamond. The bulk and slab electrostatic potentials are aligned [202] to place the slab valence band maximum at zero. Only bands in the vicinity of the band-gap are shown. Occupied and empty bands are shown in blue and red, respectively.

4.2.2 AlO_2

Moving forward with an increase in Al, diamond surfaces with an O:Al ratio of 2 are discussed.

As the Al:O ratio increases, there are proportionately fewer anions to offset the Al cations. The resulting structures include Al–Al neighbours, and it can be seen that the formations become less energetically favorable (Table 11). Upon examination of the band structure (Figure 53), one can observe AlO_2 termination is metallic and a marked increase in the surface normal distance

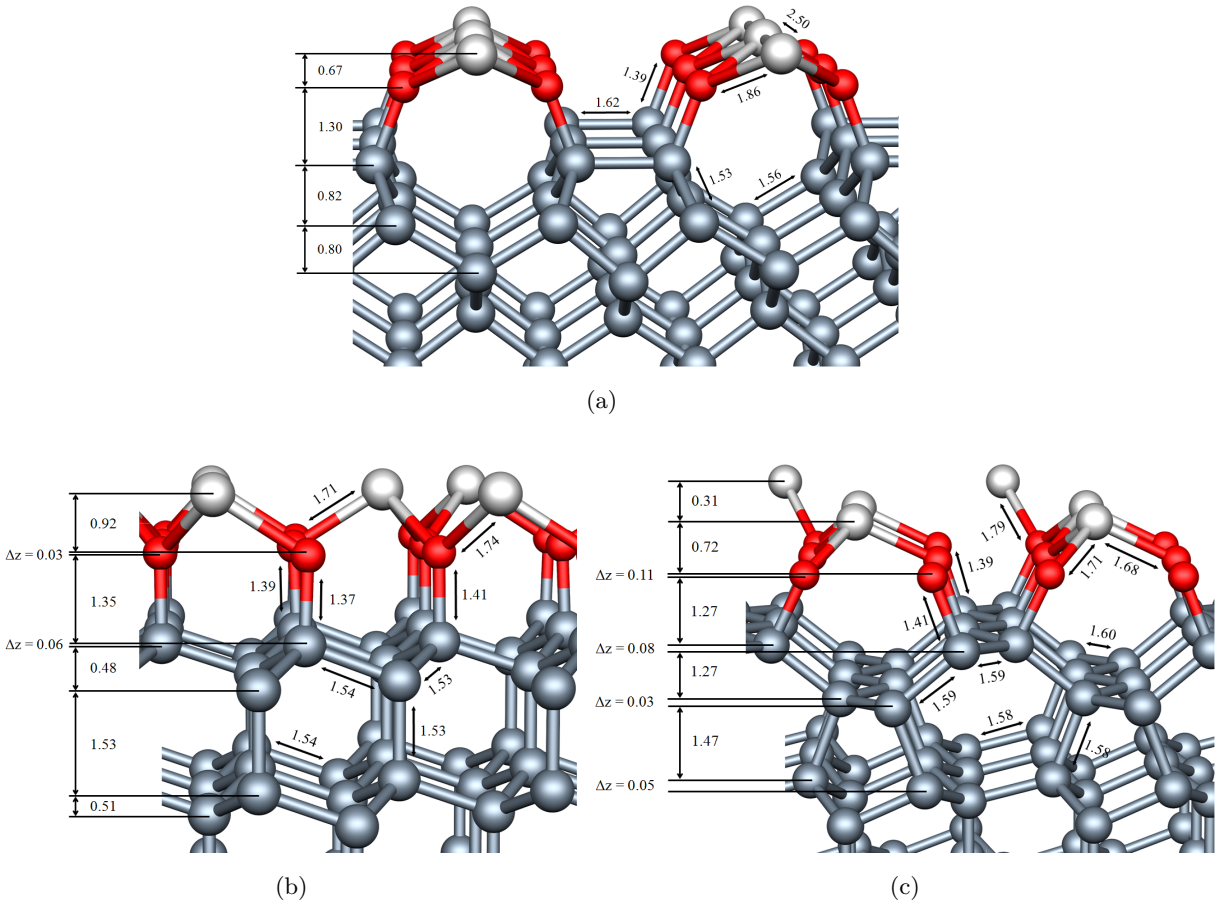

Figure 54: AlO_2-terminated diamond surfaces. (a) (001)-(2×1), (b) (111)-(1×1) and (c) (111)-(2×1). Colours and directions are as in Figure 45, and distances are in Å.

Table 11: Calculated EAs (eV), formation energies (eV per diamond surface site), and O–Al displacement in the surface-normal direction (Å) for AlO_2 termination.

	(001)-(2×1)	(111)-(1×1)	(111)-(2×1)
EA	+1.0	−0.1	−0.3
E_{ads}	−0.05	−0.05	+1.21
O–Al Z_{surf}	0.7	0.9	0.7–1.0

(Figure 54); normal displacements are 0.2–0.4 Å for AlO_3, and range between 0.7 and 1.0 Å for AlO_2. Al–Al distances (Figures 54(a) and 55(a)) are similar to those of AlO_3 surfaces containing unterminated O-sites (Figure 47) at around 2.50 Å.

pDoS spectra of these surfaces (Figure 56) show the degree with which Al states are now delocalised, compared to the distinct and sharp peaks of Figure 51.

In addition to the reduction in adsorption energy, there is a decrease in the charge polarisation, making the EA less negative (Table 11), and in the (001) surface, changing it to a PEA. Figure 57

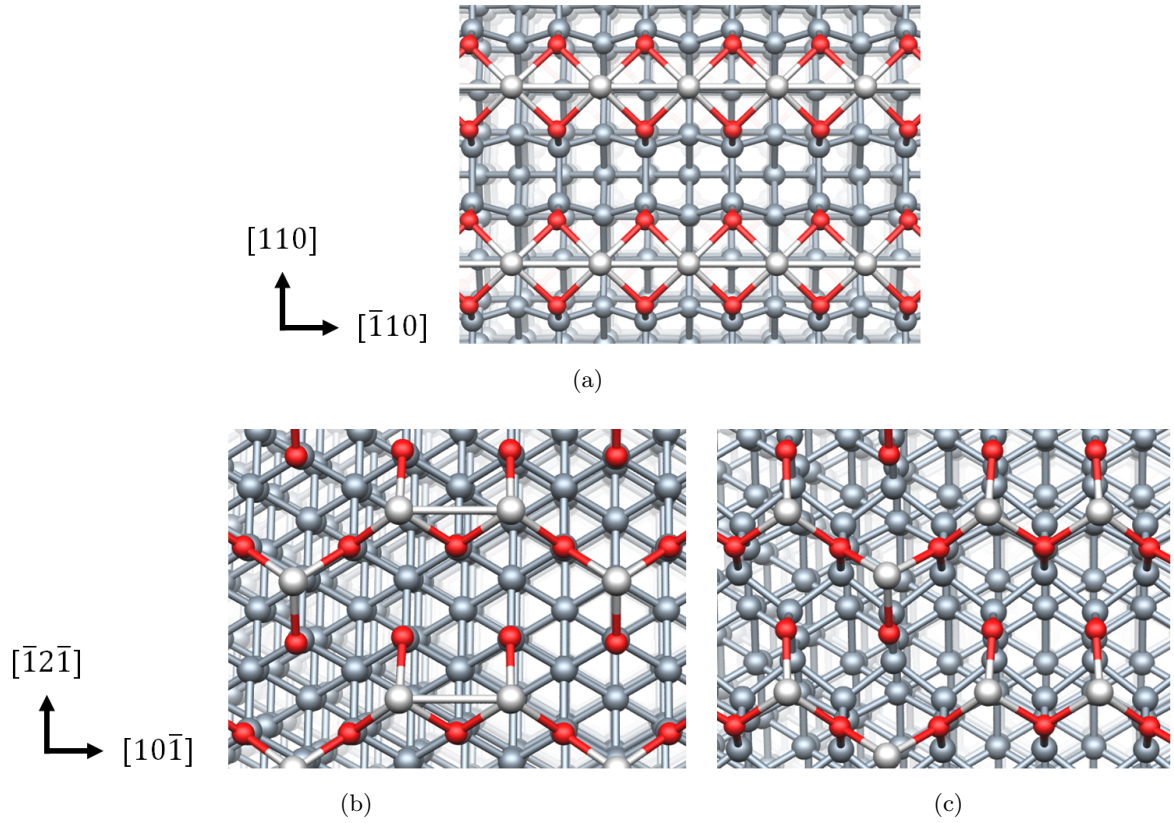

Figure 55: Plan view of structures shown in Figure 54. AlO_2 (a) (001)-(2×1), (b) (111)-(1×1), and (c) (111)-(2×1) terminated diamond surfaces with Al-O bond angles as viewed from above. Lengths in Å. Colours are as in Figure 45.

highlights the (001)-(2×1) prominent states. Focusing in on the relative size and spread of the (001)-(2×1) oxygen and aluminium peaks compared to AlO_3, Figure 56 shows the oxygen peaks have an increased diamond surface contribution, and the orbitals pertaining to the aluminium are more delocalised, agreeing well with the extended peak of Figure 56 in the 0.5–5.0 eV energy range for the same surface.

Figure 53(b) illustrates the effect of an increasing Al areal-density upon the band structure, with a clearly metallic behaviour. At the zone centre, partially occupied bands (0.8–1.1 eV) surrounding the Fermi energy are combinations of vacuum and surface states, where the surface states are characterised by both contributions from the valence band and strong C–O interactions. If such surface terminations were to be formed, they would be expected to contribute to a surface conductive channel.

4.2.3 Al_2O_3

Finally, structures with a termination of the bulk Al_2O_3 stoichiometry. Al_2O_3 terminated surfaces are relatively energetically unstable and generally exhibit PEAs (Table 12). Figures 58 and 59 show examples of the complex bonding networks typical for this Al:O ratio. Although

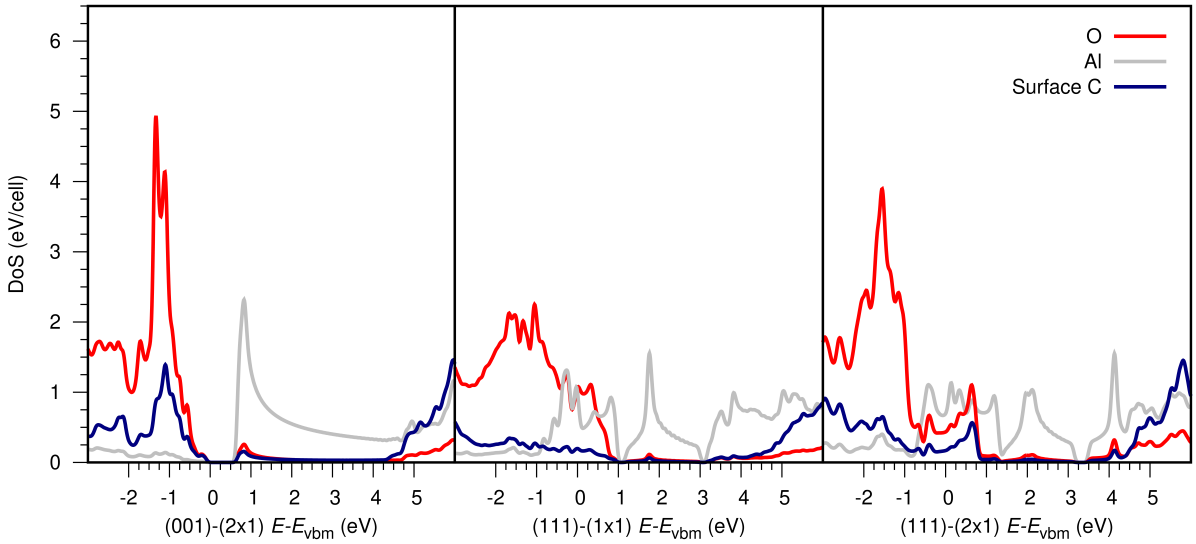

Figure 56: pDoS spectra for Al, O and surface C layers on the (001)-(2×1) (a), (111)-(1×1) (b) and (111)-(2×1) (c) surfaces with AlO_2 stoichiometry.

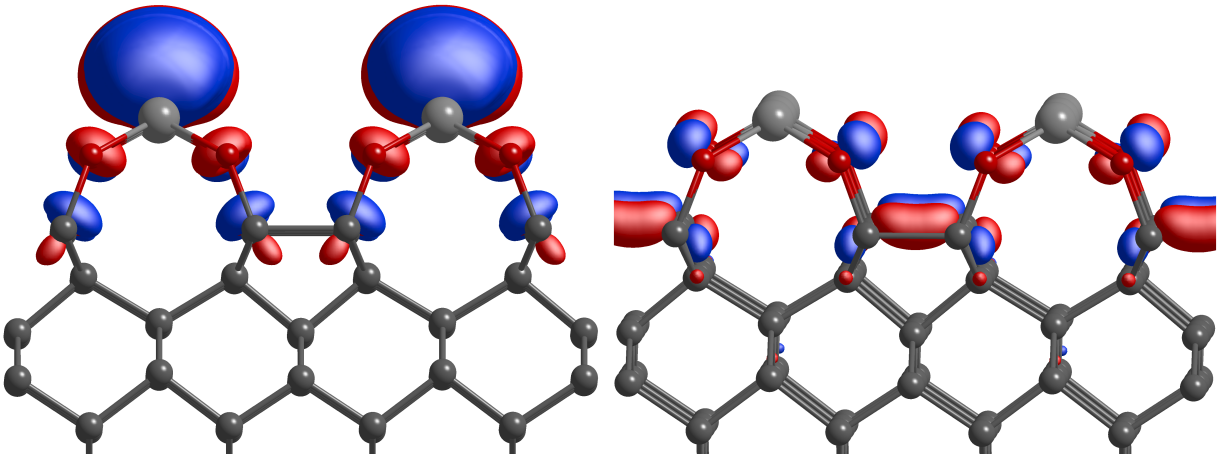

(a) (b)

Figure 57: Isosurface plots showing the states represented by a peak in Figure 56 on (001)-(2×1) at −1.1 eV(a) and 0.8 eV(b) at Γ. Silver, red and dark-grey spheres represent aluminium, oxygen and carbon atoms respectively.

most structures contain Al–Al bonds, Figure 58(c) shows a (111) oriented structure with only Al–O and C–O bonding.

Nevertheless, these structures yield the largest calculated PEA (1.70 eV), indicating that the relative partial charges are unfavourable for a NEA. Figure 58 also illustrates Al–O and C–O bond lengths of $1.78 - 1.89$ Å and $1.38 - 1.41$ Å, respectively. The relatively wide range of distances is correlated with the low-symmetry structures with non-equivalent O and Al species. Some Al–O bond-lengths are larger than in bulk Al_2O_3, suggesting a weaker interaction, consistent with the imbalance in anions and cations.

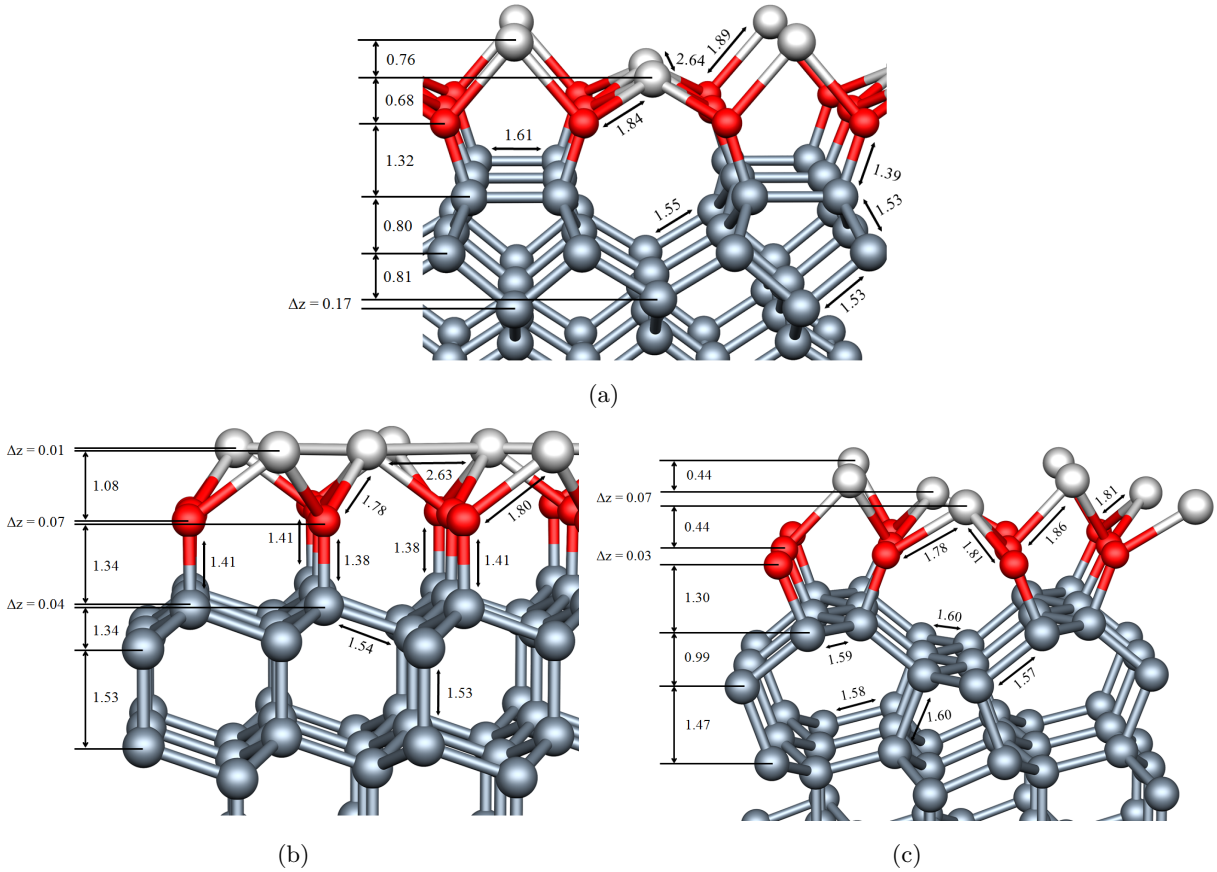

Figure 58: Al_2O_3 terminated diamond surfaces (a) (001)-(2×1), (b) (111)-(1×1) and (c) (111)-(2×1). bond lengths given in Å.

Table 12: Calculated EAs (eV), formation energies (eV per diamond surface site), and O–Al displacement in the surface-normal direction (Å) for Al_2O_3 termination.

	(001)-(2×1)	(111)-(1×1)	(111)-(2×1)
EA	+1.0	+1.7	+1.2
E_{ads}	+1.45	+1.63	+2.76
O–Al Z_{surf}	0.7–1.4	1.1	0.4–1.0

This general trend of charge imbalance from AlO_3 to Al_2O_3 is best observed in the pDoS breakdowns for each surface. For AlO_2 and Al_2O_3 these states begin to smear out as the surface becomes metallic/more metallic. Figure 61(b) reveals continuous surface aluminium states, indicative of their metallicity. Overlapping C-O-Al states produce less distinct inward pointing dipoles, and in some cases outward PEA creating dipoles. Figure 60 shows O layer states are much less pronounced, and Al surface states exist over a much broader energy range. Less marked peaks suggest charge that is more disperse, further blurring the lines between cation and anion.

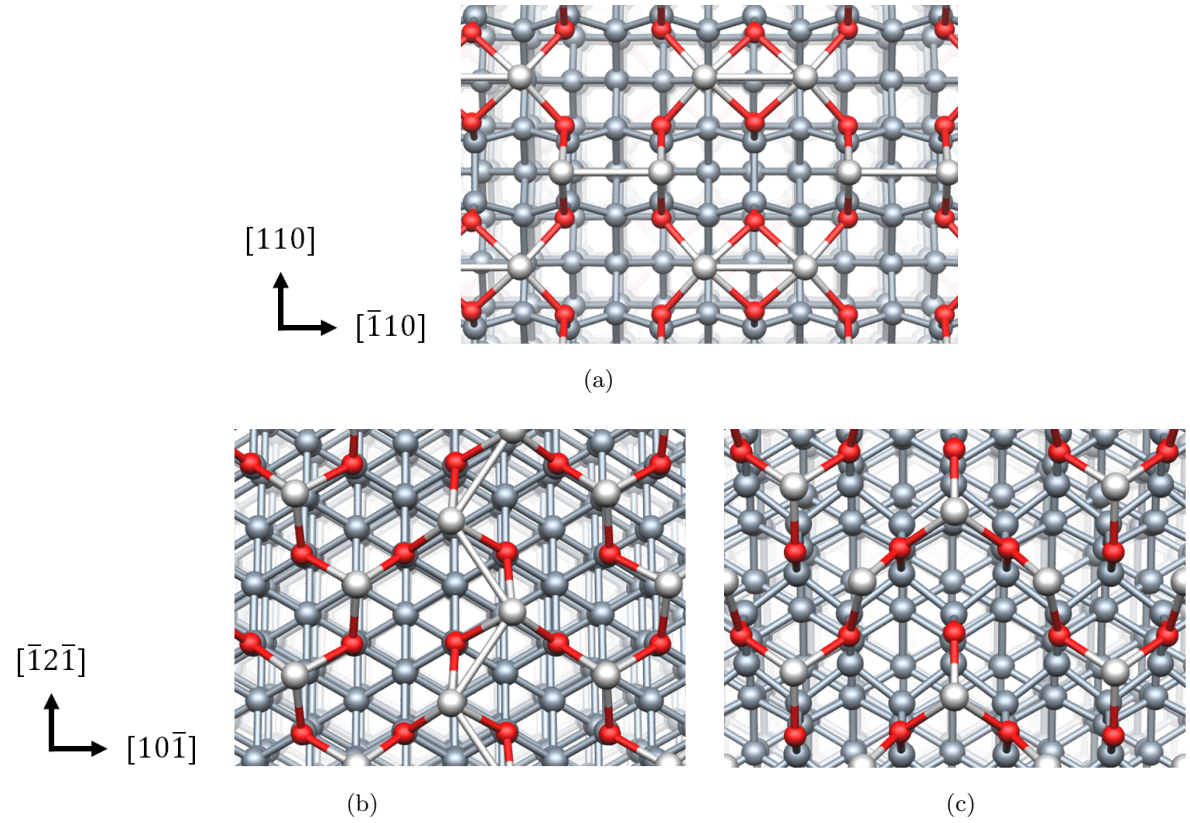

Figure 59: Plan view of structures shown in Figure 58. Al_2O_3 (a) (001)-(2×1), (b) (111)-(1×1), and (c) (111)-(2×1) terminated diamond surfaces with Al-O bond angles as viewed from above. Lengths in Å. Colours are as in Figure 58.

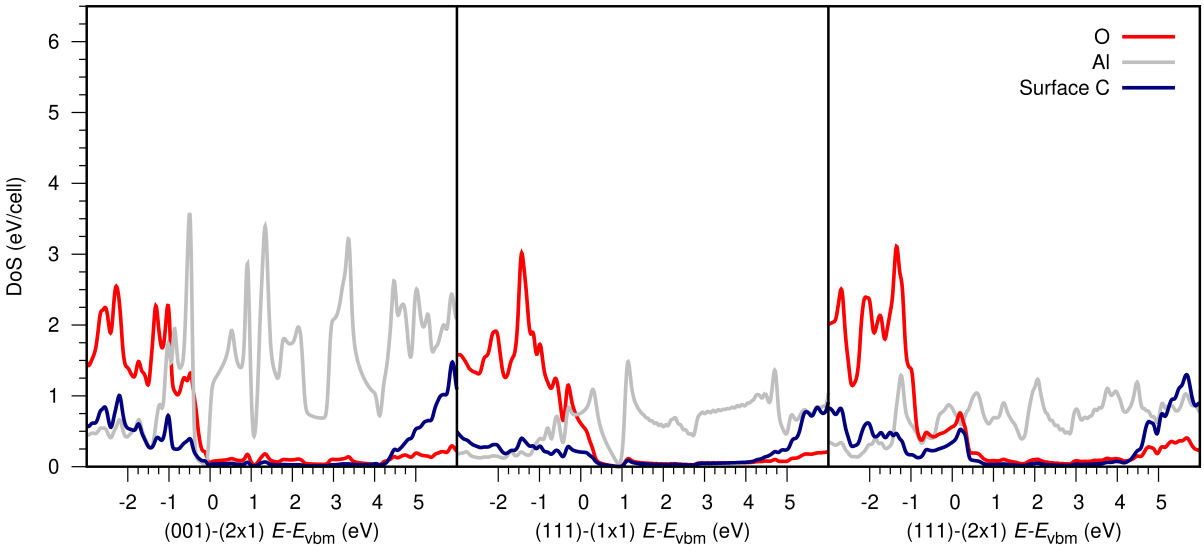

Figure 60: pDoS spectra for Al, O and surface C layers on the (001)-(2×1) (a), (111)-(1×1) (b) and (111)-(2×1) (c) surfaces with Al_2O_3 stoichiometry.

4.2.4 Conclusions

Density-functional simulations of the effects of surface arrangement and stoichiometry of aluminium oxide on the (111) and (001) diamond surfaces have determined the stability and elec-

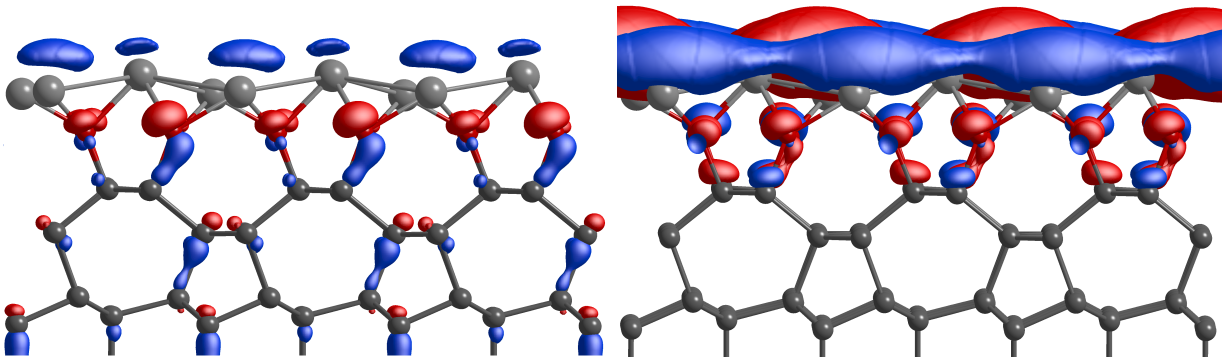

(a) (b)

Figure 61: Isosurface plots showing the states represented by a peak in Figure 60 on (111)-(2×1) at −1.25 eV(a) and 0.25 eV(b) at Γ. Silver, red and dark-grey spheres represent aluminium, oxygen and carbon atoms respectively.

Table 13: Total work function reduction (−) or increase (+) for each surface as a function of Al/O ratio.

	(001)-(2×1)	(111)-(1×1)	(111)-(2×1)
AlO_3	−2.84	−4.94	−2.6
AlO_2	+0.26	−1.64	−0.59
Al_2O_3	+0.26	+0.16	+0.91

tron affinity for a range of Al:O ratios. Generally, diamond–O–Al arrangements are more stable, wherein the oxygen may be considered to be in the −1 oxidation state. This in turn yields a stoichiometric monolayer with an AlO_3 composition. With this ratio of terminating species, large NEAs are predicted, estimated at −3 eV. Consequently, very low work functions result as shown by Table 13, suggesting the potential for use in thermionic emission applications [249]. The thermal stability, as judged by the exothermic reaction between the unterminated diamond and bulk Al_2O_3, suggests that such monolayer terminations would be more viable for electron emission and related applications up to higher temperatures than for other terminations such as copper, cesium, vanadium, nickel, zinc and their respective oxides and in good competition with titanium and lithium [236, 237, 46, 238]. Although one can draw attention to the rule of thumb and generalities dominating the role of terminations on the surface, it is difficult to make a comprehensive general conclusion regarding the impact upon, say, the magnitude of the electron affinity of surface species due to the wide range of factors including the equilibrium stoichiometries, surface orientations, termination thickness and underlying geometry.

Higher Al:O ratios of 50% and 67% result in a marked decrease in energetic stability and severely

reduced NEAs or even PEAs. However, since the most stable termination is that with the most favourable NEA, it seems plausible that even if a mixed termination is realized experimentally, careful control over the deposition conditions is expected to result in viable surface treatments. For example, the most stable Al_2O_3 monolayer termination results in a very Al-rich surface, and it would be these Al atoms that will be most susceptible to desorption.

4.3 Crystallogens

Recently [250, 251] silicon and germanium termination has been examined, focusing on the EA for optimisation of the NV^- state. The proposal is that producing an ordered surface not favouring the formation of oxygen functional groups might better control the surface electronic properties, stabilising the NV centre charge state. Indeed, 950°C annealed monolayer coverage followed by *in situ* low-energy electron diffraction (LEED) measurements directly observed a (3×1) periodicity for both Si and Ge terminations, with x-ray photoelectron spectroscopy (XPS) data supporting a detailed surface structure where Ge or Si adatoms sit on the C site as labelled in Figure 62. In the model inferred from the experimental observations, each crystallogen is bound to two surface carbon atoms and two adjacent adatoms. The electronic structure has also been obtained from the experiments, with the data suggesting empty states in the band-gap and an occupied surface state lying around 1.7 eV below the diamond valence band top [251]. A definitive origin of this resonant state is not provided, with indicative findings discussed below.

Silicon and germanium are group-IV elements with chemistry similar to that of carbon. Their electronegativities of 1.90 and 2.00, respectively, are less than that of carbon, so surface termination by these species may be expected to produce an NEA, as is the case with hydrogen. Given the similar electronegativities and inter-atomic distances (Si 2.34 Å and Ge 2.48 Å [252, 253]), one might anticipate similar structures when terminating diamond. Optimal surface packing and adatom arrangement with respect to chemical species is expected to influence the detailed geometry and EA. In this section are the results of density functional simulations of a range of surface number-densities of Si or Ge on the (001)-diamond surface in order to shed light on the equilibrium density of adatoms and the subsequent observable properties.

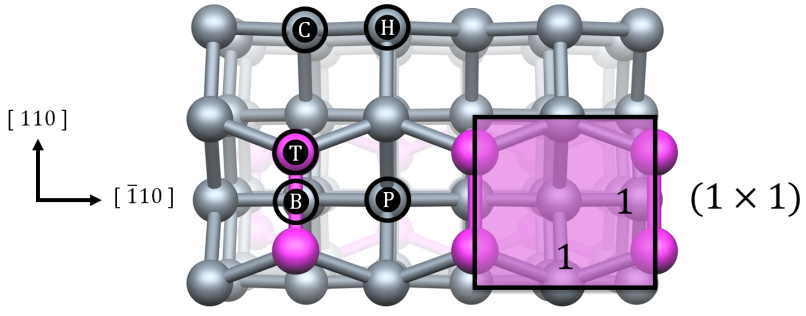

Figure 62: Top down view of unterminated (001)-(2×1) surface with in-plane lattice vectors and repeats to show periodicity. High symmetry surface sites labelled in line with convention [254, 255]. The area shown includes three reconstructions, and therefore a total of six surface sites. The shaded area shows the underlying $[\bar{1}10]a_0/2\times[110]a_0/2$ footprint of the diamond surface.

A range of sub-monolayer coverages of silicon or germanium are explored on the (001)-(2×1) diamond surface with varying surface areas and periodicities. Indeed, periodicity and geometry play a crucial role in the energy of a given coverage fraction, and are a focus of the presented data. One monolayer is defined as one adatom for every surface carbon site.

Group-IV elements might be expected to exist in a four-fold co-ordinated arrangement, but the differences in electronegativity would be anticipated to result in polar-covalent bonds between the adsorbates and the underlying diamond surface. Furthermore, given the much greater covalent radii of Si and Ge in comparison to that of carbon, one must take care in interpretation of the Si–Si and Ge–Ge interaction, and the net bonding of the adsorbates. This, coupled with the PEA of the unterminated diamond surface, would be expected to result in relatively small EAs, with the sign depending upon the coverage and the relative size of the surface dipoles with and without adsorbates.

4.3.1 Silicon

For 25% and 50% coverages, silicon atoms form C-Si-C bridge structures with bond-lengths in the range of 1.87–1.92 Å, and adjacent Si-Si neighbours are 2.5 Å apart. These values broadly agree with inter-nuclear distances in SiC (1.89 Å) and bulk silicon (2.34 Å), respectively [252, 253, 71]. Where more silicon is added, the underlying surface reconstruction tends to be lost, consistent with formation of C-Si-C structures being chemically and energetically favourable, consistent with the exothermic nature of the reactions listed in Table 14.

Table 14: Calculated EAs (eV), formation energies (eV per surface site), and C–Si displacement in the surface-normal direction in (Å) for Si termination. Coverages represent the ratio of the number of adsorbates to the number of carbon surface sites. Period states the in-plane surface footprint as a multiple of the shaded unit area in Figure 62.

Coverage (%)	EA	E_{ads}	$Z_{\text{C–Si}}$	Period
25	−0.43	−0.30	1.48	2×4
50	−0.69	−0.60	1.28	2×2
67	−0.80	−0.98	1.16	3×2
75	−0.81	−0.95	1.15–1.23	4×2
100	−0.96	−0.79	1.88	2×1

Of particular note is the 67% coverage structure (Figure 63), which is the same as the model proposed based upon experimental observations [251]. Silicon atoms sit atop the C site, co-

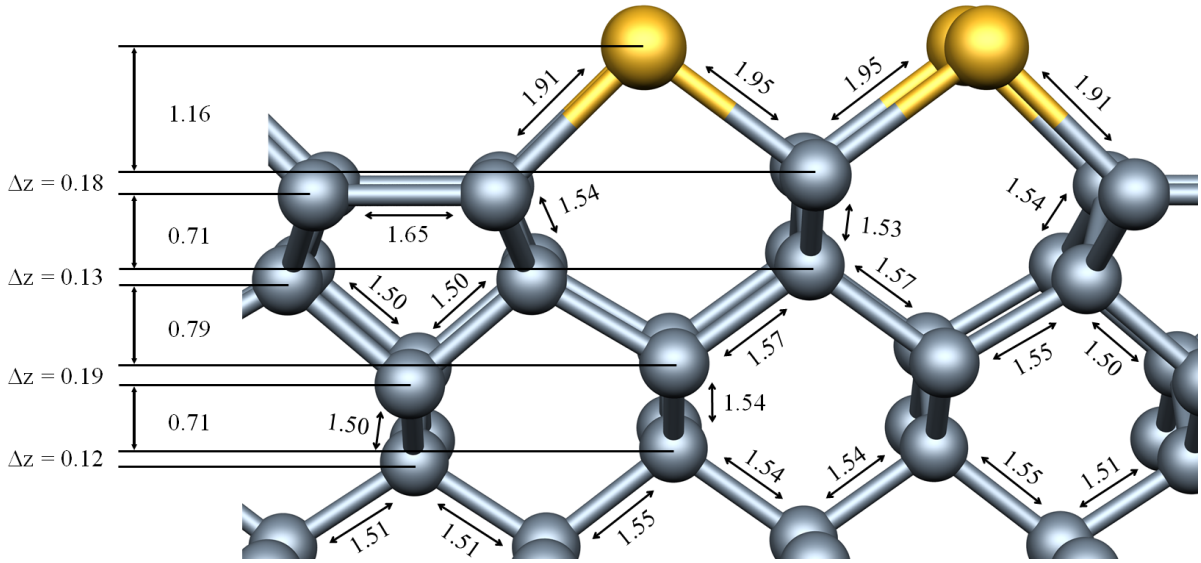

Figure 63: 67% silicon terminated (001)-(2×1) surface. Lengths are in Å. Yellow and dark-gray spheres represent silicon and carbon atoms respectively.

ordinating with two carbon atoms and two adjacent silicon adatoms. There is a relatively large energy gain of −0.98 eV per surface site, and a corresponding NEA of −0.80 eV, which is close to the reported figure of −0.89 eV.

Shedding further light on the properties of this surface arrangement, the pDoS is calculated and shown in Figure 64. The plot shows the pDoS for a layer within the slab but well away from the surface that exhibits the familiar overall DoS of bulk diamond and the energy gap. Figure 65 shows a focus upon the band-gap energy range, illustrating the decay with distance from the surface; the gap-states effectively disappear within four atomic layers.

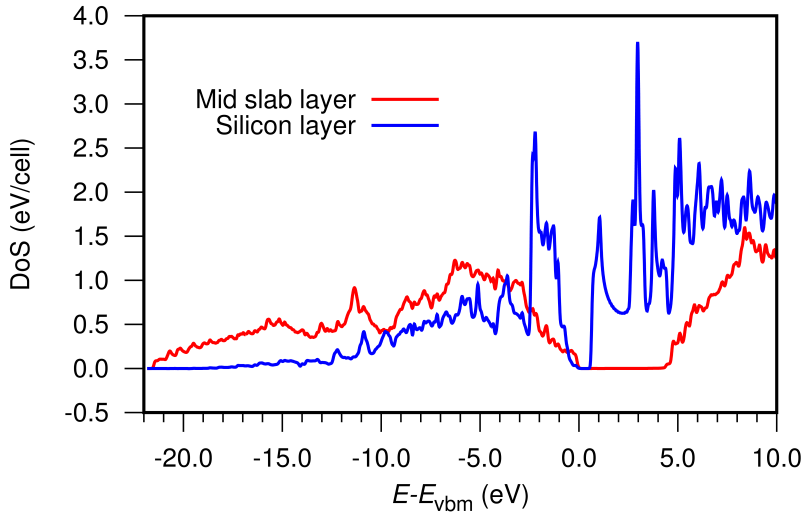

Figure 64: pDoS spectra for the silicon surface layer (blue) and the bulk like middle diamond layer (red). The energy scale is chosen such that the underlying bulk diamond valence band maximum is at 0 eV.

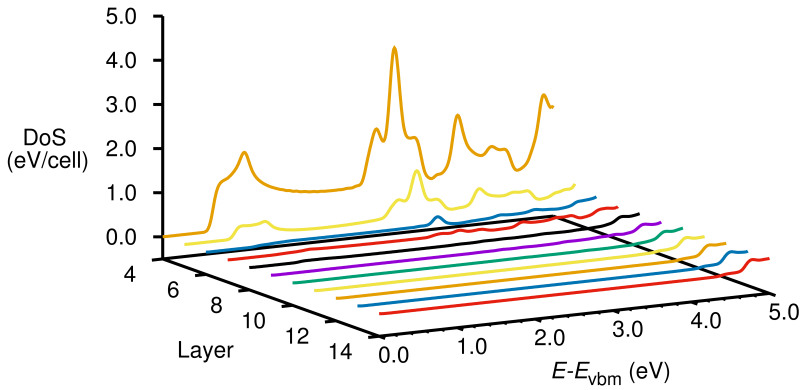

Figure 65: pDoS spectra as a function of distance from the surface in the region of the band-gap (0–5 eV). The energy scale is set as in Figure 64.

To provide additional insight into the origin and nature of the surface states lying in the band-gap, it is necessary to examine the associated wave functions. The electronic structure of the 67% surface is provided alongside two unoccupied states (Figure 66 (a)) that show considerable dispersion, spanning 1.45 eV between k-point branches. Figure 66 (b) shows the state at Γ is strongly centred on silicon atoms with additional contributions from the surface carbon layer. Breakdown of the orbital angular momentum shows this silicon state is *spd*-like and the *p*-orbitals centred on the carbon are oriented towards the surface normal. Ref. [251] identifies several unoccupied surface states in the bandgap with similar energy levels as shown in Figure 66 (a). Figure 66 (c) shows the same state 1.45 eV higher in energy at X, whose orbitals are seemingly more diffuse than at Γ, with a small degree of π bonding along the C–C dimer. The gap states are all unoccupied, indicating that in this geometry the surface is non-metallic, although the effective surface band-gap is small.

Let's now return to the resonant peak in the DoS. Ref. [251] alludes to a resonant occupied state 1.75 eV below the diamond valence band maximum. The paper tentatively ascribes this state to silicon dangling bonds, where each silicon adsorbate is co-ordinated with 2 carbons and is 2.5 Å from the nearest adjacent silicon, slightly greater than the bulk interatomic distance [252, 253]. The calculated pDoS shown in Figure 67 reveals a broad band between around -1 and -2.5 eV, absent from the pDoS deeper in the slab and therefore belonging to the silicon layer. Wave function analysis of these states show them to be *spd*-hybridised covalent σ-bonding between adjacent silicon atoms (Figure 68) along the $[1\bar{1}0]$ direction, and not related to dangling bonds. Indeed, such bonding may well be anticipated for four-fold co-ordinated silicon atoms.

The data in Table 14 show that 75% Si-coverage is the second most energetically favourable with $E_{\text{ads}} = -0.95$ eV, just 30 m eV less stable per surface site than the 66% coverage model of Figure 63. 75% coverage has the same bonding arrangement as the aforementioned 67% coverage albeit with an additional period (3×2 to 4×2) in the [110] direction. Surface carbon atoms co-

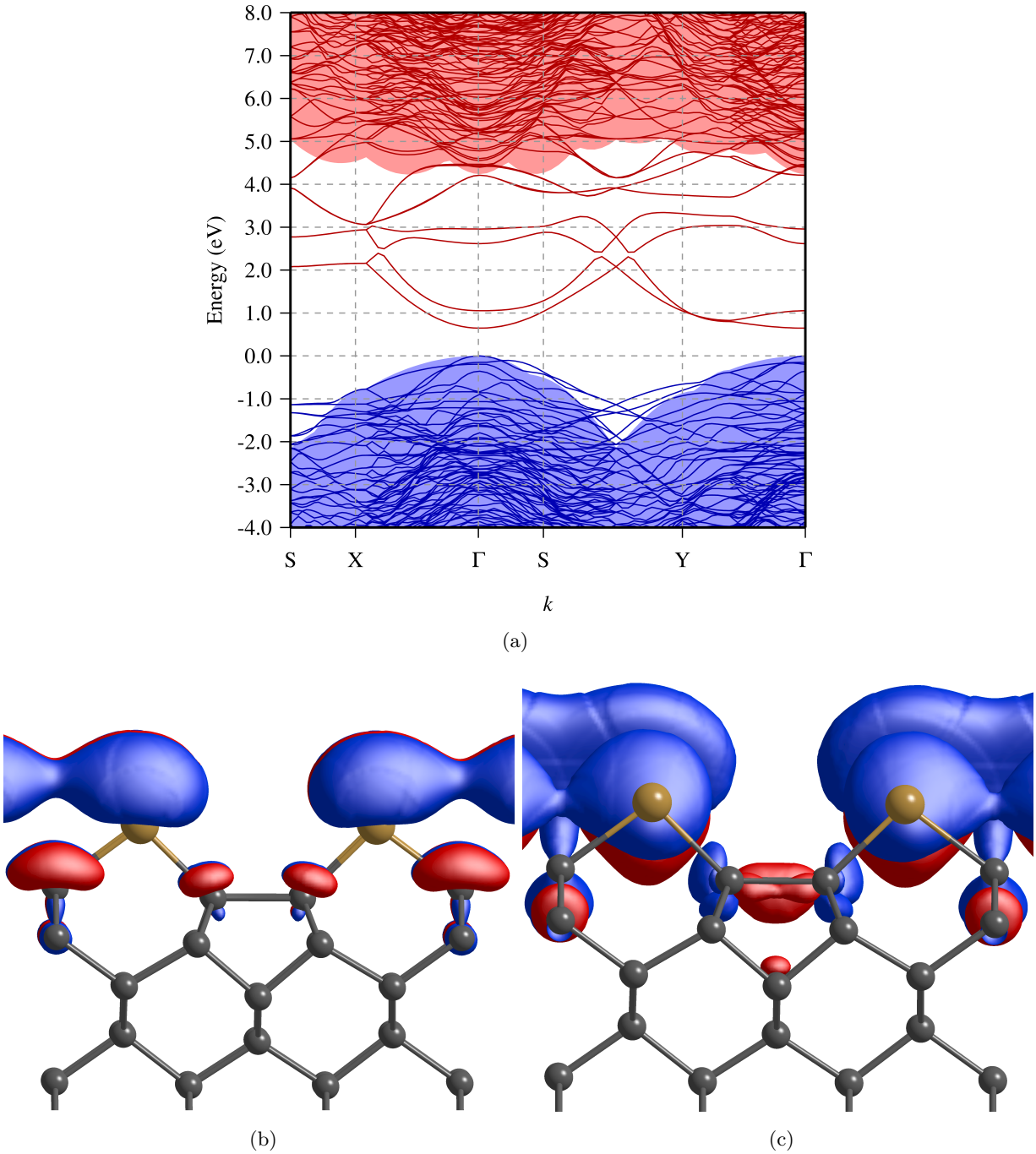

Figure 66: Electronic structure (a) and Isosurface plots showing the lowest unoccupied states at Γ (b) and X (c) of the 67% silicon terminated surface. Yellow and dark-grey spheres represent silicon and carbon atoms respectively.

ordinate with 2 C atoms in the layer below within the diamond, another C atom involved in the reconstruction, and one silicon atom. Un-reconstructed C-sites, unique to the 75% system, bond with two carbon atoms in the surface layer and two silicon atoms. Silicon atoms in these sites sit 0.08 Å higher than C atoms co-ordinated with the reconstruction.

The 75% coverage appears to reflect the maximum Si:C ratio where adatoms can exist in the C-Si-C formation, as 100% coverage of silicon is fully reconstructed, and forms a Si-Si square

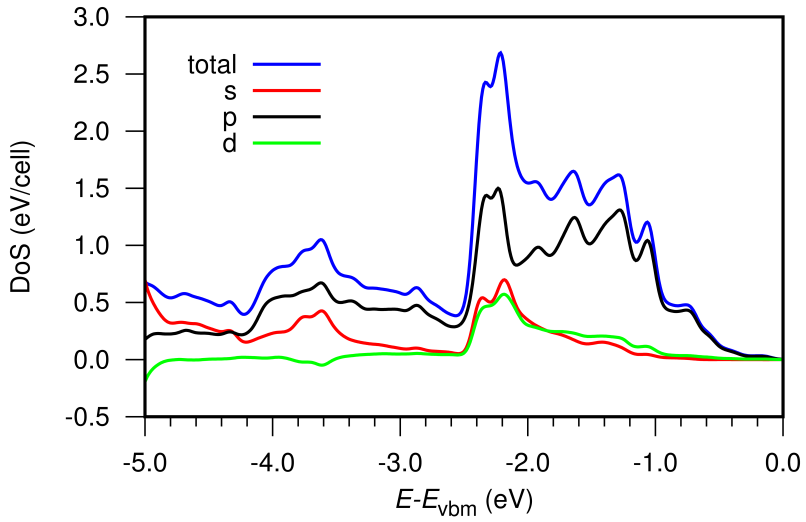

Figure 67: Decomposition of the pDoS for the 67% Si-terminated surface layer by orbital angular momentum in the region of the valence-band resonance close to −2 eV. The energy scale is set as in Figure 64.

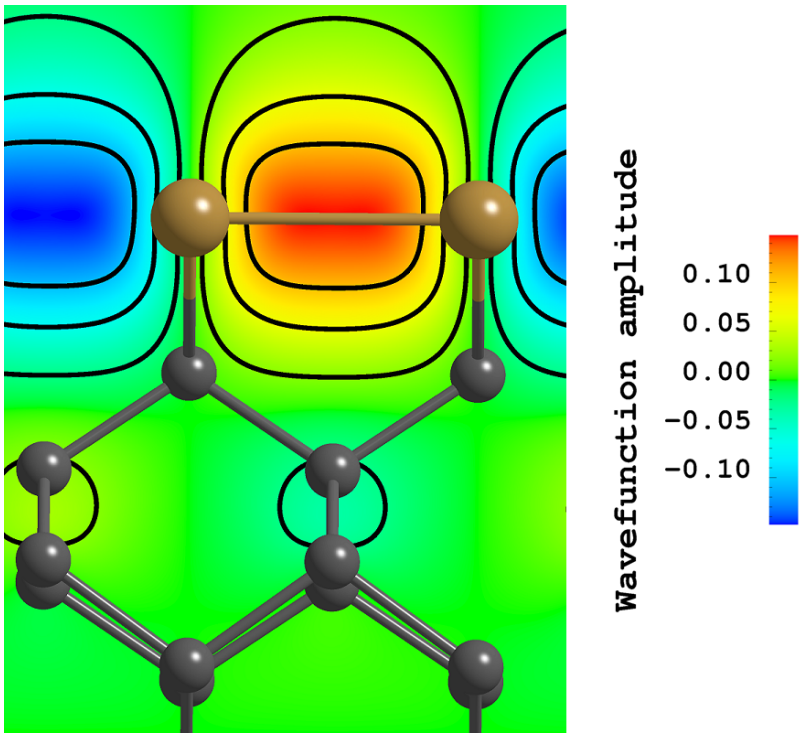

Figure 68: Contour plot of the σ-bonding contributing to the peak in the density of states seen in Figure 67 between silicon adatoms when viewed down the [110] direction. Amplitude units are in a.u.$^{\frac{-3}{2}}$

overlayer network akin to the lowest energy 100% germanium structure. The introduction of additional silicon on the 75% structure favours P site positions and co-ordination with 3 adjacent silicon atoms, 0.42 eV per surface site less favourable in energy.

A fully co-ordinated 100% silicon layer has shorter Si-C bond lengths and further from the

surface with distances of 1.92 and 1.88 Å respectively.

4.3.2 Germanium

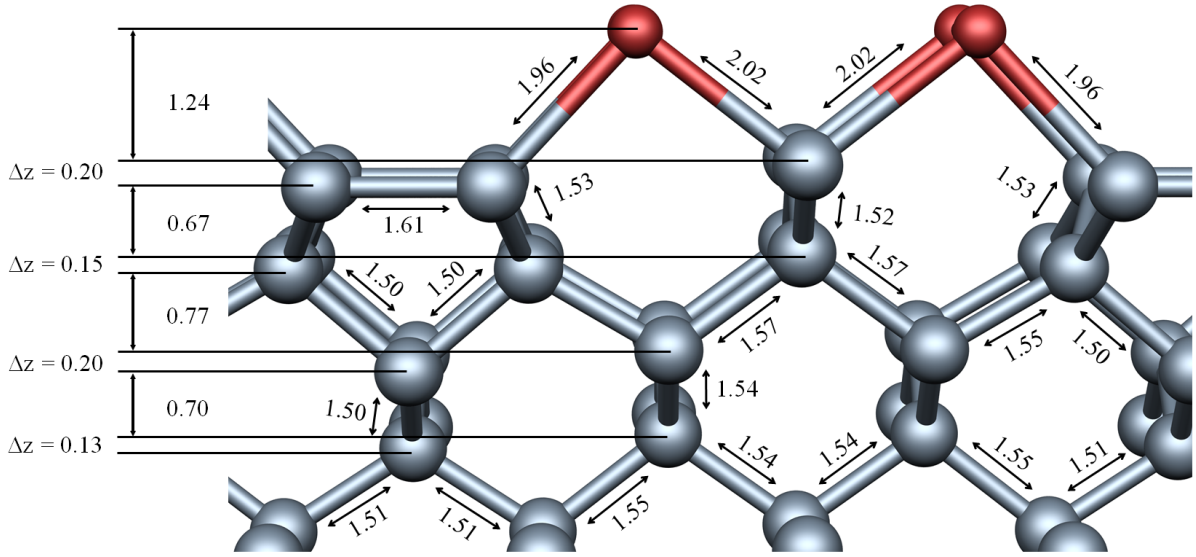

Figure 69: 67% germanium terminated (001)-(2×1) surface. Lengths are in Å. Brown and dark-gray spheres represent germanium and carbon atoms respectively.

As with the silicon termination, it can be seen that for cases with the lower percentage coverage favours the C-Ge-C bridge structures over the H and C sites maintaining full surface reconstruction. 67% coverage (Figure 69) includes C-Ge-C bridging along with a partial loss of the underlying diamond reconstruction.

Table 15: Calculated EAs (eV), formation energies (eV per diamond surface site), and C–Ge displacement in the surface-normal direction in (Å) for Ge termination. Coverages and periodicity are as defined in Table 14.

Coverage (%)	EA	E_{ads}	$Z_{\text{C–Ge}}$	Period
25	−0.43	−0.29	1.59	2×4
50	−0.77	−0.60	1.36	2×1
67	−0.85	−0.87	1.24	3×2
75	−0.95	−0.73	1.31–1.48	4×2
100	−0.92	−0.80	1.96	2×1

Each Ge atom co-ordinates with 2 carbon atoms and 2 adjacent adatom germaniums. From the optimised geometries, the 1.24 Å value of $Z_{\text{C–Ge}}$ is the smallest obtained for any Ge-termination (Table 15). Indicative of a generally substantial surface normal displacement, Ge surface normal

displacement values are systematically greater than found for the Si case.

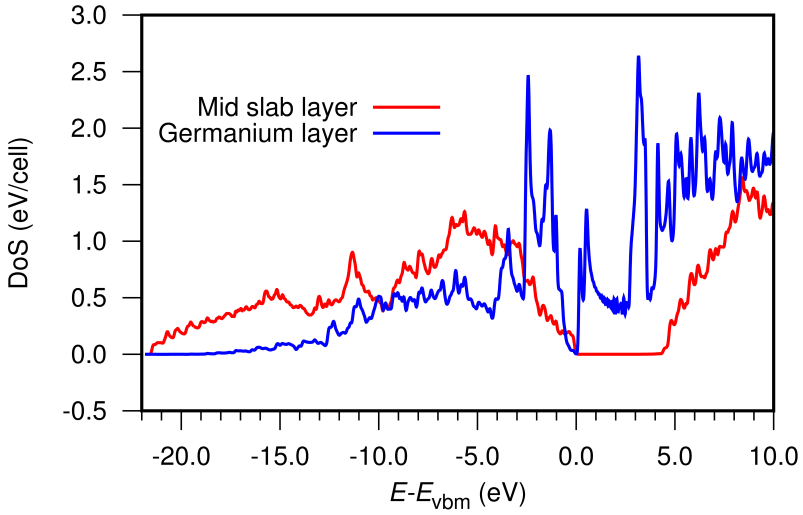

Figure 70: pDoS spectra for the 67% germanium surface layer (blue) and the bulk like middle diamond layer (red). VBM set to 0 eV.

The 67% structure, as with the silicon case, is found to be the most energetically favourable of those evaluated. The adsorption energy of −0.87 eV per surface site is slightly less than that found for the same Si-containing structure from the surface and an NEA of slightly greater than the corresponding silicon case at −0.85 eV.

The modest differences between Si and Ge termination are consistent with the chemical and structural similarities of these two species, and one might then expect similar outcomes for mixed termination.

Presented are the pDoS for Ge termination in line with the results presented for Si. The pDoS show that the Ge-layer also introduces states into the bandgap region (Figure 70) with an even smaller gap between the surface states and the underlying diamond valence band (around 0.1 eV for 67% coverage). Figure 71 (a) displays how close the unoccupied state is to the VBM and still the surface is non-metallic. Figures 71 (b) and (c) are similar in composition to their silicon counterparts in Figure 66, however the lowest unoccupied state spans 2.6 eV across k-points. At Γ, orbitals centred on germanium atoms are not interconnected along the [110] direction unlike the same isosurface plots for silicon.

Peaks are also observed (Figure 72) resonant with the valence band in the −2.5 to −1.0 eV range, which are also *spd*-hybrids in σ-bonding orbits between neighbouring Ge atoms (Figure 73), and one can predict that the observation of resonant states for Si in ARPES data would be replicated for germanium terminated diamond surface.

75% coverage represents a similar structure to that of the 67% with a further loss of the under-

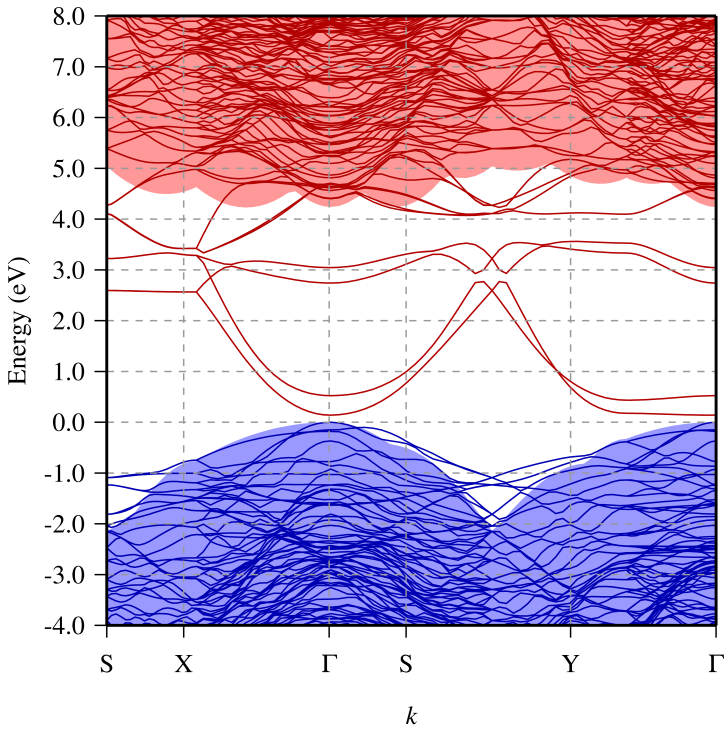

(a)

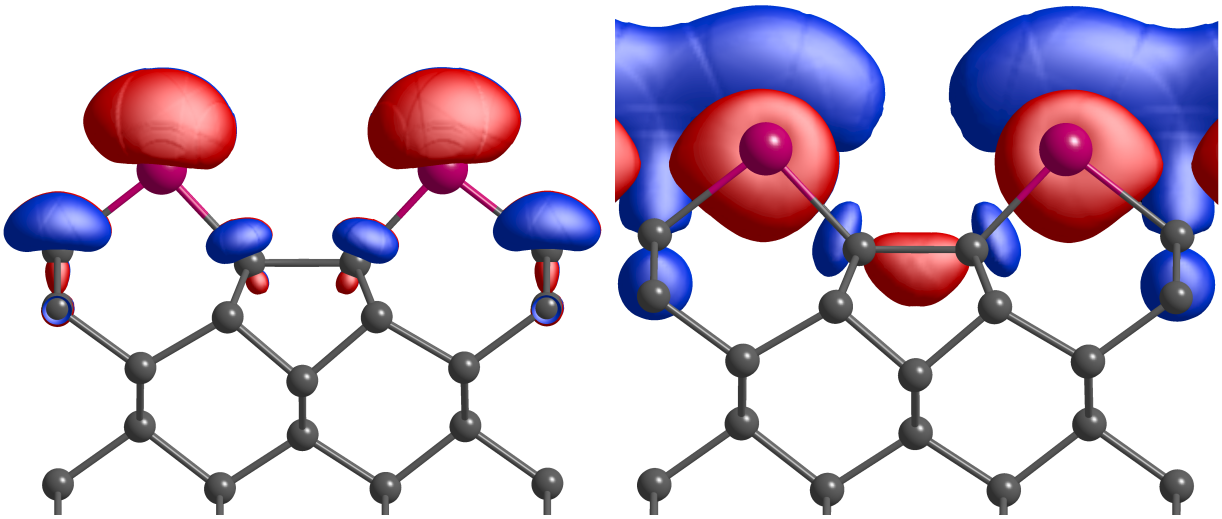

(b) (c)

Figure 71: Electronic structure (a) and Isosurface plots showing the lowest unoccupied states at Γ (b) and X (c) of the 67% germanium terminated surface. Brown and dark-grey spheres represent germanium and carbon atoms respectively.

lying diamond surface reconstruction. This increases the periodic cell size in the [110] direction from $[330]a_0/2$ to $[220]a_0$. Much like the same coverage of silicon, germanium atoms form bridges between surface carbon site and bond to two adjacent Ge atoms. The Ge-C bond-length for all coverages is in the region of 1.96 Å and 2.02 Å, in good agreement with distances in germanium carbide [256].

Monolayer coverage shows a fully covalent tetravalently bonded square network on the surface

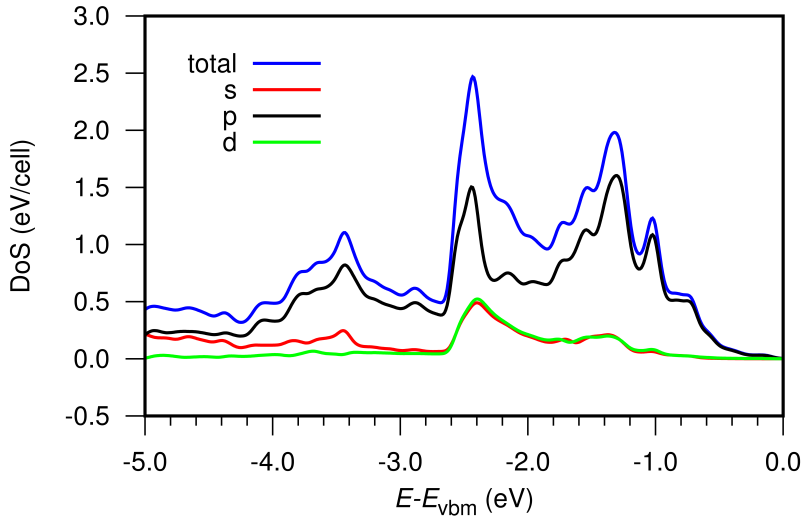

Figure 72: Germanium surface layer composition with focus on peak at −2.5 eV. The underlying diamond valence band maximum is set to 0 eV.

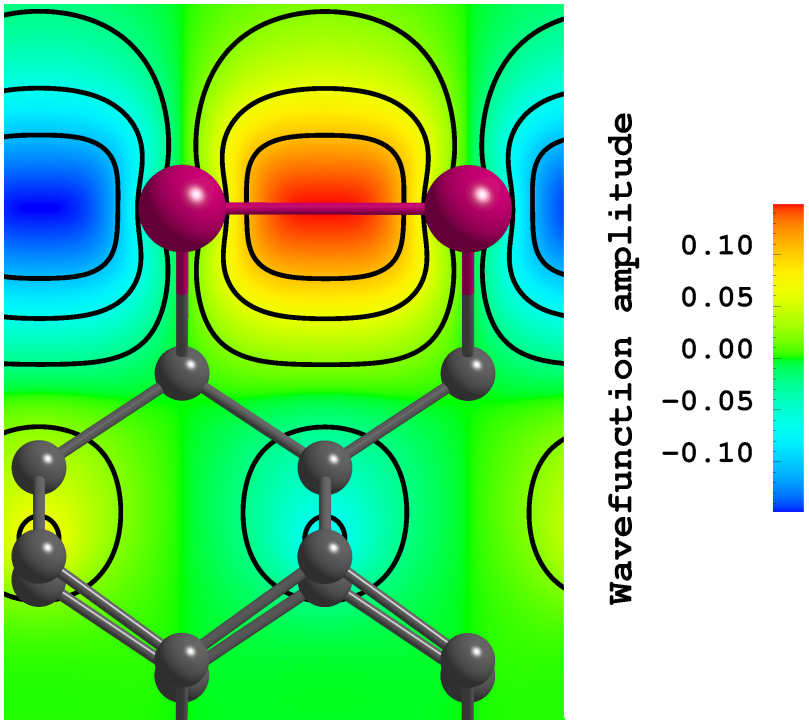

Figure 73: Contour plot of the σ-bonding contributing to the peak in the density of states seen in Figure 72 between germanium adatoms when viewed down the [110] direction. Amplitude units are in a.u.$^{\frac{-3}{2}}$

(Figure 74). Ge–Ge bond-lengths are determined to lie between 2.48 and 2.52 Å, consistent with those of bulk germanium [252, 253]. Germanium surface atoms co-ordinate with 4 adjacent germanium atoms and one carbon. This represents the second lowest energy structure with −0.80 eV per surface site gain in energy and a significant NEA at −0.92 eV.

For Ge all coverages studied represent an exothermic reaction relative to the unterminated surface and bulk Ge, and possess a NEA. Indeed, all Si and Ge coverages exhibit these properties,

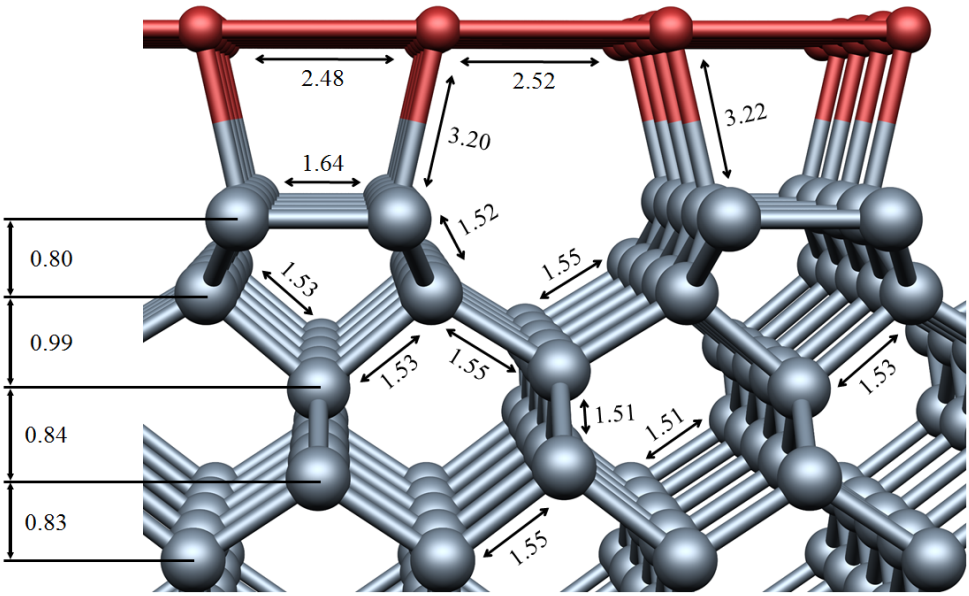

Figure 74: 100% germanium terminated (001)-(2×1) surface. Lengths are in Å. Brown and dark-gray spheres represent germanium and carbon atoms respectively.

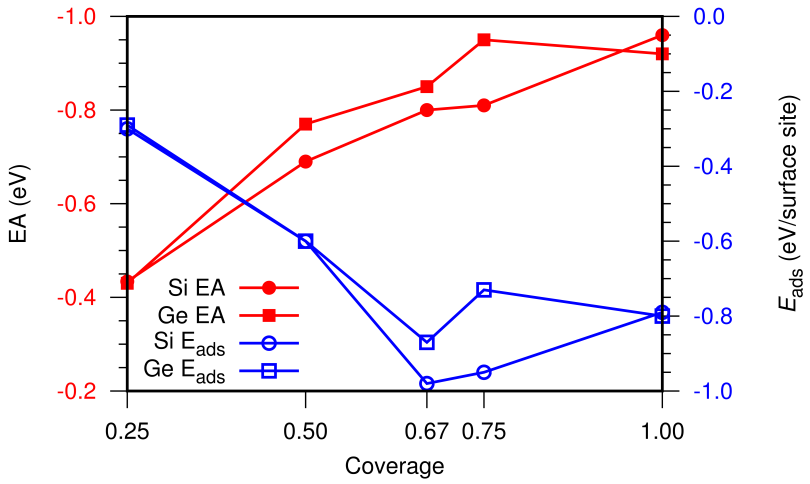

Figure 75: EA and E_{ads} trends with increasing coverage for both Si (circles) and Ge (squares) as a function of coverage fraction.

as illustrated in Figure 75. Therefore in the event of an (001)-diamond surface with variable coverages and surface sites, which may be the case in experiment, an NEA will still be demonstrated. This may be important for device fabrication, as disorder in the surface structure is expected to be less of a factor in generating conductive states.

Finally, one can reflect upon the differences found between Si and Ge. A key factor between the geometry of silicon and germanium structures with the same coverage is due to the different covalent radii of the of the two species. The structures of Si-terminated diamond (Table 14) result in generally higher adsorption energies than the corresponding Ge cases, which have larger surface normal displacements, consistent with the generally larger NEAs for Ge termination.

4.3.3 Conclusions

Density functional calculations of the diamond surface terminated by Si or Ge under a range of submonolayer coverages lead to the prediction that such reactions are exothermic and the treatments would produce a NEA. Adatoms prefer C-X-C bridge arrangements over other locations such as H and C sites. Silicon, partly due to its covalent radius, is expected to be more likely to exist in this configuration at higher coverages. In comparison to Si, Ge terminations tend to be energetically less favourable but exhibit larger NEAs, but both species exhibit the lowest energy structures at the same coverage. Si and Ge atoms at 67% coverage sit above the C site and co-ordinate fully, twice with carbon and adjacent crystallogen atoms. Relatively modest NEAs for all coverages (peaking at around $-0.8\,\mathrm{eV}$) may be of some use for field emission and NV stabilisation purposes, provided that these surfaces do not chemically degrade under operation or in atmosphere. Evaluation of the energetics and properties of the oxides of silicon and germanium is beyond the scope of this thesis, but is a relevant avenue of further research upon which these results and others provide an initial foundation The energy liberated upon addition of Si or Ge to an otherwise unterminated (001)-diamond surface is calculated to be 0.9–1.0 eV per surface site. This relatively modest energy is difficult to interpret on an absolute scale, as the reaction energies necessitate the presumption of the reactants involved. However, the stabilisation of the (001)-diamond surface by the addition of Si is broadly consistent with the experimental observation of Si termination up to about 1200 °C [257].

5. 4H–SiC Surfaces

5.1 Fundamental Aspects

5.1.1 Defining the cell

The origins of polytypes lie in the stacking sites of the hexagonal close packing (HCP) structure. Figure 76(a) shows a plane of HCP spheres (atoms). Taking the central sphere as our origin, the spaces between each sphere are either 60° or 120° apart. The site of each additional layer on top determines the stacking sequence and hence the polytype.

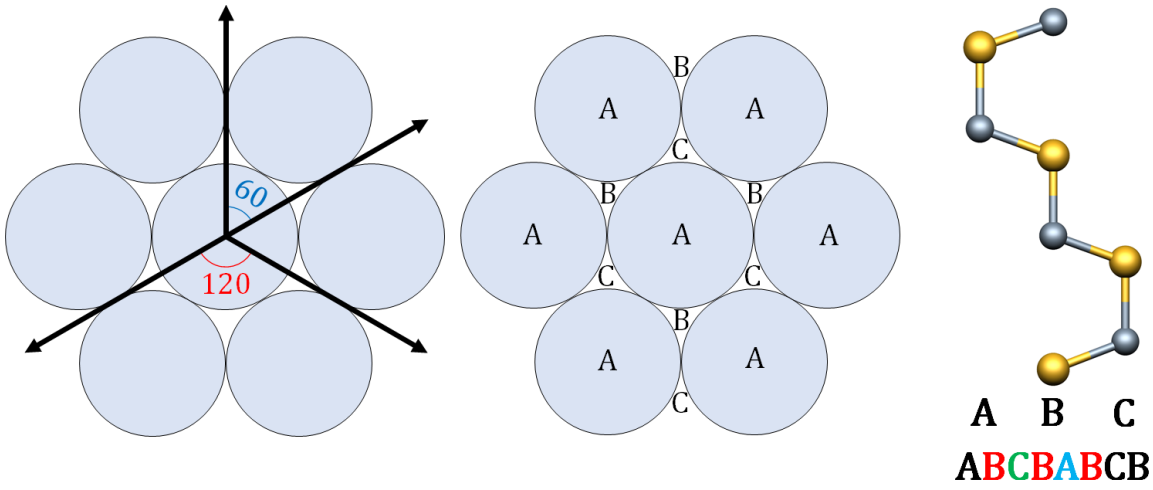

Figure 76: Hexagonal close packing (HCP) plane of atoms (left) and the angles between planar A atoms and B and C stacking sites (middle). The difference between B and C stacking sites is a 60° rotation. Choice of stacking site and periodicity determines the structure hence the polytype obtained (right).

4H–SiC has the stacking sequence $ABCB$ in the c-axis direction with a unit cell consisting of 8 atoms in 4 2-atom pairs (Figure 77(b)). The calculated lattice constants are $a = 3.06$ Å and $c = 10.03$ Å within 1% of theory and experiment [258, 259, 260]. The average bond length is 1.84 Å.

An indirect band gap 2.2 eV wide is obtained (Figure 78) in good agreement with other calcuated work [261].

Unlike diamond, pure bulk 4H–SiC is unable to be modelled with inversional symmetry, as depicted in Figure 79. Although covalently bonded, the difference in electronegativity creates strong ionicity in the Si-C bond in the [0001] direction. This spontaneous polarisation effect presents as piezoelectricity in the material, where a piezopotential created by an external stress

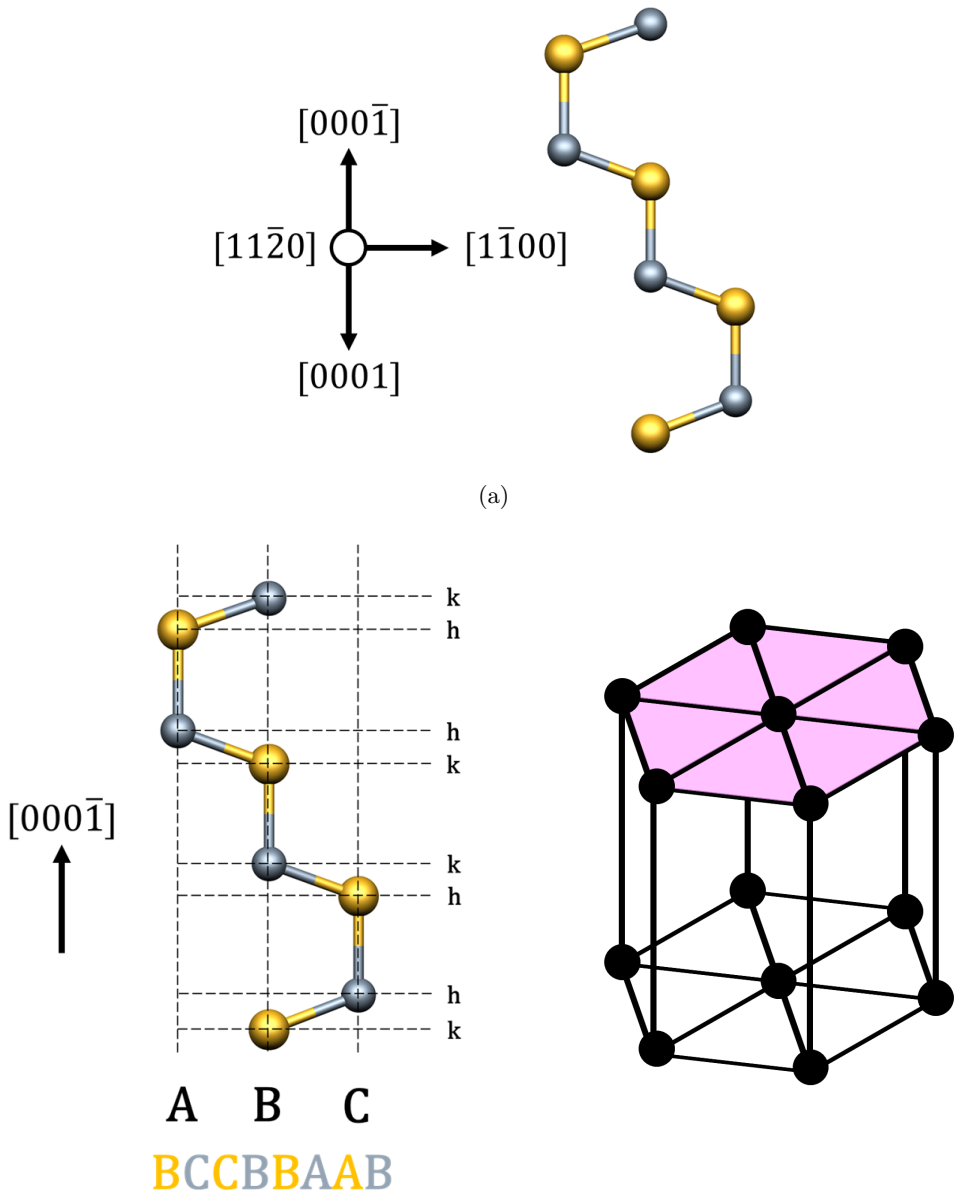

Figure 77: 8 atom 4H–SiC cell with main crystallographic directions (a) with the stacking sequence (b) and inequivalent h (hexagonal and k (cubic) sites. The (0001) plane of a hexagonal lattice (c) highlighted in pink. Hexagonal lattices are typically described using 4 vectors instead of the usual 3. The rationale behind this is explained in Chapter 7.2.

e.g. in a heterostructure has a considerable effect on transport properties [262]. This property and the effects therein, particularly on the surface, feature as an important methodological issue for the modelling of such structures.

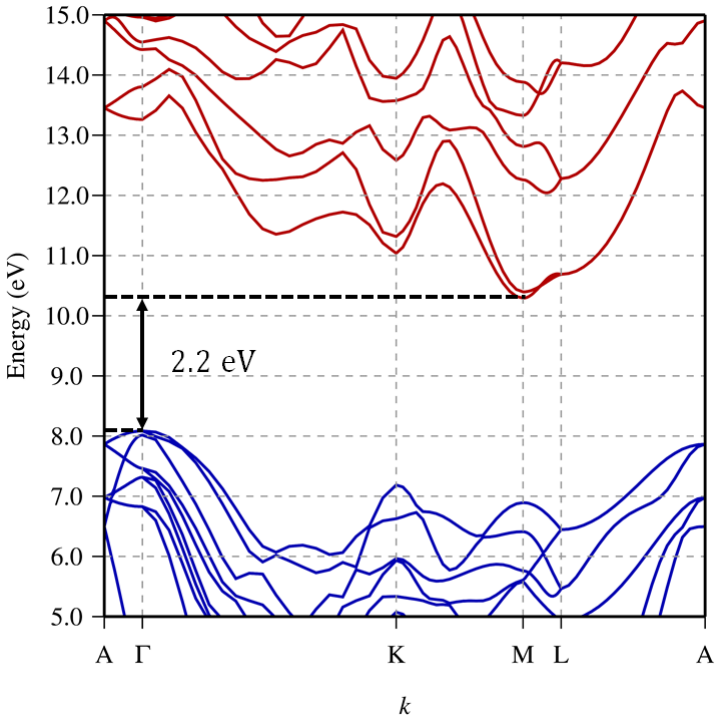

Figure 78: Bulk 8 atom 4H–SiC bandstructure with calculated indirect bandgap of 2.2 eV.

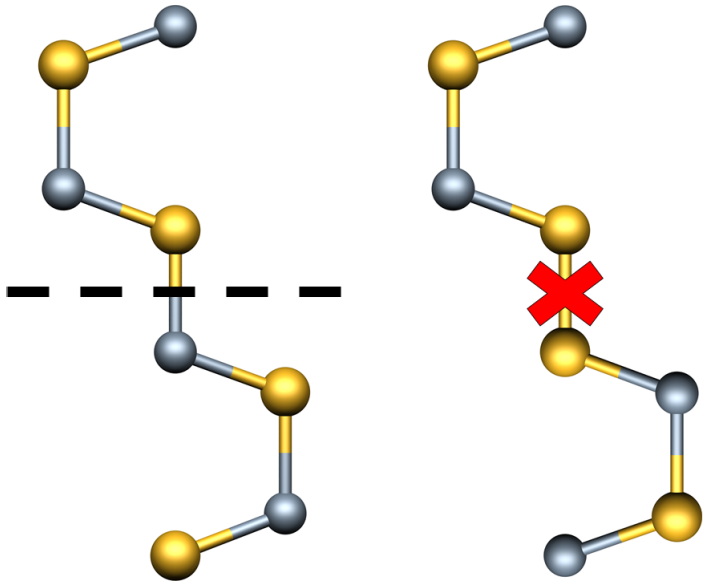

Figure 79: Symmetrically inverting an 8 atom 4H–SiC cell through the origin thus creating an incorrect model.

5.2 Unterminated $(11\bar{2}0)$ Surface

The $(11\bar{2}0)$ surface has gained significant attention for device applications, in particular as an alternative face to improve inversion channel mobility in MOSFETs [263, 264]. As previously discussed in Section 1.3, the (0001)-oxide interfaces yield debilitating channel characteristics. Additionally, the non-polar planes have been identified for significant micropipe reduction through repeated a-face growth [166]. The structure and electronic properties of the surface when terminated with common chemical elements, as detailed in the upcoming section, is crucial in the further development of high quality crystal growth and device enhancement.

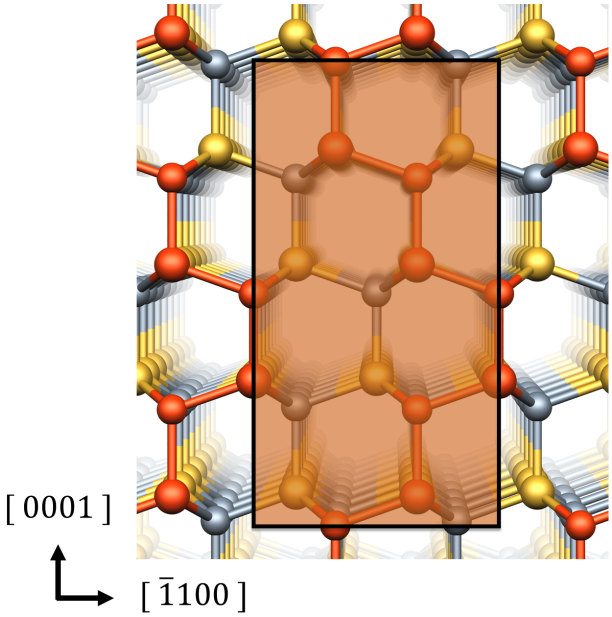

Figure 80: Top down view of unterminated $(11\bar{2}0)$ surface with in-plane lattice vectors. Unit cell highlighted in orange. Yellow, gray and orange spheres represent silicon, carbon, and surface sites, respectively.

Experimental data [265] show that from room temperature to 990 °C there is no reconstruction of the $(11\bar{2}0)$ surface so the footprint remains unaltered at (1×1). The $(11\bar{2}0)$ surface is comprised from an equal number of Si and C atoms. The unrelaxed ideal surface consists of one dangling bond per surface site. Figure 103 shows our optimised structure, indicating bondlength shortening of up to 8% relative to the average bulk value of 1.87 Å, and a modest average surface-normal relaxation of 0.02 Å. The buckling at the surface moves carbon atoms outwards and the silicons atoms relax into the surface by an average of 0.2 Å.

The bond-length range of 1.73–1.76 Å agrees well with previous data [266]. We find that the second layer is less perturbed, but also exhibits shorter bondlengths of 1.84 Å. The third layer exhibits slightly dilated bonds (1.91–1.92 Å), but below this layer inter-atomic distances are not significantly different from bulk.

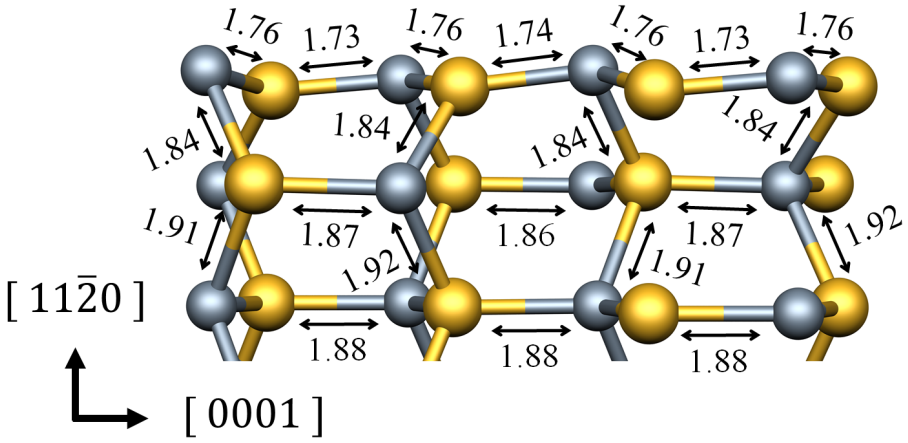

Figure 81: Fully relaxed unterminated (11$\bar{2}$0) surface viewed along the [$\bar{1}$100]. Atom colours are as in Figure 80, and bond-lengths are in Å.

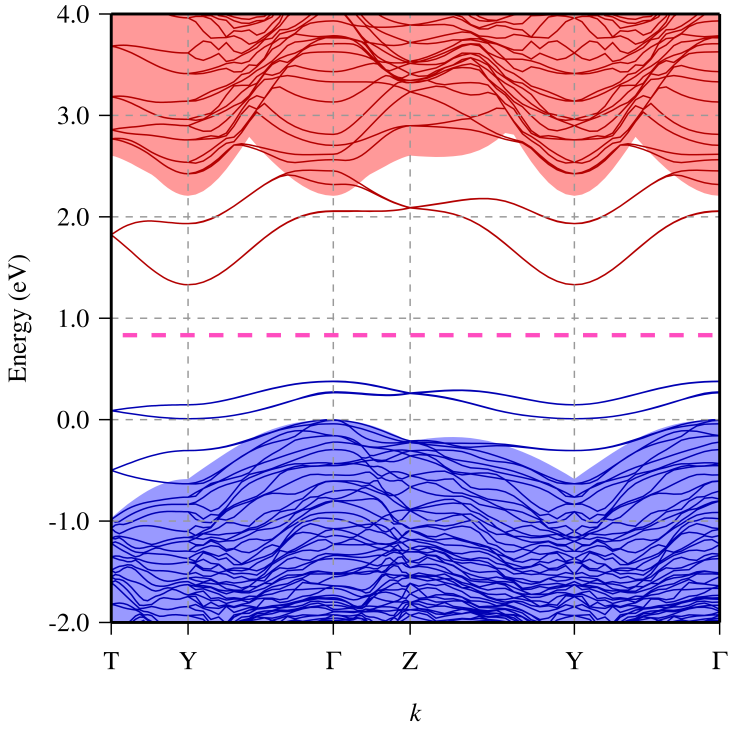

Figure 82: Electronic band structure of the (11$\bar{2}$0) unterminated 4H-SiC surface, along high symmetry branches of the two dimensional, orthorhombic surface Brillouin zone. The labels for the k-axis follows the conventional notation [248], with the [0001] and [$\bar{1}$100] directions of the underlying material corresponding to the $\Gamma - Z$ and $\Gamma - Y$ branches, respectively. The energy scale is defined so that zero is the valence band maximum. Only bands in the vicinity of the band-gap are shown. Occupied and empty bands are shown in blue and red, respectively. Pink dashed line denotes Fermi level E_{f}. The underlying shading shows the corresponding bands of bulk SiC.

The rearrangement of the surface can be understood as arising from the redistribution of charge between the Si and C site radicals, leading to sets of negatively charged carbon sites and posi-

tively charged Si sites. This can be further understood as resulting in lone-pairs on the carbon atoms, with relatively delocalised orbitals pointing into the vacuum, corresponding to surface electric dipoles with components pointing out of the SiC. Outward pointing electric dipoles increase the potential step between the SiC and vacuum, and indeed we find the unterminated surface to have a positive EA (PEA) of 2.49 eV. The associated ionisation potential is 5.72 eV, which is within 1% of comparable theoretical work [266], providing confidence in our general approach.

Additional light can be shed upon the properties of the unterminated surface from the electronic band structure. Figures 82 and 83 show two pairs of doubly degenerate occupied states localised to the surface layers positioned 0.3–0.4 eV above the valence band maximum. The states at Γ and T are strongly surface associated, with considerable weighting towards C atoms. The degeneracy of each band is a result of the two equivalent surfaces in the slab model, so each band pair should be considered as yielding one state per surface. Further separation of the pDoS by orbital angular momentum (not shown) reveals these 4 states are dominated by the p component and point along the direction of bonding expected, akin to the direction of other C atoms in the layers below. States located at -0.5 eV are again surface C atom focused at T and a mixture of surface and bulk-like character at Γ.

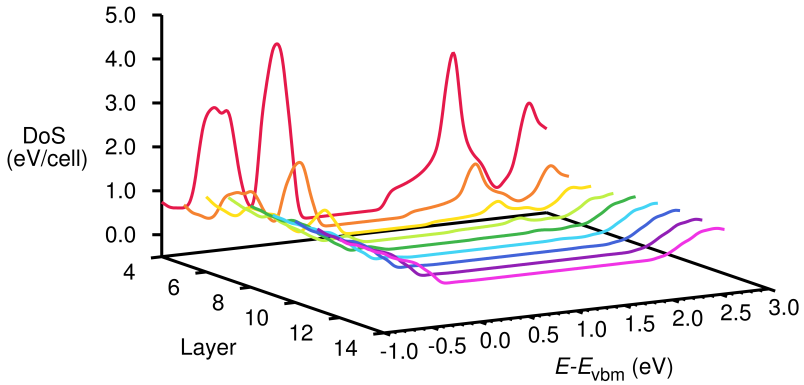

Figure 83: pDoS spectra of the unterminated surface by atomic layer as a function of distance from the surface in the region of the band-gap (0–5 eV). Zero on the energy scale is the valence band maximum.

Moving onto the unoccupied bands, the lowest energy state exhibits significant dispersion of around 1 eV, centred about 0.2 eV below the conduction band minimum. These states are characterised as dominated by sp^3 hybrids on the surface silicon atoms, consistent with previous analysis of this surface [267].

5.3 Terminated $(11\bar{2}0)$ Surface

To summarise Section 1.3, silicon carbide (SiC) is renowned for its excellent material properties including carrier mobility, breakdown field and thermal conductivity [71, 268]. In particular, the 4H–polytype has superior qualities to its counterparts, promoting large scale investment in this area. The intrinsic strength of the Si–C bond provides the foundation for a large Young's and bulk modulus, and its chemical inertia. When combined with a large band-gap and low carrier removal rate, SiC is naturally favoured for high temperature and radiative environments [69, 16], and SiC-based devices, particularly sensors [151], are capable of excelling in hostile conditions. Understanding how different elements, gases, temperatures and pressures effect surfaces of sensors, and hence their electron affinity, is therefore of great importance. The thermal stability of the terminating species is one indication of how easy it is to reverse a given reaction and how susceptible the surface is to any unwanted adsorbates that may occupy surface sites and reduce sensing surface area and efficiency. Atomically flat surfaces, as is the case of the $(11\bar{2}0)$ surface under study [269], are advantageous for certain sensing applications and indeed the transport of charge carriers through materials for all applications [270].

Surface termination by, for example, monovalent elements results in the formation of surface electric dipoles, that might be tuned to engineer favourable properties for technological applications.

More generally, Si and C with electronegativities of 1.90 and 2.55 on the Pauling scale [241] can be terminated with relatively electropositive or electronegative elements to affect electron affinity. Fluorine termination, for example, would be expected to form $C^{+\delta_1}$–$F^{-\delta_1}$ and $Si^{+\delta_2}$–$F^{-\delta_2}$ dipoles, lowering the underlying SiC conduction band minimum relative to vacuum, increasing the electron affinity. In emitter focused applications the EA of a surface represents a barrier to emission. If the EA is negative, the barrier is lowered significantly and electrons emit efficiently in to the vacuum [131]. Nanostructured SiC has been widely studied for field emission applications [271, 272]. However, the surfaces under termination for the reduction of work function has to our knowledge not yet been discussed. SiC material properties make it a superb candidate for emission based devices if a negative EA can be realised [106].

Although there are data relating to band offsets [273, 274, 275] currently there is a paucity of data relating to the impact of surface termination on the EA of SiC. Most surface data for unterminated, hydrogenated and oxidised 4H–SiC surfaces mainly focuses on structure and energetics without information on the EA [269, 265, 267].

With many surfaces and adsorbates there is great potential for the realisation and optimisation

of surface-focused devices including field emitters, sensors, and electrochemistry.

5.3.1 Method Specifics

Atoms are modelled using pseudopotentials [192], with Kohn-Sham functions expanded using atom-centred sets of independent *s*- and *p*-type Gaussian orbital functions [276] with four widths, with the addition of either one or two sets of *d*-type Gaussian functions for variational freedom, totalling 28 functions for Si, C, F and Cl and 22 functions for Li. Hydrogen is treated using basis functions made up from two fixed linear combinations of four *s*-type orbitals, with the addition of a set of *p*-type orbitals for polarisation, resulting in five functions per atom in total.

Surface formation energies are calculated [277] according to the equation:

$$E_{\text{surf}} = \frac{1}{2nm}\{E_{\text{tot}} - E_{\text{slab}} - N_{\text{x}}\mu_{\text{x}}\} \tag{33}$$

where nm is the number of surface sites per surface and the 2 arises as there are two surfaces per slab. E_{tot} is the energy of the optimised terminated structure, E_{slab} is the energy of the unterminated reference slab and N_x is the total number of adsorbate atoms per system. μ_{x} is the chemical potential of the single adsorbate atom taken from the respective elemental phase (H_2, F_2, Cl_2 and BCC lithium).

5.3.2 Hydrogen termination

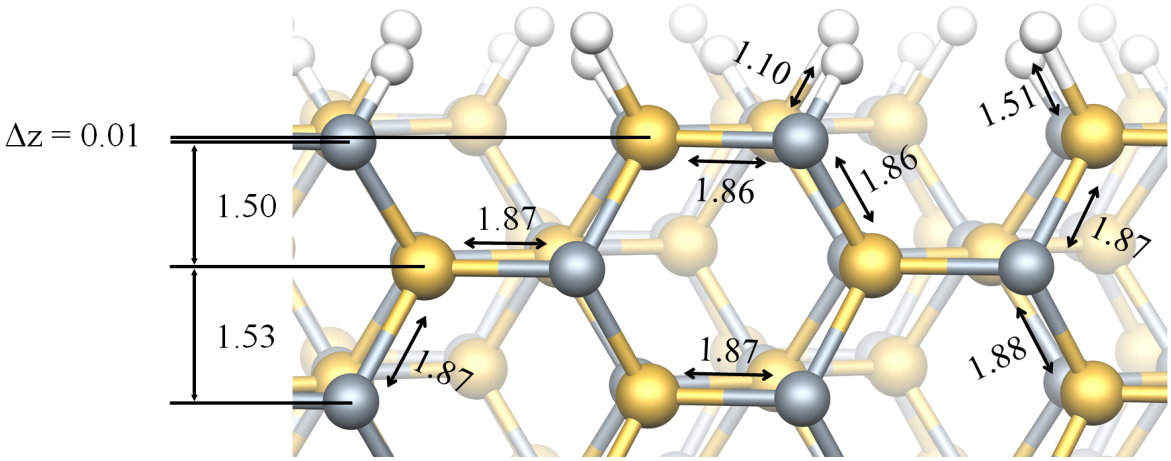

Figure 84: Schematic structure of the H-terminated (11$\bar{2}$0)-surface (up) viewed along [0001]. Distances are shown in Å. White, gray and yellow spheres represent hydrogen, carbon and silicon respectively.

Table 16 lists key quantitative data for H-terminated (11$\bar{2}$0) 4H–SiC obtained in this study. The data reveal hydrogen termination reduces the EA by 0.63 eV to 1.86 eV. This is a much

smaller affect than the 2.5 eV difference in EA between unterminated and hydrogenated (001)-(2×1) diamond [205]. As alluded to in the introduction, there is a difference of 0.65 in the electronegativities of C and H, with the value for H (2.20) lying between those of Si and C. This suggests that H-terminated SiC should be considered as an array of opposing dipoles. The C-H inward pointing surface electric field reduces the total potential step between the SiC and vacuum relative to an unterminated surface. The Si–H bonds retain an outward pointing dipole.

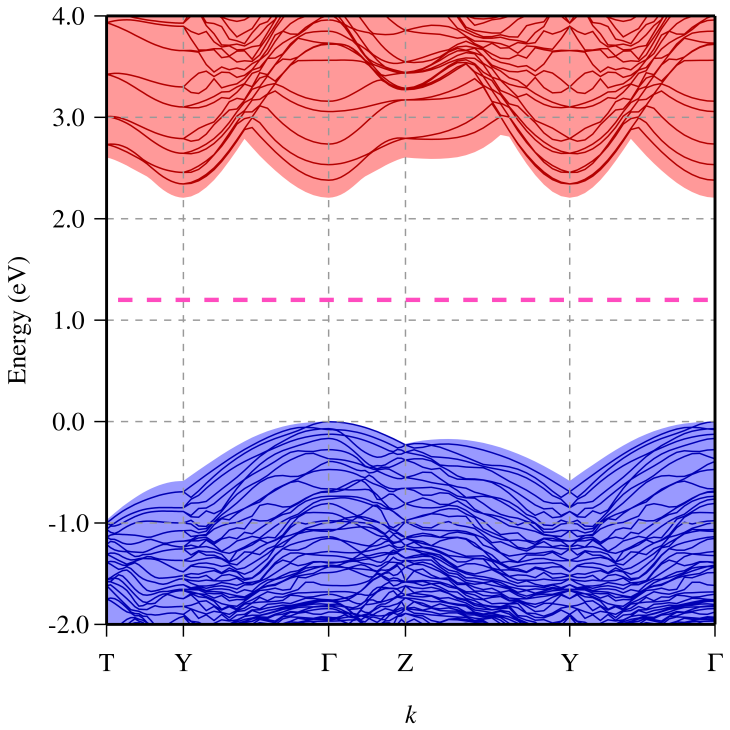

Figure 85: Electronic band structure of the $(11\bar{2}0)$ fully hydrogenated 4H–SiC surface. Scales, colours and lines are as for Figure 82.

Here there is only a modest energy gain of 1.39 eV/surface site relative to hydrogen gas and an unterminated surface. This shows some consistency with previous difficulty in fully H-terminating SiC [278]. Partial H-termination is understood to be chemically selective as experimentally, H desorbs fully from surface Si atoms by 580°C, whereas C–H bonds survive to 820 °C [265]. This is consistent with additional calculations performed where only either C or Si sites are terminated with hydrogen; where only C sites are terminated, obtained an energy 0.42 eV/surface site lower than where only Si-sites are H-terminated.

The hydrogen surface layer pDoS mirrors the bulk layers, consistent with the simple chemical passivation of the surface provided by the H-termination. The hydrogen termination case therefore provides control data for the following cases of halogen and Li termination, where it shall be shown that although the species are monovalent, other contributions to the electronic structure of the adsorbates leads to surface states.

Table 16: Calculated EAs (eV), surface formation energies (eV per surface site) and distances to terminating species (Å) from C and Si atoms for $(11\bar{2}0)$-X surface structures. The unterminated surface formation energy (1.37 eV/surface site, 0.22 eV/Å) agrees very well with previous theoretical data [269]. Also listed are the adsorbate electronegativitys (χ) on the Pauling scale [241]. The values for C and Si are 2.55 and 1.90, respectively. $Z_{\mathrm{C-X}}$ and $d_{\mathrm{C_X}}$ represent the surface normal component of the C–X bonds and the total C–X bond-length, respectively, with corresponding Si–X values also listed. For each bond-length, the percentage deviation from the sum of covalent radii is indicated for 0.38, 0.71, 0.99, 1.34, 0.77 and 1.11 Å for H, F, Cl, Li, C and Si, respectively (positive values mean that the sum of the covalent radii are greater than the calculated bond-length). For the SiC terminated case the surface energy is the formation energy per surface site relative to bulk 4H–SiC, whereas for X=H, F, Cl and Li it represents the adsorption energy as defined in Eq. 33.

X	χ	EA	E_{surf}	$Z_{\mathrm{C-X}}$ ($d_{\mathrm{C-X}}$)	$Z_{\mathrm{Si-X}}$ ($d_{\mathrm{Si-X}}$)
none	–	2.49	1.37	–	–
H	2.20	1.86	−1.39	0.90 (1.10, +4.5%)	1.24 (1.51, −1.3%)
F	3.98	5.05	−4.40	1.15 (1.41, +5.0%)	1.47 (1.58, +13.2%)
Cl	3.16	3.90	−1.41	1.23 (1.80, −2.3%)	2.18 (2.18, −3.8%)
Li	0.98	0.08	−0.77	0.80–1.89 (2.01–2.07, +1.9–4.7%)	0.87–1.91 (2.38–2.44, +0.4–2.9%)

5.3.3 Fluorine termination

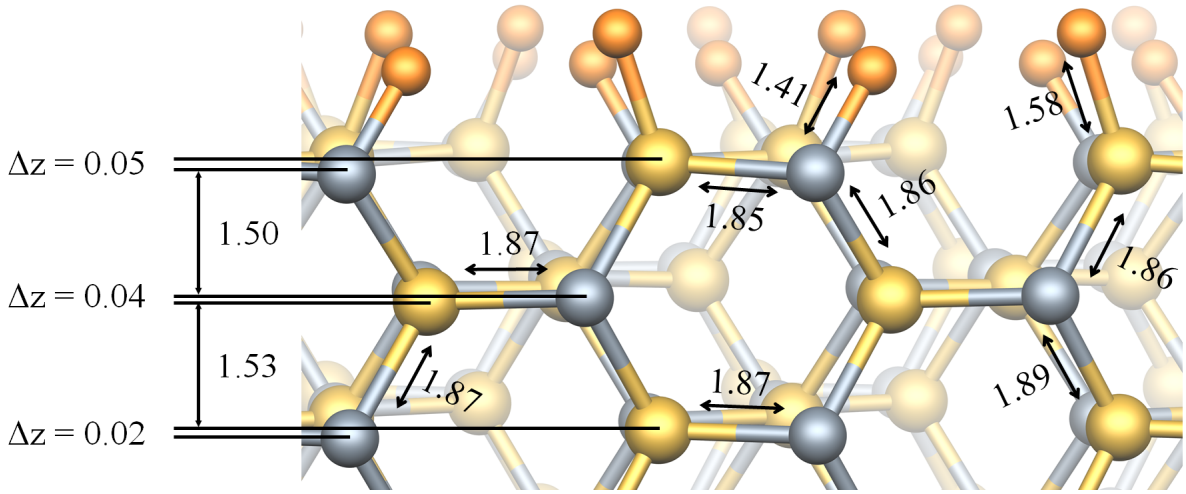

Figure 86: Schematic structure of the F-terminated $(11\bar{2}0)$-surface (up) viewed along [0001]. Distances are shown in Å. Gray, yellow and orange spheres represent carbon, silicon and fluorine, respectively.

Fluorine is much more electronegative than Si, C or H, but is monovalent and therefore is

chemically expected to saturate the $(11\bar{2}0)$-surface with one F-atom per surface site (Figure 86). There is a comparatively large energy gain per F-atom with respective to the other adsorbates, estimated at 4.40 eV per surface site (Table 16). This is in part due to the relatively weak bonding in the bulk reference for fluorine, with diatomic fluorine having a disassociation energy around half that of chlorine and just a third that of hydrogen [279]. The electronegativity of F is the largest of any element, so the electric dipoles all point out of the surface resulting in an extremely large predicted PEA of 5.05 eV, one of the largest reported for any semiconductor surface.

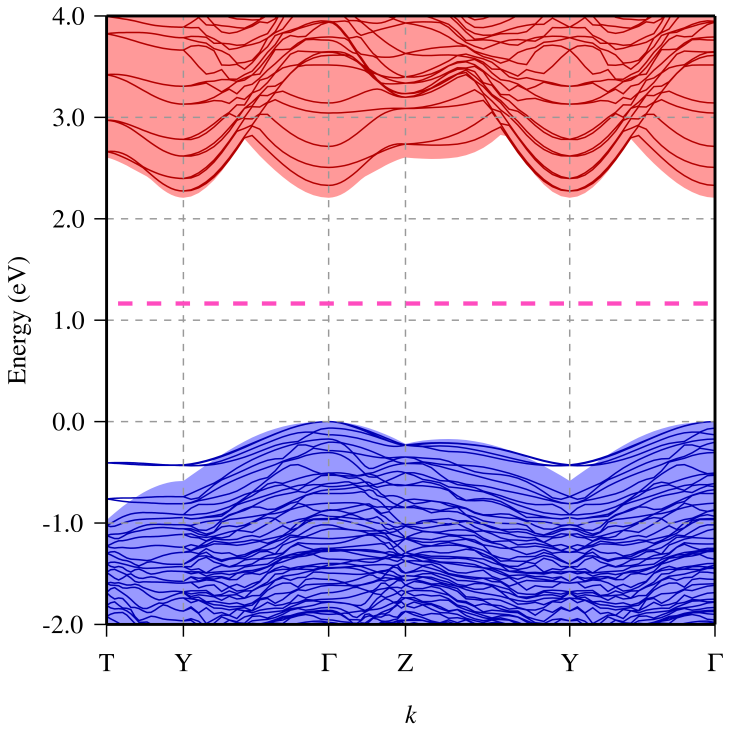

Figure 87: Electronic band structure of the $(11\bar{2}0)$ fluorine-terminated 4H–SiC surface. Scales, colours and lines are as for Figure 82.

Figure 87 shows the band structure for the fully fluorine-terminated surface. There are surface states resonant with the valence band that can be seen in the T–Y branch and in the vicinity of Y on the plot. These states are made up from p-orbital lone-pairs on the F-atoms. It is shown below that this is more pronounced for Cl-termination.

Figure 88 shows the pDoS for the fluorine adatom layer. The hydrogen-termination case provides a useful reference for where there are no surface states in the vicinity of the band-gap. The peaks in the states in the -1 to 0 eV range of Figure 88 can be directly mapped to the surface related bands seen in the same energy range of Figure 87. The highest occupied states at Γ in Figure 87 exhibit a mixed fluorine p-orbital/SiC bulk-like character, whereas the states at T are strongly associated with surface F atoms.

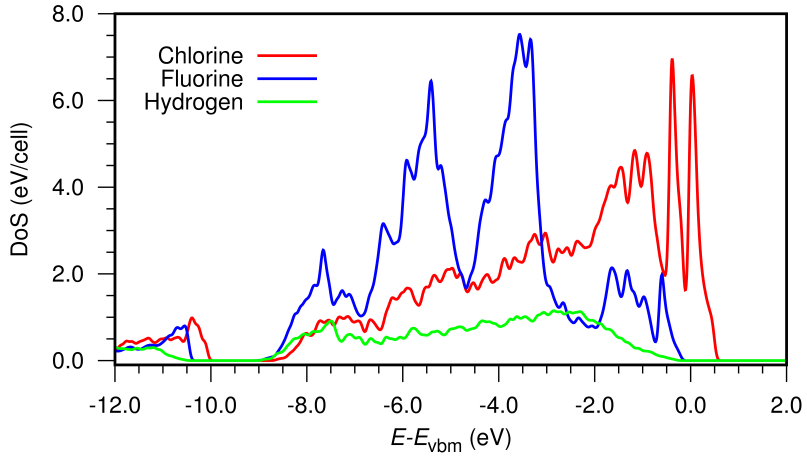

Figure 88: pDoS spectra for the fluorine (blue) and chlorine (red) atoms. The hydrogen-termination case is shown in green as a reference where there are no gap states. Zero on the energy scale is the valence band maximum.

This is entirely consistent with a set of non-bonding p-orbitals associated with the F atoms giving rise to a surface-state band resonant with the underlying SiC valence band.

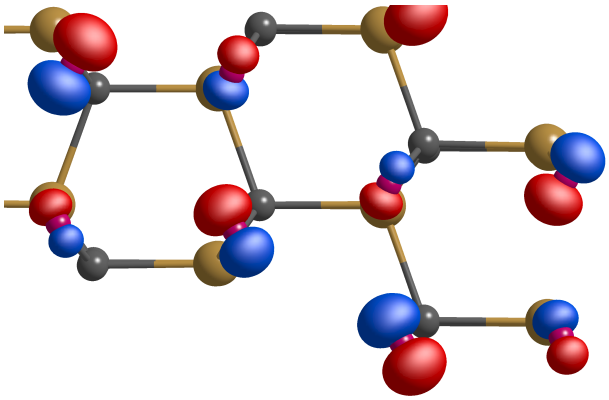

Figure 89: Plots showing the isosurfaces of the highest energy fluorine peak at $-3.5\,\text{eV}$ on Figure 88. Pink, dark-gray and yellow spheres represent fluorine, carbon and silicon respectively.

The prominent pDoS peaks at -5.5 and $-3.5\,\text{eV}$ are also characterised by p-orbitals on the F-atoms (Figure 89), with the higher energy peak being more focused upon F-atoms bonded to Si. These states are visible in ARPES experiments [251, 280], and represent targets to confirm the outcomes of the modelling.

5.3.4 Chlorine termination

Also with a high electronegativity, chlorine termination is found to result in a large PEA of $3.90\,\text{eV}$. Unlike F, however, there is a relatively modest energy gain in full termination of the surface, estimated at $1.41\,\text{eV/surface site}$, similar to the hydrogen case. This is not an expected result on the basis of the binding energies of H_2 and Cl_2, which are $4.52\,\text{eV}$ and $2.52\,\text{eV}$,

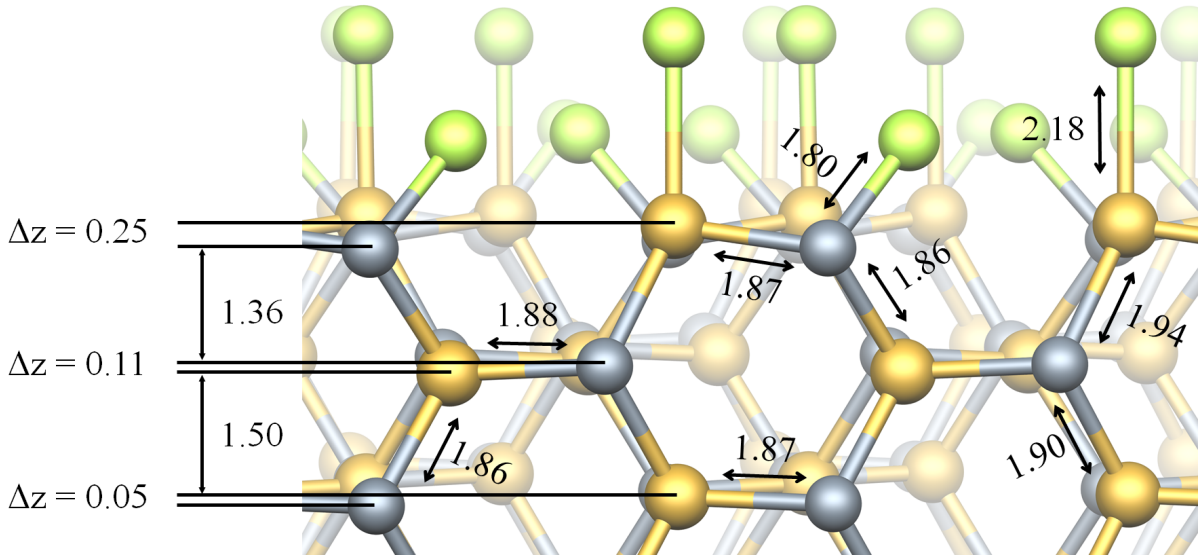

Figure 90: Schematic structure of the Cl-terminated $(11\bar{2}0)$-surface (up) viewed along [0001]. Distances are shown in Å. Gray, yellow and green spheres represent carbon, silicon and chlorine, respectively.

respectively. Since Cl_2 is less difficult to dissociate, one might expect a greater energetic yield from the saturation of the SiC surface.

Figure 90 shows a significant distortion in the underlying SiC layers, particularly in the vicinity of Si-Cl bonds where Si–C bond-lengths vary from 1.88–1.94 Å and surface normal displacement is 0.25 Å. Focusing upon the Si–Cl bonds, the orientation of the bond is very close to the surface normal direction which necessitates bond-angles that deviate significantly from the approximately tetrahedral angle of bulk SiC.

The band-structure of the Cl-terminated case shows the clear introduction of bands in the vicinity of the valence band maximum (Figure 91), with bands below the valence band top visible in the T–Y branch as they were for the fluorine case.

Wavefunction analysis of the state at both the T and Γ branches reveal the highest occupied molecular orbitals, represented by the band at 0.5 eV at the Γ-point of Figure 91, are non-bonding p-orbital lone-pairs on the Cl atoms, as illustrated in Figure 92. The pDoS for the adsorbates (Figure 88) exhibits pronounced peaks in the energy range of the surface states in the −0.5–0.5 eV associated with these lone-pairs. The pair of bands just below this that straddle the 0.0 eV are composed of a mix of surface only Cl atom p-orbital lone-pairs and the other is bulk-like with minor, localised contributions from strained Cl atoms. As with the F-case, this is consistent of the crossing of and mixing of valence band states with the localised surface states. These bands at the zone-edge (e.g. at the T-point) are very clearly Cl p-orbital related.

To further explore the steric repulsion, optimised structures with partial Cl termination are

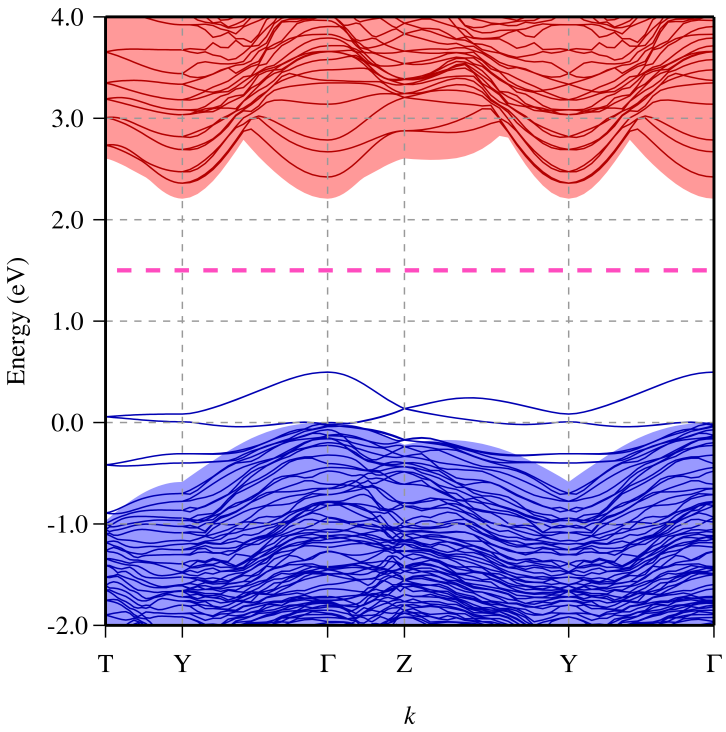

Figure 91: Electronic band structure of the $(11\bar{2}0)$ chlorine-terminated 4H–SiC surface. Scales, colours and lines are as for Figure 82.

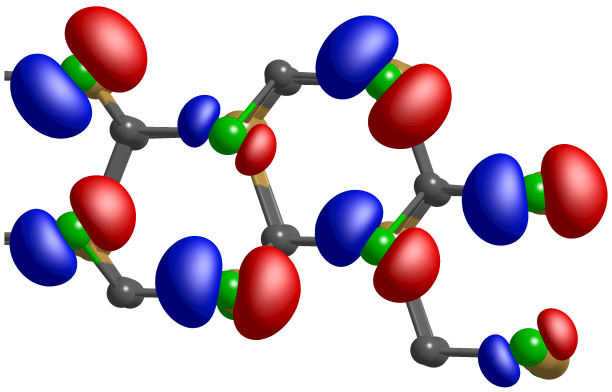

Figure 92: Plots showing the isosurfaces of the highest energy surface state of Figure 91 as viewed down the $(11\bar{2}0)$. Green, dark-gray and yellow spheres represent chlorine, carbon and silicon respectively.

explored. Up to 50% coverage, Cl adatoms favour a mix of Si and C termination sites at angles similar to those of Figures 84 and 86. This 50% coverage is $-0.96\,\text{eV}$/surface site lower in energy in this configuration than the unterminated surface. Above 50% coverage adatoms begin to adopt the vertical Si–Cl structure of 100% termination. These adatoms achieve a smaller energy gain per atom compared to the first 50% but ultimately still contribute to lowering the surface energy and stabilising the surface. Cl prefers a monolayer co-ordination with Si and C surface sites where the availability of Cl allows, but in cases where Cl-supply is limited you could anticipate the steric repulsion leading to a partial termination.

5.3.5 Lithium termination

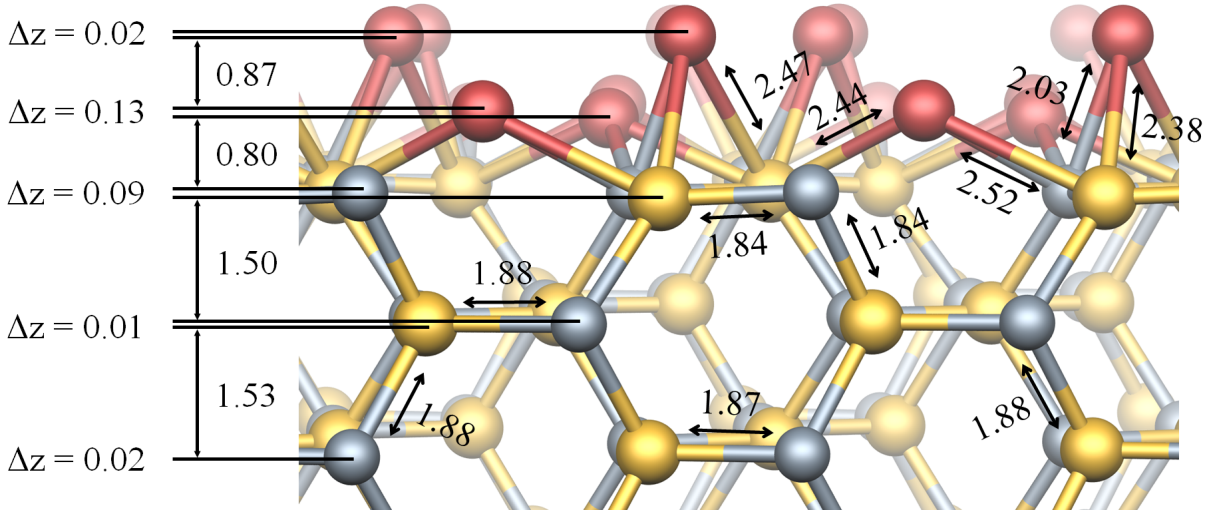

Figure 93: Schematic structure of the Li-terminated $(11\bar{2}0)$-surface (up) viewed along [0001]. Distances are shown in Å. Gray, yellow and red spheres represent carbon, silicon and lithium, respectively.

Now let's turn to a highly electropositive adsorbate species. Lithium is a light and highly reactive alkali-metal. The Li_2 bond-energy is 1.10 eV [281], and the cohesive energy of Li-metal is 1.69 eV [282]. On the basis that Li is monovalent, in line with H, F and Cl the SiC surface is saturated with one Li atom per surface site. The adsorption energy of just 0.77 eV (Table 16) reflects a relatively weak bonding to the surface, and since the covalent radius of Li is 43% greater than the average of Si and C, the low binding energy may be a consequence of Li–Li interactions in the adsorbate layer.

The optimised Li-termination forms a relatively complex arrangement. Alkali-metals such as lithium are known to induce novel surface reconstructions [283, 284] on semiconductors with elaborate surface geometries. Bulk lithium metal at room temperature preferentially orders itself in a body-centred cubic structure where it co-ordinates with 8 adjacent lithiums [285]. Small lithium clusters of Li_n $(n = 2 - 8)$ have received significant theoretical and experimental focus, but their seemingly straightforward geometry and electronic properties are still in debate [286, 287, 288] as the element transitions from diatom to bulk metal.

For the equilibrium structure, the Li–Li interatomic distances lie in the range of 2.47–2.68 Å, considerably shorter than bond lengths of 3.04 Å in bcc metal and 2.69–3.21 Å in the small clusters [286, 288]. The calculated C–Li and Si–Li bond lengths are in the ranges of 2.01–2.23 Å and 2.37–2.52 Å respectively, which agree well with calculated geometries of lithium on diamond and silicon surfaces [238, 289], providing some support for the reliability of the properties obtained for Li on SiC. Based upon the structure, it seems more appropriate to interpret Li-termination as a

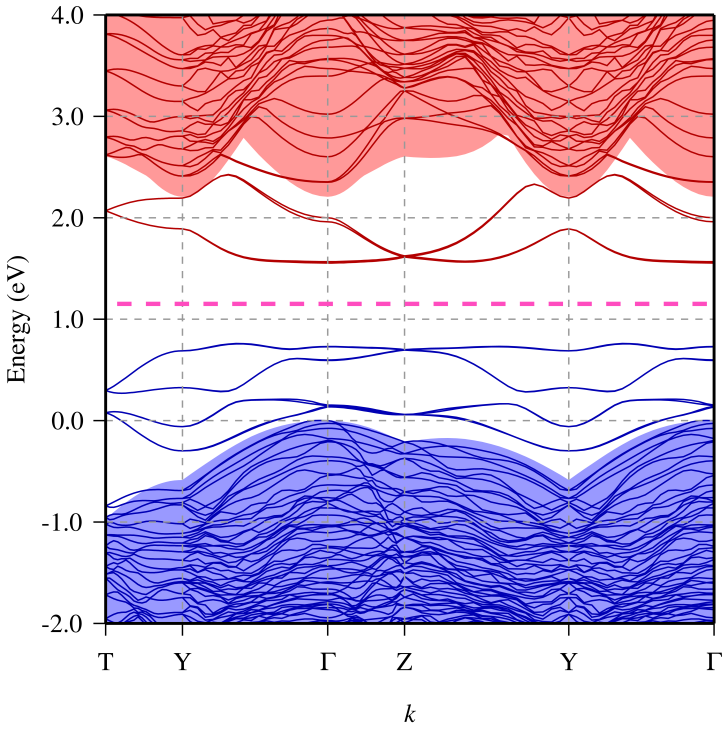

Figure 94: Electronic band structure of the $(11\bar{2}0)$ fully lithiated 4H–SiC surface. Scales, colours and lines are as for Figure 82.

series of stronger individual reactions with the surface moderated by weaker Li-Li interactions. Indeed, analysis of the electrostatic potential along chains of Li atoms reveal no substantial charge density, meaning there is no evidence of any direct Li-Li chemical bonding.

Lastly, the electronic and electrical properties of Li-termination are presented. Figure 94 shows introduction of several surface bands, but there is a clear energy gap between the occupied and empty bands. The nature of these bands are further expressed through Figure 95(a). The occupied states in the 0.0–1.0 eV are predominantly of *s*- and *p*-character. Figures 95 (b) and (c) shows the orbital description of the occupied resonant peaks in the lithium surface layer. These states have equal contributions from lithium and carbon atoms belonging to the immediate surface layer below. Orbitals pertaining to yet not centred on lithium atoms are observed in the regions between them. Previous studies [288, 290] on small lithium clusters reveal the electrons localise in interstitial regions of 6-atom planar structures, giving further credence to the idea of weak Li-Li interaction. Generally, the occupied and unoccupied surface bands in the 0.0–2.0 eV region of Figure 94 are delocalised, distributed over the whole lithium layer interstitially, and attenuating relatively slowly into the SiC slab.

Li has one of the lowest values of electronegativity of 0.98 [241], much lower than both Si and C. This would suggest in a simple pairing between Li adsorbates and unsaturated surface Si and C atoms, that a set of dipoles directed into the surface would form, reducing the potential difference between the SiC and vacuum, as seen in lithiated diamond and silicon [238, 47, 291].

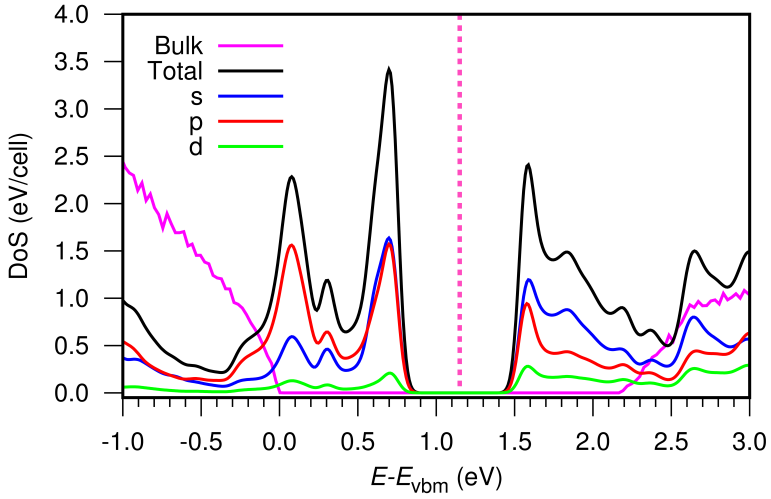

(a)

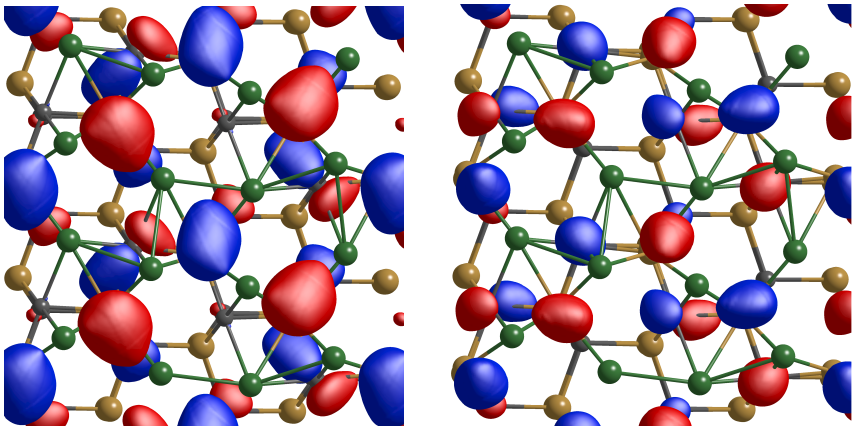

(b) (c)

Figure 95: pDoS spectra for the lithium surface layer (a) including a breakdown by orbital angular momentum. The DoS for bulk SiC is included as a reference to the band-gap. Zero on the energy scale is the valence band maximum. Pink dashed line denotes Fermi level E_f. Plots showing the isosurfaces of the 0.08 eV (b) and 0.7 eV (c) peaks of (a) as viewed down the $(11\bar{2}0)$. Dark-green, dark-gray and yellow spheres represent lithium, carbon and silicon respectively.

The EA calculated for the equilibrium structure shown in Figure 93 is just 0.08 eV (Table 16). This represents an immediate gain in the context of emission, where a near zero or negative electron affinity (NEA) facilitates the spontaneous emission of electrons at the bottom of the conduction band into vacuum. Given the relatively shallow [292] donor energies of n-type doped SiC, one can envisage this could achieve an increase in efficiency and efficacy of emitters and the applications there-in.

5.3.6 Conclusions

Density functional calculations are performed, analysing the properties of 4H–SiC $(11\bar{2}0)$ surfaces terminated by a range of elements suitable for technological applications.

Each surface is covered by one full monolayer of the terminating species. Despite each species reacting exothermically with the unterminated SiC surface, realising some of these structures in experiment may be technologically challenging. Hydrogen and fluorine appear to be the most plausible as the former has been shown to be possible [278] in experiment already and the latter represents such a large energy gain with a comfortably packed surface arrangement. With particular respect to Cl however, the strained nature of Si-Cl atoms and the relatively weak surface energy gains of 1.41 eV/surface site suggest strong steric interactions might favour a partial or mixed termination with another species. Lithium too may encounter the same limiting factors surrounding the relatively weak exothermic reaction of the disordered lithiated surface with SiC, and raise concerns over fabrication of a full monolayer and or the longevity of such a device in the extreme environments in which SiC excels.

In the context of electron affinity, hydrogen lies at the mid-range of electronegativities. The impact upon electron affinity results from a mixture of inward and outward pointing electric dipoles. As a result, the difference between hydrogenated and unterminated SiC is not so large as to represent a major technological gain in the areas of which EA factors.

Halogen termination produces uniformly outward pointing dipoles leading to very high and positive EAs. Large PEAs by termination of fluorine have previously been explored as a way of charge state control of the NV centre in diamond [293]. Vacancies in SiC [294] have been identified that have similar optical and electrical properties to diamond NV that too could benefit from chemical termination thus qubit optimisation.

In contrast, lithium termination leads to large inward pointing dipoles, and it can be seen that for full termination by Li the electron affinity effectively vanishes. Where EA plays a direct role, field emission [295] becomes more efficient with low or negative EA. Cold cathode emission is a favourable efficiency advantage for applications such as charge neutralisation for spacecraft [296, 297] and flue gas abatement [298, 120].

5.4 Polar Surfaces

Like many compound semiconductors such as GaN, AlN, PbSe, GaAs and numerous others, 4H–SiC is a polar material. In the [0001], each atomic layer is comprised of only one element, meaning adjacent layers in the same plane will be of a different species. Carbon has an electronegativity of 2.55 to silicon's 1.90. Much like the theory behind terminating species mentioned in Section 3.7, charge is drawn from the silicon to exist closer to the carbon atom creating an electric dipole that points towards the carbon atom (Figure 96).

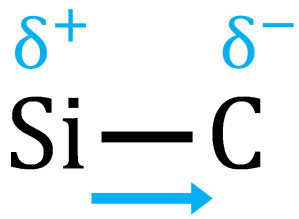

Figure 96: A silicon carbide molecule existing in the [0001] direction.

Speaking more generally, if we imagine a system of dipoles where there are equal and opposite sets of alternating charges in a 1D sequence where a unit cell is defined as one positive and one negative charge set. According to Figure 97 choosing either the red or blue unit cells will necessarily flip the direction of the electric dipole.

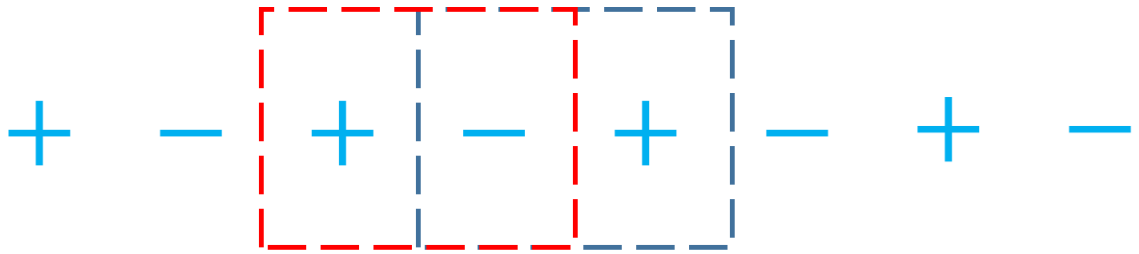

Figure 97: A set of equal and opposite charged in a one dimensional system.

If the blue unit cell is chosen then there is a dipole across the structure of:

$$p = q * d \tag{34}$$

where p is the given dipole with a total charge of q seperated by the distance d, and if the red unit cell is chosen the dipole is $p = -q * d$. The properties defining of an infinitely large system in this case can not be contingent upon the choice of origin, therefore no electric field is present across a bulk polar structure.

Only when a surface is introduced to the system does this dipole picture become relevant. The rationale is thus: Figure 97 represents a one dimensional infinite chain of equal positive and

negative charges, like one might expect in the polar directions of bulk 4H–SiC. The unit cell of this system is a positive and negative pair of charges. Adjacent unit cells must be identical under the periodic boundary condition.

Introducing a surface defines the origin and interrupts the periodicity, necessitating an inequivalence in the cell at the two surfaces and the introduction of an electric field. Periodic boundary conditions in all three directions then demands that a permanent electrical dipole exist across the material in the directions which exhibit the mono-species layers, including those of the c–axis: (0001) and (000$\bar{1}$). This electric field must be offset across the vacuum (Figure 98) to cancel out that electric field across the slab; preventing a net dipole accumulating across an infinitely repeating system.

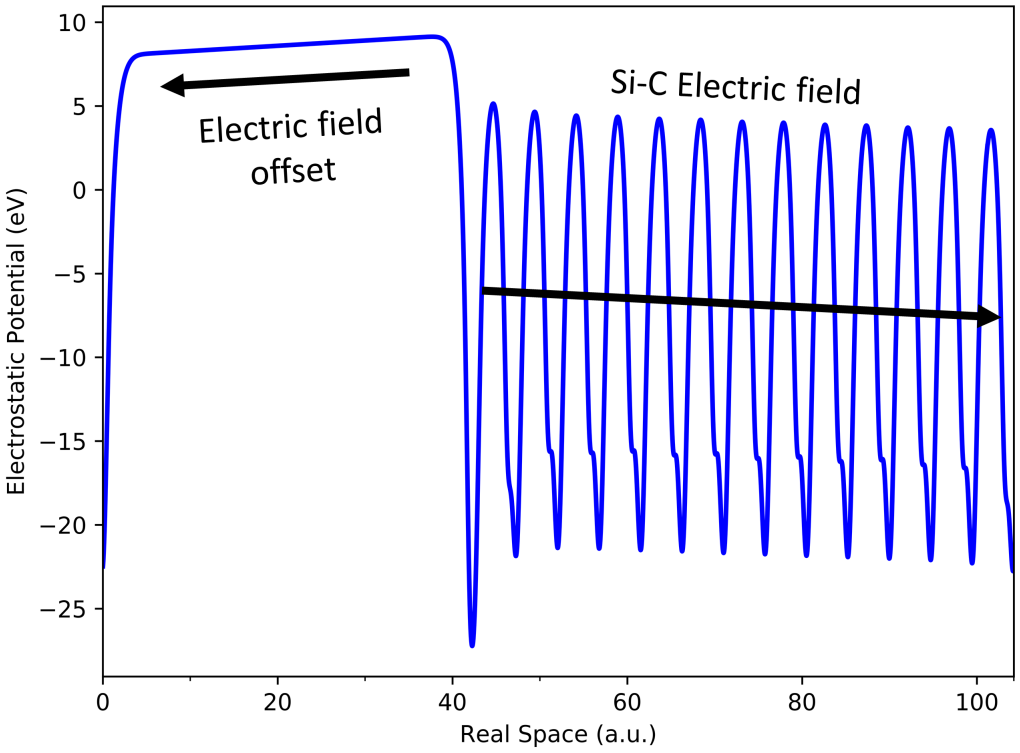

Figure 98: Electric field arising from dipoles in the polar (0001) direction across the structure and the same electric field being offset across the vacuum.

5.5 (0001) and (000$\bar{1}$) Surfaces

Some previous studies aiming to address the issue of spontaneous electric polarisation have introduced additional difficulties. For example, Refs. [299] and [206] propose the use of group-IV layers in the middle of the slab to artificially enforce inversional symmetry not present in polar materials. Lattice matching the polar material and the group-IV layer is not generally possible, and mismatched lattices introduce strain affecting electronic structure and geometry. A popular approach implemented by several researchers [300, 301] utilises pseudo-hydrogen with fractional charges and/or altered surface-adatom distances in conjunction with a self-consistent correction scheme [302] to eliminate the electric-field in the vacuum. Such additional chemical components introduce challenges in systematically modelling different surface terminations.

The impact of slab and vacuum thicknesses on electronic structure has not been widely evaluated. Due to the bulk polarisation, increasing the slab thickness increases the potential difference between the surfaces, reducing and ultimately eliminating the band-gap. It is not clear that the choice of slab thickness is always considered or justified in this respect. To our knowledge, no study so far has addressed a large data set composed of structures many lattice constants thick, with particular emphasis on adsorbates and how they may influence choice of underlying slab size. Ideally a consistent and broadly applicable method independent of cell parameters would permit accurate and comparable surface species analysis with experiment. This work attempts to further the methodology and shed light on key structural choices. We report the results of density-functional modelling of polar 4H–SiC surfaces, presenting computed values of EAs for H-, F- and Cl-terminated surfaces.

5.5.1 Method Specifics

Kohn-Sham functions were expanded using atom-centred, independent *s*- and *p*-type Gaussian orbital functions [276] of four widths for H, with the addition of two sets of *d*-type orbitals for Si, C, Cl and F to account for polarisation. This amounts to 16 functions per H atom and 28 per atom in all other cases. (0001) and (000$\bar{1}$) surfaces were made up from non-primitive, orthorhombic cells with in-plane lattice vectors along [11$\bar{2}$0] and [1$\bar{1}$00]. All surface cells have two-dimensional Brillouin zones due to confinement along the *c*-axes, and were sampled using 10×6 in-plane MP-sampling.

Cells ranging in thickness from $3c$ to $16c$ with 70 a.u. of vacuum were constructed. For the $6c$-thick slab vacuum thickness was also varied in the range 70–260 a.u.. Unterminated surfaces remained unconstructed with their primitive (1×1) footprint (Figure 99).

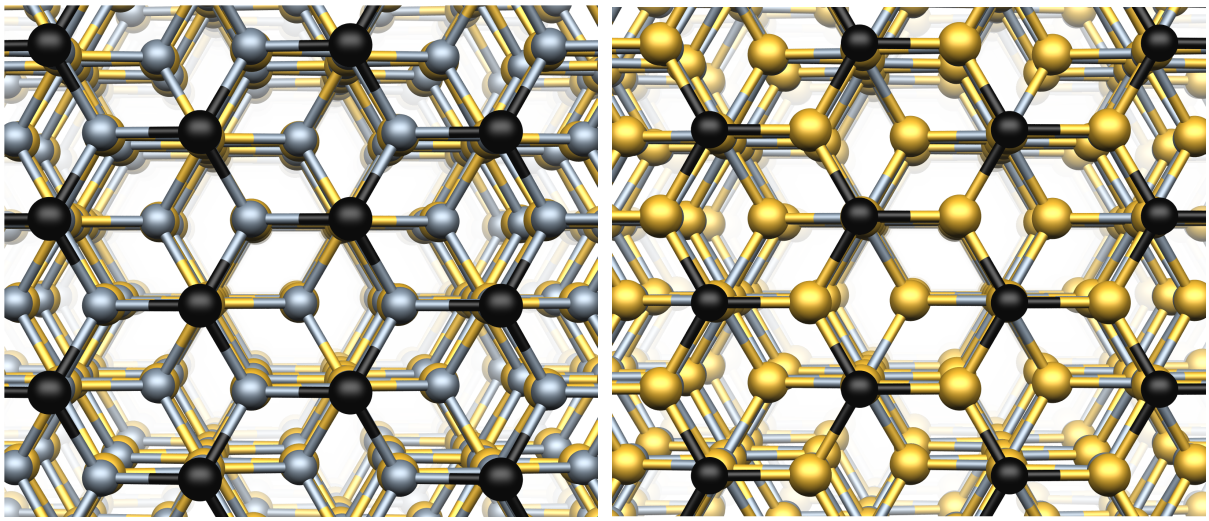

(a) (b)

Figure 99: Plan views of (a) the (0001) Si-terminated and (b) the (000$\bar{1}$) C-terminated 4H–SiC surfaces. Dark-grey, yellow and black spheres represent C, Si and surface sites, respectively.

5.5.2 Electron affinity calculations

The standard method for determining a surface EA based upon aligned electrostatic potentials (Section 3.7) suitable for non-polar cases is problematic for polar cases where there are electric fields within each slab and vacuum. Figure 100 illustrates the underlying gradient in the bulk and slab cases.

As there is a cancelling electric field in the vacuum, the periodic potential varies with an underlying triangular waveform.

For triangular potentials where the vacuum potential is not well defined, one could approximate an EA as the difference in energy of the conduction band just inside the SiC and the vacuum just outside. In practice one might *post hoc* add a constant electric field cancelling the vacuum field exactly to obtain a constant potential in the vacuum region. Addition of a cancelling field everywhere results is a series of vacuum potentials separated by twice the potential difference across the original SiC slab.

Alternatively a field can be added to cancel the field inside the SiC, as illustrated in Figure 101. The valence-band maximum and conduction-band minimum inside the slabs are position dependent, but their values close to the surfaces can be obtained by comparison with the bulk electrostatic potential in a fashion similar to that for non-polar cases [202]. The vertical lines in Figure 101 indicate the points where the charge density has decayed to negligible value. The energy difference between the conduction band minimum and where these vertical lines cross the electrostatic potential is the estimate of the local EA. This approach is termed the triangular

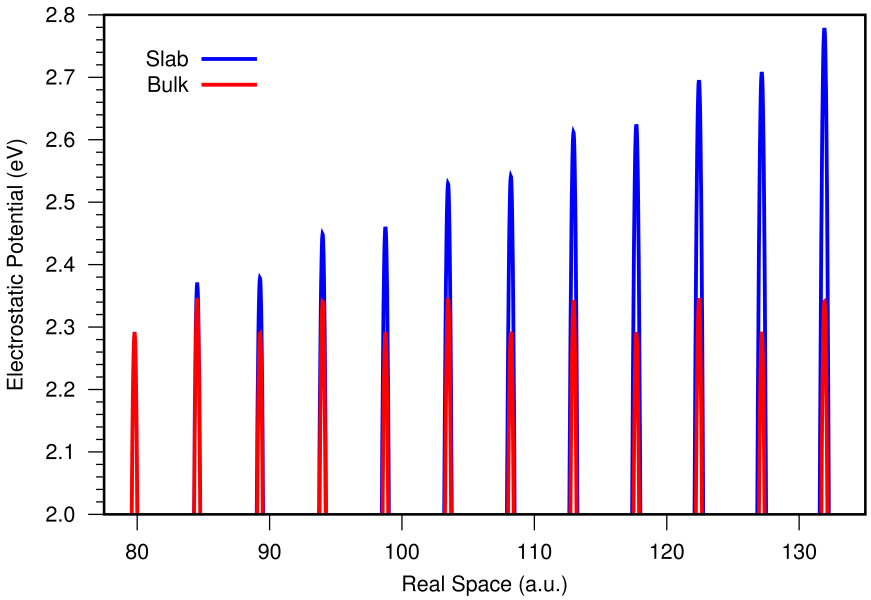

(a)

Figure 100: Illustrative plot of the in-plane average electrostatic potential as a function of position along the [0001]-direction. The red, bulk 4H–SiC case shows simple periodic oscillations with a peak corresponding to the points between SiC bilayers. The corresponding potential for H-terminated slab (blue curve) shows the same oscillations superimposed upon a linearly increasing background corresponding to the electric field across the slab.

potential method.

The vacuum electric field can also be eliminated by construction of periodic systems with pairs of slabs alternating between [0001] and [000$\bar{1}$] along z. These are referred to as back to back (b2b) systems. This approach has the disadvantage of doubling the system size, significantly increasing computational load. Although there is no net dipole, since each slab has an internal electric field the pairs form an electric quadropole so there are alternating positive and negative electrostatic potential steps between constant vacuum potentials along [0001] (Figure 102). The EAs can be obtained from b2b calculations by fitting the bulk electrostatic potentials in a similar fashion to the triangular potential cases.

To explore the use of triangular potential and b2b geometries in determination of EAs, including the roles of the slab and vacuum thicknesses, electrostatic potentials for a wide range of conditions are analysed. Results and analysis are presented first for a triangular potential system and then for b2b for each termination type as a function of vacuum thickness then slab thickness.

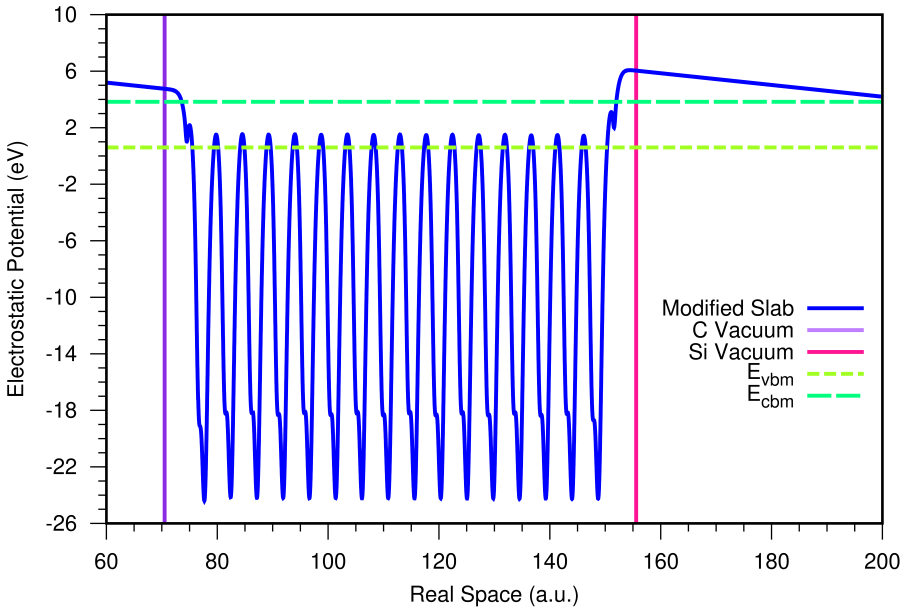

Figure 101: A plot of the modified in-plane average electrostatic potential for 4c-thick 4H–SiC terminated by H. The C and Si faces are at the left and right ends of the plot, respectively. The vertical lines indicate the nominal limits of the charge density of the slab, and the horizontal lines show the location of the valence-band maximum and conduction-band minimum as inferred from the potential alignment method.

5.5.3 Si and C termination

Si- and C-terminated surfaces are constrained in our calculations to 1×1 structures, resulting in one dangling bond per surface atom. Figure 103 illustrates the optimised surface geometries, showing a significant relaxation, particularly on the $(000\bar{1})$ face. Bondlengths and displacements are consistent with previous theoretical work on unterminated 4H–SiC surfaces [303, 304].

The band structure of the unterminated 6c-thick slab is shown in Figure 104. The narrowing of the band-gap for the surfaces is a consequence of the built-in electric field, so the conduction-band minimum for the slab corresponds to the opposite surface for the valence-band maximum. In the 0.0–0.7 eV range there exist two pairs of surface states. The electron chemical potential crosses the surface states in this energy range, so the 1×1 surfaces are metallic.

The pDoS for layers in the vicinity of the two surfaces are plotted in Figure 105. The peak in the Si-face pDoS is 0.1 eV higher than that of the carbon face, and slightly broader. A stronger electronegativity on the carbon surface atoms and more spatially diffuse orbitals, particularly in the directions parallel to the surface normal, explain these differences, with similar states observed for 6H-SiC (0001)-(1×1) surfaces [305]. Analysis of the valence-band maximum orbitals indicates a significant overlap between surface and bulk states centred on carbon atoms, consistent with previous studies [306]. While both faces exhibit surface states dominated by p-

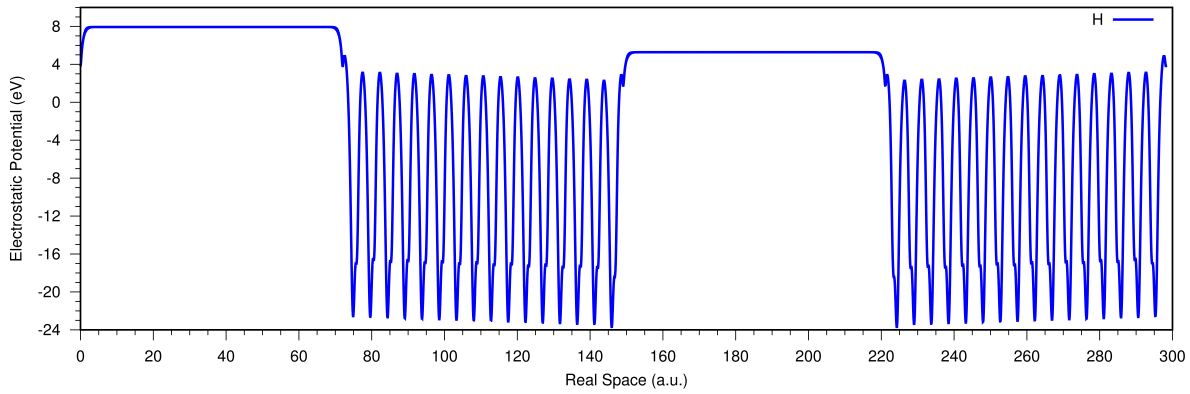

Figure 102: Illustration of the in-plane averaged electrostatic potential for a pair of 4c-thick 4H–SiC H-terminated slabs within the back to back model, showing the two non-equivalent vacuum regions.

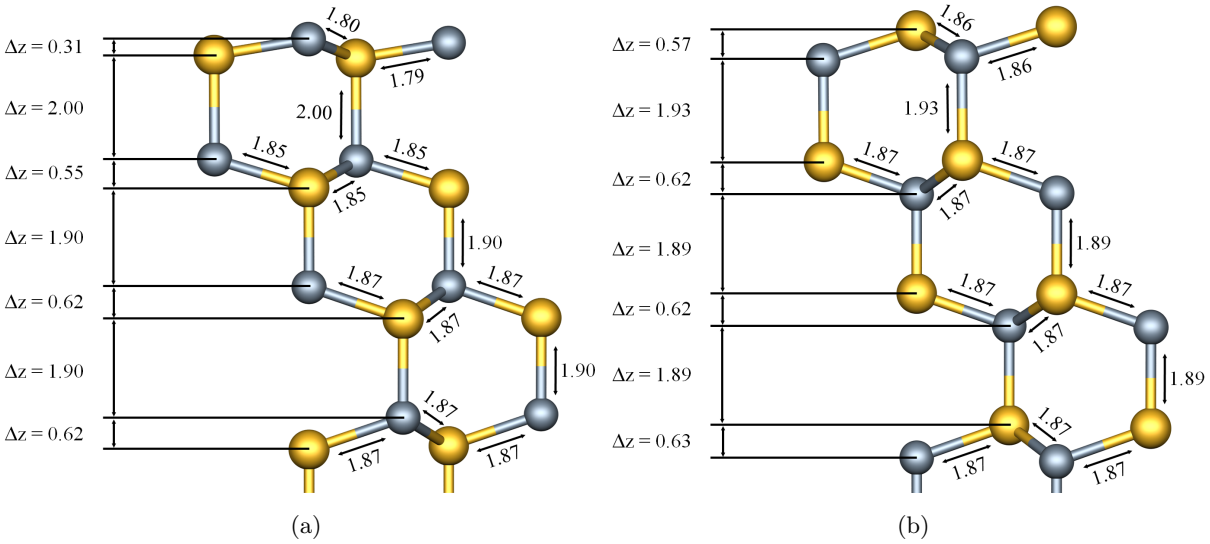

Figure 103: Structure of (a) the $(000\bar{1})$ and (b) the (0001) unterminated surfaces. The vertical directions are along the surface normal, so the surface is at the top of each image, and the horizontal is $[\bar{1}100]$ and $[1\bar{1}00]$ for (a) and (b), respectively. Bondlengths are in Å. Gray and yellow spheres represent carbon and silicon atoms respectively.

contributions, we find that the surface states extend relatively deeper into the C-face, consistent with these bands lying closer to the valence-band maximum in the adjacent region of the slab than for the Si-face.

Modelling of unterminated 4H–SiC forms a baseline for the investigation of chemically satisfied cases, and the impact on the slab and vacuum variables, and it is on these that focus is subsequently placed.

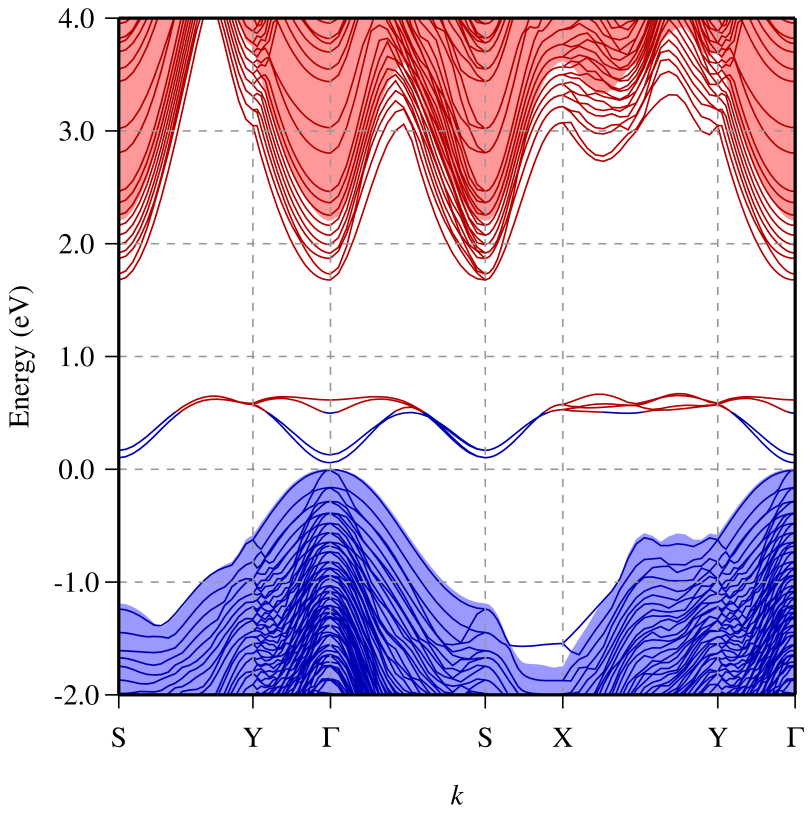

Figure 104: Electronic band structure in the vicinity of the band-gap of a 6c-thick unterminated 4H–SiC slab along high symmetry branches of the two dimensional surface Brillouin zone. k-axis labels follow Ref. [248], with the $[11\bar{2}0]$ and $[\bar{1}100]$ directions corresponding to the S–Y and Γ–Y branches, respectively. The energy scales are defined with the valence band top at zero, with occupied and empty bands shown in blue and red, respectively. The underlying shading shows the envelope for the corresponding bands of bulk 4H–SiC.

5.5.4 Vacuum Thickness - Triangular potential

The space between periodic images has to be sufficient to ensure no significant overlap of the evanescent surface states and produce a linear potential. However, an excessively wide vacuum impacts computation time. Periodic boundary conditions (Section 3.6) applied to the non-centrosymmetric polar systems leads to electrostatic interactions between images, irrespective of vacuum size. Figure 106 shows that the electric field across the slab, E_{slab}, converges to different values depending upon the terminating species. This shows significant image-image electrostatic contributions to E_{slab} for vacuum thicknesses.

Additionally much larger vacuum thicknesses were also examined, and the results are listed in Table 17. It can be seen that from 500–1500 a.u. data, the values of the field across the slab are far from converged even at 250 a.u..

The magnitude of the electric field across the vacuum is such that it cancels the potential

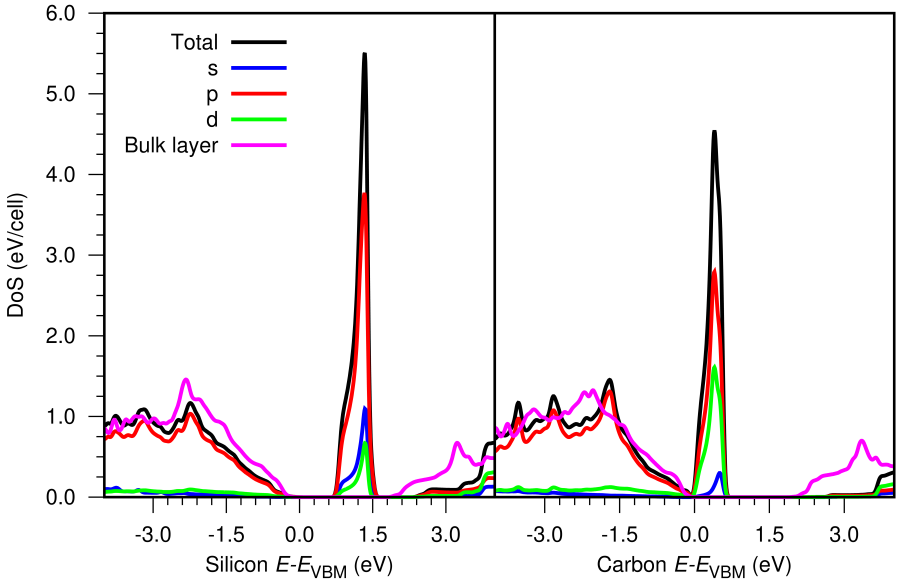

Figure 105: pDoS for the Si-terminated (left) and C-terminated Si (right) surface bilayers, including contribution by orbital angular momentum. The corresponding pDoS of a mid-slab bilayer 10 bilayers from each respective surface is included as a bulk-SiC reference. Zero on the energy scale is both the valence band maximum for the bulk-like and surface bilayers.

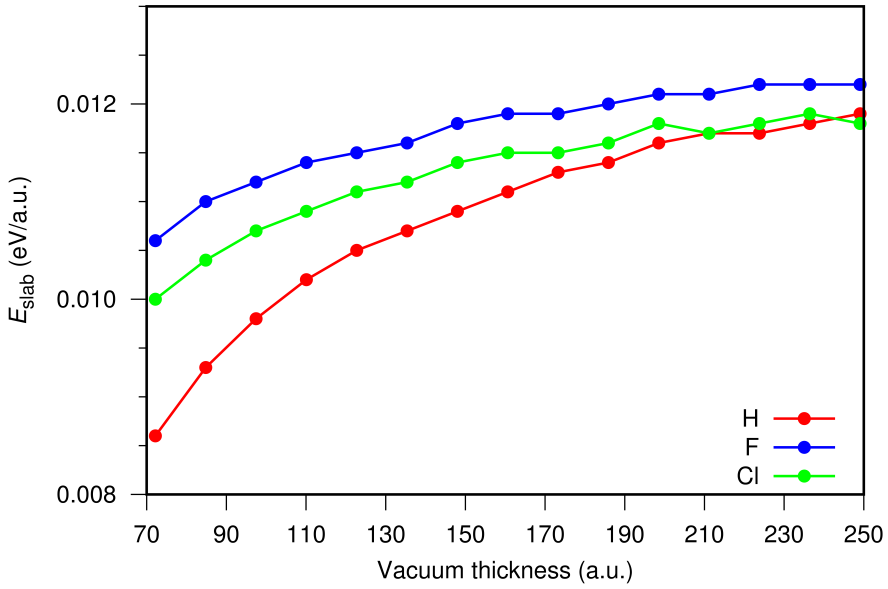

Figure 106: Magnitude of electric field across the 6c-thick slab as a function of vacuum thickness in a triangular potential system for different chemical terminations.

difference across the slab. Naturally, for a fixed slab the electric field across the vacuum, E_{vac}, must tend to zero as a function of vacuum size. Figure 107 shows this trend.

Figure 108 shows a plot of the potential across the vacuum, ΔV_{vac}, as a function of vacuum thickness. It reveals a modest increase over the range, consistent with the changes in E_{slab}.

Table 17: E_{slab} (V/a.u.) as a function of vacuum thickness for H, F and Cl terminated triangular potential calculations.

Vacuum (a.u.)	H	F	Cl
500	0.0128	0.0128	0.0125
1000	0.0133	0.0130	0.0129
1500	0.0135	0.0131	0.0127

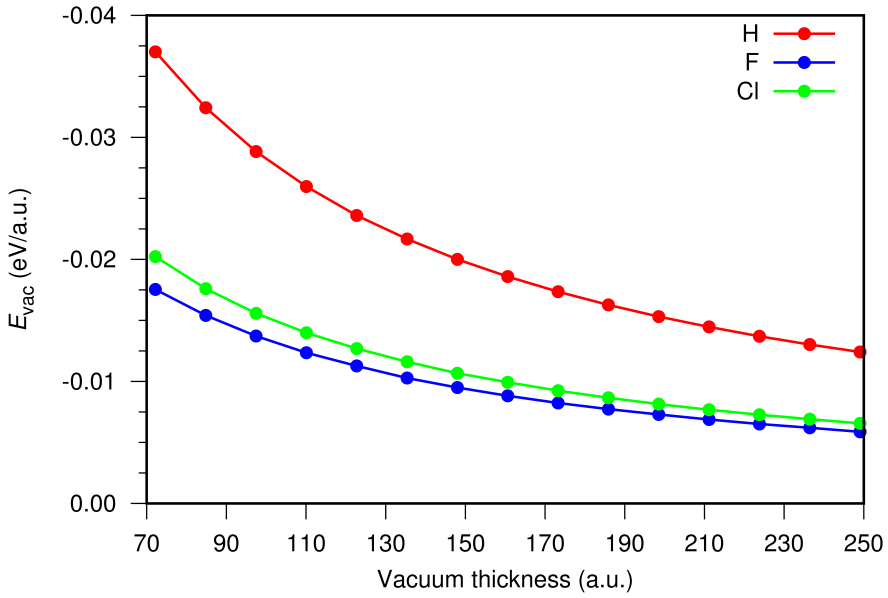

Figure 107: Magnitude of electric field across the vacuum for a 6c-thick slab as a function of vacuum thickness in a triangular potential system for different chemical terminations.

5.5.5 Vacuum Thickness - Back to Back

Now presented are the results from b2b structures. Figures 109 and 110 show E_{slab} and ΔV_{vac}, respectively, for the b2b simulations. In contrast to the triangular potential the values are essentially independent of vacuum width.

The b2b values are consistent with the data in Table 18. H-termination produces the largest electric field of the cases examined. This is consistent with the surface dipoles in each case: for H-termination they point in the [0001] direction due to H having an electronegativity between those of C and Si, whereas for F and Cl the surface dipoles are all directed towards the vacuum, so partially cancel out. The trend of the triangular potentials to converge to those of the vacuum-thickness independent values of the b2b model (Figures 109 and 110) strongly advocate the use of the b2b approach to mitigate vacuum thickness effects.

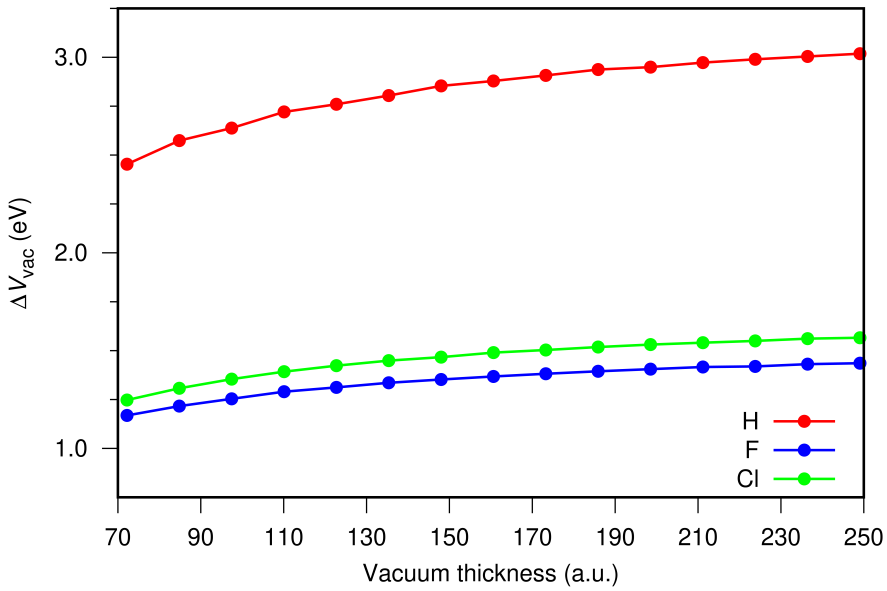

Figure 108: Potential difference across the vacuum as a function of vacuum thickness in a triangular potential system with the 6c-thick slab for different terminating species.

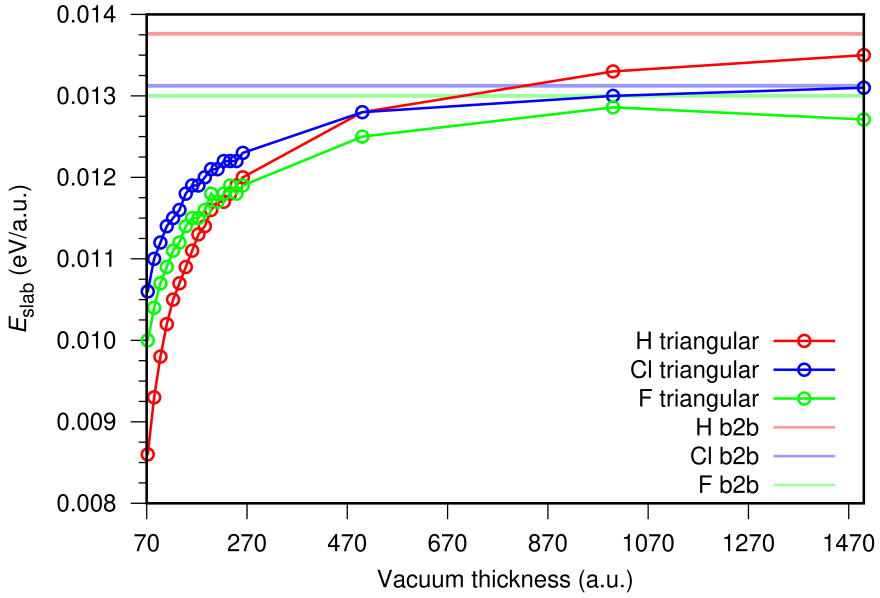

Figure 109: Magnitude of electric field across the slab for the 6c-thick slab as a function of vacuum thickness for the b2b model for different terminations. Values for the triangular potentials (Figure 106 and Table 17) are included for comparison.

Moving on from vacuum thickness, the dependence of derived properties on the thickness of the polar material is discussed.

5.5.6 Slab Thickness - Triangular Potential

One might seek to converge properties of surface by increasing the thickness of the underlying crystalline material. For non-polar materials such an approach is limited only by the computa-

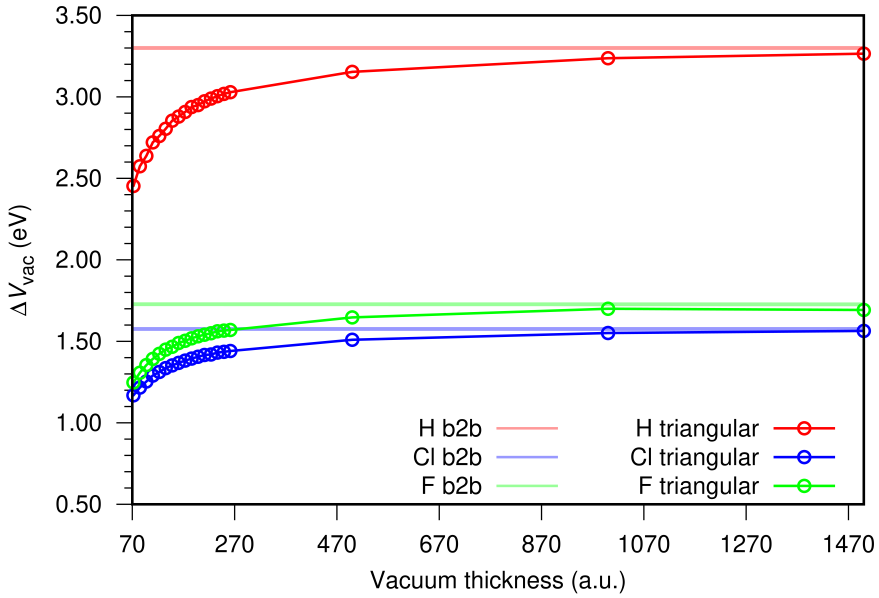

Figure 110: Potential difference across the vacuum as a function of vacuum thickness in a b2b system with the 6c-thick slabs for different terminating species. Values for the triangular potential (Figure 108) are included for comparison.

tional effort required. For polar materials we generally still seek structural models that converge, for example, surface geometry, and the underlying crystal structure should closely match the equilibrium geometry of the bulk material. However, polar materials potentially possess an upper limit of slab thickness, since the band-gap narrows and ultimately vanishes with thickness. When the valence band maximum at one surface lies higher in energy than the conduction band minimum at the other, charge transfer will occur. Figure 111 shows this narrowing of the band-gap, and for all terminations there is a reduction in the band-gap with thickness.

The magnitude of the band-gap for a given slab-thickness is termination-species dependent. For Cl-termination the band-gap vanishes for a relatively thin slab, being around 11c for the triangular potential method. In comparison, for F-termination this occurs at around 16c, and for H-termination a band-gap is present for all thicknesses examined. The physical origin of the termination-dependence lies in the existence of surface states in the case of halogen termination, which are absent for H-termination [307].

The pDoS for the Cl-termination (Figure 112) reveal a number of key features. The Cl pDoS on each surface exhibit a sharp peak followed by a hard shoulder and drop-off to 0 eV/cell at higher energies. The shape is similar in nature to that observed in 2D materials such as graphene [308] and hexagonal boron-nitride [309]. The prominent surface-state peaks are predominantly lone pair Cl-centred p-orbitals with small contributions from the top-most SiC layer (Figure 113).

It is useful to examine the correlation of the host bands with the surface states. When the $(000\bar{1})$

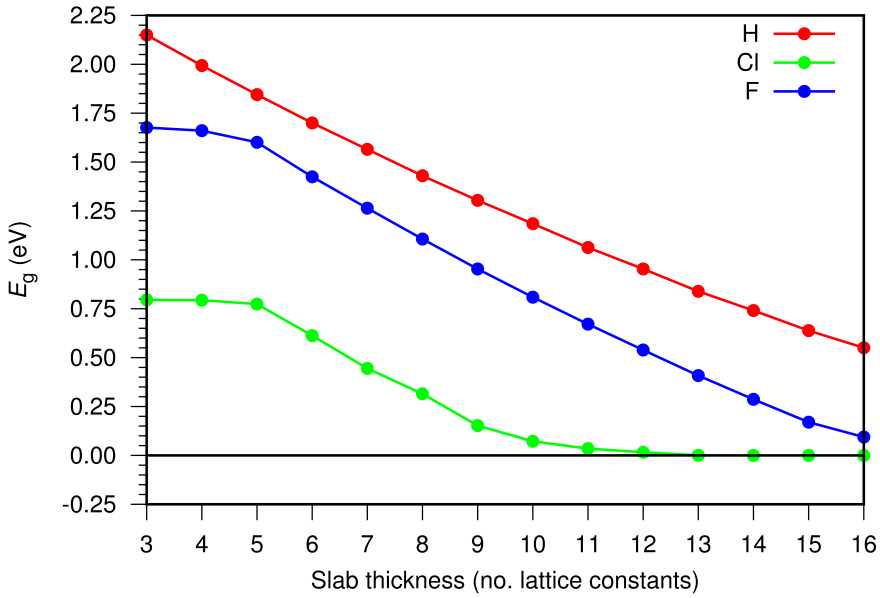

Figure 111: Band-gap as a function of slab thickness for different terminations for the triangular potential model.

surface-states are fixed at zero (Figure 112(a)) the peaks for the (0001) surface-states shown in shades of blue between around $-0.2\,\text{eV}$ to $1.0\,\text{eV}$, that track with where the valence band DoS vanishes (shades of grey) which co-incendently cover the same energy range. The (0001) surface-states (blue peaks) increase in energy in approximately equal increments until the slab thickness coincides with disappearance of the band-gap (Figure 111) at $11c$ (ninth peak). For greater slab thicknesses the charge transfer between the two surfaces offsets any further shift in the relative position of the surface states.

An additional feature of Figure 111 is also explained by the pDoS. Figure 111 shows the band-gap as approximately constant up to $5c$. For the relatively thin slabs the (0001) surface-states are lower in energy than those from the $(000\bar{1})$ face. In Figure 112(a) the (blue) (0001) surface state high-energy limit only exceeds that of the $(000\bar{1})$ surface states at around $1.2\,\text{eV}$ for thicknesses exceeding $5c$. Once this happens, as the thickness increases the (0001) surfaces states continue to increase in energy relative to those of the $(000\bar{1})$ surface, corresponding to the most rapid phase of band-gap reduction in Figure 111. The same effect can be seen in Figures 112(b) relative to the (0001) surface states. The transition can also be seen in the wave functions (Figure 113); the highest energy surface states are p-orbitals centred on Cl atoms of the C face for 3 and 4 lattice constants, transitioning to Cl atoms of the Si face for all Cl-SiC slabs 5 lattice constants and above.

The general trend is repeated for fluorine termination. The highest energy occupied states are associated with F atoms on the $(000\bar{1})$ surface for slabs up to $4c$ in thickness, being overtaken in energy by the (0001) surface states for thicker slabs (the initial flat region in Figure 111). This

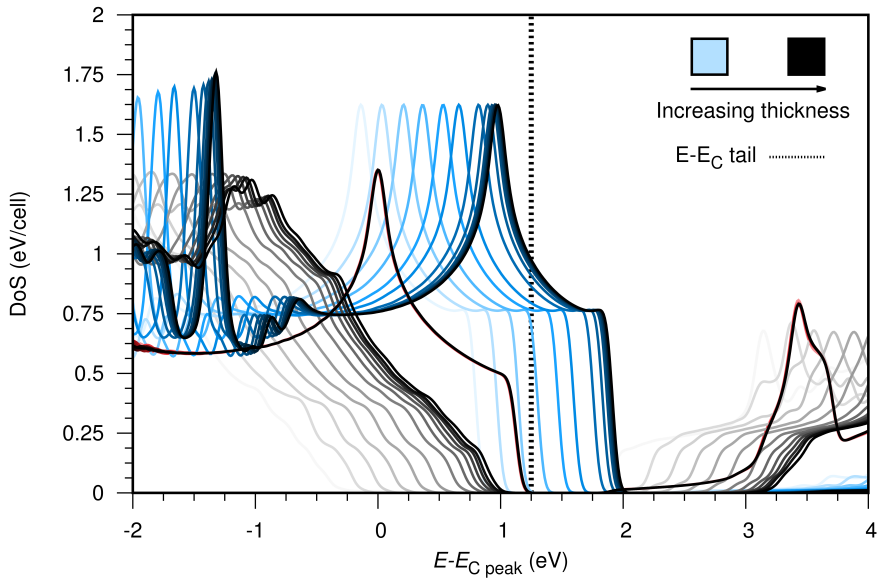

(a)

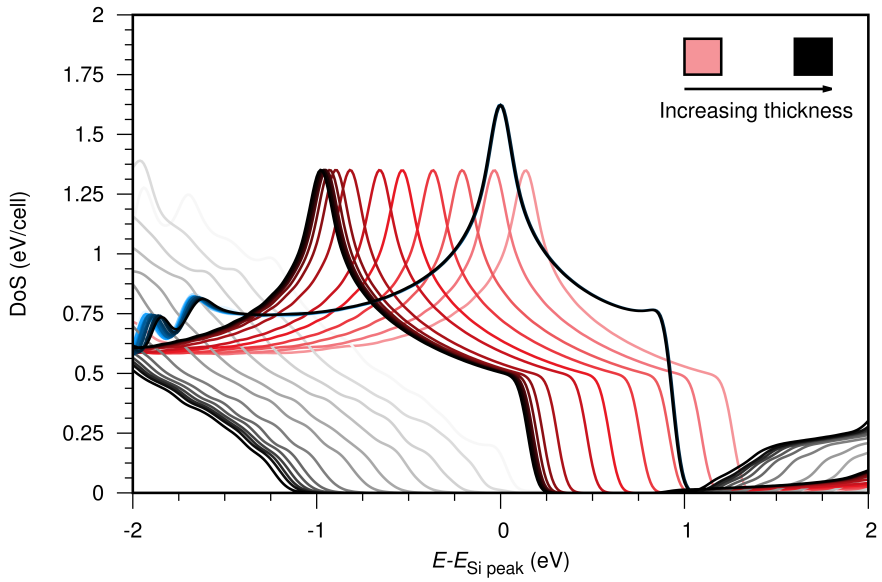

(b)

Figure 112: pDoS for Cl-terminated the C surface (red), Si surface (blue) and bulk layer states (grey) as a function of thickness. For (a), the grey bulk states are a fixed distance from the Si surface, and for (b) a fixed distance from the C surface. The zero on the energy is fixed at the peak position of the Cl surface state peak on (a) the C-face and (b) the Si-face. Slab thickness is represented by a gradient from the lightest (3 lattice constants) to darkest (16 lattice constants) in each case.

effect is absent in H-terminated surface, as there are no lone-pair orbitals in this case to form the characteristic surface states.

The three terminating species examined for this study illustrate the complex dependence of the band-gap on slab thickness and different surface states associated with the (0001) and (000$\bar{1}$)

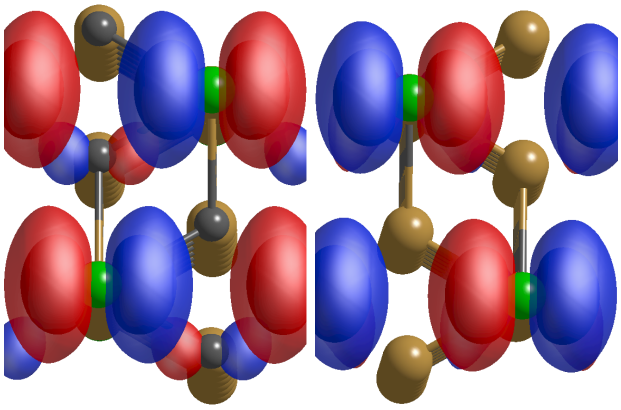

(a) (b)

Figure 113: Isosurface plots showing the highest energy surface states on (a) the silicon face and (b) and carbon face of units 0.1 a.u.$^{\frac{-3}{2}}$. Red and blue isosurfaces represent opposite wave function phases. Green, dark-gray and yellow spheres represent chlorine, carbon and silicon atoms respectively.

surfaces.

We now focus upon the regime under which the band-gap vanishes. Our calculations show that where the band-gap is eliminated, the extent of charge transfer is that which generates an electric-field in opposition of the bulk polarisation. Its magnitude is such that the associated electrostatic potential cancels out the increase that corresponding to the bulk polarisation. This effect is shown in the change of gradient at around $10c$ for Cl-termination in Figures 114, 115 and 116. Focusing on Figure 114, a consistent trend is observed from 3 to 9 lattice constants for all terminations. As the slabs increase in thickness, the proportionate contribution of the surface dipoles decreases, and all terminations show the same general trend. For Cl termination the loss of a band-gap increases the rate of decrease in electric field, and fixes the potential across the slab (and hence the vacuum) to a constant (Figure 116).

The absolute values of the electric fields and the potential drops across the slabs, ΔV, can be further illustrated in terms of the dipole size and direction on each surface, touched upon previously. Table 18 shows the direction of the electric-dipoles for each termination. The dipoles for hydrogen termination point in the same direction, and in the same net direction as the bulk polarisation. The sum of the two dipoles increase the electric field. In contrast, the fluorine and chlorine cases have surface dipoles that will tend to cancel, leading to smaller electric fields relative to H-termination, consistent with Figures 115 and 116. The magnitudes of F and Cl dipoles must be similar as they lead to very similar profiles of electric field strength and potential difference.

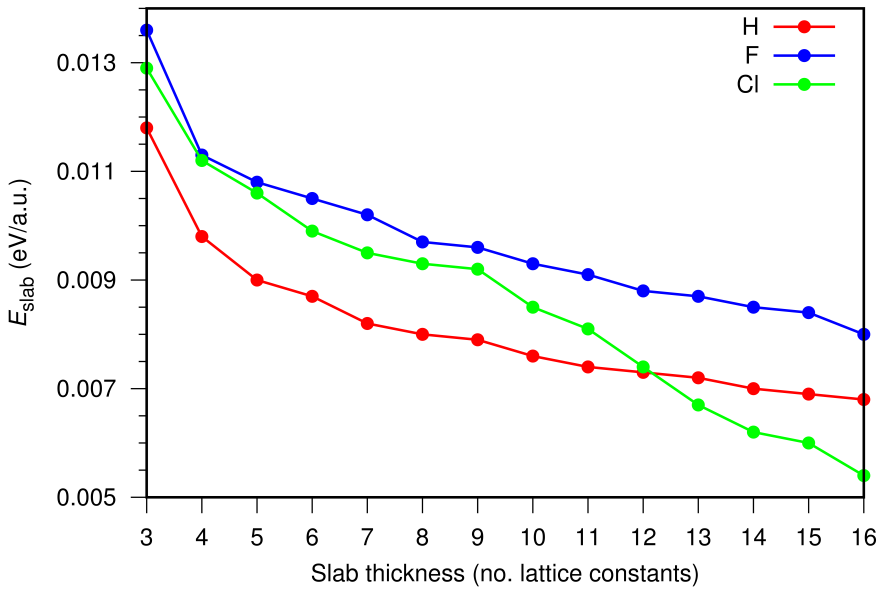

Figure 114: Magnitude of electric field across the slab as a function of slab thickness using the triangular potential approach for a fixed vacuum of 72 a.u..

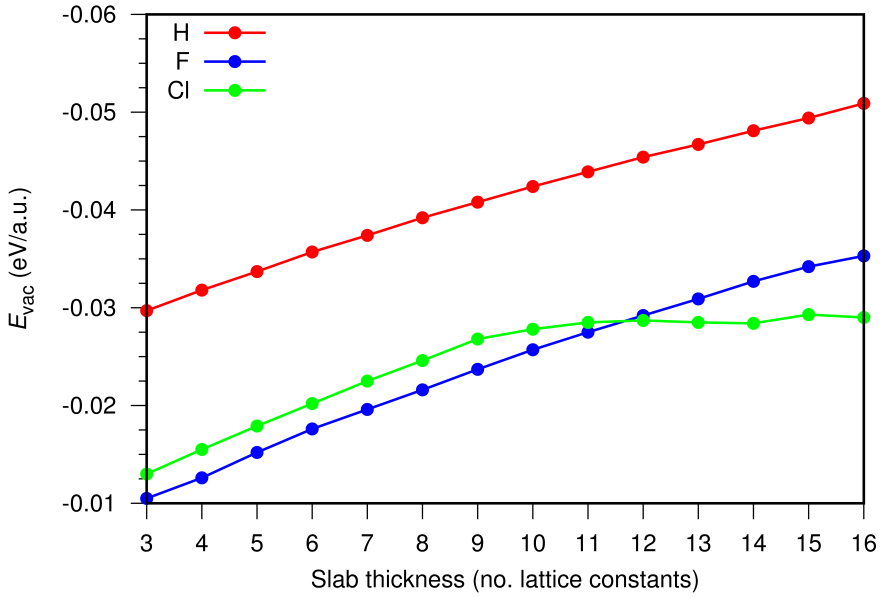

Figure 115: Magnitude of the electric field across the vacuum as a function of slab thickness using the triangular potential approach for a fixed vacuum of 72 a.u.

5.5.7 Slab Thickness - Back to Back

Some elements are common between back to back and triangular potential approaches. Although there is no electric field in the vacuum, there is inside the slabs, so there remains a slab-thickness dependence of the band-gap. We find the same general trends in band-gap as for the triangular potential approach (Figures 117 and 111), but b2b systems show a more rapid reduction in band-gap with slab thickness.

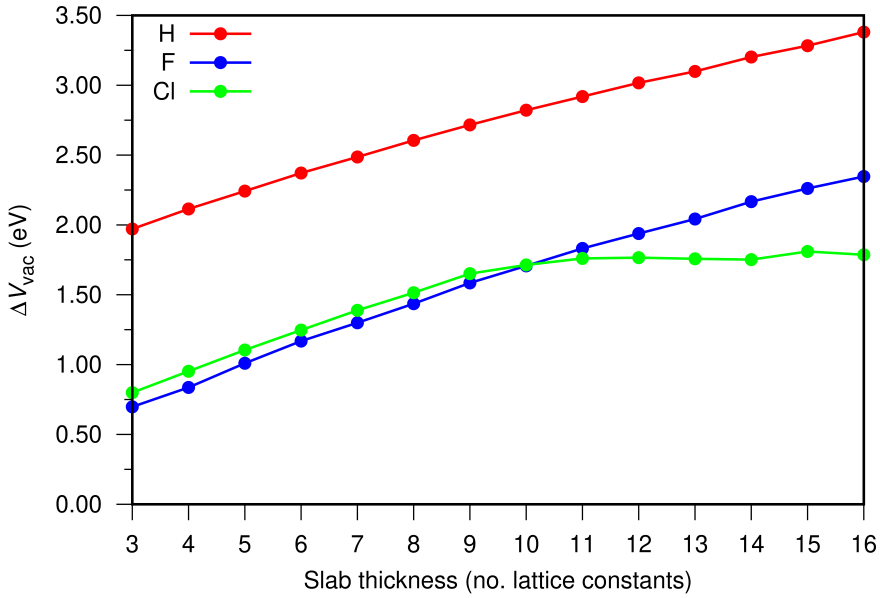

Figure 116: Potential difference across the vacuum as a function of slab thickness in a triangular potential model with a fixed vacuum size of 72 a.u.

Table 18: Dipole directions at each surface for different terminations.

	H		F		Cl	
Surface species	H-C	Si-H	F-C	Si-F	Cl-C	Si-Cl
Dipole directions	←	←	←	→	←	→

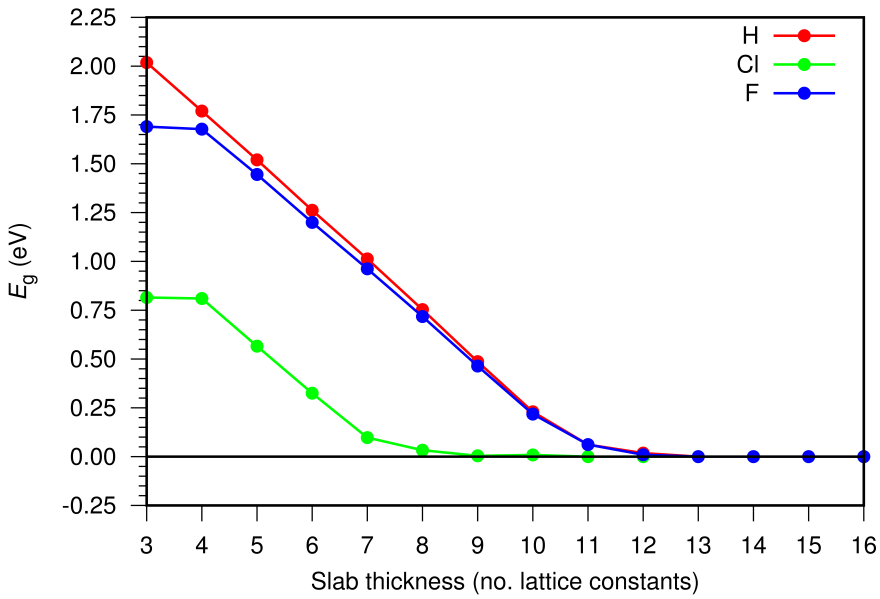

Figure 117: Band-gap as a function of slab thickness for different terminations for the b2b model.

This is a consequence of the higher electric field magnitudes in the b2b slabs, as shown in Figures 118 and 109. At all thicknesses and surface-species the electric field in the slab is higher in the b2b model than the single-slab approach with a triangular potential. Taking 6c-slabs as an example, E_{slab} for the H, F and Cl terminations with the b2b model are 0.014, 0.013 and 0.013 eV/a.u. respectively, compared to 0.009, 0.011 and 0.010 eV/a.u. for the triangular potentials. The consequences of a larger slab electric field are that the potential difference between states is higher, and their dispersion through space is larger.

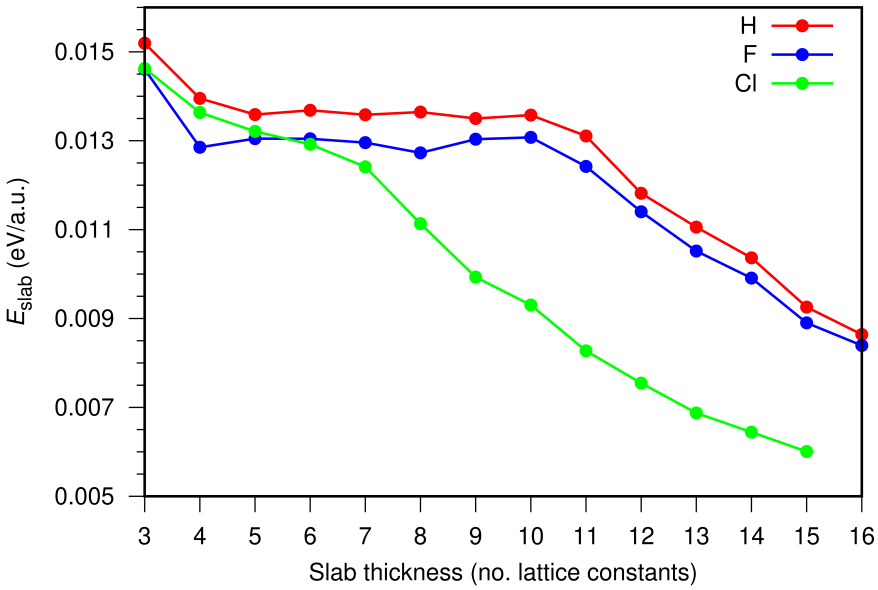

Figure 118: Electric field size across the slab as a function of slab thickness in a back to back system with a fixed vacuum size of 72 a.u.

The confinement effect can also be seen in E_{slab} values with a direct comparison between methods. In Section 5.5.6, E_{slab} values in the region of 4-9 lattice constants for Figure 114 decrease linearly for all terminations. H- and F-termination E_{slab} values in Figure 118 are both higher and more consistent with thickness compared to the same variables for the triangular method.

Taking H-surface as a specific example, Figure 114 shows that with varying thickness H-termination has the lowest E_{slab} values for all thicknesses except for when Cl becomes metallic at 10 lattice constants. However this trend is the opposite for the back to back case where in Figure 118 H-surfaces have higher E_{slab} values for all thicknesses.

5.5.8 EA Dependence

To illustrate the impact of the use of triangular potential or b2b methods, we have calculated the EA for the systems studies for this paper. The results are listed in Table 19.

Table 19 lists estimated EA values as a function of termination, slab thickness and vacuum thick-

Table 19: Electron affinity values (eV). Where two value ranges are expressed, EA for thicknesses with and without an appreciable band-gap (>0.1 eV) are represented by values outside and inside brackets respectively. The ranges are for slab thickness with constant vacuum width, and for the fixed 6c slab-thickness with varied vacuum width. There is no significant variation in EA with vacuum width for b2b calculations.

	Triangular potential		Back to Back	
Termination	Slab thickness	Vacuum width	Slab thickness	Vacuum width
	C Face			
Hydrogen	0.94–0.97	0.89–0.81	0.90–0.83 (0.81–0.73)	0.79
Fluorine	4.99–5.03	4.99–4.95	5.05–4.96 (4.96–4.87)	4.99
Chlorine	3.40–3.41 (3.41–3.37)	3.39–3.35	3.44–3.38 (3.36–3.25)	3.39
	Si Face			
Hydrogen	2.33–2.29	2.39–2.47	2.33–2.39 (2.39–2.45)	2.42
Fluorine	5.06–5.00	5.05–5.01	4.95–4.98 (4.98–5.05)	4.96
Chlorine	3.50–3.48 (3.48–3.51)	3.50–3.55	3.44–3.48 (3.49–3.53)	3.47

ness. The ranges in values indicated provide the limits accumulated over the various slab and vacuum thicknesses. For triangular potential calculation the impact of slab-thickness is modest (0.02–0.06 eV). Vacuum thickness has a greater impact (0.04–0.08 eV). For b2b calculations, slab thickness yields a more significant variation than the triangular potential approach (0.09–0.19 eV). However, the vacuum-width dependence is completely removed. The electric field in b2b slabs where band-gaps remain is much larger than in the triangular potential scheme, reducing the range of viable slab thicknesses for surface-property modelling.

5.5.9 Discussion and conclusions

Reliable methods to determine surface properties for polar materials, such as structure and electron affinity, are problematic when using periodic boundary conditions. Comparisons are made between two schemes to extract electrostatic data for 4H–SiC surfaces with different terminations. Under the assumption that complete saturation of (0001) and (000$\bar{1}$) surfaces is possible, it has been shown that relatively narrow ranges of values of electron affinity can be obtained from both a single and double slab model.

The existence of an electric field across the polar material in either model necessitates a maximum slab thickness that can be achieved before the band-gap is eliminated with the conduction band

minimum at one face to lie below the valence band top at the other. The loss of band gap makes it energetically favourable for charge to move from one surface to the other, generating an additional electric field in opposition to the bulk polarisation. In the event that the surfaces are metallic, such as in the unterminated (1×1)–(0001) surfaces, the dependence of the charge accumulation at the surface will be a combination of rearrangement of charge at the metallic surface that would be expected to occur in nature, and a transfer between opposing surfaces that is simulation-model dependent.

Although completely unterminated surfaces are of largely academic interest, less than 100% chemical termination is quite probable. For example, hydrogen termination is a species that has historically proved challenging to achieve full surface coverage [303, 310, 311]. Incomplete coverage both alters the surface dipole density affecting the extent to which electron affinity is changed compared to an unterminated surface, but also generates surface states that may be non-physically populated by charge transfer between surfaces in the event that the slab thickness is sufficiently large to eliminate the band-gap.

However, there are some general points that can be made regarding a preference between the triangular potential and b2b approaches. The latter completely eliminates the dependence of the vacuum width on the slab properties, such as electron affinity. However, the b2b method shows a more rapid decrease in band-gap with slab-thickness, so that the range of slabs for which charge transfer between the two surfaces can be safely avoided is smaller.

Furthermore, the computational cost of b2b calculations is significantly higher than the triangular potential approach. Conversely, single layer calculations that exhibit the triangular potential show very slow convergence with slab thickness of properties such as the electric field inside the slabs.

So far as the 4H–SiC specific results are concerned, electron affinity estimates for H, F and Cl termination of both (0001) and $(000\bar{1})$ surfaces are provided for the first time. The largest values are found for F-termination, being around 5 eV for both surfaces. The smallest EA is obtained for H-termination on the $(000\bar{1})$ face at around 1 eV. These values and their associated ranges would be anticipated and indeed are similar to previous 4H–SiC non-polar terminated surfaces [312] with matching surface coverage and species.

6. Final Thoughts

This project documents the potential for extreme-environment based application gains through the novel termination of both SiC and diamond. Density functional theory provides the ability to explain and, perhaps more significantly, predict experiment. Avenues of experimental research that without the underlying theory may seem too risky or costly to explore become increasingly more plausible as the wealth of theory driven data builds up behind it. This is especially pertinent for diamond, where a trial and error approach to innovation would prove very costly.

The study of aluminium oxide terminated diamond presented the relative thermal stability and EA of 3 different surfaces as a function of Al:O stoichiometry. AlO_3 adsorption produced the most exothermic reaction with the surface and the largest NEA (-3 eV). Creating such a surface experimentally would be a considerable challenge. Monolayer ALD is possible with aluminium oxide in the form of Al_2O_3 but how to achieve uniform fractional monolayer coverage is a potential source of further theoretical and experimental endeavour. As the concentration of aluminium increased on the surface so did the chance of Al-Al bonding in the plane parallel to the surface, reducing dipole polarity leading to a positive EA. Surface heat treatments could highlight the thermodynamic and kinetic properties of the given surface. If as a result of surface conditioning clumps of Al preferentially rearrange/desorb from the surface to the most stable arrangement with high uniformity it could be the gateway into the realisation of such a surface for electron emission based application.

Crystallogen termination is another such approach for the creation of a thermally stable and negative EA surface. Evaluation of the structural and electronic properties as a function of Si and Ge surface coverage suggests the most energetically probable configuration is 67% of a monolayer. This produces both modest NEAs and surface stability. Experimental observation of Si-terminated diamond revealed an underlying 3×1 periodicity of the surface and a proposed model from the authors identical to that of the Si and Ge 67% geometries. Furthermore an experimentally observed but unknown resonant state placed in relation to the valence band is seen by density of state analysis in the same energy range and ascribed to Si-Si and Ge-Ge σ-bonding. The ability to produce conforming and mutually validating results consistently is a big win for the rationale behind theoretical research. Clearly, Si and Ge and their respective oxide forms too are of technological relevance for surfaces and interfaces. A natural progression from this work would be to assess SiO_x and GeO_x. If the surfaces arrange themselves akin to the aforementioned aluminium oxide results one could anticipate large NEAs.

Terminated 4H-SiC surface analytics are sparse throughout literature. The electronic properties and structural parameters under even the most common terminating species such as hydrogen are not widely reported. To our knowledge, this work contains the first reporting of a variety of terminations on the $(11\bar{2}0)$ and their EA values. Unsurprisingly, F and Cl produce strong positive EAs whilst H reduces the EA through a mixed dipolar array. Most notable is the near zero EA from Li termination and the relatively complex nature of the adatom co-ordination. It is therefore likely that a negative EA is possible for SiC under perhaps a LiO or other oxide monolayer; a plethora of surface science and the resulting application is to be unpicked through further work in this area.

Polar materials such as SiC possess a unique barrier in terms of modelling when compared to other semiconductors such as diamond. An intrinsic heterogeneity arising from the ionicity between Si and C provides a whole host of qualities and, in the case of modelling, certain difficulties. The final results section addresses a methodological issue in ascertaining EA values stemming from periodic boundary conditions applied in all directions to a polar surface. The triangular potential method gives a tighter range of EAs but deals with the issue of polarity in a *post hoc* sense, still impacted by the slab and vacuum thicknesses. The back to back method is more methodologically sound, in that it removes the electric field present across the vacuum but necessarily doubles the total atoms in the cell. The EA values span a larger range compared to the triangular potential, this is a consequence of the triangular method artificially decreasing the size of the electric field across the slab whereas the full field is felt under the back to back scheme. As pertaining to the method proffered, a less idealised structure is surely the next step for exploration; reconstructed 2×1 surfaces and the effects of surface coverage again as a function of cell parameters. This area of surface modelling is still in its relative infancy and there exists a huge potential for other approaches to be offered as whole or partial solutions to this intrinsic problem.

7. Appendices

7.1 Making Non-primitive Cells

Using the (111) surface as a model, the process through which the 2 atom diamond basis is transformed in to a surface slab is described.

Any non-primitive cell can be expressed as a linear combination of the primitive lattice vectors. In the case of (111) we know that this will represent one of our non-primitive lattice vectors in the surface normal direction. If the primitive lattice vectors are $\vec{v}_1$, $\vec{v}_2$ and $\vec{v}_3$ we know that the first non-primitive lattice vector $\vec{u}_1$ that lies along (111) is

$$\vec{u}_1 = \vec{v}_1 + \vec{v}_2 + \vec{v}_3 \tag{35}$$

The (111) surface is hexagonal, so the other two non-primitive lattice vectors ($\vec{u}_2$ and $\vec{u}_3$) should be both orthogonal to the surface normal direction and 120° apart from each other to create a hexagonal lattice type. Through the symmetry of the cell two known directions 120° apart are $(1\bar{1}0)$ and $(11\bar{2})$ which linear combinations of give the remaining two non-primitive lattice vectors:

$$\begin{aligned} \vec{u}_2 &= \vec{v}_1 - \vec{v}_2 \\ \vec{u}_3 &= \vec{v}_1 + \vec{v}_2 - 2\vec{v}_3 \end{aligned} \tag{36}$$

As the non-primitive cell is constructed through a sum of primitive vectors, the volume of the non-primitive cell will be an integer multiple of the primitive cell volume.

$$\begin{aligned} V_p &= \vec{v}_1 \cdot (\vec{v}_2 \times \vec{v}_3) \\ V_{np} &= \vec{u}_1 \cdot (\vec{u}_2 \times \vec{u}_3) \\ R &= V_{np}/V_p \end{aligned} \tag{37}$$

V_{p} is the volume of the primitive cell, V_{np} is the volume on the non-primitive cell and R is the ratio of the non-primitive and primitive cell volumes. A non-primitive cell R times larger in volume than the primitive will have R times as many atoms *and* R times as many lattice points. If we have a lattice point at the origin of our co-ordinate system, we can work out how many lattice points fall inside the boundary of our non-primitive volume. At each of the non-primitive lattice points we place our original primitive basis and thus have successfully constructed our new non-primitive cell with the selected lattice vectors.

7.2 4 Vector Notation

Miller indices represent the notation system that describe crystallographic planes in crystal structures. Lattice planes are described using a set of three integers using rounded brackets "( )" and lattice directions with square brackets "[ ]".

Cubic crystals have symmetrically equivalent directions that are permutations of their indices. For example, the direction [100] is equivalent to [010] and [001] as they just represent different edges of the same cube albeit 90° apart from each other. Indeed, opposite directions too are equivalent: $[00\bar{1}]$, $[0\bar{1}0]$ and $[\bar{1}00]$. This family of equivalent directions can be represented by the notation "⟨ ⟩" i.e. ⟨100⟩. This is always true for cubic systems but is not the case for hexagonal ones.

Along the basal plane of a hexagonal lattice, directions which are 60° or multiples of 60° apart are equivalent, but that does not guarantee equivalent directions will be direct permutations of their indices.

Take for example the directions [100] and [010]. They are 120° apart, symmetrically equivalent and a permutation of each other just like the cubic system described above. Another equivalent direction however is [110]; clearly not a permutation of either [100] or [010].

To combat this, a 4 vector notation system called Miller-Bravais indices is invoked. The first three numbers describe a symmetrically equivalent set on the basal plane. The third number is redundant, which can be derived from the first two vectors of a [h k i l] system by the relation:

$$i = -(h + k) \tag{38}$$

Where i is just the negative sum of h and k. The third number is introduced specifically to ensure that equivalent directions of the same family have directions which are permutations of each other. Now [100], [010] and [110] converted to 4 vector notation through a set of relational equations become $[2\bar{1}\bar{1}0]$, $[11\bar{2}0]$ and $[\bar{1}2\bar{1}0]$. It is significantly easier to deduce permutational equivalence between these directions compared to the 3 indices system.

This system is merely used as a visual aid, and it is still perfectly correct to use the three vector notation.

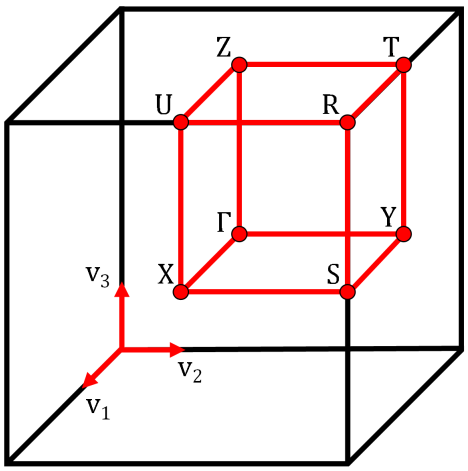

Figure 119: A simple orthorhombic lattice Brillouin zone. Providing the system has the D_{2h} point group, the primitive cell is reduced to $\frac{1}{8}$th its original volume. Each vector boundary is now half their original length, where the $\Gamma - R$ branch can be described as 0,0,0 to 0.5,0.5,0.5 with units as fractions of the original Brillouin zone.

7.3 Bandstructure Brilliouin zone

How the electron energy (y-axis) varies as a function of electron wave vector (x-axis) is often very informative for a given system. The Brillouin zone, as discussed in Section 3.5 is the reciprocal space primitive cell in which points are chosen to represent points along the x-axis of a bandstructure calculation. Each lattice type has a unique Brillouin zone which, through a set of crystal symmetry operations belonging to the system, can be simplified to a small set of high symmetry branches that make up the *irreducible wedge* of the Brillouin zone.

Figure 119 shows how a full Brillouin zone can be reduced down to a wedge that is just a fraction of the original shape and space yet contains all the same information of the former. We can exploit this to reduce the band structure calculation to only require the dispersion relation of the electron energy of a few select points in k-space whilst maintaining sampling density.

Each vertex of the irreducible wedge can be described as a fraction of the Brillouin zone and is given a notional letter representing that point in space. A full description of the energy-dispersion relation requires an adequate path through the all high symmetry points.

References

[1] M. Bruzzi. Radiation damage in silicon detectors for high-energy physics experiments. *IEEE Transactions on nuclear science*, 48(4):960–971, 2001.

[2] Z. Li. Radiation hardness/tolerance of Si sensors/detectors for nuclear and high energy physics experiments. *Proc. of Pixel*, 2002, 2002.

[3] J. Watson and G. Castro. A review of high-temperature electronics technology and applications. *Journal of Materials Science: Materials in Electronics*, 26(12):9226–9235, 2015.

[4] F. J. Morin and J. P. Maita. Conductivity and Hall effect in the intrinsic range of germanium. *Phys. Rev.*, 94:1525–1529, Jun 1954.

[5] P. G. Neudeck, R. S. Okojie, and Liang-Yu Chen. High-temperature electronics - a role for wide bandgap semiconductors? *Proceedings of the IEEE*, 90(6):1065–1076, June 2002.

[6] R. W. Johnson, J. L. Evans, P. Jacobsen, J. R. Thompson, and M. Christopher. The changing automotive environment: high-temperature electronics. *IEEE Transactions on Electronics Packaging Manufacturing*, 27(3):164–176, July 2004.

[7] J. Srour and D. Lo. Universal damage factor for radiation-induced dark current in silicon devices. *IEEE Transactions on Nuclear Science*, 47(6):2451–2459, 2000.

[8] P. R. Chalker. Wide bandgap semiconductor materials for high temperature electronics. *Thin Solid Films*, 343:616–622, 1999.

[9] R. W. Keyes. Physical limits of silicon transistors and circuits. *Reports on Progress in Physics*, 68(12):2701, 2005.

[10] P. Neudeck and G. Sujan. Silicon carbide electronic devices. *Reference Module in Materials Science and Materials Engineering*. Elsevier, 2016.

[11] J. Castaing, P. Veyssiere, L. P. Kubin, and J. Rabier. The plastic deformation of silicon between 300 °C and 600 °C. *Philosophical Magazine A*, 44(6):1407–1413, 1981.

[12] R. W. Johnson, J. L. Evans, P. Jacobsen, J. R. Thompson, and M. Christopher. The changing automotive environment: high-temperature electronics. *IEEE transactions on electronics packaging manufacturing*, 27(3):164–176, 2004.

[13] J. Hornberger, A. B. Lostetter, K. Olejniczak, T. McNutt, S. M. Lal, and A. Mantooth. Silicon-carbide (SiC) semiconductor power electronics for extreme high-temperature en-

vironments. *2004 IEEE Aerospace Conference Proceedings (IEEE Cat. No. 04TH8720)*, volume 4, pages 2538–2555. IEEE, 2004.

[14] T. Ericsen. Future navy application of wide bandgap power semiconductor devices. *Proceedings of the IEEE*, 90(6):1077–1082, 2002.

[15] L. M. Tolbert, B. Ozpineci, S. K. Islam, and M. S. Chinthavali. Wide bandgap semiconductors for utility applications. *semiconductors*, 1:3, 2003.

[16] A. A. Lebedev, V. V. Kozlovski, N. B. Strokan, D. V. Davydov, A. M. Ivanov, A. M. Strelchuk, and R. Yakimova. Radiation hardness of wide-gap semiconductors (using the example of silicon carbide). *Semiconductors*, 36(11):1270–1275, 2002.

[17] E. Barberis, J. Boissevain, N. Cartiglia, J. Ellison, P. Ferguson, J. Fleming, K. Holzscheiter, S. Jerger, D. Joyce, J. Kapustinsky, et al. Temperature effects on radiation damage to silicon detectors. *Nuclear Instruments and Methods in Physics Research Section A: Accelerators, Spectrometers, Detectors and Associated Equipment*, 326(1-2):373–380, 1993.

[18] E. Borchi and M. Bruzzi. Radiation damage in silicon detectors. *La Rivista del Nuovo Cimento (1978-1999)*, 17(11):1–63, 1994.

[19] J. W. Corbett. Radiation damage, defects and surfaces. *Surface Science*, 90(2):205 – 239, 1979.

[20] A. Erdemir and C. Donnet. Tribology of diamond-like carbon films: recent progress and future prospects. *Journal of Physics D: Applied Physics*, 39(18):R311, 2006.

[21] M. Seal and W. Van Enckevort. Applications of diamond in optics. *Diamond Optics*, volume 969, pages 144–152. International Society for Optics and Photonics, 1989.

[22] M. N. Yoder. Wide bandgap semiconductor materials and devices. *IEEE Transactions on Electron Devices*, 43(10):1633–1636, Oct 1996.

[23] K. Spear and J. Dismukes. *Synthetic Diamond: Emerging CVD Science and Technology*. The ECS Series of Texts and Monographs. Wiley, 1994.

[24] T.-H. Kim, W. M. Choi, D.-H. Kim, M. A. Meitl, E. Menard, H. Jiang, J. A. Carlisle, and J. A. Rogers. Printable, flexible, and stretchable forms of ultrananocrystalline diamond with applications in thermal management. *Advanced Materials*, 20(11):2171–2176, 2008.

[25] H. Umezawa, M. Nagase, Y. Kato, and S.-i. Shikata. High temperature application of diamond power device. *Diamond and related materials*, 24:201–205, 2012.

[26] C. J. Wort and R. S. Balmer. Diamond as an electronic material. *Materials Today*, 11(1):22 – 28, 2008.

[27] S. C. Eaton, A. B. Anderson, J. C. Angus, Y. E. Evstefeeva, and Y. V. Pleskov. Co-doping of diamond with boron and sulfur. *Electrochemical and solid-state letters*, 5(8):G65–G68, 2002.

[28] S. J. Sque, R. Jones, J. P. Goss, and P. R. Briddon. Shallow donors in diamond: Chalcogens, pnictogens, and their hydrogen complexes. *Physical Review Letters*, 92(1):017402, 2004.

[29] I. Sakaguchi, N. Mikka, Y. Kikuchi, E. Yasu, H. Haneda, T. Suzuki, T. Ando, et al. Sulfur: A donor dopant for n-type diamond semiconductors. *Physical Review B*, 60(4):R2139, 1999.

[30] H. Kato, S. Yamasaki, and H. Okushi. n-type doping of (001)-oriented single-crystalline diamond by phosphorus. *Applied Physics Letters*, 86(22):222111, 2005.

[31] S. Kajihara, A. Antonelli, J. Bernholc, and R. Car. Nitrogen and potential n-type dopants in diamond. *Physical review letters*, 66(15):2010, 1991.

[32] J. P. Goss and P. R. Briddon. Theoretical study of Li and Na as *n*-type dopants for diamond. *Physical Review B*, 75(7):075202, 2007.

[33] J. Lagrange, A. Deneuville, and E. Gheeraert. Activation energy in low compensated homoepitaxial boron-doped diamond films. *Diamond and Related Materials*, 7(9):1390 – 1393, 1998.

[34] J. P. Goss, B. Hourahine, R. Jones, M. I. Heggie, and P. R. Briddon. p-type surface doping of diamond: a first-principles study. *Journal of Physics: Condensed Matter*, 13(40):8973, 2001.

[35] S. J. Sque, R. Jones, J. P. Goss, P. R. Briddon, and S. berg. First-principles study of C 60 and C 60 F 36 as transfer dopants for p-type diamond. *Journal of Physics: Condensed Matter*, 17(2):L21, 2005.

[36] C. Wei, Q. Dongchen, G. Xingyu, and W. Andrew. Surface transfer doping of semiconductors. *Progress in Surface Science*, 84(9-10):279, 2009.

[37] J. Ristein, M. Riedel, F. Maier, B. F. Mantel, M. Stammler, and L. Ley. Surface doping: a special feature of diamond. *Journal of Physics: Condensed Matter*, 13(40):8979, 2001.

[38] F. Maier, M. Riedel, B. Mantel, J. Ristein, and L. Ley. Origin of surface conductivity in diamond. *Physical review letters*, 85(16):3472, 2000.

[39] K. Hayashi, S. Yamanaka, H. Okushi, and K. Kajimura. Study of the effect of hydrogen on transport properties in chemical vapor deposited diamond films by hall measurements. *Applied physics letters*, 68(3):376–378, 1996.

[40] H. Kawarada, H. Tsuboi, T. Naruo, T. Yamada, D. Xu, A. Daicho, T. Saito, and A. Hiraiwa. CH surface diamond field effect transistors for high temperature (400 °C) and high voltage (500 V) operation. *Applied physics letters*, 105(1):013510, 2014.

[41] K.-S. Song, T. Sakai, H. Kanazawa, Y. Araki, H. Umezawa, M. Tachiki, and H. Kawarada. Cl–sensitive biosensor used electrolyte-solution-gate diamond FETs. *Biosensors and bioelectronics*, 19(2):137140, November 2003.

[42] J. A. Garrido, A. Hartl, S. Kuch, M. Stutzmann, O. A. Williams, and R. B. Jackmann. pH sensors based on hydrogenated diamond surfaces. *Applied Physics Letters*, 86(7):073504, 2005.

[43] J. B. Cui, J. Ristein, M. Stammler, K. Janischowsky, G. Kleber, and L. Ley. Hydrogen termination and electron emission from CVD diamond surfaces: a combined secondary electron emission, photoelectron emission microscopy, photoelectron yield, and field emission study. *Diamond and Related Materials*, 9(36):1143–1147, 2000.

[44] K. Larsson and S. Lunell. Stability of halogen-terminated diamond (111) surfaces. *The Journal of Physical Chemistry A*, 101(1):76–82, 1997.

[45] A. K. Tiwari, J. P. Goss, P. R. Briddon, N. G. Wright, A. B. Horsfall, R. Jones, H. Pinto, and M. J. Rayson. Calculated electron affinity and stability of halogen-terminated diamond. *Physical Review B*, 84(24):245305, 2011.

[46] A. K. Tiwari, J. P. Goss, P. R. Briddon, N. G. Wright, A. B. Horsfall, and M. J. Rayson. Electronic and structural properties of diamond (001) surfaces terminated by selected transition metals. *Physical Review B*, 86(15):155301, 2012.

[47] O. K. M., E. M. T., R. Juergen, T. Anton, T. Lars, W. QiHui, P. C. I., and L. Lothar. Diamond surfaces with airstable negative electron affinity and giant electron yield enhancement. *Advanced Functional Materials*, 23(45):5608–5614.

[48] A. K. Tiwari. *Diamond-based thermo-tunnel devices for hostile environments.* PhD thesis, Newcastle Uuniversity, 2013.

[49] H. Andrews, E. Simakov, R. Fleming, B. Choi, K. Nichols, J. Lewellen, and D. Shchegolkov. Current experimental work with diamond field-emitter array cathodes. 2018.

[50] D. Takeuchi, S. Koizumi, T. Makino, H. Kato, M. Ogura, H. Ohashi, H. Okushi, and S. Yamasaki. Negative electron affinity of diamond and its application to high voltage vacuum power switches. *physica status solidi (a)*, 210(10):1961–1975, 2013.

[51] M. G. Dutt, L. Childress, L. Jiang, E. Togan, J. Maze, F. Jelezko, A. Zibrov, P. Hemmer, and M. Lukin. Quantum register based on individual electronic and nuclear spin qubits in diamond. *Science*, 316(5829):1312–1316, 2007.

[52] M. W. Doherty, V. V. Struzhkin, D. A. Simpson, L. P. McGuinness, Y. Meng, A. Stacey, T. J. Karle, R. J. Hemley, N. B. Manson, L. C. Hollenberg, et al. Electronic properties and metrology applications of the diamond NV- center under pressure. *Physical review letters*, 112(4):047601, 2014.

[53] F. Jelezko, T. Gaebel, I. Popa, A. Gruber, and J. Wrachtrup. Observation of coherent oscillations in a single electron spin. *Phys. Rev. Lett.*, 92:076401, Feb 2004.

[54] K.-M. C. Fu, C. Santori, P. E. Barclay, and R. G. Beausoleil. Conversion of neutral nitrogen-vacancy centers to negatively charged nitrogen-vacancy centers through selective oxidation. *Applied Physics Letters*, 96(12):121907, 2010.

[55] L. Rondin, G. Dantelle, A. Slablab, F. Grosshans, F. Treussart, P. Bergonzo, S. Perruchas, T. Gacoin, M. Chaigneau, H.-C. Chang, V. Jacques, and J.-F. Roch. Surface-induced charge state conversion of nitrogen-vacancy defects in nanodiamonds. *Phys. Rev. B*, 82:115449, Sep 2010.

[56] C. Santori, P. E. Barclay, K.-M. C. Fu, and R. G. Beausoleil. Vertical distribution of nitrogen-vacancy centers in diamond formed by ion implantation and annealing. *Phys. Rev. B*, 79:125313, Mar 2009.

[57] M. V. Hauf, B. Grotz, B. Naydenov, M. Dankerl, S. Pezzagna, J. Meijer, F. Jelezko, J. Wrachtrup, M. Stutzmann, F. Reinhard, and J. A. Garrido. Chemical control of the charge state of nitrogen-vacancy centers in diamond. *Phys. Rev. B*, 83:081304, Feb 2011.

[58] H. Pinto, R. Jones, D. W. Palmer, J. P. Goss, A. K. Tiwari, P. R. Briddon, N. G. Wright, A. B. Horsfall, M. J. Rayson, and S. Öberg. First-principles studies of the effect of (001) surface terminations on the electronic properties of the negatively charged nitrogen-vacancy defect in diamond. *Phys. Rev. B*, 86:045313, July 2012.

[59] C. Schreyvogel, V. Polyakov, R. Wunderlich, J. Meijer, and C. Nebel. Active charge state control of single NV centres in diamond by in-plane Al-schottky junctions. *Scientific reports*, 5:12160, 2015.

[60] S. Karaveli, O. Gaathon, A. Wolcott, R. Sakakibara, O. A. Shemesh, D. S. Peterka, E. S. Boyden, J. S. Owen, R. Yuste, and D. Englund. Modulation of nitrogen vacancy charge state and fluorescence in nanodiamonds using electrochemical potential. *Proceedings of the National Academy of Sciences*, 113(15):3938–3943, 2016.

[61] Y. Y. Hui, C.-L. Cheng, and H.-C. Chang. Nanodiamonds for optical bioimaging. *Journal of Physics D: Applied Physics*, 43(37):374021, sep 2010.

[62] C. J. Weijer. Visualizing signals moving in cells. *Science*, 300(5616):96–100, 2003.

[63] S.-J. Yu, M.-W. Kang, H.-C. Chang, K.-M. Chen, and Y.-C. Yu. Bright fluorescent nanodiamonds: no photobleaching and low cytotoxicity. *Journal of the American Chemical Society*, 127(50):17604–17605, 2005.

[64] R. Lam and D. Ho. Nanodiamonds as vehicles for systemic and localized drug delivery. *Expert Opinion on Drug Delivery*, 6(9):883–895, 2009. PMID: 19637985.

[65] A. Nagl, S. R. Hemelaar, and R. Schirhagl. Improving surface and defect center chemistry of fluorescent nanodiamonds for imaging purposes–a review. *Analytical and bioanalytical chemistry*, 407(25):7521–7536, 2015.

[66] N. Bar-Gill, L. M. Pham, A. Jarmola, D. Budker, and R. L. Walsworth. Solid-state electronic spin coherence time approaching one second. *Nature communications*, 4:1743, 2013.

[67] F. Bechstedt, P. Kckell, A. Zywietz, K. Karch, B. Adolph, K. Tenelsen, and J. Furthmller. Polytypism and properties of silicon carbide. *physica status solidi (b)*, 202(1):35–62, 1997.

[68] Wolfspeed SiC and GaN materials catalog. Accessed: 2019-01-17.

[69] M. Wijesundara and R. Azevedo. *Silicon Carbide Microsystems for Harsh Environments*. MEMS Reference Shelf. Springer New York, 2011.

[70] G. Pensl, H. Morkoc, B. Monemar, and E. Janzen. Silicon carbide, III-nitrides and related materials. I. *Materials Science Forum(Switzerland)*, volume 264, page 672, 1997.

[71] G. L. Harris. *Properties of silicon carbide*. Number 13. Iet, 1995.

[72] T. Hatayama, S. Hino, N. Miura, T. Oomori, and E. Tokumitsu. Remarkable increase in the channel mobility of SiC-MOSFETs by controlling the interfacial SiO_2 layer between Al_2O_3 and SiC. *IEEE Transactions on Electron Devices*, 55(8):2041–2045, Aug 2008.

[73] V. Afanas ev, A. Stesmans, M. Bassler, G. Pensl, and M. Schulz. Shallow electron traps at the 4H–SiC/SiO_2 interface. *Applied Physics Letters*, 76(3):336–338, 2000.

[74] M. Di Ventra and S. T. Pantelides. Atomic-scale mechanisms of oxygen precipitation and thin-film oxidation of SiC. *Phys. Rev. Lett.*, 83:1624–1627, Aug 1999.

[75] J. M. Knaup, P. Deák, T. Frauenheim, A. Gali, Z. Hajnal, and W. Choyke. Defects in SiO_2 as the possible origin of near interface traps in the SiC/ SiO_2 system: A systematic theoretical study. *Physical Review B*, 72(11):115323, 2005.

[76] J. Robertson and B. Falabretti. Band offsets of high k gate oxides on III-V semiconductors. *Journal of Applied Physics*, 100(1):014111, 2006.

[77] M. K. Linnarsson, A. Halln, S. Khartsev, S. S. Suvanam, and M. Usman. Interface between Al_2O_3 and 4H-SiC investigated by time-of-flight medium energy ion scattering. *Journal of Physics D: Applied Physics*, 50(49):495111, 2017.

[78] S. Diplas, M. Avice, A. Thgersen, J. S. Christensen, U. Grossner, B. G. Svensson, O. Nilsen, H. Fjellvg, S. Hinder, and J. F. Watts. Interfacial studies of Al_2O_3 deposited on 4H-SiC(0001). *Surface and Interface Analysis*, 40(34):822–825, 2008.

[79] D. J. Lichtenwalner, V. Misra, S. Dhar, S.-H. Ryu, and A. Agarwal. High-mobility enhancement-mode 4H-SiC lateral field-effect transistors utilizing atomic layer deposited Al_2O_3 gate dielectric. *Applied Physics Letters*, 95(15):152113, 2009.

[80] J. Urresti, F. Arith, K. Vassilevski, A. K. Tiwari, S. Olsen, N. G. Wright, and A. G. O'Neill. High-mobility SiC MOSFETs using a thin-SiO_2/Al_2O_3 gate stack. *Silicon Carbide and Related Materials 2017*, volume 924 of *Materials Science Forum*, pages 494–497. Trans Tech Publications, 7 2018.

[81] N. S. Mohamed, N. G. Wright, and A. B. Horsfall. High linearity silicon carbide detectors for medical applications. *2016 IEEE Nuclear Science Symposium, Medical Imaging Conference and Room-Temperature Semiconductor Detector Workshop (NSS/MIC/RTSD)*, pages 1–5, Oct 2016.

[82] S. Buschhorn and K. Vogel. Saving money: SiC in UPS applications. *PCIM Europe 2014; International Exhibition and Conference for Power Electronics, Intelligent Motion, Renewable Energy and Energy Management*, pages 1–7. VDE, 2014.

[83] D.-P. Sadik, J. Colmenares, G. Tolstoy, D. Peftitsis, M. Bakowski, J. Rabkowski, and H.-P. Nee. Short-circuit protection circuits for silicon-carbide power transistors. *IEEE transactions on industrial electronics*, 63(4):1995–2004, 2016.

[84] K. Hamada, M. Nagao, M. Ajioka, and F. Kawai. SiCemerging power device technology for next-generation electrically powered environmentally friendly vehicles. *IEEE Transactions*

on Electron Devices, 62(2):278–285, Feb 2015.

[85] K. L. Jensen. A tutorial on electron sources. *IEEE Transactions on Plasma Science*, 46(6):1881–1899, 2018.

[86] J. Houston and H. Webster. Thermionic energy conversion. *Advances in electronics and electron physics*, volume 17, pages 125–206. Elsevier, 1963.

[87] V. C. Wilson. Conversion of heat to electricity by thermionic emission. *Journal of Applied Physics*, 30(4):475–481, 1959.

[88] K. G. Hernqvist, M. Kanefsky, and F. H. Norman. Thermionic energy converter. *RCA Rev.*, 19:2, 6 1958.

[89] K. Hernqvist. Analysis of the arc mode operation of the cesium vapor thermionic energy converter. *Proceedings of the IEEE*, 51(5):748–754, 1963.

[90] H. Dominguez-Andrade, A. Croot, G. Wan, J. A. Smith, and N. A. Fox. Characterisation of thermionic emission current with a laser-heated system. *Review of Scientific Instruments*, 90(4):045110, 2019.

[91] G. Xiao, G. Zheng, M. Qiu, Q. Li, D. Li, and M. Ni. Thermionic energy conversion for concentrating solar power. *Applied Energy*, 208:1318 – 1342, 2017.

[92] F. A. Koeck and R. J. Nemanich. Advances in thermionic energy conversion through single-crystal n-type diamond. *Frontiers in Mechanical Engineering*, 3:19, 2017.

[93] L. W. Swanson and R. W. Strayer. Fieldelectronmicroscopy studies of cesium layers on various refractory metals: Work function change. *The Journal of Chemical Physics*, 48(6):2421–2442, 1968.

[94] D. V. Paramonov and M. S. El-Genk. A review of cesium thermionic converters with developed emitter surfaces. *Energy Conversion and Management*, 38(6):533 – 549, 1997.

[95] F. A. Koeck, R. J. Nemanich, A. Lazea, and K. Haenen. Thermionic electron emission from low work-function phosphorus doped diamond films. *Diamond and Related Materials*, 18(5):789 – 791, 2009. Proceedings of Diamond 2008, the 19th European Conference on Diamond, Diamond-Like Materials, Carbon Nanotubes, Nitrides and Silicon Carbide.

[96] J. H. Lee, I. Bargatin, T. O. Gwinn, M. Vincent, K. A. Littau, R. Maboudian, Z.-X. Shen, N. A. Melosh, and R. T. Howe. Microfabricated silicon carbide thermionic energy converter for solar electricity generation. *2012 IEEE 25th International Conference on Micro Electro Mechanical Systems (MEMS)*, pages 1261–1264. IEEE, Jan 2012.

[97] J. H. Lee, I. Bargatin, K. Iwami, K. A. Littau, M. Vincent, R. Maboudian, Z. Shen, N. A. Melosh, and R. T. Howe. Encapsulated thermionic energy converter with stiffened suspension. *Proc. Solid-State Sens., Actuators, Microsyst. Workshop*, pages 493–496, 2012.

[98] Y. Momozaki and M. S. El-Genk. Investigations of the performance of grooved electrodes thermionic converters at collector temperatures up to 1023K. *Energy conversion and management*, 45(7-8):1153–1173, 2004.

[99] F. A. M. Koeck and R. J. Nemanich. Substrate-diamond interface considerations for enhanced thermionic electron emission from nitrogen doped diamond films. *Journal of Applied Physics*, 112(11):113707, 2012.

[100] G. Y. McDaniel, S. T. Fenstermaker, W. V. Lampert, and P. H. Holloway. Rhenium ohmic contacts on 6H-SiC. *Journal of Applied Physics*, 96(9):5357–5364, 2004.

[101] G. N. Hatsopoulos and E. P. Gyftopoulos. Thermionic energy conversion. volume i. processes and devices. Technical report, Massachusetts Institute of Technology Press, Cambridge, MA (United States), 1973.

[102] F. A. Koeck, R. J. Nemanich, Y. Balasubramaniam, K. Haenen, and J. Sharp. Enhanced thermionic energy conversion and thermionic emission from doped diamond films through methane exposure. *Diamond and Related Materials*, 20(8):1229 – 1233, 2011.

[103] J. R. Smith, G. L. Bilbro, and R. J. Nemanich. Considerations for a high-performance thermionic energy conversion device based on a negative electron affinity emitter. *Physical Review B*, 76(24):245327, 2007.

[104] J. R. Smith, G. L. Bilbro, and R. J. Nemanich. Theory of space charge limited regime of thermionic energy converter with negative electron affinity emitter. *Journal of Vacuum Science & Technology B: Microelectronics and Nanometer Structures Processing, Measurement, and Phenomena*, 27(3):1132–1141, 2009.

[105] T. Sun, F. A. Koeck, A. Rezikyan, M. M. Treacy, and R. J. Nemanich. Thermally enhanced photoinduced electron emission from nitrogen-doped diamond films on silicon substrates. *Physical Review B*, 90(12):121302, 2014.

[106] X. Fang, Y. Bando, U. K. Gautam, C. Ye, and D. Golberg. Inorganic semiconductor nanostructures and their field-emission applications. *Journal of Materials Chemistry*, 18(5):509–522, 2008.

[107] T. Masuzawa, Y. Shiraki, Y. Kudo, I. Saito, H. Yamaguchi, T. Yamada, and K. Okano. Clarification of band structure at metaldiamond contact using device simulation. *Applied*

Surface Science, 254(19):6285 – 6288, 2008. Fifth International Symposium on Control of Semiconductor Interfaces.

[108] H. Yamaguchi, T. Masuzawa, S. Nozue, Y. Kudo, I. Saito, J. Koe, M. Kudo, T. Yamada, Y. Takakuwa, and K. Okano. Electron emission from conduction band of diamond with negative electron affinity. *Physical Review B*, 80(16):165321, 2009.

[109] T. S. Fisher and D. G. Walker. Thermal and Electrical Energy Transport and Conversion in Nanoscale Electron Field Emission Processes . *Journal of Heat Transfer*, 124(5):954–962, 09 2002.

[110] J. D. Jarvis, H. L. Andrews, C. A. Brau, B. K. Choi, J. Davidson, W. P. Kang, and Y. M. Wong. Uniformity conditioning of diamond field emitter arrays. *Journal of Vacuum Science and Technology B*, 27(5):2264–2269, 2009.

[111] E. I. Simakov, H. L. Andrews, M. J. Herman, K. M. Hubbard, and E. Weis. Diamond field emitter array cathodes and possibilities of employing additive manufacturing for dielectric laser accelerating structures. *AIP Conference Proceedings*, volume 1812, page 060010. AIP Publishing, 2017.

[112] P. R. Schwoebel, C. A. Spindt, and C. E. Holland. High current, high current density field emitter array cathodes. *Journal of Vacuum Science & Technology B*, 23(2):691–693, 2005.

[113] D. R. Whaley, B. M. Gannon, C. R. Smith, C. M. Armstrong, and C. A. Spindt. Application of field emitter arrays to microwave power amplifiers. *IEEE transactions on plasma science*, 28(3):727–747, 2000.

[114] X. Li, C. Yang, J. Feng, J. Cai, G. Bai, M. Ding, F. Zhang, and F. Liao. Effect of ageing process on performance of molybdenum field emission arrays. *Applied Surface Science*, 251(1):210 – 214, 2005. The 5th International Vacuum Electron Sources Conference.

[115] K. Sawhney, I. Dolbnya, M. Tiwari, L. Alianelli, S. Scott, G. Preece, U. Pedersen, and R. Walton. A test beamline on diamond light source. *AIP conference proceedings*, volume 1234, pages 387–390. AIP, 2010.

[116] H. Nowell, S. A. Barnett, K. E. Christensen, S. J. Teat, and D. R. Allan. I19, the small-molecule single-crystal diffraction beamline at diamond light source. *Journal of synchrotron radiation*, 19(3):435–441, 2012.

[117] J. C. Spence. *High-resolution electron microscopy*. OUP Oxford, 2013.

[118] R. Pease. Electron beam lithography. *Contemporary Physics*, 22(3):265–290, 1981.

[119] J. C. Person and D. O. Ham. Removal of SO2 and NOx from stack gases by electron beam irradiation. 31:1–8, 12 1988.

[120] A. Chmielewski, J. Licki, A. Pawelec, B. Tymiski, and Z. Zimek. Operational experience of the industrial plant for electron beam flue gas treatment. 71:441–444, 09 2004.

[121] J. Scholtz, D. Dijkkamp, and R. Schmitz. Secondary electron emission properties. *Philips journal of research*, 50(3-4):375–389, 1996.

[122] J. Smedley, I. Ben-Zvi, J. Bohon, X. Chang, R. Grover, A. Isakovic, T. Rao, and Q. Wu. Diamond amplified photocathodes. *MRS Online Proceedings Library Archive*, 1039, 2007.

[123] D. Dowell, I. Bazarov, B. Dunham, K. Harkay, C. Hernandez-Garcia, R. Legg, H. Padmore, T. Rao, J. Smedley, and W. Wan. Cathode r&d for future light sources. *Nuclear Instruments and Methods in Physics Research Section A: Accelerators, Spectrometers, Detectors and Associated Equipment*, 622(3):685 – 697, 2010.

[124] I. Ben-Zvi and E. Muller. Study of electron transport and amplification in diamond. 1 2015.

[125] T. Rao, I. BenZvi, A. Burrill, X. Chang, S. Hulbert, P. D. Johnson, and J. Kewisch. Diamond amplifier for photocathodes. *AIP Conference Proceedings*, 737(1):178–190, 2004.

[126] E. Wang, I. Ben-Zvi, X. Chang, Q. Wu, T. Rao, J. Smedley, J. Kewisch, and T. Xin. Systematic study of hydrogenation in a diamond amplifier. *Phys. Rev. ST Accel. Beams*, 14:061302, Jun 2011.

[127] A. Chvyreva and A. J. M. Pemen. Experimental investigation of electron emission from dielectric surfaces due to primary electron beam: a review. *IEEE Transactions on Dielectrics and Electrical Insulation*, 21(5):2274–2282, Oct 2014.

[128] K. I. Grais and A. M. Bastawros. A study of secondary electron emission in insulators and semiconductors. *Journal of Applied Physics*, 53(7):5239–5242, 1982.

[129] X. Chang, Q. Wu, I. Ben-Zvi, A. Burrill, J. Kewisch, T. Rao, J. Smedley, E. Wang, E. M. Muller, R. Busby, et al. Electron beam emission from a diamond-amplifier cathode. *Physical review letters*, 105(16):164801, 2010.

[130] J. Lapington, V. Taillandier, B. Cann, J. Howorth, and J. Milnes. Investigation of the secondary electron emission characteristics of alternative dynode materials for imaging photomultipliers. *Journal of Instrumentation*, 7(03):C03018, 2012.

[131] J. E. Yater and A. Shih. Secondary electron emission characteristics of single-crystal and polycrystalline diamond. *Journal of Applied Physics*, 87(11):8103–8112, 2000.

[132] F. Nava, C. Canali, C. Jacoboni, L. Reggiani, and S. Kozlov. Electron effective masses and lattice scattering in natural diamond. *Solid State Communications*, 33(4):475 – 477, 1980.

[133] T. Rao, I. Ben-Zvi, A. Burrill, X. Chang, J. Grimes, J. Rank, Z. Segalov, and J. Smedley. Role of diamond secondary emitters in high brightness electron sources. Technical report, Brookhaven National Lab.(BNL), Upton, NY (United States), 2005.

[134] E. Wang, I. Ben-Zvi, T. Rao, D. Dimitrov, X. Chang, Q. Wu, and T. Xin. Secondary-electron emission from hydrogen-terminated diamond: Experiments and model. *Physical Review Special Topics-Accelerators and Beams*, 14(11):111301, 2011.

[135] J. Isberg, J. Hammersberg, E. Johansson, T. Wikström, D. J. Twitchen, A. J. Whitehead, S. E. Coe, and G. A. Scarsbrook. High carrier mobility in single-crystal plasma-deposited diamond. *Science*, 297(5587):1670–1672, 2002.

[136] K. M. O'Donnell, M. T. Edmonds, J. Ristein, K. J. Rietwyk, A. Tadich, L. Thomsen, C. I. Pakes, and L. Ley. Direct observation of phonon emission from hot electrons: spectral features in diamond secondary electron emission. *Journal of Physics: Condensed Matter*, 26(39):395008, 2014.

[137] A. Shih, J. Yater, C. Hor, and R. Abrams. Secondary electron emission studies. *Applied surface science*, 111:251–258, 1997.

[138] Y. V. Pleskov. Electrochemistry of diamond: A review. *Russian Journal of Electrochemistry*, 38(12):1275–1291, 2002.

[139] H. Girard, N. Simon, D. Ballutaud, E. de La Rochefoucauld, and A. Etcheberry. Effects of controlled anodic treatments on electrochemical behaviour of boron doped diamond. *Diamond and related materials*, 16(4-7):888–891, 2007.

[140] E. Popa, Y. Kubota, D. A. Tryk, and A. Fujishima. Selective voltammetric and amperometric detection of uric acid with oxidized diamond film electrodes. *Analytical chemistry*, 72(7):1724–1727, 2000.

[141] M. Panizza and G. Cerisola. Application of diamond electrodes to electrochemical processes. *Electrochimica Acta*, 51(2):191–199, 2005.

[142] G. M. Swain, A. B. Anderson, and J. C. Angus. Applications of diamond thin films in electrochemistry. *MRS Bulletin*, 23(9):5660, 1998.

[143] J. Hees, R. Hoffmann, A. Kriele, W. Smirnov, H. Obloh, K. Glorer, B. Raynor, R. Driad, N. Yang, O. A. Williams, and C. E. Nebel. Nanocrystalline diamond nanoelectrode arrays and ensembles. *ACS Nano*, 5(4):3339–3346, 2011. PMID: 21413786.

[144] D. Zhu, L. Zhang, R. E. Ruther, and R. J. Hamers. Photo-illuminated diamond as a solid-state source of solvated electrons in water for nitrogen reduction. *Nature materials*, 12(9):836, 2013.

[145] S. A. Yao, R. E. Ruther, L. Zhang, R. A. Franking, R. J. Hamers, and J. F. Berry. Covalent attachment of catalyst molecules to conductive diamond: Co2 reduction using smart electrodes. *Journal of the American Chemical Society*, 134(38):15632–15635, 2012.

[146] N. Yang, S. Yu, J. MacPherson, Y. Einaga, H. Zhao, G. Zhao, G. Swain, and X. Jiang. Conductive diamond: Synthesis, properties, and electrochemical applications. *Chemical Society Reviews*, 48(1):157–204, 1 2019.

[147] W. Yang, O. Auciello, J. E. Butler, W. Cai, J. A. Carlisle, J. E. Gerbi, D. M. Gruen, T. Knickerbocker, T. L. Lasseter, J. N. Russell, et al. DNA-modified nanocrystalline diamond thin-films as stable, biologically active substrates. *Nature materials*, 1(4):253–257, 2002.

[148] T. Strother, T. Knickerbocker, J. N. Russell, J. E. Butler, L. M. Smith, and R. J. Hamers. Photochemical functionalization of diamond films. *Langmuir*, 18(4):968–971, 2002.

[149] R. G. Compton, J. S. Foord, and F. Marken. Electroanalysis at diamond-like and doped-diamond electrodes. *Electroanalysis: An International Journal Devoted to Fundamental and Practical Aspects of Electroanalysis*, 15(17):1349–1363, 2003.

[150] F. Nava, G. Bertuccio, A. Cavallini, and E. Vittone. Silicon carbide and its use as a radiation detector material. *Measurement Science and Technology*, 19(10):102001, aug 2008.

[151] N. G. Wright and A. B. Horsfall. SiC sensors: a review. *Journal of Physics D: Applied Physics*, 40(20):6345, 2007.

[152] G. Müller, G. Krötz, and E. Niemann. SiC for sensors and high-temperature electronics. *Sensors and Actuators A: Physical*, 43(1-3):259–268, 1994.

[153] N. G. Wright, A. B. Horsfall, and K. Vassilevski. Prospects for SiC electronics and sensors. *Materials Today*, 11(12):16–21, 2008.

[154] K.-S. Kim and G.-S. Chung. Characterization of porous cubic silicon carbide deposited with Pd and Pt nanoparticles as a hydrogen sensor. *Sensors and Actuators B: Chemical*, 157(2):482 – 487, 2011.

[155] A. Sanger, P. K. Jain, Y. K. Mishra, and R. Chandra. Palladium decorated silicon carbide nanocauliflowers for hydrogen gas sensing application. *Sensors and Actuators B: Chemical*, 242:694 – 699, 2017.

[156] M. T. Soo, K. Y. Cheong, and A. F. M. Noor. Advances of SiC-based MOS capacitor hydrogen sensors for harsh environment applications. *Sensors and Actuators B: Chemical*, 151(1):39 – 55, 2010.

[157] D. G. Senesky, B. Jamshidi, K. B. Cheng, and A. P. Pisano. Harsh environment silicon carbide sensors for health and performance monitoring of aerospace systems: A review. *IEEE Sensors Journal*, 9(11):1472–1478, 2009.

[158] R. Yakimova, R. M. Petoral, G. R. Yazdi, C. Vahlberg, A. L. Spetz, and K. Uvdal. Surface functionalization and biomedical applications based on SiC. *Journal of Physics D: Applied Physics*, 40(20):6435–6442, oct 2007.

[159] A. Oliveros, A. Guiseppi-Elie, and S. E. Saddow. Silicon carbide: a versatile material for biosensor applications. *Biomedical Microdevices*, 15(2):353–368, Apr 2013.

[160] G. Cicero, A. Catellani, and G. Galli. Atomic control of water interaction with biocompatible surfaces: The case of SiC(001). *Phys. Rev. Lett.*, 93:016102, Jul 2004.

[161] A. Härtl, E. Schmich, J. A. Garrido, J. Hernando, S. C. Catharino, S. Walter, P. Feulner, A. Kromka, D. Steinmüller, and M. Stutzmann. Protein-modified nanocrystalline diamond thin films for biosensor applications. *Nature materials*, 3(10):736–742, 2004.

[162] M. Schwander and K. Partes. A review of diamond synthesis by CVD processes. *Diamond and related materials*, 20(9):1287–1301, 2011.

[163] M. Ashfold, P. May, C. Rego, and N. Everitt. Thin film diamond by chemical vapour deposition methods. *Chemical Society Reviews*, 23(1):21–30, 1994.

[164] K. Zekentes and K. Vasilevskiy. *Advancing Silicon Carbide Electronics Technology II: Core Technologies of Silicon Carbide Device Processing*. Materials Research Foundations. Materials Research Forum LLC, 2020.

[165] T. Kimoto. Bulk and epitaxial growth of silicon carbide. *Progress in Crystal Growth and Characterization of Materials*, 62(2):329–351, 2016.

[166] D. Nakamura, I. Gunjishima, S. Yamaguchi, T. Ito, A. Okamoto, H. Kondo, S. Onda, and K. Takatori. Ultrahigh-quality silicon carbide single crystals. *Nature*, 430(7003):1009–1012, 2004.

[167] J. E. Butler and R. L. Woodin. Thin film diamond growth mechanisms. *Philosophical Transactions of the Royal Society of London. Series A: Physical and Engineering Sciences*, 342(1664):209–224, 1993.

[168] A. Hallén, M. Janson, A. Y. Kuznetsov, D. Åberg, M. K. Linnarsson, B. Svensson, P. Persson, F. Carlsson, L. Storasta, J. Bergman, et al. Ion implantation of silicon carbide. *Nuclear Instruments and Methods in Physics Research Section B: Beam Interactions with Materials and Atoms*, 186(1-4):186–194, 2002.

[169] S. Koizumi, T. Teraji, and H. Kanda. Phosphorus-doped chemical vapor deposition of diamond. *Diamond and Related Materials*, 9(3-6):935–940, 2000.

[170] K. Ushizawa, K. Watanabe, T. Ando, I. Sakaguchi, M. Nishitani-Gamo, Y. Sato, and H. Kanda. Boron concentration dependence of raman spectra on {100} and {111} facets of B-doped CVD diamond. *Diamond and related materials*, 7(11-12):1719–1722, 1998.

[171] T. Kimoto. Material science and device physics in SiC technology for high-voltage power devices. *Japanese Journal of Applied Physics*, 54(4):040103, 2015.

[172] I.-N. Lin, S. Koizumi, J. Yater, and F. Koeck. Diamond electron emission. *MRS Bulletin*, 39(6):533, 2014.

[173] M. Born and R. Oppenheimer. Zur quantentheorie der molekeln. *Annalen der physik*, 389(20):457–484, 1927.

[174] D. R. Hartree. The wave mechanics of an atom with a non-coulomb central field. part I. theory and methods. *Mathematical Proceedings of the Cambridge Philosophical Society*, 24(1):89110, 1928.

[175] F. Bloch. Quantum mechanics of electrons in crystal lattices. *Z. Phys*, 52:555–600, 1928.

[176] J. C. Slater. A simplification of the Hartree-Fock method. *Physical review*, 81(3):385, 1951.

[177] P. Hohenberg and W. Kohn. Inhomogeneous electron gas. *Physical review*, 136(3B):B864, 1964.

[178] W. Kohn and L. J. Sham. Self-consistent equations including exchange and correlation effects. *Physical review*, 140(4A):A1133, 1965.

[179] J. P. Perdew and Y. Wang. Accurate and simple analytic representation of the electron-gas correlation energy. *Phys. Rev. B*, 45:13244–13249, Jun 1992.

[180] J. P. Perdew, K. Burke, and M. Ernzerhof. Generalized gradient approximation made simple. *Phys. Rev. Lett.*, 77:3865–3868, Oct 1996.

[181] J. P. Perdew. Density functional theory and the band gap problem. *International Journal of Quantum Chemistry*, 28(S19):497–523, 1985.

[182] T. Hom, W. Kiszenik, and B. Post. Accurate lattice constants from multiple reflection measurements. II. lattice constants of germanium silicon, and diamond. *Journal of Applied Crystallography*, 8(4):457–458, 1975.

[183] M. L. Cohen. Calculation of bulk moduli of diamond and zinc-blende solids. *Physical Review B*, 32(12):7988, 1985.

[184] M. J. Rayson and P. R. Briddon. Highly efficient method for Kohn-Sham density functional calculations of $500 - 10,000$ atom systems. *Phys. Rev. B*, 80:205104, Nov 2009.

[185] P. R. Briddon and M. J. Rayson. Accurate Kohn–Sham DFT with the speed of tight binding: current techniques and future directions in materials modelling. *physica status solidi (b)*, 248(6):1309–1318, 2011.

[186] M. J. Rayson and P. R. Briddon. Rapid iterative method for electronic-structure eigenproblems using localised basis functions. *Computer Physics Communications*, 178(2):128–134, 2008.

[187] J. Kohanoff. *Electronic structure calculations for solids and molecules: theory and computational methods*. Cambridge University Press, 2006.

[188] V. Blum, R. Gehrke, F. Hanke, P. Havu, V. Havu, X. Ren, K. Reuter, and M. Scheffler. The Fritz Haber Institute ab initio molecular simulations package (FHI-aims), 2009.

[189] L. Lehtovaara, V. Havu, and M. Puska. All-electron density functional theory and time-dependent density functional theory with high-order finite elements. *The Journal of chemical physics*, 131(5):054103, 2009.

[190] J. P. Goss. Theory of hydrogen in diamond. *Journal of Physics: Condensed Matter*, 15(17):R551, 2003.

[191] R. Jones and P. Briddon. The ab initio cluster method and the dynamics of defects in semiconductors. *Semiconductors and semimetals*, 51:287–349, 1998.

[192] C. Hartwigsen, S. Goedecker, and J. Hutter. Relativistic separable dual-space Gaussian pseudopotentials from H to Rn. *Phys. Rev. B*, 58:3641–3662, Aug 1998.

[193] J. R. Shewchuk et al. An introduction to the conjugate gradient method without the agonizing pain, 1994.

[194] P. Pulay. Ab initio calculation of force constants and equilibrium geometries in polyatomic molecules: I. theory. *Molecular Physics*, 17(2):197–204, 1969.

[195] J. Kohanoff. *Electronic structure calculations for solids and molecules: theory and computational methods*. Cambridge University Press, 2006.

[196] P. Haas, F. Tran, and P. Blaha. Calculation of the lattice constant of solids with semilocal functionals. *Physical Review B*, 79(8):085104, 2009.

[197] H. Holloway, K. C. Hass, M. A. Tamor, T. R. Anthony, and W. F. Banholzer. Isotopic dependence of the lattice constant of diamond. *Phys. Rev. B*, 44:7123–7126, Oct 1991.

[198] F. Jensen. Polarization consistent basis sets: Principles. *The Journal of Chemical Physics*, 115(20):9113–9125, 2001.

[199] J. Kohanoff. *Electronic structure calculations for solids and molecules: theory and computational methods*. Cambridge University Press, 2006.

[200] H. J. Monkhorst and J. D. Pack. Special points for Brillouin-zone integrations. *Phys. Rev. B*, 13:5188–5192, Jun 1976.

[201] A. Allred. Electronegativity values from thermochemical data. *Journal of Inorganic and Nuclear Chemistry*, 17(3):215 – 221, 1961.

[202] M. J. Rutter and J. Robertson. Ab initio calculation of electron affinities of diamond surfaces. *Phys. Rev. B*, 57:9241–9245, Apr 1998.

[203] N. E. Singh-Miller and N. Marzari. Surface energies, work functions, and surface relaxations of low-index metallic surfaces from first principles. *Physical Review B*, 80(23):235407, 2009.

[204] V. Fiorentini and M. Methfessel. Extracting convergent surface energies from slab calculations. *Journal of Physics: Condensed Matter*, 8(36):6525, 1996.

[205] S. J. Sque, R. Jones, and P. R. Briddon. Structure, electronics, and interaction of hydrogen and oxygen on diamond surfaces. *Physical Review B*, 73(8):085313, 2006.

[206] E. Kaxiras, Y. Bar-Yam, J. D. Joannopoulos, and K. C. Pandey. Ab initio theory of polar semiconductor surfaces. I. methodology and the (22) reconstructions of GaAs (111). *Phys. Rev. B*, 35:9625–9635, Jun 1987.

[207] C. E. Dreyer, A. Janotti, and C. G. Van de Walle. Absolute surface energies of polar and nonpolar planes of GaN. *Physical Review B*, 89(8):081305, 2014.

[208] G. Kern and J. Hafner. Ab initio calculations of the atomic and electronic structure of clean and hydrogenated diamond (110) surfaces. *Physical Review B*, 56(7):4203–4210, 1997.

[209] D. Riley. Lattice constant of diamond and the C–C single bond. *Nature*, 153(3889):587, 1944.

[210] H. Lofas, A. Grigoriev, J. Isberg, and R. Ahuja. Effective masses and electronic structure of diamond including electron correlation effects in first principles calculations using the GW-approximation. *AIP Advances*, 1(3):032139, 2011.

[211] M. T. Edmonds, A. Tadich, M. Wanke, K. M. O'Donnell, Y. Smets, K. J. Rietwyk, J. D. Riley, C. I. Pakes, and L. Ley. Valence-band structure and critical point energies of diamond along [100]. *Phys. Rev. B*, 87:085123, Feb 2013.

[212] L. F. Sutcu, C. J. Chu, M. S. Thompson, R. H. Hauge, J. L. Margrave, and M. P. DEvelyn. Atomic force microscopy of (100), (110), and (111) homoepitaxial diamond films. *Journal of Applied Physics*, 71(12):5930–5940, 1992.

[213] C. J. Chu, M. P. DEvelyn, R. H. Hauge, and J. L. Margrave. Mechanism of diamond growth by chemical vapor deposition on diamond (100), (111), and (110) surfaces: Carbon13 studies. *Journal of Applied Physics*, 70(3):1695–1705, 1991.

[214] A. Tallaire, J. Achard, A. Boussadi, O. Brinza, A. Gicquel, I. Kupriyanov, Y. Palyanov, G. Sakr, and J. Barjon. High quality thick CVD diamond films homoepitaxially grown on (111)-oriented substrates. *Diamond and Related Materials*, 41:34 – 40, 2014.

[215] M.-A. Pinault-Thaury, B. Berini, I. Stenger, E. Chikoidze, A. Lusson, F. Jomard, J. Chevallier, and J. Barjon. High fraction of substitutional phosphorus in a (100) diamond epilayer with low surface roughness. *Applied Physics Letters*, 100(19):192109, 2012.

[216] C. Wild, N. Herres, and P. Koidl. Texture formation in polycrystalline diamond films. *Journal of Applied Physics*, 68(3):973–978, 1990.

[217] C. Wild, R. Kohl, N. Herres, W. Mller-Sebert, and P. Koidl. Oriented CVD diamond films: twin formation, structure and morphology. *Diamond and Related Materials*, 3(4):373 –

381, 1994. Proceedings of the 4th European Conference on Diamond, Diamond-like and Related Materials.

[218] P. Kruger and J. Pollmann. Dimer reconstruction of diamond, Si, and Ge (001) surfaces. *Phys. Rev. Lett.*, 74:1155–1158, Feb 1995.

[219] S. Hong and M. Y. Chou. Theoretical study of hydrogen-covered diamond (100) surfaces: A chemical-potential analysis. *Phys. Rev. B*, 55:9975–9982, Apr 1997.

[220] K. Tsugawa, H. Noda, K. Hirose, and H. Kawarada. Schottky barrier heights, carrier density, and negative electron affinity of hydrogen-terminated diamond. *Phys. Rev. B*, 81:045303, Jan 2010.

[221] A. Malshe, B. Park, W. Brown, and H. Naseem. A review of techniques for polishing and planarizing chemically vapor-deposited (CVD) diamond films and substrates. *Diamond and Related Materials*, 8(7):1198 – 1213, 1999.

[222] G. Kern, J. Hafner, J. Furthmller, and G. Kresse. (2x1) reconstruction and hydrogen-induced de-reconstruction of the diamond (100) and (111) surfaces. *Surface Science*, 352-354:745 – 749, 1996. Proceedings of the 15th European Conference on Surface Science.

[223] J. Furthmüller, J. Hafner, and G. Kresse. Dimer reconstruction and electronic surface states on clean and hydrogenated diamond (100) surfaces. *Phys. Rev. B*, 53:7334–7351, Mar 1996.

[224] Y. Wang, K. Wong, S. Lee, M. Nishitani-Gamo, I. Sakaguchi, K. Loh, and T. Ando. Recent studies on diamond surfaces. *Diamond and Related Materials*, 9(9):1582 – 1590, 2000.

[225] F. Maier, J. Ristein, and L. Ley. Electron affinity of plasma-hydrogenated and chemically oxidized diamond (100) surfaces. *Physical Review B*, 64(16):165411, 2001.

[226] J. Michl, T. Teraji, S. Zaiser, I. Jakobi, G. Waldherr, F. Dolde, P. Neumann, M. W. Doherty, N. B. Manson, J. Isoya, and J. Wrachtrup. Perfect alignment and preferential orientation of nitrogen-vacancy centers during chemical vapor deposition diamond growth on (111) surfaces. *Applied Physics Letters*, 104(10):102407, 2014.

[227] S. Ramaseshan. The cleavage properties of diamond. *Proceedings of the Indian Academy of Sciences - Section A*, 24(1):114, Jul 1946.

[228] O. A. Shenderova, D. W. Brenner, A. Omeltchenko, X. Su, and L. H. Yang. Atomistic modeling of the fracture of polycrystalline diamond. *Phys. Rev. B*, 61:3877–3888, Feb 2000.

[229] S. V. Pepper. Electron spectroscopy of the diamond surface. *Applied Physics Letters*, 38(5):344–346, 1981.

[230] S.-T. Lee and G. Apai. Surface phonons and ch vibrational modes of diamond (100) and (111) surfaces. *Physical Review B*, 48(4):2684, 1993.

[231] A. Petukhov, D. Passerone, F. Ercolessi, E. Tosatti, and A. Fasolino. (meta) stable reconstructions of the diamond (111) surface: Interplay between diamond and graphitelike bonding. *Physical Review B*, 61(16):R10590, 2000.

[232] D. R. Alfonso, D. A. Drabold, and S. E. Ulloa. Structural, electronic, and vibrational properties of diamond (100), (111), and (110) surfaces from *ab initio* calculations. *Physical Review B*, 51(20):14669–14685, 1995.

[233] P. K. Baumann and R. J. Nemanich. Electron affinity and Schottky barrier height of metaldiamond (100), (111), and (110) interfaces. *Journal of Applied Physics*, 83(4):2072–2082, 1998.

[234] J. van der Weide and R. J. Nemanich. Schottky barrier height and negative electron affinity of titanium on (111) diamond. *Journal of Vacuum Science & Technology B*, 10(4):1940–1943, 1992.

[235] R. Nemanich, P. Baumann, M. Benjamin, S. King, J. Van der Weide, and R. Davis. Negative electron affinity surfaces of aluminum nitride and diamond. *Diamond and Related Materials*, 5(6-8):790–796, 1996.

[236] A. K. Tiwari, J. P. Goss, P. R. Briddon, A. B. Horsfall, N. G. Wright, R. Jones, and M. J. Rayson. Unexpected change in the electron affinity of diamond caused by the ultra-thin transition metal oxide films. *EPL (Europhysics Letters)*, 108(4):46005, 2014.

[237] K. P. Loh, X. Xie, S. Yang, J. Pan, and P. Wu. A spectroscopic study of the negative electron affinity of cesium oxide-coated diamond (111) and theoretical calculation of the surface density-of-states on oxygenated diamond (111). *Diamond and Related Materials*, 11(7):1379 – 1384, 2002.

[238] K. M. O'Donnell, T. L. Martin, N. A. Fox, and D. Cherns. Ab initio investigation of lithium on the diamond C(100) surface. *Phys. Rev. B*, 82:115303, Sep 2010.

[239] K. M. O'Donnell, M. T. Edmonds, A. Tadich, L. Thomsen, A. Stacey, A. Schenk, C. I. Pakes, and L. Ley. Extremely high negative electron affinity of diamond via magnesium adsorption. *Phys. Rev. B*, 92:035303, Jul 2015.

[240] M. Ritala, K. Kukli, A. Rahtu, P. I. Räisänen, M. Leskelä, T. Sajavaara, and J. Keinonen. Atomic layer deposition of oxide thin films with metal alkoxides as oxygen sources. *Science*, 288(5464):319–321, 2000.

[241] L. Pauling. The nature of the chemical bond. IV. the energy of single bonds and the relative electronegativity of atoms. *Journal of the American Chemical Society*, 54(9):3570–3582, 1932.

[242] W. E. Pickett. Negative electron affinity and low work function surface: cesium on oxygenated diamond (100). *Physical review letters*, 73(12):1664, 1994.

[243] P. E. Pehrsson, J. Long, M. J. Marchywka, and J. E. Butler. Electrochemically induced surface chemistry and negative electron affinity on diamond (100). *Applied physics letters*, 67(23):3414–3416, 1995.

[244] I. P. Batra. Electronic structure of $\alpha - Al_2O_3$. *Journal of Physics C: Solid State Physics*, 15(26):5399, 1982.

[245] J. Lewis, D. Schwarzenbach, and H. D. Flack. Electric field gradients and charge density in corundum, α-Al_2O_3. *Acta Crystallographica Section A*, 38(5):733–739, Sep 1982.

[246] Y. Jia, W. Zhu, E. G. Wang, Y. Huo, and Z. Zhang. Initial stages of ti growth on diamond (100) surfaces: From single adatom diffusion to quantum wire formation. *Physical Review Letters*, 94(8):086101, 2005.

[247] A. Downs. *Chemistry of Aluminium, Gallium, Indium and Thallium.* Springer Netherlands, 1993.

[248] Y. Hinuma, G. Pizzi, Y. Kumagai, F. Oba, and I. Tanaka. Band structure diagram paths based on crystallography. *Computational Materials Science*, 128:140 – 184, 2017.

[249] M. C. James, F. Fogarty, R. Zulkharnay, N. A. Fox, and P. W. May. A review of surface functionalisation of diamond for thermionic emission applications. *Carbon*, 2020.

[250] M. J. Sear, A. K. Schenk, A. Tadich, B. J. Spencer, C. A. Wright, A. Stacey, and C. I. Pakes. Germanium terminated (100) diamond. *Journal of Physics: Condensed Matter*, 29(14):145002, feb 2017.

[251] A. K. Schenk, A. Tadich, M. J. Sear, D. Qi, A. T. S. Wee, A. Stacey, and C. I. Pakes. The surface electronic structure of silicon terminated (100) diamond. *Nanotechnology*, 27(27):275201, may 2016.

[252] J. C. Slater. Atomic radii in crystals. *The Journal of Chemical Physics*, 41(10):3199–3204, 1964.

[253] J. Phillips. *Bonds and Bands in Semiconductors*. Materials Science and Technology. Elsevier Science, 2012.

[254] Y. Jia, W. Zhu, E. G. Wang, Y. Huo, and Z. Zhang. Initial stages of Ti growth on diamond (100) surfaces: From single adatom diffusion to quantum wire formation. *Phys. Rev. Lett.*, 94:086101, Mar 2005.

[255] Y. Morikawa, K. Kobayashi, and K. Terakura. First-principles molecular dynamics study of alkali-metal adsorption on a Si (001) surface. *Surface Science*, 283(1):377 – 382, 1993.

[256] A. Gke and E. Aktrk. A first-principles study of n-type and p-type doping of germanium carbide sheet. *Applied Surface Science*, 332:147 – 151, 2015.

[257] M. J. Sear, A. K. Schenk, A. Tadich, A. Stacey, and C. I. Pakes. Thermal stability and oxidation of group IV terminated (100) diamond surfaces. *physica status solidi (a)*, 215(22):1800283, 2018.

[258] K. Kamitani, M. Grimsditch, J. C. Nipko, C.-K. Loong, M. Okada, and I. Kimura. The elastic constants of silicon carbide: A brillouin-scattering study of 4H and 6H SiC single crystals. *Journal of Applied Physics*, 82(6):3152–3154, 1997.

[259] H. Yao, L. Ouyang, and W.-Y. Ching. Ab initio calculation of elastic constants of ceramic crystals. *Journal of the American Ceramic Society*, 90(10):3194–3204, 2007.

[260] M. Levinshtein, S. Rumyantsev, and M. Shur. *Properties of Advanced Semiconductor Materials: GaN, AlN, InN, BN, SiC, SiGe*. A Wiley-Interscience publication. Wiley, 2001.

[261] C. H. Park, B.-H. Cheong, K.-H. Lee, and K. J. Chang. Structural and electronic properties of cubic, 2H, 4H, and 6H SiC. *Phys. Rev. B*, 49:4485–4493, Feb 1994.

[262] G. Koley, M. V. S. Chandrashekhar, C. I. Thomas, and M. G. Spencer. *Polarization in Wide Bandgap Semiconductors and their Characterization by Scanning Probe Microscopy*, pages 265–305. Springer US, Boston, MA, 2008.

[263] T. Kimoto, Y. Kanzaki, M. Noborio, H. Kawano, and H. Matsunami. Interface properties of metal–oxide–semiconductor structures on 4h-sic {0001} and (1120) formed by n2o oxidation. *Japanese journal of applied physics*, 44(3R):1213, 2005.

[264] H. Yano, T. Hirao, T. Kimoto, and H. Matsunami. A cause for highly improved channel mobility of 4h-sic metal–oxide–semiconductor field-effect transistors on the (1120) face. *Applied Physics Letters*, 78(3):374–376, 2001.

[265] T. Seyller, R. Graupner, N. Sieber, K. Emtsev, L. Ley, A. Tadich, J. Riley, and R. Leckey. Hydrogen terminated 4H-SiC ($1\bar{1}00$) and ($11\bar{2}0$) surfaces studied by synchrotron x-ray photoelectron spectroscopy. *Physical Review B*, 71(24):245333, 2005.

[266] G. P. Brandino, G. Cicero, B. Bonferroni, A. Ferretti, A. Calzolari, C. M. Bertoni, and A. Catellani. Polarization properties of ($1\bar{1}00$) and ($11\bar{2}0$) SiC surfaces from first principles. *Phys. Rev. B*, 76:085322, Aug 2007.

[267] M. Sabisch, P. Krüger, and J. Pollmann. Ab initio calculations of SiC(110) and GaAs(110) surfaces: A comparative study and the role of ionicity. *Phys. Rev. B*, 51:13367–13380, May 1995.

[268] B. B. Jayant. *Silicon carbide power devices*. World scientific, 2006.

[269] E. Rauls, Z. Hajnal, P. Deak, and T. Frauenheim. Theoretical study of the nonpolar surfaces and their oxygen passivation in 4H-and 6H-SiC. *Physical Review B*, 64(24):245323, 2001.

[270] C. Darmody and N. Goldsman. The intrinsic atomic-level surface roughness mobility limit of 4H-SiC. *Journal of Applied Physics*, 124(10):105702, 2018.

[271] Z. Pan, H.-L. Lai, F. C. Au, X. Duan, W. Zhou, W. Shi, N. Wang, C.-S. Lee, N.-B. Wong, S.-T. Lee, et al. Oriented silicon carbide nanowires: synthesis and field emission properties. *Advanced Materials*, 12(16):1186–1190, 2000.

[272] M.-G. Kang, H. J. Lezec, and F. Sharifi. Stable field emission from nanoporous silicon carbide. *Nanotechnology*, 24(6):065201, 2013.

[273] S. Y. Davydov. On the electron affinity of silicon carbide polytypes. *Semiconductors*, 41(6):696–698.

[274] V. Brudnyi and A. Kosobutsky. Electronic properties of SiC polytypes: Charge neutrality level and interfacial barrier heights. *Superlattices and Microstructures*, 111:499 – 505, 2017.

[275] A. A. Lebedev. Heterojunctions and superlattices based on silicon carbide. *Semiconductor Science and Technology*, 21(6):R17–R34, April 2006.

[276] J. G. M. Shaw and P. Briddon. *Marker-Method Calculations for Electrical Levels Using Gaussian-Orbital Basis Sets*, pages 69–94. Springer Berlin Heidelberg, Berlin, Heidelberg, 2007.

[277] A. Stekolnikov, J. Furthmuller, and F. Bechstedt. Absolute surface energies of group-IV semiconductors: dependence on orientation and reconstruction. *Physical Review B*, 65(11):115318, 2002.

[278] N. Sieber, B. F. Mantel, T. Seyller, J. Ristein, L. Ley, T. Heller, D. R. Batchelor, and D. Schmeier. Electronic and chemical passivation of hexagonal 6H-SiC surfaces by hydrogen termination. *Applied Physics Letters*, 78(9):1216–1218, 2001.

[279] R. Macomber. *Organic Chemistry*. Number v. 1 in Organic Chemistry. University Science Books, 1996.

[280] J. M. A. Beattie, J. P. Goss, M. J. Rayson, and P. R. Briddon. Silicon and germanium terminated (001)-(2×1) diamond surface. *Journal of Physics: Condensed Matter*, 31(39):395001, jul 2019.

[281] J. Dean and N. Lange. *Lange's handbook of chemistry*. Lange's Handbook of Chemistry. McGraw-Hill, 1992.

[282] R. A. Silverman and W. Kohn. On the cohesive energy of metallic lithium. *Phys. Rev.*, 80:912–913, Dec 1950.

[283] L. Lottermoser, E. Landemark, D.-M. Smilgies, M. Nielsen, R. Feidenhans'l, G. Falkenberg, R. L. Johnson, M. Gierer, A. P. Seitsonen, H. Kleine, H. Bludau, H. Over, S. K. Kim, and F. Jona. New bonding configuration on Si(111) and Ge(111) surfaces induced by the adsorption of alkali metals. *Phys. Rev. Lett.*, 80:3980–3983, May 1998.

[284] T. M. Grehk, M. Göthelid, M. Björkqvist, G. Le Lay, and U. O. Karlsson. Li-induced phase transition from the Ge(111)3×1 : Li surface reconstruction to the Ge(111)$\sqrt{3} \times \sqrt{3}$: Li lithium germanide. *Phys. Rev. B*, 61:4963–4967, Feb 2000.

[285] K. Doll, N. M. Harrison, and V. R. Saunders. A density functional study of lithium bulk and surfaces. *Journal of Physics: Condensed Matter*, 11(26):5007–5019, Jan 1999.

[286] B. Brito, L. Cndido, J. T. Rabelo, and G.-Q. Hai. Binding energies of small lithium clusters: A comparison of different theoretical calculations. *Chemical Physics Letters*, 616-617:212 – 216, 2014.

[287] S. E. Wheeler, K. W. Sattelmeyer, P. v. R. Schleyer, and H. F. Schaefer. Binding energies of small lithium clusters (Li n) and hydrogenated lithium clusters (LinH). *The Journal of Chemical Physics*, 120(10):4683–4689, 2004.

[288] R. Rousseau and D. Marx. Exploring the electronic structure of elemental lithium: From small molecules to nanoclusters, bulk metal, and surfaces. *Chemistry A European Journal*, 6(16):2982–2993, 2000.

[289] O. Malyi, V. V. Kulish, T. L. Tan, and S. Manzhos. A computational study of the insertion of Li, Na, and Mg atoms into Si(111) nanosheets. *Nano Energy*, 2(6):1149 – 1157, 2013.

[290] B. Temelso and C. D. Sherrill. High accuracy ab initio studies of Li 6+, Li 6-, and three isomers of Li 6. *The Journal of chemical physics*, 122(6):064315, 2005.

[291] L. Johansson and B. Reihl. Alkali metals on Si(100)2×1: comparative study of the surface electronic structures for Li, Na and K adsorption. *Surface Science*, 287-288:524 – 528, 1993.

[292] M. A. Capano, J. A. Cooper, M. R. Melloch, A. Saxler, and W. C. Mitchel. Ionization energies and electron mobilities in phosphorus- and nitrogen-implanted 4H-silicon carbide. *Journal of Applied Physics*, 87(12):8773–8777, 2000.

[293] H. Pinto, R. Jones, D. Palmer, J. Goss, A. K. Tiwari, P. Briddon, N. G. Wright, A. B. Horsfall, M. Rayson, and S. Öberg. First-principles studies of the effect of (001) surface terminations on the electronic properties of the negatively charged nitrogen-vacancy defect in diamond. *Physical Review B*, 86(4):045313, 2012.

[294] W. F. Koehl, B. B. Buckley, F. J. Heremans, G. Calusine, and D. D. Awschalom. Room temperature coherent control of defect spin qubits in silicon carbide. *Nature*, 479(7371):84, 2011.

[295] M.-G. Kang, H. J. Lezec, and F. Sharifi. Stable field emission from nanoporous silicon carbide. *Nanotechnology*, 24(6):065201, 2013.

[296] K. L. Aplin and V. P. Tarakanov. Modelling studies of charged particle interactions for a space application. *Conference Series - Institute of Physics*, volume 178, pages 221–226. Philadelphia; Institute of Physics; 1999, 2004.

[297] S. T. Lai. *Spacecraft charging*. American Institute of Aeronautics and Astronautics, 2011.

[298] K. Skalska, J. S. Miller, and S. Ledakowicz. Trends in NOx abatement: A review. *Science of The Total Environment*, 408(19):3976 – 3989, 2010.

[299] S. Mankefors, P. Nilsson, and J. Kanski. Semiconductor polar surfaces: mechanisms of the stability of non-reconstructed III–V $(\bar{1}\bar{1}\bar{1})$ surfaces. *Surface science*, 443(3):L1049–L1054, 1999.

[300] S. Krukowski, P. Kempisty, and P. Strak. Electrostatic condition for the termination of the opposite face of the slab in density functional theory simulations of semiconductor surfaces. *Journal of Applied Physics*, 105(11):113701, 2009.

[301] P. Kempisty, S. Krukowski, P. Strak, and K. Sakowski. Ab initio studies of electronic properties of bare GaN (0001) surface. *Journal of Applied Physics*, 106(5):054901, 2009.

[302] J. Neugebauer and M. Scheffler. Adsorbate-substrate and adsorbate-adsorbate interactions of Na and K adlayers on Al(111). *Physical Review B*, 46(24):16067–16080, 1992.

[303] J. Olander and K. Larsson. Influence of adsorbed species on the reconstruction of 4H-SiC(0001) surfaces. *The Journal of Physical Chemistry B*, 105(32):7619–7623, 2001.

[304] E. Wachowicz and A. Kiejna. Structure and energetics changes during hydrogenation of 4H-SiC {0001} surfaces: a DFT study. *Journal of Physics: Condensed Matter*, 24(38):385801, 2012.

[305] M. Sabisch, P. Krüger, and J. Pollmann. Ab initio calculations of structural and electronic properties of 6H-SiC (0001) surfaces. *Physical Review B*, 55(16):10561, 1997.

[306] K. Emtsev, T. Seyller, L. Ley, L. Broekman, A. Tadich, J. Riley, R. Leckey, and M. Preuss. Correlation effects at ideal SiC {0001}-(1×1) surfaces. *Physical Review B*, 73(7):075412, 2006.

[307] M. Rashid, A. K. Tiwari, J. P. Goss, M. J. Rayson, P. R. Briddon, and A. B. Horsfall. Surface-state dependent optical properties of OH-, F-, and H-terminated 4H-SiC quantum dots. *Phys. Chem. Chem. Phys.*, 18:21676–21685, 2016.

[308] V. Eremenko, V. Sirenko, I. Gospodarev, E. Syrkin, S. Feodosyev, I. Bondar, and K. Minakova. Anisotropic behavior and inhomogeneity of atomic local densities of states in graphene with vacancy groups. *Journal of Science: Advanced Materials and Devices*, 1(2):167 – 173, 2016. Special Issue in Memory of Dr. P.E. BROMMER.

[309] R. Wang, J. Yang, X. Wu, and S. Wang. Local charge states in hexagonal boron nitride with Stone–Wales defects. *Nanoscale*, 8(15):8210–8219, 2016.

[310] H. Tsuchida, I. Kamata, and K. Izumi. Si–H bonds on the 6H–SiC (0001) surface after H_2 annealing. *Japanese journal of applied physics*, 36(6A):L699, 1997.

[311] J. Olander and K. Larsson. An ab initio study of 4HSiC(0001) and $(000\bar{1})$ surface processes at experimental temperatures. *Thin Solid Films*, 458(1):191 – 196, 2004.

[312] J. Beattie, J. Goss, M. Rayson, and P. Briddon. Structure and electron affinity of $(11\bar{2}0)$X 4HSiC surface. *Applied Surface Science*, 518:145986, 2020.